

Non-radiative relaxation mechanisms of electronically excited phenylalanine in model peptides

Mališ, Momir

Doctoral thesis / Disertacija

2015

Degree Grantor / Ustanova koja je dodijelila akademski / stručni stupanj: **University of Zagreb, Faculty of Science / Sveučilište u Zagrebu, Prirodoslovno-matematički fakultet**

Permanent link / Trajna poveznica: <https://um.nsk.hr/um:nbn:hr:217:496033>

Rights / Prava: [In copyright](#)/[Zaštićeno autorskim pravom.](#)

Download date / Datum preuzimanja: **2024-08-15**



Repository / Repozitorij:

[Repository of the Faculty of Science - University of Zagreb](#)





University of Zagreb
FACULTY OF SCIENCE

Momir Mališ

**NON-RADIATIVE RELAXATION MECHANISMS OF
ELECTRONICALLY EXCITED PHENYLALANINE IN
MODEL PEPTIDES**

DOCTORAL THESIS

Supervisor:
Dr. Nađa Došlić, Senior Scientist

Zagreb, 2015



Sveučilište u Zagrebu
PRIRODOSLOVNO-MATEMATIČKI FAKULTET

Momir Mališ

**NERADIJATIVNI RELAKSACIJSKI MEHANIZMI
ELEKTRONSKI POBUĐENOG FENILALANINA U
MODELNIM PEPTIDIMA**

DOKTORSKI RAD

Mentor:
dr. sc. Nađa Došlić, zn. savj.

Zagreb, 2015

baki Milki

Zahvala/Acknowledgment

Veliko hvala/Huge thank you...

...mentorici dr. sc. Nađi Došlić na svim savjetima, kako znanstvenim tako i životnim, pomoći, kritikama, korekcijama, konferencijama, a ponajviše na velikome strpljenju te vedrom i veselom duhu.

...Jurici, Ivanu i Darku na pomoći oko programiranja, diskusijama, savjetima te ugodnoj i motivirajućoj radnoj atmosferi.

...Marinu, Marku, Danku i Saši na znanstvenim diskusijama.

...Vladimiru Damjanoviću, najboljem cimeru i prijatelju, na moralnoj potpori, velikome optimizmu i nesebičnoj pomoći.

...Zlatku Brkljači na lekturi, korekcijama i diskusijama.

...to Michel, Eric, Yohan, Valérie and Benjamin for all the experiments performed on NAPA and NAPMA as well as for the enjoyable stay in Paris.

...to Dr. Christophe Jouvét for performing some Hessian matrix calculations.

...to Dr. Sergy Yu. Grebenshchikov and Dr. Ralph Gebauer for the discussion.

...Emiru i Hrvoju na pomoći oko računalnih resursa CRO-NGI-ja i EGI-ja.

...mami, tati i sestri na beskrajnoj ljubavi i potpori.

Momir Mališ

Contents

Abstract	ix
Sažetak	xi
Prošireni sažetak	xiii
1 Introduction	1
2 Literature overview	6
2.1 Experimental results	6
2.1.1 Ground and excited state properties of NAPA in gas phase	6
2.1.2 Excited state lifetimes of deuterated NAPA isotopologues and NAPMA	7
2.2 Previous theoretical results	10
2.2.1 Electronic ground state properties of NAPA conformers	10
2.2.2 Electronic absorption spectrum of NAPA conformers	13
2.3 Non-radiative deactivation (NRD) mechanism of analogue chromophores	15
2.3.1 NRD pathway of benzene and toluene S_1 excited states	15
2.3.2 Vertical excited states of the amide groups in peptide systems	17
2.3.3 NRD mechanisms of formamide	18
2.3.4 H-transfer assisted NRD mechanism between amide groups in peptide systems	20
2.3.5 NRD mechanisms in Phe or Trp containing peptide systems	21
2.3.6 Non-adiabatic molecular dynamics of Trp systems	26
3 Theory and Methods	28
3.1 Initial axioms and approximations of the quantum system	28
3.2 Conical intersection	34
3.3 Derivation and concepts of surface hopping non-adiabatic molecular dynamics	42
3.4 Dynamical couplings in linear response time dependent density functional theory	55
3.5 Implementation of non-adiabatic molecular dynamics procedure	70
3.6 Methods and program packages	72
4 Results and Discussion	75
4.1 Nature and energetics of NAPA conformers excited states	75
4.1.1 NAPA excited states	75
4.1.2 NAPA vibronic states	81
4.1.3 NAPA excited states at the LR-TDDFT level of theory	84

4.1.4	NAPMA ground and excited states	87
4.2	Non-adiabatic molecular dynamics of NAPA conformer B	90
4.2.1	Mechanism II	92
4.2.2	Mechanism III	96
4.2.3	Mechanism I	97
4.3	Refinement of NRD mechanisms	99
4.3.1	Refinement of mechanism III	99
4.3.2	Refinement of mechanism I	102
4.4	Refinement of mechanism II	107
4.4.1	Local minimum structures of $n\pi^*_{(\text{II})}$ state	108
4.4.2	$\pi\pi^*/n\pi^*_{(\text{II})}$ CI points	111
4.5	Accessibility of the $\pi\pi^*/n\pi^*_{(\text{II})}$ CI seam	115
4.5.1	Mechanism II in NAPA and NAPMA conformers A and C	137
4.6	Phenyl ring-puckering mechanism	139
4.7	Interplay of NRD mechanisms	141
5	Conclusion	145
6	References	147
	Curriculum vitae	xxiii



University of Zagreb
Faculty of Science
Department of Chemistry

Doctoral Thesis

ABSTRACT

NON-RADIATIVE RELAXATION MECHANISMS OF ELECTRONICALLY EXCITED PHENYLALANINE IN MODEL PEPTIDES

Momir Mališ

Ruder Bošković Institute, Bijenička cesta 54, 10000 Zagreb, Croatia

A systematic study of the non-radiative deactivation mechanisms of the three photoexcited *N*-acetylphenylalanyl amide conformers was conducted in order to disclose the experimentally observed conformational dependent lifetime of phenyl vibrationless ${}^1\pi\pi^*$ excited state. The all-atom trajectory surface hopping non-adiabatic molecular dynamics simulations, based on linear response time dependent density functional theory, were utilized for blind screening of relaxation pathways and revealed a number of excitation transfer mechanisms from ${}^1\pi\pi^*$ to the ${}^1n\pi^*$ excited states localized on each of the two amide groups. Possible pathways were further refined by obtaining conical intersection barrier energies from corresponding reaction paths constructed at the coupled cluster (CC2) level of theory. Finally, from semiclassical consideration of conical intersection accessibility with only the nuclear zero point vibrational energy and from the increased rigidity of the second amide group towards distortion upon its methylation, it was concluded that the classically accessible part of conical intersection seam for population transfer to the ${}^1n\pi^*$ state of the second amide group is the largest for the conformer with the shortest ${}^1\pi\pi^*$ state lifetime.

(157 + xxv pages, 41 figures, 14 tables, 183 references, original in English)

Thesis deposited in Central Chemical Library, Horvatovac 102A, Zagreb, Croatia and National and University Library, Hrvatske bratske zajednice 4, Zagreb, Croatia.

Keywords: CC2/Conical intersection seam/Non-adiabatic molecular dynamics/Non-radiative deactivation/Peptide/Phenylalanine/TDDFT

Supervisor: Dr. Nađa Došlić, Senior Scientist

Reviewers: Dr. Zlatko Mihalić, Professor
Dr. Piero Decleva, Professor
Dr. Nađa Došlić, Senior Scientist

Thesis accepted: May 27, 2015



Sveučilište u Zagrebu
Prirodoslovno-matematički fakultet
Kemijski odsjek

Doktorska disertacija

SAŽETAK

NERADIJATIVNI RELAKSACIJSKI MEHANIZMI ELEKTRONSKI POBUĐENOG FENILALANINA U MODELNIM PEPTIDIMA

Momir Mališ

Institut Ruđer Bošković, Bijenička cesta 54, 10000 Zagreb, Hrvatska

Provedeno je sustavno istraživanje neradijativnih deaktivacijskih mehanizama odgovornih za eksperimentalno opaženu konformacijsku ovisnost vremena života vibracijski osnovnog pobuđenog fenilnog ${}^1\pi\pi^*$ elektronskog stanja u tri konformera *N*-acetilfenilalanilamida. Simulacije metodom neadijabatske molekulske dinamike, s preskokom među plohama elektronske potencijalne energije dobivenih vremenski ovisnom teorijom funkcionala gustoće, ukazale su na nekoliko mehanizama prijenosa ekscitacije iz ${}^1\pi\pi^*$ u ${}^1n\pi^*$ stanja locirana na pojedinim amidnim grupama. Pronađeni mehanizmi potom su utočnjeni pripadajućim vrijednostima energijama barijera koničnih presjecišta dobivenih ih reakcijskih puteva izračunatim na razini teorije spregnutih grozdova (CC2). Konačno, iz poluklasičnog razmatranja dostupnosti koničnog presjecišta samo na temelju nuklearne vibracijske energije nulte točke te iz povećanja rigidnosti druge peptidne skupine naspram njene deformacije usljed metilacije, određeno je kako klasično dostupan dio šava koničnog presjecišta za prijenos populacije u ${}^1n\pi^*$ stanje druge peptidne skupine je najveći u konformeru s najkraćim vremenom života pobuđenog ${}^1\pi\pi^*$ stanja.

(157 + xxv stranica, 41 slika, 14 tablica, 183 literaturna navoda, jezik izvornika: engleski)

Rad je pohranjen u Središnjoj kemijskoj knjižnici, Horvatovac 102A, Zagreb i Nacionalnoj i sveučilišnoj knjižnici, Hrvatske bratske zajednice 4, Zagreb.

Ključne riječi: CC2/fenilalanin/neadijabatska molekulska dinamika/neradijativna deaktivacija/peptidi/šav koničnih presjecišta/vremenski ovisna teorija funkcionala gustoće

Mentor: dr. sc. Nađa Došlić, znan. savj.

Ocjenitelji: prof. dr. sc. Zlatko Mihalić
prof. dr. sc. Piero Decleva
dr. sc. Nađa Došlić, zn. savj.

Rad prihvaćen: 27. svibnja 2015



Sveučilište u Zagrebu
Prirodoslovno-matematički fakultet
Kemijski odsjek

Doktorska disertacija

PROŠIRENI SAŽETAK

Uvid u fotokemiju proteina bitan je za razumijevanje procesa prijenosa energije u prirodi, a kratki peptidi predstavljaju izvrsne teorijske i eksperimentalne modelne sustave. [15–17]

Eksperimenti pump-probe UV identifikacije konformera modelnog peptida *N*-acetilfenilalanilamida (NAPA, primarna struktura: Ac-Phe-NH₂) prisutnih u plinskoj fazi ukazali su na izostanak fluorescencije u jednom od tri konformera prethodno detektiranih tehnikom fotoionizacije. [20] Usporedbom teorijskog IR spektra s eksperimentalnim pridružena mu je struktura $\gamma_L(g+)$ sedmeročlanog prstena (Toniolova nomenklatura sekundarnih peptidnih struktura), a mjerenja brzine depopulacije njegovog vibracijski najnižeg prvog pobuđenog fenilnog $\pi\pi^*$ elektronskog stanja ($\tau = 1.5 \pm 0.3$ ns) pokazala su, za red veličine, kraće vrijeme srednjeg života s obzirom na preostala dva detektirana konformera, $\gamma_L(g-)$ (35 ± 2 ns) i $\beta_L(a)$ (70 ± 2 ns), [23] ukazujući na brzi neradijativni relaksacijski mehanizam pobuđenog $\pi\pi^*$ stanja prisutnog u $\gamma_L(g+)$ konformeru. Detaljni teorijski računi osnovnih elektronskih stanja potvrdili su kako su tri pronađena konformera energijski najstabilniji, [36, 38] a opaženi fenomen možda objašnjava odsutnost signala najstabilnijih konformera u sličnim peptidnim sustavima. [25] Osim rada Došlić *et al.* koji su uz vrlo detaljnu vibracijsku analizu osnovnog stanja reproducirali elektronska prijelaze triju konformera, [38] nema poznatih drugih istraživanja pobuđenih stanja molekule NAPA, kao ni objašnjenja anomalnog efekta kratkog vremena života njenog pobuđenog $\gamma_L(g+)$ konformera. NAPA stoga predstavlja idealni model za detaljno teorijsko razmatranje dinamike u pobuđenim elektronskim stanjima. Nadalje, eksperimentalno je pokazano kako metiliranje druge amidne skupine značajno produljuje vrijeme života $\gamma_L(g+)$ konformera molekule *N*-acetilfenilalanilmetilamida (NAPMA, primarna struktura: Ac-Phe-NHMe) na 48 ± 3 ns, dok su vremena života preostala dva konformera, istih analognih struktura preostalim dvama konformerima molekule NAPA, neznatno promijenjena na 62 ± 3 ns za $\gamma_L(g-)$ i 67 ± 3 ns za $\beta_L(a)$ konformer. [33] Deuterijski izotopolozi triju konformera molekule NAPA ne pokazuju nikakav signifikantan izotopni efekt na neradijativne deaktivacijske procese pobuđenog $\pi\pi^*$ stanja uslijed supstitucije određenih procijevih atoma vezanih za dušikove atome amidnih skupina. [23]

Valni paket atomskih jezgara, pobuđen u više elektronsko stanje apsorpcijom elektro-

magnetskog zračenja, evoluirala po plohama elektronske energije (PEE) prelazeći s jedne na drugu najčešće kroz konična presjecišta (engl. *conical intersection*, CI) ili pak emisijom zračenja (fluor- ili fosforescencijom) ukoliko je prvi način onemogućen. [79] Početni uvjeti te topologija PEE-a definirat će njegovu vremensku propagaciju tj. skup aktivnih fotokemijskih mehanizama, a raznolikost istih ovisit će o prisutnim kromoforima.

Tako proteini, uz nukleinske kiseline, sa svojim mnoštvom kromofora imaju potencijalno bogatu fotokemiju. Kromofori s najvećim apsorpcijskim koeficijentom tj. prijelaznim dipolnim momentom su indolni, fenolni i fenilni bočni ogranci aminokiselina triptofana (Trp), tirozina (Tyr) i fenilalanina (Phe). Uvijek prisutne amidne skupine (uključujući i one u bočnim lancima asparagina i glutamina) zajedno sa slobodnim karboksilnim skupinama čine tamna $n\pi^*$ i $\pi\pi^*$ stanja sustava, koja su zbog malog prijelaznog dipolnog momenta nedostupna direktnom apsorpcijom [54, 55]. Tu su još i stanja koja uključuju slobodne elektronske parove, Rydbergova te stanja s prijenosom naboja (engl. *charge transfer*, CT). [54–56] Interakcija pobuđenih $\pi\pi^*$ elektronskih stanja konjugiranih kromofornih prstenova s ovalikim brojem ostalih stanja čini fotokemiju proteina daleko složenijom od fotodinamike izoliranih kromofora. [180]

Zbog svoje izrazite kompleksnosti, istraživanja ultrabrzih relaksacijskih mehanizama u proteinima predstavljaju stanovit izazov. Razvoj modernih kvantno-kemijskih metoda za opis pobuđenih elektronskih stanja poput vremenski ovisne teorije funkcionala gustoće (TDDFT), spregnutih grozdova (CC) i dr. te neadijabatske molekulske dinamike u pobuđenim stanjima omogućio je prekretnicu u istraživanju fotokemije proteina sustavnom teorijskom analizom fotodinamike peptida, aminokiselina i analognih spojeva u plinskoj fazi, često potpomognute eksperimentima vremenski razlučene spektroskopije.

Od tri glavne skupine kromofora, najizučavanije su molekule s Trp u svojoj strukturi, budući da koncepti za objašnjenje izostanka njegove intrinzične fluorescencije mogu poslužiti u rasvjetljavanju fotodinamike drugih aminokiselina. Tako su Shemesh *et al.* predložili mehanizam za objašnjenje nepravilnosti vibronskih prijelaza u eksperimentalnom spektru konformera molekule Ac-Trp-NHMe, [26, 32] strukturno analognih NAPA konformerima. Uz postojanje minimuma indolnog $\pi\pi^*$ stanja koje se može relaksirati u osnovno homolitičkom disocijacijom indole NH veze, autori su pronašli jedan stabilniji minimum na pobuđenoj PPE koji odgovara $n\pi^*$ pobuđenom stanju s distorziranom amidnom skupinom N -kraja. Kod konformera s jakom vodikovom vezom unutar sedmeročlanog γ_L prstena procijenjena barijera iz koničnog presjecišta $\pi\pi^*$ i $n\pi^*$ stanja je najmanja za prijenos populacije iz $\pi\pi^*$ u $n\pi^*$ stanje, nakon čega se potonje stanje može prekriziti s CT stanjem mehanizmom prijenosa protona s druge na prvu amidnu skupinu duž spomenute vodikove veze. Prilikom prijenosa vodikova atoma paralelno se destabilizira osnovno stanje što konačno završava međusobnim križanjem osnovnog i CT stanja.

Ovaj rezultat zajedno sa sličnim rezultatima dobivenih na analognim peptidnim sustavim [30] po prvi puta detaljno sugerira važnost amidne skupine u depopulaciji aromatskog $\pi\pi^*$ stanja, a predloženi mehanizam istovremeno objašnjava konformacijsku specifičnost molekule Ac-Trp-NHMe. Međutim, predloženi mehanizam relaksacije kao i način lokacije kritičnog minimuma $n\pi^*$ stanja nužno uključuje motiv vodikove veze. Nadovezujući se na neradijativne deaktivacijske mehanizme formamida kao najjednostavnijeg modela amidne skupine, [57] relaksacija u osnovno stanje pobuđene amidne skupine moguća je disocijacijom C-N ili predisocijacijom C=O veze bez posredovanja vodikove veze. Simulacije relaksacije pobuđenog formamida korištenjem neadijabatske molekulske dinamike potvrdile su prethodno istraženu raznolikost. [58]

Za slučaje modelnih peptida s Phe, Shemesh i suradnici objasnili su izostanak signala konformera tripeptida Gly-Phe-Ala s dvostrukom γ_L strukturom ponovo ukazujući na efikasnu depopulaciju preko $n\pi^*$ stanja prve amidne skupine potaknute istezanjem vodikove veze. [31] Na skupu zaštićenih Ac-Phe-Xxx-NH₂ (Xxx = L-Ala, D-Ala) dipeptida, isti autori razmotrili su utjecaj apsolutne konfiguracije na svoj predloženi mehanizam. [62] Iako rezultati ponovno upućuju kako je mehanizam prijenosa pobude iz $\pi\pi^*$ u $n\pi^*$ stanje bitan za depopulaciju prvog stanja, mehanizmi su u oba slučaja opet unaprijed pretpostavljeni. Za razliku od prethodnih, Mercier *et al.* su upotrijebili neadijabatsku CPMD za sustavniju analizu relaksacije pobuđenog stanja slobodnog i mikrosolvatiranog TrpH⁺ kationa te time izbjegli pretpostavljanje a priori deaktivacijskog mehanizma, ali osim disocijacije C-N veze preko $\pi\sigma^*$ stanja te izlaska molekule amonijaka nisu detaljnije pretraživali PPE pobuđenog stanja. [64]

Iz prethodno navedenog proizlazi kako je potreban sustavniji pristup pronalaženju deaktivacijskih mehanizama elektronski pobuđenih peptida. Pristup bez, po mogućnosti ikakvog, pretpostavljanja relaksacijskog puta unaprijed. Neadijabatska molekulska dinamika na razini vremenski ovisne teorije funkcionala gustoće u aproksimaciji linearnog odziva (engl. *linear response time dependent density functional theory*, LR-TDDFT) stoga predstavlja opravdani izbor kao metoda za slijepo pretraživanje neradijativnih deaktivacijskih procesa u sustavima veličine modelnih peptida, međutim na račun izostavljanja kvantnih efekata poput tuneliranja, energije nulte točke, interferencija valnih paketa itd. Također, sama upotreba LR-TDDFT metode za konstrukciju PPE-a potencijalno može podcjeniti ili precjeniti aktivnost određenih mehanizama. Ipak, provjerom svakog potencijalnog mehanizma na višoj razini teorije za opis elektronske strukture moguće je ukloniti intrinzične nedostatke nastale korištenjem niže razine teorije. Nuklearni kvantni efekti mogu se uvesti naknadno.

Stoga je cilj ove disertacija objasniti neradijativne deaktivacijske mehanizme aktivne u konformerima molekule NAPA pomoću strategije utočnjavanja indikativnih relaksacijskih

mehanizama dobivenih metodom neadijabatske molekulske dinamike. Dinamički uvid u depopulaciju popuđenih stanja kao i globalna topologija šava koničnih presjecišta u peptidnim sustavima također će biti razmatrana.

Napisan je vlastiti računalni kôd u programskom jeziku Fortran 90 za opis evolucije sustava u pobuđenim elektronskim stanjima metodom neadijabatske molekulske dinamike. [23] U korištenom pristupu, elektronski dio sustava opisan je linearnom kombinacijom osnovnog i nekoliko pobuđenih elektronskih stanja u adijabatskoj reprezentaciji čije su populacije određene vremenski ovisnom Schrödingerovom jednađbom, dok je dinamika jezgara opisana Newtonovim jednađbama gibanja propagiranih isključivo samo po jednoj, trenutno zaposjednutoj, adijabatskoj plohi potencijalne energije sve dok elektronska populacija ne zadovolji uvjete za promjenu zaposjednutosti. [99] Elektronski dio parametarski ovisi o koordinatama jezgara pa je uz energije te analitički gradijent trenutno zaposjednutog elektronskog stanja potrebno još izračunati neadijabatske sprege između svih parovima elektronskih stanja. Newtonove jednađbe propagiraju se Verletovim algoritmom u diskretnim vremenskim koracima Δt , pri čemu se u svakom koraku konstruiraju elektronska stanja, dok se neadijabatska sprega između para stanja računa numeričkom derivacijom promijene istih stanja u vremenu koja se svodi na određivanje integrala prekrivanja između valnih funkcija trenutnog i prethodnog koraka trajektorije. Budući kako se za konstrukciju elektronskih stanja koristi LR-TDDFT metoda, sprege među stanjima računaju se koristeći pomoćne valne funkcije, u čijem opisu osnovno stanje je dano Slaterovom determinantom sačinjenu od popunjenih Kohn-Shamova (KS) orbitala, dok je svako pobuđeno stanje linearna kombinacija singletnih jednostruko pobuđenih Slaterovih determinanti u kojoj je jedna okupirana KS orbital zamijenjena virtualnom KS orbitalom. [115, 116, 118–121] Time određivanje članova neadijabatskih sprega postaje zbrajanje determinanti s elementima integrala prekrivanja određenih KS orbitala, [117] što je efikasno ubrzano SMP načinom paralelizacije te isključivanjem iz sume članova čiji su koeficijenti determinanti manji od unaprijed zadane vrijednosti. Pri tome se podešavaju predznaci koeficijenata i KS orbitala prema predznacima u prethodnom koraku kako bi se vrijednosti neadijabatskih sprega kontinuirano mijenjale tokom propagacije. Unutar svakog nuklearnog koraka trajektorije, koeficijenti populacije elektronskih stanja propagiraju se s $N (> 0)$ konsekutivnih korištenja Shampine-Gordonove integracijske metode s vremenskim korakom od $\Delta t/N$ pri čemu se svaki put Tullyevim algoritmom [99] odredi trenutno zauzeta ploha. [107] Ukoliko dođe do zamijene stanja, brzine jezgara se skaliraju kako bi ukupna energija ostala očuvana, dok prijelaz u elektronsko stanje veće energije od ukupne nije moguć. Program koristi Turbomole programski paket za sve potrebne TDDFT izračune. [133] Osim neadijabatske dinamike program može vršiti propagaciju trajektorija samo u osnovnom elektronskom stanju, po potrebi termostatiranu na određenu

temperaturu primjenom Berendsenovog termostata.

Rekonstruirani S_1 fenilni $\pi\pi^*$ apsorpcijski prijelazi NAPA konformera na RI-CC2/cc-pVDZ razini teorije [138, 139, 144, 181, 182] korigirani za energiju nulte točke vibracijskih stanja u dobrom su slaganju s eksperimentalnim [20, 23] i teorijskim [38] vrijednostima. Odmah do vertikalne geometrije S_1 stanja postoji minimum ($M_{\pi\pi^*}$) istog stanja sličan S_1 minimumu benzena i toluena. [39, 41] U geometrijama minimuma matrice drugih derivacija elektronske energije potrebne za harmonijsku korekciju dobivene su numeričkim postupkom. Drugo i treće pobuđeno stanje odgovara lokalnim $n\pi^*$ ekscitacijama pojedinih amidnih grupa, dok je četvrto stanje drugo pobuđeno stanje fenila. Izbor korelacijsko-izmjenjskog funkcionala prilikom korištenja TDDFT metode ne utječe na sustavno podizanje energija svih stanja za $\sim 0,2$ eV ili više u odnosu na CC2 vrijednosti, a spuštanje stanja CT karaktera među lokalne ekscitacije česta je pojava. PBE0 [140, 142, 143, 183] i BHLYP [141] funkcionali s Dunningovim cc-pVDZ osnovnim skupom izabran je kao najbolji kompromis između točnosti i računске zahtjevnosti te je isti korišten i u neadijabatskoj molekularnoj dinamici. Hibridni funkcionali s manjim udjelom egzaktne Hartreejeve izmjene, uključujući PBE, PBE0 i B3LYP, ne mogu reproducirati minimum S_1 stanja u NAPA $\gamma_L(g+)$ i $\gamma_L(g-)$ konformerima zbog križanja CT stanja s početnim fenilnim stanjem. Sva svojstva elektronskih stanja NAPMA konformera potpuno su analogna svojstvima NAPA konformera.

Neadijabatska molekularna dinamika izvedena je na NAPA $\gamma_L(g+)$ konformeru budući da isti ima jaku vodikovu vezu unutar γ_L prstena i slabu $NH \cdots \pi$ interakciju. Početni uvjeti (geometrije i brzine) dobiveni su iz 50 ps duge trajektorije u osnovnom stanju propagacijom na DFT(PBE)/SVP razini teorije te termostatiranoj na temperaturu od 298 K. Nakon uklanjanja ekvibracijskog perioda, 44 početna uvjeta odabrana su za simulaciju relaksacije iz pripadajućeg prvog pobuđenog stanja, gdje je svaka pojedina trajektorija propagirana sve do križanja s osnovnim elektronskim stanjem. Detaljna analiza trajektorija ukazala je na potencijalno tri različita mehanizma relaksacije početnog pobuđenog stanja: U mehanizmu I prijenos ekscitacije iz fenilnog $\pi\pi^*$ u $n\pi^*$ stanje prve amidne skupine popraćen je deformacijom iste skupine, u mehanizmu II prijenos ekscitacije iz fenilnog $\pi\pi^*$ u $n\pi^*$ stanje druge amidne skupine uzrokuje deformaciju iste skupine dok je mehanizam III prijenos ekscitacije iz fenilnog $\pi\pi^*$ u CT stanje spregnut s prijenosom vodikova atoma iz susjedne $N_{Phe}H$ skupine na *ortho (ipso)* ugljikov atom fenilnog prstena, što silno uzrokuje destabilizaciju osnovnog elektronskog stanja i njeno križanje s CT stanjem. Deaktivacije prva dva mehanizma u osnovno stanje uzrokovana je predisocijacijom C-N i C=O veza pobuđenih amidnih skupina slično deaktivaciji pobuđenih molekula formamida i acetamida. [58] [169] U mehanizmu I moguć i prijenos vodikova atoma s druge na prvu amidnu skupinu duž vodikove veze, slično predloženim mehanizmima od strane Shemesh

et al. [30–32,62]

Utočnjavanju predloženih mehanizama pristupilo se na RI-CC2/cc-pVDZ razini teorije korištenjem triju komplementarnih pristupa: (i) optimizacijom reprezentativnih geometrija pobuđenih stanja dobivenih neadijabatskom molekulskom dinamikom; (ii) optimizacijama s restrikcijom određene duljine veze na fiksnu vrijednost kako bi se konstruirao put najmanje energije definiran istom vezom; (iii) konstrukcijom reakcijskih puteva interpolacijom (engl. *linear interpolation path*, LIP) između dvaju odabranih geometrija u internim koordinatama [30–32,62]. Tako su pune optimizacije reprezentativnih geometrija pobuđenih amidnih skupina dale nekoliko minimuma na odgovarajućim PPE. Ekvivalentni minimumi potom su rekonstruirani i za NAPMA $\gamma_L(g+)$ konformer supstitucijom distalnog vodika metilnom skupinom, dok su analogni minimumi pojedinačno rekonstruirani i za preostala dva NAPA i NAPMA konformera namještanjem odgovarajućih internih koordinata naprema $\gamma_L(g+)$ strukturama.

Za provjeru ispravnosti mehanizma III konstruiran je reakcijski put najmanje energije istežanjem $N_{\text{Phe}}\text{-H}$ veze prema fenilnom prstenu počevši od $M_{\pi\pi^*}$ strukture sve dok sila među atomima nije postala odbojna. Put je utočnjen LIP dobivenim energijama iz kojega je za NAPA $\gamma_L(g+)$ konformer procijenjena barijera od 0.48 eV. Barijera je samo adijabatski rez oko šava koničnog presjecišta između $\pi\pi^*$ i CT plohe s koničnim presjecištem minimalne energije od 0.76 eV. Puna optimizacija pokrenuta iz geometrije s repulzivnim silama između N_{Phe} i H atoma vodi ka prijenosu vodikova atoma na *ortho* ugljikov atom fenilnog prstena uz križanje CT i osnovnog elektronskog stanja. NAPA $\gamma_L(g-)$ konformer pokazuje pravo konično presjecište na 0.64 eV iznad $\pi\pi^*$ minimuma, dok je $\beta_L(a)$ konformer sličniji $\gamma_L(g+)$ samo s barijerom od 0.55 eV. Ovako visoke barijere duž kojih je tuneliranje vodikova atoma zanemarivo uz eksperimentalni izostanak bilo kakvog izotopnog efekta samo potvrđuje kako neradijativna relaksacija $\pi\pi^*$ stanja nije moguća preko mehanizam III, odnosno kako je isti mehanizam samo artefakt korištenog PBE0 funkcionala. Potpuno identičan scenarij je među konformerima molekule NAPMA. Upravo konstrukcija početnih uvjeta iz trajektorije osnovnog stanja termostatirane na višoj temperaturi nego stvarnoj (eksperimentalna vibracijska temperatura je 0 K) omogućili su pretraživanja šireg dijela konfiguracijskog prostora PPE pobuđenog stanja. U suprotnome, trajektorije bi slijedile samo strmi gradijent CT stanja prema osnovnome čime bi mehanizam III bio jedini dominantni reakcijski kanal dobiven neadijabatskom dinamikom.

U NAPA $\gamma_L(g+)$ konformeru pet distinktnih minimuma na $n\pi_{(1)}^*$ PPE prve amidne skupine razlikuju se u relativnim položajima C=O i $N_{\text{Phe}}\text{-H}$ veza. Minimumi su pojedinačno za -0.78 , -0.69 , -0.72 , -0.58 i -0.68 eV stabilniji od $M_{\pi\pi^*}$, dok je pripadajuće stanje povezano s početnim $\pi\pi^*$ stanjem preko koničnih presjecišta koja čine barijeru između dvaju stanja. Vrijednosti barijera konstruirane LIP pristupom između odgovarajućih mi-

nimuma kreću se u rasponu od 0.23 do 0.46 eV. Put najmanje energije konstruiran je za istežanje C=O veze i gotovo bez barijere vodi ka koničnom presjecištu između $n\pi^*$ i osnovnog elektronskog stanja. Samo kod prvog minimuma istežanje C=O veze uzrokuje subtrakciju vodikova atoma s NH_2 skupine. Ekvivalentne strukture s gotovo istim vrijednostima energija minimuma i koničnih presjecišta nađene su na $n\pi_{(\text{II})}^*$ PPE u NAPMA $\gamma_{\text{L}}(g+)$ konformeru.

Mehanizam II potpuno je analogan mehanizmu I, osim što je pobuda na drugoj amidnoj skupini. Međutim kako eksperiment ukazuje na značajno produljenje vremena života $\pi\pi^*$ stanja uslijed metilacije NH_2 skupine u NAPA $\gamma_{\text{L}}(g+)$ konformeru, mehanizmi relaksacije preko iste skupine detaljnije su proučeni. Dva minimuma $n\pi_{(\text{II})}^*$ PPE koji se međusobno razlikuju u relativnom položaju C=O skupine naspram fenilnog prstena čine lokalne atraktore, a i b , nekolicine minimuma koji se međusobno pak razlikuju u smjerovima pojedinih N-H veza deplanariziranog dušikovog atoma. Po dva dodatna minimuma oko oba atraktora su pronađena te su za vrijednosti energija, danih u tablici I, svi stabilniji od $M_{\pi\pi^*}$ strukture. Niže energije barijera koničnih presjecišta $\pi\pi^*$ i $n\pi_{(\text{II})}^*$ stanja su na strani a atraktora (tablica I).

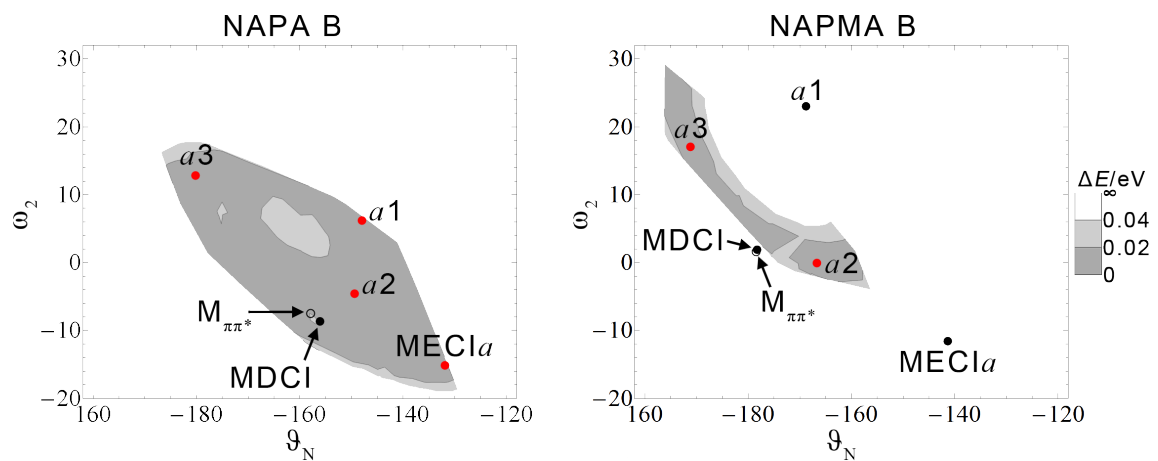
Tablica I: Relativne energije (u eV) reprezentativnih minimuma $n\pi_{(\text{II})}^*$ PPE (M_{II}) i reprezentativnih točaka šava $\pi\pi^*/n\pi_{(\text{II})}^*$ koničnog presjecišta (CI) s obzirom na energiju minimuma $\pi\pi^*$ stanja NAPA i NAPMA $\gamma_{\text{L}}(g+)$ konformera. Crtkana linija razdvaja gornje (donje) četiri strukture a (c) atraktora $n\pi_{(\text{II})}^*$ PPE, dok je s dvostrukom crtom odvojeno konično presjecište najbliže $\pi\pi^*$ minimumu. CI_{HAR} su energije točaka šava u harmoničkoj aproksimaciji PPE, a podebljanim slovima naznačene su točke šava u kojima je potencijalna energija duž svakog moda manja od njegove odgovarajuće energije osnovnog stanja moda.

	NAPA $\gamma_{\text{L}}(g+)$			NAPMA $\gamma_{\text{L}}(g+)$		
	M_{II}	CI	CI_{HAR}	M_{II}	CI	CI_{HAR}
MECI a	–	0.13	0.13	–	0.17	0.34
$a1$	–0.71	0.21	0.20	–0.72	0.32	0.38
$a2$	–0.69	0.19	0.17	–0.63	0.24	0.25
$a3$	–0.64	0.25	0.26	–0.62	0.25	0.26
MECI b	–	0.16	0.95	–	0.17	0.66
$b1$	–0.73	0.42	0.78	–0.74	0.45	0.88
$b2$	–0.72	0.35	0.34	–0.68	0.33	0.33
$b3$	–0.69	0.29	0.24	–0.67	0.32	0.43
MDCI	–	0.22	0.25	–	0.28	0.31

Optimizacijom struktura šava koničnog presjecišta [152] konstruirane su dvije strukture minimuma koničnih presjecišta (engl. *minimum energy conical intersection*, MECI), kao i struktura šava geometrijski najbliža početnoj $M_{\pi\pi^*}$ geometriji (engl. *minimum distance conical intersection*, MDCI), tablica I. Općenito, prijelaz iz jednog stanja u drugo određen

je vjerojatnošću prijelaza nuklearnog valnog paketa kroz konično presjecište što pak ovisi o jakosti sprege među stanjima kao i o samoj vjerojatnost nalaženja valnog paketa u konfiguracijskom prostoru šava koničnog presjecišta. U režimu nanosekundnog vremena života $\pi\pi^*$ stanja PPE je u slaboj sprezi s ostalim stanjima tj. više je dijabatična, dok geometrijska sličnost NAPA i NAPMA točaka šava ukazuje na elektronsku sličnost te time i samu sličnost vrijednosti sprege stanja između dva sustava. U gruboj aproksimaciji razlika vjerojatnosti prijelaza stanja među molekulama definirana je samo razlikom veličina dostupnih dijelova šava koničnih presjecišta. Kako sama dimenzionalnost sustava ne omogućuje egzaktni uvid u evoluciju nuklearnog valnog paketa, isti je opisan kvazi-stacionarnim osnovnim nuklearnim vibracijskim stanjem $\pi\pi^*$ elektronskog stanja koristeći harmonijski razvoj PPE oko $M_{\pi\pi^*}$ minimuma. Isključivanjem viših članova Taylorovog razvoja PPE anharmoničnost neće biti razmotrena kao ni sprege među pojedinim vibracijskim modovima. Dostupnost konfiguracije koničnog presjecišta pojedinom modu tada je samo omjer potencijalne energije moda u koničnom presjecištu i njegove ukupne energije osnovnog vibracijskog stanja, odnosno njegove nulte točke: V/ZPE . U poluklasičnom opisu [175] područja konfiguracijskog prostora, gdje je dani omjer V/ZPE manji od jedan, klasično su dostupna dok gdje je on veći vjerojatnost opada zbog nužnosti tuneliranja moda. Premda su anharmonični dijelovi plohe izuzeti iz opisa, harmonični dijelovi PPE nisu jednako dostupni među NAPA i NAPMA $\gamma_L(g+)$ konformerima kao što ukazuje provjera reprezentativnih točaka $\pi\pi^*/n\pi_{(II)}^*$ šava koničnog presjecišta (zadebljana slova tablice I). Kako bi se dobio uvid u odnos klasično dostupnih dijelova šava, linearnom superpozicijom reprezentativnih točaka a atraktora konstruirane su točke šava i projicirane u prostor razapet torzijskim kutevima (slika I) najrelevantnijim za opis razlike među strukturama a atraktora ($\omega_2 \equiv C_i^\alpha - C_i - N_{i+1} - C_{i+1}$ i $\vartheta_N \equiv C_i^\alpha - H_{i+1} - N_{i+1} - C_{i+1}$). Iz odnosa klasično dostupnih područja $\gamma_L(g+)$ konformera među molekulama NAPA i NAPMA jasno je vidljiv doprinos metilne skupine rigidnosti druge amidne skupine u molekuli NAPMA i njenog utjecaja na smanjenje klasično dostupnog dijela šava.

U $\gamma_L(g+)$ konformerima molekula NAPA i NAPMA još samo dio $\pi\pi^*/n\pi_{(I)}^*$ šava klasično je dostupan, a iz strukturne sličnosti prve amidne skupine među NAPA i NAPMA molekulama može se zaključiti kako su u oba sustava klasično dostupni šavovi podjednakih volumena. U preostalim konformerima NAPA i NAPMA molekula, jedino klasično dostupno područje šava odnosi se na manje područje oko $a3$, MECI*b* i $b2$ tipova koničnih presjecišta u NAPA $\gamma_L(g-)$ konformeru, jer isti konformer ukazuje određeno produljenje života uslijed metilacije druge amidne skupine. U svim preostalim konformerima, na temelju sličnosti s vremenom života $\pi\pi^*$ stanja benzena i toluena, [29, 41] kompeticijski deaktivacijski kanal međusustavnog križanja singletnog i tripletnog stanja fenila dominira nad mahanizmima prijenosa ekscitacije na amidne skupine.



Slika I: Klasično dostupan dio šava a atraktora (sivo) konstruiran je superpozicijom kalsično dostupnih (nedostupnih) reprezentativnih točaka šava označenih punim crvenim (crnim) točkama. Minimum $\pi\pi^*$ stanja označen je šupljim kružićem.

1 Introduction

The very presence of indole, phenole and phenyl groups as chromophoric side chains of amino acids tryptophane (Trp), tyrosine (Tyr) and phenylalanine (Phe), respectively, endows their containing peptide or protein systems with a potentially rich photochemistry after the absorption of near ultraviolet (UV) radiation (250-280 nm). Immediately after the absorption, the chromophore's populated excited electronic state relaxes to the ground vibronic state either by directly dissipating the excess energy as radiation in a process of fluorescence or converts the excess energy into nuclear motions through coupling of electronic and nuclear degrees of freedom. The kinetics of the two competing processes (radiative *vs.* non-radiative) determine the systems fluorescence quantum yield and its photochemistry, where both are highly dependent on the electronic and nuclear properties and on the absorbed energy. Although the near UV light absorption spectra for the three aforementioned amino acids are only slightly perturbed when compared to their containing chromophores, their quantum yields however are strongly reduced, [1] indicating that existing or new non-radiative deactivation (NRD) pathways are active in amino acids. The quantum yields of the three chromophores decrease in the same order, and the trend is followed within their containing amino acids, being five times larger in Trp than Phe. [1] Within the peptide or protein structures, the quantum yields further change, displaying chromophores high sensitivity on the local environment. Although correlations between the local three dimensional structure and chromophore absorption and fluorescent emission spectra have been quite well established, relations with their quantum yields or excited state lifetimes remains uncorrelated. The latter complicates the use of time-dependent fluorescent methods in elucidating protein structure and dynamics. However, an empirically well known fact that fluorescence quantum yields of Trp, Tyr and particularly of Phe in peptide/protein systems are generally (extremely) low has been established, [1,2] indicating that non-radiative processes play a key role in deactivation of protein excited states. Of course, the three conjugated ring systems are not the only UV absorbing centers in peptide systems. Carboxyl groups as part of peptide C-terminals or as side chains in aspartic and glutamic amino acids absorbed at lower wavelengths. The same is true for other conjugated systems in proteins like the imidazole ring of histidine, guanine motive of arginine or the ubiquitous amide groups of peptide bonds which have a very small transition dipole moments, i.e., absorption coefficients and whose excited states are higher in energy. Nonetheless all these excited states can indirectly contribute to proteins excited state properties. Apart from protein spectroscopy, protein photochemistry is also widely studied and mostly focused on radical formation, dissociation and rearrangement reactions induced by the absorption of near UV radiation usually by the three chromophores. [3-7] These reactions constitute a set of reactive NRD mechanisms in pro-

tein systems. But protein systems alone are not known as photoactivated reaction centers in biological systems. Any protein of this type always comes with an additional cofactor chromophore molecule, where the protein part serves as an optimized environment which promotes the photoinduced chemical reaction of chromophore to high efficiency (best known examples include *cis-trans* photoisomerization of retinal in rhodopsin [8], and photoinduced redox reactions of chlorophyll in light-harvesting complex [9,10]). Even the class of green fluorescent proteins [11] and their synthetic variants [12] contain a non-nascent chromophore which is derived from the constituting amino acids in a process of maturation [13]. It seems that the protein major photochemical mechanisms are related with their photostability and quenching of fluorescence, like base pairs in DNA, [1] where they play an important role in preserving protein functionality. So a set of non-reactive NRD processes competes with reactive NRD pathways to diminish any destructive transformation of the initial protein structure. These kind of mechanisms might have been especially important in the prebiotic phase of life evolution. [14–17] Although giving no new photoproducts, non-reactive NRD pathways constitute alternative deactivation processes of photoexcited proteins which together with other NRD mechanisms make up a broad variety of possible photochemical and photophysical processes in peptide systems, far more versatile than the isolated chromophores would exhibit. Therefore, the quest of elucidating NRD mechanisms of photoexcited proteins is of fundamental interest to the understanding of energy transfer processes in nature.

Theoretical and computational chemistry aided with modern experimental femtosecond time-resolved spectroscopy measurements play a key role in unraveling NRD mechanisms. Both approaches are not without their limitations, where the joint problem is the size of the systems, so studies of protein NRD mechanisms over the past few years have mainly focused on small model peptide systems. Particular focus is on gas phase studies, where the solvent free environment provided a direct insight into the intrinsic excited state peptide dynamics, governed solely by intramolecular forces. From the experimental standpoint this represents a huge advantage over the solution experiments. Using pump-probe and spectral hole burning techniques, some conformers present in gas phase can be detected and their structures identified by comparing their vibrational spectrum with the theoretically predicted spectrum. Their excited electronic state lifetimes can be precisely measured. In computation the absence of solvent is a huge simplification, enabling larger molecular systems to be theoretically examine in detail. Concepts developed on isolated molecular systems can then be applied to larger systems or used to elucidate the differences in solvated systems. With this systematic approach, direct dependence of excited state lifetimes on exact peptide conformation can be observed, and the same can be theoretically simulated. A great deal of work has been conducted on Trp, as a free

amino acid or part of a smaller model peptide chain in gas phase. Trp is the obvious choice due to its favorable spectroscopic properties (low absorption energy, high fluorescence quantum yield), and its excited state dynamics was extensively compared with the excited state properties of indole and indole derivatives. Phe on the other hand has a smaller transition dipole moment, its first excited state is higher in energy than Trp, but is more frequent in the proteome than Trp (three times more frequent in vertebrate genome than Trp [18]), while its almost negligible fluorescence quantum yield indicates that a variety of potentially easy accessible NRD mechanisms are triggered by Phe absorption. A number of studies have also suggested the role of Phe in protein fluorescence, in which absorbed Phe energy is transferred to fluorescing Trp, described usually with the Förster resonance energy transfer process. [2]

Few detailed experimental studies conducted on gas phase molecules containing Phe have shown interesting properties of the Phe excited electronic state, [19–21] particularly the experiment of Chin *et al.* conducted on one of the smallest Phe containing model peptide, the *N*-acetylphenylalanineamide (NAPA). [20] With its primary structure Ac-Phe-NH₂ the two protective groups introduce two additional amide groups in the system which make the molecule suitable for studying gas phase secondary structures of a model dipeptide (Scheme 1.1). Using a one-color resonance two-photon ionization (R2PI) method three conformers of NAPA molecule were detected in gas phase, and their three-dimensional structures were identified from their vibrational spectra, which correspond to computationally predicted three most stable structures. The three conformers, shortly abbreviated as A, B and C, belong to two classes of Toniolo’s secondary structure peptides. [22] The conformer A is a β_L strand exhibiting a weak hydrogen bond which links the two amide groups. The two other conformers, B and C, belong to a class of γ_L structures which exhibit a stronger H-bond between their C end amino group and the oxygen atom of the first amide group, enclosing a seven membered ring structure. The only major difference between the two conformers is the relative orientation of the phenyl ring relative to the peptide backbone, where the former conformer is of *gauche*(+) conformation, while the latter is of *gauche*(-). Conformer B also exhibits a H-bond between its H atom of the first amide group with the phenyl ring. Two-color laser techniques can also be used for conformer detection. If the conformers are probed using the laser induced fluorescent (LIF) technique instead of R2PI, conformer B proved absent from the spectrum. This unintentional observation forced the authors to measure the NAPA conformers excited state lifetimes. They obtained for the vibrationless S₁ electronic excited states lifetime values of 62 ± 2 and 42 ± 2 ns for conformers A and C, respectively. For conformer B the authors concluded that a fast NRD mechanism is active which effectively quenches the conformer excited state before it can be detected by LIF. Later repeated measurement

using shorter pulses of picosecond instead of nanosecond duration showed that the S_1 excited state lifetime of conformer B is 1.5 ± 0.3 ns, [23] but the anomaly between conformer excited state lifetimes and the mechanism behind this remain unknown. Such a large discrepancy between the conformer excited state lifetimes could not be solely explained on the basis of differences in conformers structure and vertical electronic excitations. A similar excited state lifetime anomaly was also detected previously for neutral conformers of Phe, but with a less profound differences between conformers excited state lifetimes. [19] There the authors had suggested that the dark electronic states of carboxyl group could influence the excited state lifetimes, but did not provide any mechanism. The presence of unknown NRD mechanisms was also accounted for the absence of spectral signals from some computationally determined most stable conformers, [21, 24, 25] or the bleaching of some vibronic progressions or excited state vibrational transitions. [26, 27] Interestingly, as explained in the next chapter, any of the previously known NRD mechanisms developed for explanation of non-radiative processes in benzene, [28] toluene [29] or analogue Phe or Trp peptide systems [30–32] were inadequate to explain the observed anomaly in lifetime difference of NAPA conformer B.

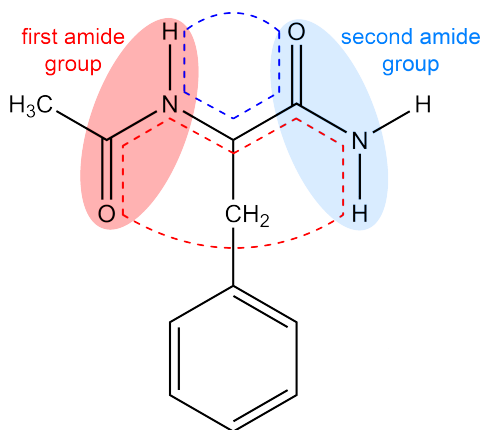


Figure 1.1: Structural formula of *N*-acetylphenylalanylamide (NAPA). The blue dashed line traces atoms within the topological five-membered ring, containing the H-bond, as characteristic of the β_L secondary structures, while the red line atoms of the seven-membered ring in γ secondary structures. The red and blue shaded areas designate the first and second amide groups, respectively.

In order to unveil the non-radiative deactivation mechanisms responsible for short excited state lifetime of NAPA conformer B a detail insight into its NRD processes is necessary. This elucidation starts by searching for possible relaxation mechanisms, either by following chemical intuition and constructing deactivation mechanism by hand, or using more sophisticated unbiased methods. Non-adiabatic molecular dynamics simulation, where the nuclear wave packet dynamics is approximated by classical trajectories propagated along multiple electronic potential energy surfaces, prove to be the most fruitful choice.

Patterns of deactivation processes can be directly obtained from these trajectories and systematized into various deactivation mechanisms. Reaction paths can then be easily constructed with corresponding barriers and conical intersections. Also, any intrinsic failure of the method used in propagation of non-adiabatic trajectories cropped up into a mechanism can be rectified by reexamining the plausibility of the process on a more accurate level of theory. Expectedly, the wave packet dynamics is better approximated using a larger number of classical trajectories, but with an appropriate sampling of initial conditions large areas of configuration space can be sampled with fewer trajectories. Unfortunately, the latter case lacks the statistically necessary amount of information from which excited state kinetic parameters, e.g. lifetimes and population branching, can be obtained directly. The quantum nuclear effects, however, cannot be treated with simple classical models, but once the mechanisms are known the missing effects can be reincluded *a posteriori*, especially if the mechanisms indirectly indicate a possibility of tunneling or the systems energy is extremely low, indicating the necessity to include zero-point energy effects.

Here, a strategy for elucidating unknown non-radiative relaxation mechanisms is developed and applied with the goal to unraveling the NRD mechanisms of photoexcited NAPA conformers. Time dependent density functional theory (TDDFT) based non-adiabatic molecular dynamics is utilized for blind screening of potential relaxation mechanisms, which are then refined on a more accurate coupled cluster (CC) level of theory. Preceding this was the coding of the non-adiabatic dynamics procedure into a home made software. In the following chapter details of previous studies conducted on NAPA and analogue peptide systems are given to account for all the missing information that need to be elucidated. The following Theory and method chapter explains the concepts of molecular non-adiabatic dynamics as well as the implementation of TDDFT into the former. Final mechanisms and their elucidation is explained in the Results and discussion section, which is followed by Conclusion. The work presented here was part of a joint theoretical-experimental research to elucidate the NRD mechanisms responsible for anomalously short excited state lifetime of conformer B, and with a wider aim to hopefully get a dynamical insight into the deactivation processes of Phe containing peptide systems. [23, 33]

2 Literature overview

2.1 Experimental results

2.1.1 Ground and excited state properties of NAPA in gas phase

Before proceeding to the explanation of NRD mechanisms in NAPA conformers, few further experimental results necessary for the understanding of the former are given. Description of the experimental setups and other details can be found in the references [20] and [23], and in the references cited therein. The NAPA molecules are transferred to the gas phase by laser desorption from a solid sample, and immediately cooled down within a supersonically expanding jet of argon gas from a pulsed valve to an estimated temperature of few Kelvins (<10 K). Although the details of the cooling processes are complex, experimental findings show that under the present preparation conditions sample molecules can be cooled down by inelastic collisions with carrier gas atoms to their most stable configurations with very little excess of internal energy. [34] With such a low amount of translational and rotational energy, the absorption lines of NAPA in near UV are extremely sharp, as obtained with one-color R2PI technique. Using UV-UV or IR-UV hole burning methods, each absorption line is further designated to a particular species present in the gas phase (Figure 2.1). For NAPA only three conformers were detected in this way. They were identified by comparing their N–H (amide A) and C=O (amide I) stretching vibrational transition frequencies with the calculated frequencies from a set of predicted NAPA conformers. In the R2PI obtained UV spectrum, NAPA conformer A absorption bands have the largest intensity and show two additional progression lines separated by 17 cm^{-1} . NAPA conformers B and C are of lower intensities, where the position of NAPA conformer B line is more blue-shifted to conformer A ($\Delta\tilde{\nu} = 107\text{ cm}^{-1}$) than conformer C (29 cm^{-1}). The lowest energy absorption lines for each NAPA conformers correspond to the origin of their UV spectra, meaning that the absorbing species have been excited to their lowest vibronic states. One can clearly see the huge advantage of gas phase spectroscopy over the solution experiments, enabling each in the expansion present conformer to be clearly identified and selectively excited to its particular vibronic state. If in the same experimental setup (laser induced) fluorescence is used for detection instead photoionization, a change in absorption intensities is observed, where the intensity of NAPA conformer B drops so low that it was firstly taken as absent from the spectrum. Such an observation clearly demonstrates that a NRD process in excited state of NAPA conformer B is more active than for the other two conformers. Using two-color pump-probe measurements the decay kinetics of NAPA excited state at the UV origins were shown to obey first-order rate law, with the corresponding monoexponential lifetimes listed in the first row of Table 2.1. A whole order smaller value for NAPA conformer B

lifetime validates the assumption of a faster non-radiative relaxation process active in this particular conformer. To test whether any excess of vibrational energy could speed up the excited state relaxation process, the vibronic $6b_0^1$ transition for conformers A and B were respectively excited, and their lifetimes measured. For this particular vibronic states, which are approximately 530 cm^{-1} higher in energy than the corresponding vibrationless UV origin states, no significant change of excited state lifetimes were observed.

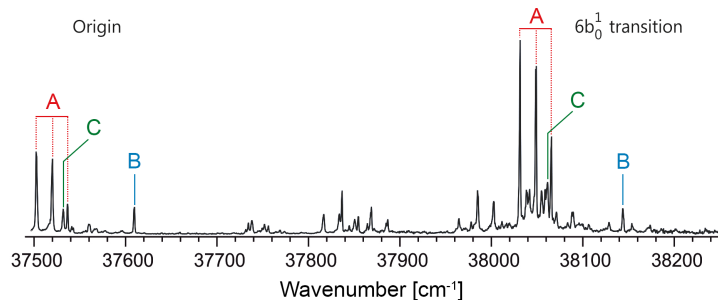


Figure 2.1: One-color R2PI UV spectrum of NAPA recorded in the domain of the first $\pi\pi^*$ transition of the phenyl ring, exhibiting the origin and an the $6b_0^1$ vibronic features of conformers A, B and C. Figure adapted from reference [23].

Table 2.1: Excited state lifetimes (in ns) of selected isotopomers of NAPA (top table) and NAPMA (bottom table) measured at the origin of the $\pi\pi^*$ transition by pump-probe experiment. Values for NAPA and NAPMA are taken from references [23] and [33], respectively.

NAPA				
Species		A	B	C
d ₀	NH/NH ₂	70±2	1.5±0.3	35±2
d ₁	NH/NHD		<3	
	ND/NH ₂			
d ₂	ND/NHD		<3	
	NH/ND ₂			
d ₃	ND/ND ₂	78±2	<3	44±2
NAPMA				
Species		A	B	C
d ₀	NH/NH ₂	67±3	48±3	62±3

2.1.2 Excited state lifetimes of deuterated NAPA isotopologues and NAPMA

Motivated by one of the proposed NRD mechanisms (see subsection 4.3.1), excited state lifetime measurements were conducted on deuterated isotopologues of NAPA conformers.

The effect of deuterium substitution of protium atoms in particular NH groups on the near UV spectrum can be seen on Figure 2.2.

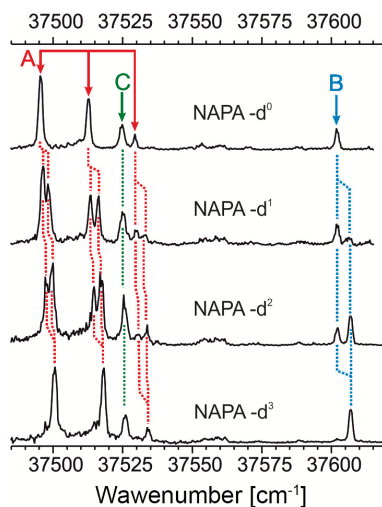


Figure 2.2: One-color R2PI spectra recorded in the spectral region of the first $\pi\pi^*$ transition of the phenyl ring on the mass channel of the isotopologues d_0 , d_1 , d_2 and d_3 of NAPA. The band systems belonging to the same conformers are indicated with the same color. Figure adapted from reference [23].

All absorption lines for mono- and bisubstituted isotopologues of NAPA conformers A and B exhibit splittings due to three different isotopomers present, while the absorption line for conformer C remains indifferent. Because the pulse linewidth was too broad to spectroscopically distinguish all three present isotopomers, two isotopomers were grouped into one signal of double intensity. Deuteration slightly blue-shifts all absorption bands, indicating that one of the electronic states is less vibrationally stabilized. The exact deuterium substitution sites in isotopomers are identified in the same way as NAPA conformers. The corresponding excited state lifetimes of all NAPA isotopologues are displayed in the rest of Table 2.1. Designations NH and NH₂ are used to clearly indicate various NAPA isotopomers. As already stated, due to poor spectral resolution, NAPA mono- and bisubstituted isotopomers of conformers A and C could not be resolved and their excited state lifetimes measured. Also the exact substitution position of one protium atom in NH₂ group for NAPA conformer B could not be resolved. No significant increase in excited state lifetime for any isotopologue or isotopomer of conformer B is observed, while an 11 and 25 percent increase in lifetime values of fully deuterated NAPA conformers A and C is observed, respectively.

Apart from isotope substitution, where all the effects originate from the vibrational contributions, chemical substitution can have a more profound effect due to direct perturbation of the system electronic structure. From gas phase studies of Gerhards *et al.* on a methylated analogue of NAPA molecule, *N*-acetylphenylalanylmethylamide (NAPMA), it

is known that this molecule has exactly the same three analogue conformers as NAPA. [35] A more precisely measured pump-probe UV spectrum of NAPMA conformers, [33] with less temperature broadening than the original, [35] is displayed in Figure 2.3, and shows a slight red-shift of $\sim 10 \text{ cm}^{-1}$ for NAPMA conformers B and C absorption lines compared to corresponding NAPA conformers, while a larger 83 cm^{-1} red-shift is observed for NAPMA conformer A origin transition.

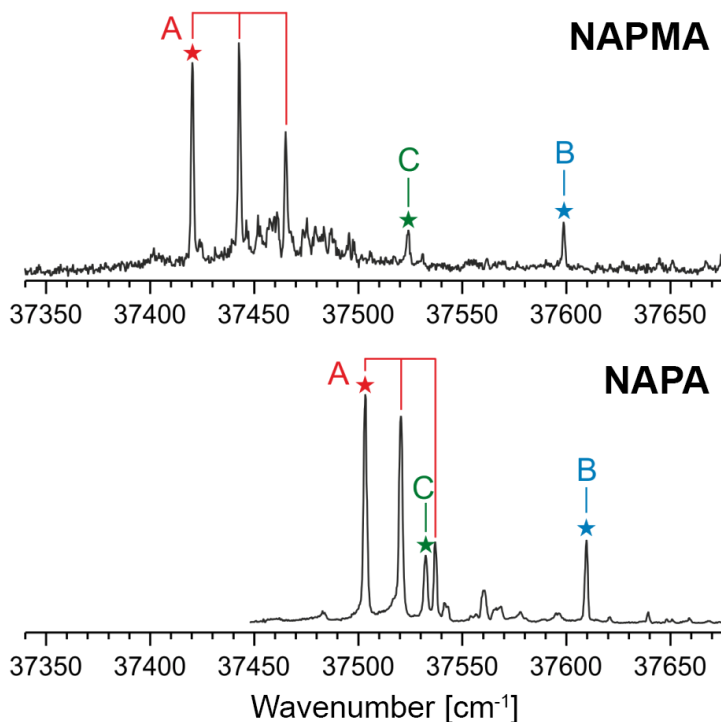


Figure 2.3: Two-color pump-probe UV spectrum of NAPMA (top) compared to NAPA UV spectrum (bottom). Stars mark the origin transition of each conformer where the pump-probe lifetime measurements experiments have been done (see Figure 2.4). Figure adapted from reference [33].

However, the substitution effects on the excited state lifetimes are completely different compared to the substitution effects on absorption changes as clearly displayed in Figure 2.4. Excited state decay curves with fitted monoexponential decay functions for each pair of NAPA (red) and NAPMA (blue) conformers are shown respectively. Fitted lifetime values are given in Table 2.1. While now NAPMA conformer A only exhibits a minor change of its excited state lifetime compared to its corresponding NAPA conformer, NAPMA conformer C excited state lifetime has doubled, while NAPMA conformer B excited state lifetime has increased almost thirty-fold compare to NAPA conformer B value. Such a significant effect indicates a huge chemical modification of the non-radiative relaxation pathway in conformer B, and parallelly, as will be explained in more details later, from the exact substitution position within the molecule a NRD mechanism can be identified.

It remains now to theoretically explain the above mentioned observations, where the first step is the explanation of the electronic ground state properties.

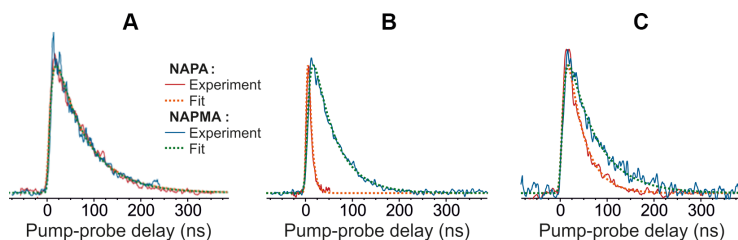


Figure 2.4: Pump-probe nanosecond signals obtained after pumping the origin transition of conformers A, B and C of NAPMA (blue) and NAPA (red). Lifetime values of best fits (dotted lines) are given in Table 2.1. Figure adapted from reference [33].

2.2 Previous theoretical results

2.2.1 Electronic ground state properties of NAPA conformers

The electronic ground state properties of NAPA were firstly computationally investigated by Chass *et al.* to identify the conformers present in the gas phase. [36] By systematically screening through all six relevant dihedral angles in NAPA molecule an initial set of secondary structures was generated, which were then subsequently optimized at the Hartree-Fock (HF) level of theory, followed by a density functional theory (DFT) level re-optimizations to better account for the missing electronic correlations. DFT calculations were only performed with the B3LYP functional. Their multi-dimensional conformational analysis led to sixteen secondary structures all within a relative energy window of 10 kcal mol⁻¹, even when zero point energy (ZPE) corrected. By comparing the calculated frequencies of the amide A and amide I regions for the obtained set of secondary structures with the corresponding experimental vibrational transitions, the three NAPA conformers were finally identified in the gas phase. In agreement with the DFT results, the three conformers are the energetically most stable forms, what is expected under the experimental ultracold conditions. However, their exact energy ordering strongly depends on the chosen basis set. For ZPE corrected energies calculated with a larger 6-311G(df,p) basis set the conformer stability decrease in the order B, A and C, while using a smaller 6-31+G(d) basis set conformer A becomes more stable than conformer B. The latter trend matches more the estimated relative conformer abundances in gas phase as deduced from the relative signal strengths in UV spectrum. The geometrical structures of the three NAPA conformers are displayed in Figure 2.5. Once again, conformer A belongs to a class of β_L strands characterized by Ramachandran angles Ψ and Φ taking both values of 180°, while conformers B and C belong to a class of equatorial γ_L -turns secondary

structures ($\Psi = +50^\circ$, $\Phi = -75^\circ$). [37] The main structural difference between the latter two conformers is in the relative position of the phenyl ring with respect to the backbone, which are accordingly designated as *gauche*(+) and *gauche*(-) structures depending on the relative orientation to the N-C $_{\alpha}$ bond in the first amide group. The conformer A phenyl ring is *anti* in this respect. A variety of intramolecular hydrogen bond interactions were indicated by the authors. Of course, the most notable are the H-bonds that hold the conformer secondary structures together, where the bent H-bond in conformer A is considered less stable than the H-bond in γ_L structures. Treating this interactions correctly is vital in computation, because, as the authors have noticed, the stability of the bent H-bond structure depends more on the inclusion of basis sets with more polarization and diffuse functions than the γ_L structures with more linear H-bond. This computational artifact is mainly responsible for the problematic energy ordering of NAPA conformers A and B, and is exhibit in any other observable to a grater or lesser extent. Other indicated interactions include the weak N_{Ph}e-H $\cdots\pi$ and the C=O \cdots H-C_{Ph}e H-bonds in NAPA conformer B, where the former one is to some extent observed in conformer C. In conformer A authors spotted a long range weak C_{Ac}=O \cdots H-C_{Ph}e interaction from atoms-in-molecules analysis. They also demonstrated that the inclusion of diffuse basis functions in conformer A diminishes the weak N_{NH₂}-H $\cdots\pi$ interaction between the second amide and phenyl group, although the two groups are favourably oriented toward each other.

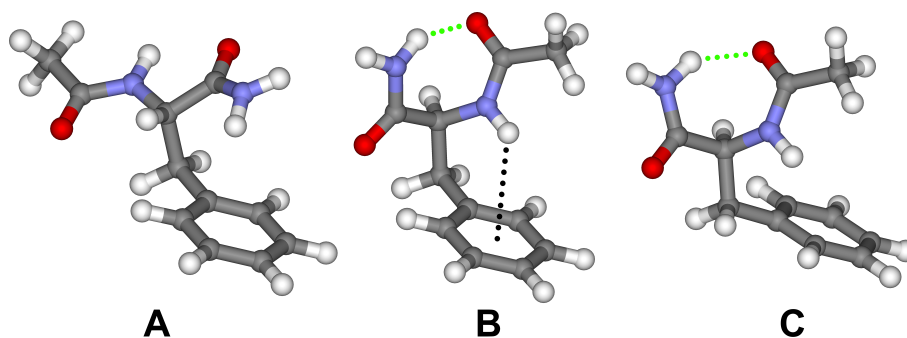


Figure 2.5: NAPA conformers A ($\beta_L(a)$), B ($\gamma_L(g+)$) and C ($\gamma_L(g-)$). The green dotted lines represent the N-H \cdots O H-bonds within the seven member γ_L rings of NAPA conformers B and C, while the black dotted line indicates the N_{Ph}e-H $\cdots\pi$ interaction in NAPA conformer B.

Došlić *et al.* further examined the intramolecular forces and the anharmonic effects within NAPA conformers to account for the relative ordering of the conformers as well as the small discrepancies between calculated and experimental vibrational transitions which still questioned the one-to-one assignment of identified conformers. [38] Their elaborate conformational search started with the basin-hopping method on force-field level, and followed by a series of optimizations on ever-increasing level of theory, validated the three

aforementioned conformers as the most stable secondary structures in a wider part of configuration space. In order to better describe the H-bonds and the dispersion interactions, diffusion functions for heavy atoms were included in all used basis sets. Calculations were also repeated using the Møller-Plesset second order perturbation (MP2) and complete active space self-consistent field/second order perturbation (CASSCF/CASPT2) methods for a more accurate treatment of dispersion interactions. At the B3LYP/6-31+G(d) and B3LYP/6-311+G(2d,p) level conformer A is more stable than conformer B, while dropping out the diffuse functions stabilizes conformer B over conformer A. The trend is preserved whether harmonic or anharmonic ZPE corrections are included or not. The basis set superposition error (BSSE) was shown to be small and not responsible for the observed energy ordering of the conformers. Regarding pure electronic energy, at the MP2/6-311+G(2d,p) level conformer B becomes almost isoenergetic with conformer A (0.06 kcal mol⁻¹ higher than conformer B), while at the CASSCF(8,8)/MS-CASPT2/cc-pVDZ level it is by 0.56 kcal mol⁻¹ more stable. From geometrical considerations it was shown how the phenyl ring causes more strain in the backbone of γ_L structures than in β_L , and concluded that this destabilizing effect competes with the stabilizing effect of H-bonds. The delicate balance of the two effects determines the correct electronic energy ordering of the conformer, and based on the two latter levels of theory conformer B is the most stable. However, only the total energy of the system determines the final energy ordering, so it is absolutely necessary to take the nuclear ZPE-s into account. Unfortunately, calculated ZPE-s are affected by the same errors corresponding electronic structure methods have, but unlike the electronic ground state energies, calculated vibrational frequencies can be compared with certain experimental values and used for rectification or selection of a more appropriate electronic structure method. Regarding the amide A region, at the B3LYP/6-31+G(d) level all harmonic N–H stretch vibrations are blue-shifted while all anharmonically corrected frequencies are red-shifted to experimentally determined transitions. Not even the use of a larger 6-311+G(2d,p) basis set made any significant improvement. Nonetheless, frequency shifting and splitting of vibrational normal modes were used for further insight into intramolecular interactions of the conformers, because both values are sensitive to the local interactions. In this way strong red-shifting of N_{Phe}–H stretch vibration confirmed the presence of N_{Phe}–H · · π H-bond in NAPA conformer B, while the absence of any significant splitting between the symmetric and asymmetric stretch vibrations in NAPA conformer A NH₂ group disprove the presence of the N–H · · π interaction in this conformer. Due to a different position of the phenyl ring in conformer C, the N_{Phe}–H · · π interaction affects the N_{Phe}–H out-of-plane vibration more than its stretching vibration. The conformer B C=O stretch vibration frequency of the second amide group is slightly red-shifted to the corresponding values in

the other two conformers due to the previously predicted weak $\text{C}=\text{O} \cdots \text{H}-\text{C}_{\text{Phe}}$ H-bond, but also to the $\text{C}=\text{O} \cdots \text{H}-\text{C}_{\beta}$ interaction in conformer B. The significant red-shift of conformers B and C first amide $\text{C}=\text{O}$ stretch vibrations support the geometrical factors that the C7 ring H-bond is more stronger than the C5 H-bond in conformer A. But although it appears that conformers B and C have more stabilizing interactions, in total sum, the vibrational ZPE of conformer A is lower. Even when the normal modes of frequencies lower than 100 cm^{-1} are omitted from the sum due to their erroneous description of shallow potentials, conformer A still has the lowest ZPE, making it the most stable conformer. Because of computer resource limitations the authors could not calculate the harmonic vibrational frequencies at the MP2/6-311+G(2d,p) level. These calculations are repeated in this work, and because NAPA ground state properties will not be discussed later, the MP2 level harmonic ZPE corrections to MP2 electronic energies are given in Table 2.2. Values for corresponding NAPMA conformers are given as well. Clearly the MP2 method reproduces the same trend in conformers total energies as the B3LYP level does. It can be finally concluded that the NAPA conformer A is energetically most stable, followed by conformer B, than conformer C.

Table 2.2: Relative ground state energies (E_0) and harmonic ZPE corrected ground state energies (E_{ZPE}) in kcal mol^{-1} at the MP2/6-311+G(2d,f) level for NAPA and NAPMA conformers.

Conformer	NAPA		NAPMA	
	E_0^\dagger	E_{ZPE}	E_0	E_{ZPE}
A	0.06	0	0	0
B	0	0.38	0.68	1.09
C	1.00	1.01	1.73	1.75

[†] Values taken from reference [38].

2.2.2 Electronic absorption spectrum of NAPA conformers

Apart from the detailed work on NAPA ground state properties, Došlić *et al.* have for the first time reproduced the UV absorption spectrum of NAPA conformers. [38] The CASSCF(8,8)/MS-CASPT2/cc-pVDZ level of theory was used. The active space consisting of eight orbitals was constructed from the two highest energy occupied (HOMO) and two lowest energy unoccupied (LUMO) molecular orbitals on the phenyl ring together with the pair of occupied and corresponding anti-bonding orbital located on each of the two carbonyl groups. From the optimized ground state geometries on CASSCF/CASPT2 level three vertical excitations have been computed for each conformer (see Table 2.3). The three obtained excitations resemble by energy, oscillator strength and character the

three lowest transitions in benzene molecule, namely the three consecutive transitions from benzene ${}^1A_{1g}$ ground state to ${}^1B_{2u}$, ${}^1B_{1u}$ and ${}^1E_{1u}$ excited states, respectively. In benzene, the three excitation energies are 4.90, 6.20 and 6.94 eV, respectively, where only the last transition is symmetry allowed and therefore does not require vibrational coupling in order to be allowed. [39,40] Actually, comparison to toluene transitions are even better, because the local symmetry of the phenyl ring in NAPA molecules is definitely of C_{2v} point group, not D_{6h} , which is further degraded to C_1 through interaction with the backbone. The 4.65 eV ${}^1A_1 \rightarrow {}^1B_2$ vibrationless (0_0^0) transition in toluene is the most simplest analog to NAPA observed transitions. [41] Thus the lowest electronic transition in NAPA belongs to the expected $\pi \rightarrow \pi^*$ transition of an electron from the phenyl occupied π HOMO orbitals to the phenyl π^* LUMO orbitals, making the first excited state of NAPA completely localized on the phenyl ring. The excited state is of singlet multiplicity, and of single excitation character, meaning that the corresponding excited electronic state wave function can be well described by just using singly excited configuration state functions (CSF). From now on, the excited states of NAPA molecules are going to be designated by simple double-letter acronym, where the multiplicity sign for singlet states will be omitted unless stated differently. Therefore, the first singlet excited state of NAPA populated by direct absorption of UV radiation is designated as $\pi\pi^*$ state, where the first character designates the newly created electronic hole or the orbital which the electron had occupied previous to absorption, while the second character marks the newly populated molecular orbital. Note, however that this is a simplified descriptions of electronic excited states, because molecular orbitals are just mathematical constructions with no real physical meaning. Returning to the calculated NAPA first vertical excitations, they all display conformational dependence, but are all blue-shifted to experimental values, and the ordering of NAPA conformer B and C transitions relative to conformer A is incorrect. Although vertical excitation is an oversimplification of the real absorption process, taking into account all the vibronic contributions to obtain a better UV spectrum for NAPA is merely impossible. However, an already better agreement with experimental values is obtained from adiabatic transitions instead of vertical, where the excited state energies are calculated in the local CASSCF optimized geometry on the same excited state. Still the conformer C is more blue-shifted than conformer B and perhaps this error could be traced back to the overstabilization of NAPA conformer B excited state on CASSCF/CASPT2 level as already noticed in the ground electronic state. But taking into account the precision of 0.02 eV for the used method, the calculated excitations are in good agreement with the experimental values. Based on these calculations it can be safely concluded that the first excited electronic states of NAPA conformers correspond to $\pi\pi^*$ state localized on the phenyl ring and that these states undergo non-radiative

deactivation. What are the photochemical processes by which the lowest excited states of NAPA conformers deactivate remains to be elucidated.

The authors had also tried to reproduced the NAPA excitation spectrum on time dependent density functional theory within linear response (LR-TDDFT) level using OLYP and several more functionals. Unlike the well separated states obtained at the CASSCF/CASPT2 level, a larger variety of excited (approx. fifteen) states are found within the same energy window ($\sim 4.2\text{--}6.0$ eV), where the majority are of charge transfer character. The excited states that were characterized as well defined $\pi\pi^*$ states are significantly blue-shifted (~ 0.4 eV) compared to the experimental and CASSCF/CASPT2 values. The ordering of conformers first $\pi\pi^*$ vertical excitations is also completely reversed. Based on these observations, the authors concluded that TDDFT based methods are not appropriate for treatment of NAPA excited states.

Table 2.3: Vertical and adiabatic excitation energies at the (I) CASSCF(8,8)/MS-CASPT2/cc-pVDZ and vertical excitations energies at the (II) TD-OLYP/TZ2P(DZP) levels of theory for the three NAPA conformers calculated by Došlić *et al.* [38] compared to the experimental values determined by Chin *et al.* [20] All values are in eV.

Conformer	I		II	Experimental
	Vertical	Adiabatic		
A	4.827	4.707	5.133	4.650
B	4.882	4.769	5.113	4.663
C	4.913	4.778	5.125	4.654

2.3 Non-radiative deactivation (NRD) mechanism of analogue chromophores

2.3.1 NRD pathway of benzene and toluene S_1 excited states

Apart from the detailed work of Došlić and co-workers, no other known study has examined NAPA's excited states, not to mentioned its NRD pathways. Nonetheless, as mentioned in the Introduction, studies of NRD pathways have been conducted on related Phe containing model peptide systems as well as other relevant systems, where an overview of only few most relevant works is given here. For start, a simple question that logically arises is what are the NRD pathways of the photoexcited phenyl group and can they effect the excited state lifetimes of NAPA conformers. The photochemistry of phenyl S_1 $\pi\pi^*$ excited electronic state has been extensively studied on benzene and its other simple derivatives in gas phase. [28, 39, 40, 42–47] The benzene S_1 potential energy surface

(PES) has a local energy minimum also of D_{6h} symmetry where all C–C bonds are slightly extended compared to their ground state values ($\Delta d(\text{C–C}) = 0.04 \text{ \AA}$). [39] Unlike NAPA, due to symmetry restrictions benzene does not have a 0_0^0 origin transition, [39,40] but the nuclear ZPE state of the corresponding S_1 minimum can be populated through hot-band absorption, e.g. 6_1^0 , which transfers the population from the excited vibronic ground state to the vibrationless S_1 state. The vibrationless S_1 state has a lifetime of $90 \pm 4 \text{ ns}$, [48] while its corresponding fluorescence quantum yield is rather small, only 0.22. [42] Due to negligible amount of photoproducts it was assumed that the rest of excited population deactivates *via* inter-system crossing (ISC) to a lower triplet electronic state, which finally drives the system back to ground electronic state. [42] Higher populated vibronic states have shorter excited state lifetimes and lower fluorescence quantum yields, while the amount of photoproducts increases. For vibronic excitations with vibrational energy over 3000 cm^{-1} above the S_1 vibrationless state, a route to a new set of NRD mechanisms becomes accessible, which completely quench benzene’s fluorescence. [49–52] These mechanisms were theoretically disclosed in a number of studies, where it was concluded that a benzene ring deformation drives the system excited and ground electronic states directly to their conical intersection (CI). [28,43–47] A ring-puckering mechanism in which one carbon atom moves out of a benzene plane has the lowest transition state (TS) point between the $\pi\pi^*$ minimum and the corresponding CI configuration, reproducing a barrier value very close to the experimentally observed 3000 cm^{-1} . The splitting of S_1 population in CI between a prefulvene or anti-Kekule structures in ground electronic state will depend on the motions that drive the S_1 populations through CI and on the part of CI seam which was accessed. [28,46] Parker *et al.* shown that the spin-orbit coupling around the benzene CI seam is not large in value, but due to the rather extended nature of this CI seam a significant amount of population can undergo ISC to the triplet state. [53] Although the ring puckering mechanism displays quite a large barrier ($\approx 0.37 \text{ eV}$ [44]) in benzene, how the interaction with neighboring groups, such as a peptide backbone, influence its value remains unknown.

Toluene, the smallest chromophore of NAPA, has a S_1 vibrationless excited state lifetime of $86.4 \pm 0.7 \text{ ns}$ and mostly undergoes ISC like benzene. [29,41] Its vibronic states show the same trend of decreasing excited state lifetime with increasing the amount of excess vibrational energy. Particularly the excited state lifetime of the vibronic state created by the $6b_0^1$ transition which has an excess energy of 532 cm^{-1} above the toluene ZPE displays a bit smaller value of $72.2 \pm 0.4 \text{ ns}$, while the analogue vibronic state in NAPA conformers shows no significant change upon excitation. Based on all these observation it can be concluded that the NRD mechanisms active in benzene and toluene do not play a dominant role in deactivation of NAPA conformers, at least not in conformer

B. The alternative conclusion would be that these mechanism are highly perturbed by the NAPA backbone. However, such scenario is quite improbable and it is more likely that other excited electronic states localized on peptide backbone contribute more to the NRD processes in NAPA conformers.

2.3.2 Vertical excited states of the amide groups in peptide systems

Amide groups electronic states were firstly addressed in a series of theoretical paper by Serrano-Andrés *et al.* to understand the absorption bands in the spectra of proteins. [54–56] Model peptide systems containing only amide groups were used. Only vertical excitations were computed on optimized ground state structures (all at the MP2/6-31G(d) level). No geometry optimization was performed on any of the excited state PES-s. A large variety of well defined excited states was found at the CASSCF/CASPT2/ANO level, ranging from local excitation on amide groups to Rydberg and charge transfer states between neighboring amide groups. The lowest energy excited states present in all models are the $n\pi^*$ states with excitations localized on the carbonyl in amide groups. Formally the unbounded electron pair (n) belongs to the oxygen atom, while the π^* is the anti-bonding C=O orbital. However, the charge of the nitrogen atom is also considerably redistributed in the excited states. These bands appear around 5.5 eV, but have weak oscillator strengths so contribute little to the protein absorption spectrum. These are followed by intense transitions to $\pi\pi^*$ states on the C=O groups with a usual excitation energy of 6.5–7.4 eV, whose exact values strongly depend on the amide’s neighboring groups. The second, higher, C=O $\pi\pi^*$ excited state is above 9.6 eV. Between these two strongly absorbing electronic states a large number of Rydberg states is intercalated, but due to their extremely small transition dipole moments (apart for few exceptions) they barely contribute at all to the absorption spectra of proteins.

On a series of models containing one amide group (formamide, acetamide, and their *N*-methylated compounds) the authors have clearly indicated that the addition of alkyl groups (methyl in their case) on nitrogen atoms stabilizes all $n\pi^*$ and $\pi\pi^*$ excited states localized on the same amide group. This was partly rationalized from findings that a large quantity of electronic charge (from population analysis estimated 0.3–0.4 e^-) is transferred from a nitrogen atom to the C=O group, especially in $\pi\pi^*$ transitions. From Mulliken charges it was concluded that the addition of electron-withdrawing methyl groups decrease the electronic charge on the nitrogen atom which destabilize the ground electronic state through decreasing the conjugation between the N and C atoms. Although no information about partial atomic charges in the excited states are given, it was reasoned that the methyl groups stabilized the nitrogen atom in the excited states. The cumulative effect is the stabilization of the excited states upon inclusion of a methyl group. As observed,

the methylation of the second amide group in NAPA causes a significant increase of conformer B excited state lifetime, so how this stabilizing effect of methyl group affects the excited state dynamics remains to be seen. In glycine di- and tripeptide a set of charge transfer (CT) states between neighboring amide groups with energies in range 7–9.5 eV was identified, showing two types of characters. The first, with an electron transfer from the occupied π C=O orbital localized on one amide group to the π^* orbital of the next amide group, while the second type of excited states include the occupied n orbitals, and are found higher in energies. Interestingly, the oscillator strengths of both types of CT excited states are not negligible. The authors also made a coarse step scan of two Ramachandran angles which distort the dipeptide geometry from its all planar structure (β_L chain) to examine how are the vertical excitation affected by structure deformation. Owing to the Gly dimer achirality, only a part of two-dimensional space was scanned, the rest was mirrored. No attempts were made to identify secondary structures in their scan. The excitation analysis for each geometry was made, where one particular geometry with Ramachandran angles $\Psi = +60^\circ$ and $\Phi = -60^\circ$ attracts attention. It is the closest structure to the γ_L secondary structure, exhibiting a deformed C_7 ring. Although its H-bonds are not optimized, the close vicinity of the two amide groups certainly stabilize its local $n\pi^*$ and $\pi\pi^*$ excited states when compared to the corresponding states in the β_L structure, while the CT states increase in energy. Few lowest triplet excited states were also calculated for simple model amide groups, and as expected, all were lower in energy than their corresponding singlet states. The amount of stabilization energy is however strongly dependent on the character of the particular state, ranging from 0.3 eV for $n\pi^*$ states to 1.5 eV for $\pi\pi^*$ states.

Returning to NAPA conformers, the inability to include the orbitals describing unbounded electron pairs on N and O atoms in full active space of their CASSCF calculations, has cost Došlić and co-workers the absence of $n\pi^*$ excited states in their reproduction of NAPA UV spectrum. In their TDDFT calculations, CT states, for reasons explained later, have dropped in energy and mixed with localized states, eventually obscuring a clear characterization of excited electronic states in NAPA conformers.

2.3.3 NRD mechanisms of formamide

To examine the general topography of amide excited states PES-s, Liu *et al.* used the formamide molecule as the simplest model for an excited amide group and found a variety of NRD mechanisms through which this system can reach the CI with the ground electronic state. [57] The mechanisms including only singlet excited states were investigated by Antol *et al.*, who also studied the branching of the initial vertical nuclear population between these various deactivation pathways using non-adiabatic molecular

dynamics simulations at the CASSCF(10,8)/6-31G(d) level of theory. [58]. It was found that the Franck-Condon region of $n\pi^*$ excited state is located on the steep part of PES 1.83 eV above the S_1 minimum energy geometry of the same character. The latter exhibits a significant C=O bond extension and a total deplanarization of the starting planar vertical geometry. Similarly, the higher vertical $\pi\pi^*$ excited state does not also possess a local minimum and descends through a cascade of CI with the lower Rydberg states until finally reaching the CI with the $n\pi^*$ state. The S_1 minimum is connected through various pathways with different types of CI points with the ground state, where each pathway has a TS barrier in between. The lowest and almost isoenergetic to S_1 minimum corresponds to the homolytic C–N pre-dissociative CI which is separated from the S_1 minimum over the lowest TS barrier of 0.45 eV, and thus causing 76 out of 100 trajectories to undergo this NRD channel. After passing the CI region the molecules fragment to CHO and NH_2 radicals, where only few recombine or exchange an H atom. The next CI corresponds to the dissociative N–H pathway but due to a 1.44 eV transition state (TS) above the S_1 minimum it is virtually unreachable and no corresponding trajectory was observed. Even higher lies the barrier for C–H bond dissociation. While no C–H bond dissociation were observed in the excited state, fragmentation does happen in the vibrational hot ground state which is reached *via* a non-dissociative deactivation pathway whose CI with the ground state is characterized by a bent O–C–N angle approaching 87° , a C=O bond extended by additional 0.05 Å, and with one N–H bond almost perpendicular to the O–C–N plane. Only 7 trajectories deactivate through this channel because the CI is 0.8 eV above the minimum. The rest of the trajectories remained in the excited state in the 1 ps long simulation time. Although C=O bond extends significantly in the S_1 state, its dissociation is only observed in the $\pi\pi^*$ state dynamics simulations, where some of its cleavage is aborted on account of vibrational energy transfer to C–N bond dissociation. However, the dominating NRD pathway in $\pi\pi^*$ state is homolytic C–N bond dissociation over the S_1 state. All mentioned CI-s and corresponding TS-s are however energetically quite above the S_1 minimum, so generalization of formamide values to other more realistic peptide systems should be done with caution. Liu *et al.* also examined the possibility of ISC between S_1 and T_1 PES-s and determined a ISC point 0.8 eV above the S_1 minimum on CASSCF(6,6)/6-31G(d) level, but did not provide the S_1/T_1 couplings. However, experiments on matrix isolated formamide molecules indicate that only through interaction with a heavy atom (such as Xe) the ISC could become the prevailing NRD pathway. [59] As stated previously by Serrano-Andrés *et al.*, [54] due to its small size and inability to delocalize its electrons formamide is not the best choice for accurate representation of the amide group. Nonetheless all above obtained NRD mechanisms are plausible in the excited amide group of real peptide system.

It is now clear that such a vast number of excited electronic states located on NAPA backbone must in some way interact with its lowest phenyl $\pi\pi^*$ state and contribute to the NRD mechanisms of its vibrationless excited state. A great deal of work has contributed to the general understanding of population transfer from one excited state to the other, including studies on amino acids and peptides, but interestingly none of the latter works examined the excited amide groups in ways similar to formamide.

2.3.4 H-transfer assisted NRD mechanism between amide groups in peptide systems

A cornerstone of NRD mechanisms in peptides was introduced by Sobolewski and Domcke in their seminal theoretical work on deactivation of excited capped Gly trimer in a β -turn conformation. Generally, in a β -turn secondary structure a H-bond connects the i -th residue with the $(i+3)$ -th residue within a 10-member ring and stabilizes this type of peptide conformation. Motivated by the H atom transfer processes within H-bonds in the deactivation mechanisms of excited DNA base pairs, [60] the authors investigated the role of H-bond motive in excited states of peptides as well. Using the second-order approximate coupled cluster singles and doubles model, shortly abbreviated as CC2, for excited state calculations, the $n\pi^*$ states localized on amide groups were easily reproduced. These so-called local excitation (LE) states have the expected vertical energies above 5.5 eV. Particularly, the S_1 energy of the ground state configuration is 5.72 eV and the corresponding excitation is completely localized on the last amide group in sequence, exactly opposite to the donating H atom residue. The expected mechanism would include a H atom transfer along the H-bond from nitrogen to oxygen atom, so the N–H distance of the first residue was set to be the driving coordinate. Using constrained optimizations for a fixed N–H distance all other degrees of freedom were optimized to construct a minimum energy path for a corresponding excited electronic state. By scanning a minimum energy path beyond 1.5 Å a new set of structures with H atom in close proximity to O atom of the opposite residue were constructed on the S_1 PES. These geometries belong to a new excited electronic state with an energy lower than LE states and of CT character, in which a single electron from the first amide group is transferred to the opposite C=O group turning the system into a biradical. Unlike the ground electronic and the S_1 LE state, the CT state is repulsive, descending in energy with N–H bond extension. At the same time, the nuclear arrangement in the CT state is highly unfavourable in the ground electronic state, causing the ground state energy to rise abruptly with only a slight extension of the N–H distance and intersecting with the CT state in a new CI. The CI between the two states was only indicated, because the CC2 method, being a single-reference method with a non-Hermitian electronic Hamilton operator is not adequate for treating CI

between the excited and ground electronic states. Also because the used implementation lacks the ability to calculate the non-adiabatic coupling vectors, the CI between the LE and CT states could not be obtained. However, two similar nuclear configurations for each electronic state were found, indicating that a real CI is somewhere between these two points. Although this CI was not determined in any way, its corresponding energy was estimated to definitely lay below the vertical excitation energy to the LE state, enabling the system to efficiently transfer its population from LE to CT state after the photoexcitation. While details for this mechanism step were not determined, it was argued that they do not deviate much from the analogue mechanisms in excited DNA base pairs, and that the population transfer is expected to happen on a similar time scale as for base pairs. When the population has been transferred to the CT state it is being immediately driven by the repulsive nature of the CT state to the CI with the ground state. Once the system is finally in the ground electronic state, the H atom is transferred back to the nitrogen atom and all excess electronic energy is converted into molecular vibrations. With this last step of the proposed NRD pathway the cycle of converting the electromagnetic radiation into harmless heat has been closed, where the authors have also clearly demonstrated the role of amide excited states. It remains to be seen how the phenyl $\pi\pi^*$ states couple with the amide excited states.

2.3.5 NRD mechanisms in Phe or Trp containing peptide systems

This was partly elucidated by Shemesh *et al.* who following the mechanism above proposed explained the absence of R2PI signal from a set of Gly-Phe-Ala tripeptide secondary structures predicted to co-exist in gas phase. [31] Valdes *et al.* argued that the non-existence of these conformations in the R2PI spectrum is due to the sub-picosecond non-radiative deactivation mechanism which depopulates the Phe $\pi\pi^*$ state before the second laser pulse could photoionize it. [21] The same set of arguments was used to explain the absence of certain conformers of Trp-Gly and Trp-Gly-Gly peptides. [24] In the critical conformers the backbones of the Phe residues are in a local structural conformation of γ -turns, where the most stable form among them has its Phe residue together with its two amide groups positioned as in NAPA conformer C. Although γ_L -turn secondary structures are quite different from β -turns, they resemble the latter structures in few key points, most importantly in the two interfacing amide groups joined by a H-bond. Therefore a similar mechanism including a H atom transfer was expected to play a role in the NRD of Gly-Phe-Ala as in the previously studied β -turn case. The N–H distance of the second amide group was taken again as the driving coordinate, while CC2 method was used for the calculation of the excited states. The optically accessible S_1 electronic state in the Gly-Phe-Ala is of phenyl $\pi\pi^*$ character, and possesses a benzene type S_1 minimum.

More importantly, a second minimum of LE character localized on the first amide group was found on the S_1 PES. This LE state is energetically more stable and geometrically different from the $\pi\pi^*$ minimum. Extending the N–H distance along the corresponding minimum energy path, a new CT state becomes more stable and drops in energy below the LE state. Like in the β -turn case, the CT state includes an electron transfer from the second to the first amide group. Unlike the $\pi\pi^*$ and LE excited states, the CT state is repulsive where further increase of the N–H distance leads the CT state directly to the CI with the ground electronic state. Once in the ground state, the H atom is transferred back to the N atom, and all excess of energy is redistributed as molecular vibrations. Again no mechanistic details about how the system reaches the CT state from the LE state are given, but a real CI point between the $\pi\pi^*$ and LE states was now found. While both states have a minimum, a linear interpolation path (LIP) between these two geometries was constructed to account for the potential energy change when going from one minimum to another. Because the LIP is constructed from interpolation between two molecular geometrical structures in internal coordinates it is not a minimum energy path between the two endpoints, and all obtained values in-between, coordinates and corresponding energies, are far from optimal. Nevertheless an estimation of CI energy can be obtained. While here one is only interested in the electronic population confined to the lower electronic state, the CI acts as a simple barrier. Although no exact value is given in the original work, the obtained CI energy was assumed to be rather small (≈ 0.2 eV). Knowing that LIP gives an overestimated value, the true barrier is even lower in energy, indicating a plausible NRD mechanism. Thus the proposed relaxation scenario consists of a population transfer from the initial $\pi\pi^*$ state through three consecutive CI points until finally reaching the ground electronic state and dissipating all excess energy into nuclear motions.

The same authors had also applied their proposed mechanism for explaining the excited state properties of *N*-acetyltryptophanmethylamide (NATMA) molecule, [32] a structural analogue of NAPMA, where only the phenyl ring is substituted by indole. Similarly to NAPMA, Dian and co-workers observed three NATMA conformers present in the gas phase, two of which are completely analogue to NAPMA conformers A and B. [26] The third and least stable form is of $\beta_L(g-)$ conformation. The main reason for the theoretical investigation of excited states properties in NATMA conformers was an observed anomaly in the UV spectrum of one NATMA conformer. It turned out that NAPMA conformer B is an exact structural analogue to this NATMA conformer, apart from the indole ring of course. While the other two NATMA conformers show sharp vibronic transitions in their corresponding UV spectra, the NATMA C7 structure has an extremely broad and structureless absorption band. The same anomaly is observed in

the C7 structure of the unmethylated molecule, *N*-acetyltryptophanamide (NATA). In fluorescence-dip infrared experiments (FDIR) it was also shown that exciting the indole's NH stretch vibrations in S_1 excited states causes a loss of fluorescence signal in NATMA C5 structures, while the rest of NH and CH stretch transitions have sharp lines in FDIR spectrum. [27] In contrast all vibrational transition in the S_1 state of the NATMA C7 structure quench the fluorescence of its S_1 excited state. While the absence of fluorescence caused by the excitation of indole NH stretch vibration can be solely explained on the basis of population transfer from indole excited state to its dissociative $\pi\sigma^*$ electronic state, the same quenching and the broadening of the UV band in NATMA C7 structure is definitely caused by some other NRD mechanism that is persistent regardless of vibration excitation in the excited state. Since the NATMA C7 structure has a γ_L -turn with a H-bond it was an excellent candidate to test whether the above proposed NRD mechanism could reveal the conformer's observed excited state properties.

To cut the above story short, an adapted graphics of proposed NRD pathway in NATMA conformer is displayed in Figure 2.6. The mechanism is completely similar to the two previous cases, with just few slight differences. Firstly, all PES were calculated using the algebraic diagrammatic construction method to the second order (ADC(2)) to better account the CI-s, because the method is based on the Hermitian electronic energy operator. Secondly, the indole ring has two low lying excited electronic states of $\pi\pi^*$ characters, the L_a and the L_b , where the latter is the first absorbing state in the vertical excitation. The two states can easily interact, and in NATMA C7 ground state structure they are separated by a merely 0.05 eV energy differences. Upon optimization the ordering of the characters is reversed, making the S_1 PES minimum of L_a . The energy difference between the vertical and S_1 minimum is also conformer dependent, being largest for the NATMA C7 structure with a value of ~ 0.4 eV. A partial explanation for a larger stabilization of L_a state in C7 structure is due to a favorable N-H $\cdots\pi$ interaction between the backbone and the indole ring. The reversal of the character of these states clearly indicates a possible population transfer from the vertically L_b states to the L_a state immediately after the absorption of radiation. However since both $\pi\pi^*$ states are fluorescent, the observed quenching is not due to the population transfer between the two states. The alternative is the deactivation to a dark electronic state, such as the LE state. Again, a cascade of three CI between four types of electronic states was constructed. Details about reaching a CT state from the LE were again not considered, but more importantly the CI-s between the L_a and LE states were estimated and they clearly indicate the differences in the relaxation dynamics between NATMA conformers. Also, for the first time, the authors address the geometries of the corresponding LE state minima, where a large geometrical distortion of the first amide group accompanies the excitation

transfer to the LE state. Most of the geometrical difference lies in the O–C–N_{Phe}–H torsion angle of the first amide group, whose value in LE state is only 81° when compared to the almost planar amide groups of the ground and L_a states. In the formamide S₁ minimum the corresponding dihedral angle is 66°. For the NATMA C7 structure the barrier is ~0.8 eV above the L_a state, while in one NATMA C5 structure it is ~0.6 eV. Although at the first glance this seems contradictory, taking into account the stabilization energy of the L_a state the barrier for the NATMA C7 structure turns out 0.3 eV above the vertical excitation, which is 0.1 eV less than the barrier for the next NATMA C5 structure. Furthermore, the NATMA C5 structures lack the deactivation of LE states through a CT channel because these conformers do not possess a favorable H-bond that would drive the H atom transfer process. No alternative deactivation pathways for these states were given. Based on the difference in energy barriers it was finally concluded that a larger portion of LE excited state manifold is accessible from the vertical excited state in NATMA C7 conformer than in C5 structures.

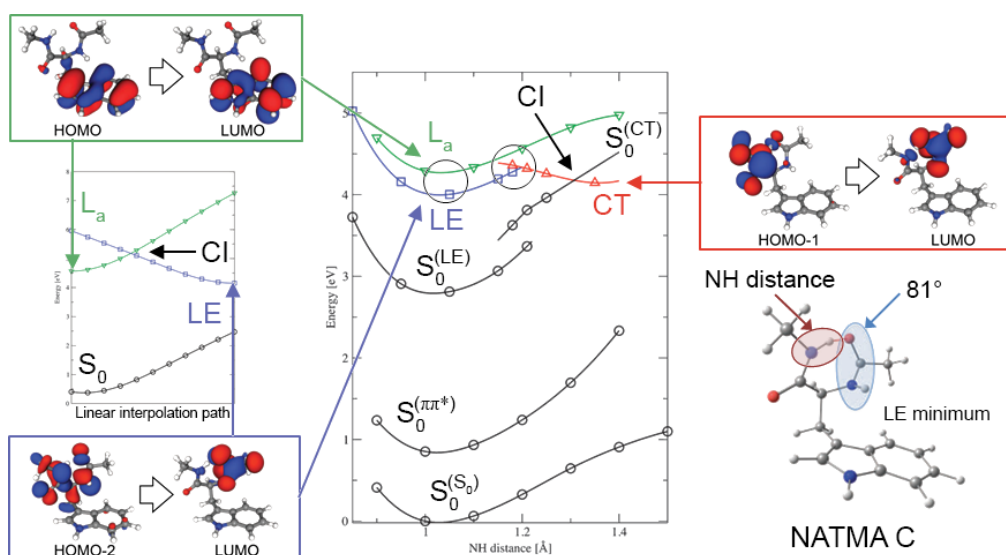


Figure 2.6: Proposed NRD mechanism of photoexcited $\pi\pi^*$ state of NATMA C conformer by Shemesh *et al.* [32] Figure adapted from the same reference. The middle image depicts the dependence of molecular L_a, LE and CT PES-s, each with its own corresponding S₀ PES, on the constrained N–H bond distance. The character of each excited state is illustrated using the largest contribution to the CIS expansion of the electronic transition displayed in terms of canonical HF orbitals. The black circles designate the geometries in configuration space which were used to obtain the corresponding CI-s between states using linear interpolation paths, as depicted on the left hand side image for a CI obtained by connecting the L_a with LE minimum. The black arrows designate the true CI-s. The right image displays the minimum geometry of the LE state, where the strongly distorted first amide group is characterized by one of its small torsional angles (shaded blue), while the NH bond distance of second amide group was used as the NRD pathway driving coordinate (shaded in red).

To reveal how the dissociative $\pi\sigma^*$ relaxation channel competes with the previous mechanism, a very simple scan of PES-s was constructed by just extending the indole N–H bond. To reach the dissociative $\pi\sigma^*$ state a barrier of 5400 cm^{-1} above the vertical excitation energy was estimated. Although its true value is lower than the estimated one and the H atom has the potential to tunnel through the barrier under the CI [61], the experimental results clearly show that the rate of indole NH dissociation does not surpass the rate of excitation transfer to LE state in NATMA C7 structure. However, the dissociative $\pi\sigma^*$ mechanism probably does compete in the other two conformers, while it becomes the dominant relaxation pathway of S_1 state with vibrationally excited indole NH stretch vibration.

The details of LE/CT CI were finally addressed by Shemesh and Domcke on Ac-Phe-Xxx-NH₂ (Xxx = L-Ala, D-Ala, Aib, where Aib stands for aminoisobutyric acid) capped model dipeptide system, [62] which Glogen *et al.* have initially used to study the effects of the residue chirality on folding of peptide secondary structures. [63] Only one conformer of Ac-Phe-L-Ala-NH₂ and Ac-Phe-D-Ala-NH₂ was identified in the gas phase whose secondary structures correspond to β_L - γ_L and β_L - γ_D , respectively. Except for the R2PI UV spectrum, no experimental measurements of excited state lifetimes or any other excited state properties were conducted on these peptide systems. Nevertheless, Shemesh and Domcke used these model systems to study how the chirality potentially effects their previously proposed NRD mechanism. The N–H bond length of the terminal NH₂ group was set as the driving coordinate. While all studied γ_L and γ_D conformer pairs of each molecule display almost the same barrier heights for the population transfer from the initially excited $\pi\pi^*$ to LE states, the authors reason that a potential reaction bottleneck could be the excitation transfer between LE and CT states. LIP-s between the LE minimum structure and the CT γ_L geometries with the N–H bond constrained to the value in LE minimum have revealed an almost barrierless avoided crossing between the two states instead of a CI point. On the contrary, the complementary γ_D -turn conformers have a CI point which gives a quite significant barrier for population transfer. Despite the fact that the obtained avoided crossing is actually a cut through PES-s near the CI seam, it displays an efficient route for population transfer between parts of configuration space. From pure geometrical similarities of the local γ_L -turns it can be concluded that the previously studied Gly-Phe-Ala and NATMA systems also have a barrierless pathway between LE and CT electronic states, confirming that the rate-limiting step of the proposed NRD is the excitation transfer from the aromatic $\pi\pi^*$ to the $n\pi^*$ state of the nearby proton-withdrawing amide group. More importantly, the local γ_L -turn in Ac-Phe-Gly-NH₂ conformer is almost geometrically identical to the γ_L -turns of NAPA conformers, so a completely analogue NRD mechanism is expected in NAPA conformers

B and C. As it will be shown in the Results section, this NRD mechanism is plausible in NAPA conformers, but not their dominant relaxation pathway.

2.3.6 Non-adiabatic molecular dynamics of Trp systems

Shemesh and co-workers have clearly demonstrated the importance of excited states localized on amide groups in the NRD pathways of excited aromatic states in peptide systems. However, many questions regarding the true nature of population transfer still remain open, where the two most notable ones are the true involvement of the H-bond and the details about the evolution of the nuclear wave packet. The above NRD mechanism is constructed around the strong H-bond motive, where the H atom transfer strongly destabilizes the ground electronic state bringing it eventually to the crossing with the populated excited state. Another advantage of this motive is that it also enables a simple and intuitive construction of the reaction mechanism. But, as stated previously for formamide, alternative deactivation pathways of excited amide group exist and the strength of the H-bond in excited states is unknown. The solution to the above questions is to move from an intuitive construction of NRD mechanisms to an all-atom scale simulations of NRD processes. While exact wave packet propagation can account for all quantum effects, a preconstructed PES-s along which the wave packet could propagate is necessary, which at the current computational and algorithm stage can be only accomplished for few atoms model systems. Reducing the full dynamics to only few degrees of freedom enables larger systems to be treated in this way, but it also immediately introduces a degree of bias to the description of the system. As hinted in Introduction, an elegant, but computationally demanding solution is to use non-adiabatic molecular dynamics simulations for a blind, unbiased search of NRD mechanisms. Prior to the publication of the results in this thesis, only one full-scale dynamics simulation was conducted by Mercier *et al.* on a protonated molecule of Trp (TrpH^+) to disclose the mechanism responsible for shorter excited state lifetime of TrpH^+ in gas phase than in liquid solution. [64] The authors used TDDFT/PBE method with plane waves to demonstrate an excitation transfer from the indole excited state to the C–N bond dissociative $\pi\sigma^*$ state that leads to an eventual NH_3 group dissociation and deactivation of the excited state. The water molecules interact strongly with the amino acid, particularly with the NH_3 group causing the dissociative $\pi\sigma^*$ state to significantly rise in energy and becoming inaccessible, hence prolonging the excited state lifetime of indole. This result is however inapplicable to NAPA where the C–N bonds strongly differ in type. In the same work, the authors also examined the photoinitiated dynamics of protonated Gly-Trp molecule. Unfortunately the primary goal was to elucidate whether an excitation transfer is possible when the two system parts are separated by one amino acid residue. Thus, the connecting amide group was cut out and

only 3-methylindole and protonated methylamide were kept at the original distance as in the starting peptide. The insight into the potential involvement of amide group was therefore left out.

To summarize this section, from all above mentioned considerations one can conclude that a vast variety of NRD mechanisms can be plausibly realized in peptide systems. However, none of them can directly explain the observed difference between excited state lifetimes of NAPA conformers. Also, the dynamical insight into NRD mechanisms of peptide systems has been generally left out. Moreover, quantum effects which may be of vital importance when dealing with the lowest vibrational states of excited PES-s were not considered at all. Therefore the goals of this thesis are crystal clear: to elucidate and examine in details the NRD mechanism of NAPA conformers. Hence a detail explanation of the underlying theoretical concepts and methods logically follows.

3 Theory and Methods

3.1 Initial axioms and approximations of the quantum system

It is now important to give a complete overview of all the theoretical concepts used in unravelling the NRD processes in NAPA molecules. An initial set of all the axioms and approximations used in the construction of the theoretical model system is explained on a single generalized molecule. Let this molecule consists of N_n atomic nuclei and of N_e electrons so that the whole molecule is electroneutral. Also, let this molecule be in a totally homogeneous and isotropic space where no external field of any kind is present so that the whole system is invariant to any arbitrary translational and rotational operation. Such conditions can be approximately reached in the diluted gas phase on the surface of Earth, e.g. under which NAPA gas phase experiments were performed. With the assumption that all the velocities in the system are significantly smaller than the speed of light, relativistic effects and their consequences shall be neglected. Therefore the particles mass, charge and spin are just their intrinsic constant properties. Taking that the space and time are absolute (Newtonian), a fixed (laboratory) point O with a corresponding Cartesian coordinate frame can be constructed, where each particle position is defined by a corresponding radius-vector, \vec{R} and \vec{r} for nuclei and electrons, respectively. Under all this assumptions, let additionally the number of electrons be even and all the nuclei be of relatively low charges so that any kind of spin interactions can be neglected and that the only forces by which all particles interact in the system are the instantaneous electric (Coulomb) forces. A system of this type can be completely described by a time dependent Schrödinger equation (TDSE) (displayed in atomic units)

$$i\frac{\partial}{\partial t} |\Psi(t)\rangle = \hat{H} |\Psi(t)\rangle, \quad (3.1)$$

where the molecular total energy Hamiltonian, \hat{H} , is only dependent on the particles positions and velocities. All properties of the system are given by the wave function $|\Psi(t)\rangle$, and can be extracted through the action of certain operators. It is also postulated that all spin symmetry properties are satisfied by the total system wave function, $|\Psi(t)\rangle$, i.e., the wave function is antisymmetrical with respect to permutation of two fermions indices, while symmetrical for the permutation of two bosons indices. Note also that Schrödinger equation (3.1) cannot be used to describe the effects of electromagnetic radiation absorption and emission. Although approximate effects of electromagnetic forces can be incorporated into the above model through additional perturbation terms, processes of electromagnetic absorption will not be studied. Instead only the dynamics of the system in an already prepared excited state $|\Psi(t_0)\rangle$ is going to be examined further. Due to this,

the competing processes of radiative relaxation (spontaneous or stimulated emission of electromagnetic radiation) cannot be treated with the above model, and therefore will not be studied explicitly further. Because no external force acts on the system, its total energy, E_{tot} , is conserved and defined by the systems initial conditions ($E = \langle \Psi(t_0) | \hat{H} | \Psi(t_0) \rangle$). The solution of equation (3.1) is usually constructed from the Born-Oppenheimer (BO) concept based on the large difference between electronic and nuclear masses, which groups the molecular Hamiltonian into two terms

$$\hat{H} = \hat{T}_{\text{n}} + \hat{H}_{\text{e}}, \quad (3.2)$$

where the nuclear kinetic energy operator in position representation is

$$\hat{T}_{\text{n}} = -\frac{1}{2} \sum_{i=1}^{N_{\text{n}}} \frac{1}{M_i} \nabla_i^2, \quad (3.3)^1$$

while the electronic Hamiltonian takes a familiar form

$$\hat{H}_{\text{e}} = -\frac{1}{2} \sum_{i=1}^{N_{\text{e}}} \nabla_i^2 - \sum_{i=1}^{N_{\text{n}}} \sum_{j=1}^{N_{\text{e}}} \frac{Z_i}{|\vec{R}_i - \vec{r}_j|} + \sum_{i=1}^{N_{\text{e}}} \frac{1}{|\vec{r}_i - \vec{r}_j|} + \sum_{i=1}^{N_{\text{n}}} \sum_{j>i} \frac{Z_i Z_j}{|\vec{R}_i - \vec{R}_j|}. \quad (3.4)$$

M_i and Z_i are common designations for the i -th atomic nucleus mass and charge, respectively, relative to the corresponding values of an electron. For any fixed nuclear configuration, $\mathbf{R} = \{\vec{R}_1, \vec{R}_2, \dots, \vec{R}_{N_{\text{n}}}\}$, the electronic Hamiltonian is (at least in principle) completely solvable through the characteristic eigensystem relation

$$\hat{H}_{\text{e}}(\mathbf{R}) |\psi_i(\mathbf{R})\rangle = V_i(\mathbf{R}) |\psi_i(\mathbf{R})\rangle, \quad (3.5)$$

where the $V_i(\mathbf{R})$ and $|\psi_i(\mathbf{R})\rangle$ are the corresponding i -th eigenvalue and eigenfunction, respectively, whose parametric dependence on nuclear configuration defines the concept of electronic PES-s and states. The number of electronic states, where each is characterized by its corresponding energy, spatial and spin symmetry of its wave function, or some other observable defined by a linear Hermitian operator, is infinite. Also, all electronic eigenfunctions are (made) mutually orthonormal in any nuclear configuration

$$\langle \psi_i(\mathbf{R}) | \psi_j(\mathbf{R}) \rangle_{\mathbf{r}} = \int \langle \psi_i(\mathbf{R}) | \mathbf{r} \rangle \langle \mathbf{r} | \psi_j(\mathbf{R}) \rangle d\mathbf{r} = \int \overline{\psi_i(\mathbf{R}, \mathbf{r})} \psi_j(\mathbf{R}, \mathbf{r}) d\mathbf{r} = \delta_{ij}. \quad (3.6)$$

Vector \mathbf{r} designates the position of all electrons. Since only ψ functions with the same eigenvalues of spin operators ($\hat{S}_{\text{tot}}^2, \hat{S}_{\text{tot}z}$, where $\hat{S}_{\text{tot}} = \sum_{i=1}^{n_{\text{e}}} \hat{S}_i$ and \hat{S}_i are spin vector oper-

¹ $\nabla_i^2 = \vec{\nabla}_i \cdot \vec{\nabla}_i$, where $\vec{\nabla} = i \frac{\partial}{\partial x} + j \frac{\partial}{\partial y} + k \frac{\partial}{\partial z}$.

ators for each electron) are considered here, namely states of singlet multiplicity, explicit designation for integration over spin states is left out of the above expression. Singlet spin states are not explicitly designated. Also, if not stated otherwise, spatial integration is performed over the entire domain of the sub-integral function. Over-bar indicates complex conjugation. In practice, however, the Hamiltonian (3.4) is analytically unsolvable for any number of electrons greater than one, and certainly all existing approximate methods for eigensystem problem (3.5) cannot obtain an infinite number of solutions. Purely mathematically, however a complete basis exists, meaning that at least in principle all possible eigensystem solutions of electronic Hamiltonian can be constructed. Thus the full system wave function can now be expanded into this new basis, in the so-called Born-Huang *ansatz*

$$\langle \mathbf{R}, \mathbf{r} | \Psi(t) \rangle_{\mathbf{R}, \mathbf{r}} = \Psi(\mathbf{R}, \mathbf{r}, t) = \sum_{i=1}^{\infty} \Phi_i(\mathbf{R}, t) \psi_i(\mathbf{R}, \mathbf{r}). \quad (3.7)$$

The time variable is assimilated into the $\{\Phi_i\}$ set of functions which are also co-dependent on nuclear positions. Although this expansion is mathematically totally arbitrary, it has its physical roots in the previously introduced Born-Oppenheimer assumption that due to the large difference between electronic and nuclear masses, the electronic velocities significantly exceeds the speeds of atomic nuclei, making the i -th electronic density instantly adjustable to any configuration of atomic nuclei. The total wave function (3.7) is expanded into its adiabatic representation. As an alternative to the Born-Huang *ansatz* of the system's full wave function one can consider the mean field separation of electronic and nuclear motions ($\Psi(\mathbf{R}, \mathbf{r}, t) = \Phi(\mathbf{R}, t) \psi(\mathbf{r}, t) \exp \left[i \int_{t_0}^t E_e(t') dt' \right]$ where $E_e(t) = \iint \bar{\Phi}(\mathbf{R}, t) \bar{\psi}(\mathbf{r}, t) \hat{H}_e \Phi(\mathbf{R}, t) \psi(\mathbf{r}, t) d\mathbf{r} d\mathbf{R}$). [65] However, as shown elsewhere, [66, 67] the concept of evolution of a photoexcited system along a single time dependent potential and the inability to obtain multiple NRD mechanisms along separable PES-s are not consistent with the general photochemical view of NRD processes, thus the mean field approach is not considered further. The same arguments and further additional complexity makes the exact separation of electronic and nuclear motions ($\Psi(\mathbf{R}, \mathbf{r}, t) = \Phi(\mathbf{R}, t) \psi(\mathbf{R}, \mathbf{r}, t)$) of Abedi *et al.* [68] also highly inappropriate for unraveling NRD pathways. [69] Inserting the Born-Huang *ansatz* into the full system's Schrödinger equation (3.1) and simplifying the obtained expression by projecting it onto an electronic state ψ_i using orthogonality relations (3.6) an adiabatic representation of the TDSE is obtained

$$i \frac{\partial \Phi_i(\mathbf{R}; t)}{\partial t} = \hat{T}_n \Phi_i(\mathbf{R}, t) + V_i(\mathbf{R}) \Phi_i(\mathbf{R}, t) - \sum_{j=1}^{\infty} \sum_{k=1}^{N_n} \frac{1}{M_k} [\vec{d}_{k,ij}(\mathbf{R}) \cdot \vec{\nabla}_k + \frac{1}{2} D_{k,ij}(\mathbf{R})] \Phi_j(\mathbf{R}, t), \quad \forall i. \quad (3.8)$$

In the above set of equations, two new terms emerge, the non-adiabatic coupling vectors whose off-diagonal ($i \neq j$) elements are of the form

$$\vec{d}_{k,ij}(\mathbf{R}) = \langle \psi_i(\mathbf{R}) | \vec{\nabla}_k | \psi_j(\mathbf{R}) \rangle_{\mathbf{r}} = \frac{\langle \psi_i(\mathbf{R}) | \vec{\nabla}_k \hat{H}_e(\mathbf{R}) | \psi_j(\mathbf{R}) \rangle_{\mathbf{r}}}{V_i(\mathbf{R}) - V_j(\mathbf{R})}, \quad (3.9)$$

while their diagonal terms ($i = j$) are pure imaginary numbers, and the scalar coupling D_{ij} terms which are

$$D_{k,ij}(\mathbf{R}) = \langle \psi_i(\mathbf{R}) | \nabla_k^2 | \psi_j(\mathbf{R}) \rangle_{\mathbf{r}}, \quad (3.10)$$

also possessing complex diagonal terms. The non-adiabatic vector terms are antihermitian, meaning $\vec{d}_{k,ij}^\dagger = -\vec{d}_{k,ji}$ and can be used to expand the scalar terms into

$$D_{k,ij} = \vec{\nabla}_k \cdot \vec{d}_{k,ij} + \sum_l \vec{d}_{k,il} \cdot \vec{d}_{k,lj}. \quad (3.11)$$

The expression for non-adiabatic vectors (3.9) was obtained using the Hellman-Feynman theorem, [70] and clearly shows how the elements relative magnitude depend on the difference between eigenvalues of the corresponding electronic functions. Up to now, the adiabatic expansion of TDSE was mathematically exact, without the use of any approximation. However, as already stated, in practical use only a limited number of electronic states are obtainable where all functions have a real values. In general, aside from the probability density, the range of a wave function is the complex plane (e.g. $\psi_i(\mathbf{R}, \mathbf{r}) : \mathbb{R}^{N_n+N_e} \rightarrow \mathbb{C}$), whose real and imaginary parts together code information about density currents. More about the complex part of the wave functions is going to be addressed later, but from now on, unless stated otherwise, all electronic wave functions considered are only real functions. This assumption causes the diagonal non-adiabatic vectors to vanish as well as the imaginary parts of their off-diagonal elements. Using relation (3.10) expression (3.8) can be further simplified into a compact matrix notation

$$i \frac{\partial \Phi(\mathbf{R}, t)}{\partial t} = \left\{ -\frac{1}{2} \sum_{k=1}^{N_n} \frac{1}{M_k} \left[\vec{\nabla}_k + \vec{d}_k(\mathbf{R}) \right]^2 + \mathbf{V}(\mathbf{R}) \right\} \Phi(\mathbf{R}, t), \quad (3.12)$$

where the Φ is a column vector, generally of infinite dimension, but usually limited to few relevant electronic states. The matrix containing non-adiabatic coupling vectors is antisymmetrical ($\vec{d}_k^T = -\vec{d}_k$), and is therefore without diagonal terms, while the potential matrix \mathbf{V} is only diagonal with its elements strictly ordered. The above expression clearly displays how the non-adiabatic coupling vectors are solely responsible for coupling of two or more excited states. If they are set to zero, one obtains a matrix expression of BO model, where each electronic state evolves independently of the others along its own

$V_i(\mathbf{R})$ PES. However, from (3.9) it is evident that when the electronic states come close in energy, the BO approximation breaks down. The denominators determine the magnitude of the coupling terms (3.9), and in degeneracy points, like CI-s, they become infinite. Because of its complicated structure, equation (3.12) is only solvable by propagating nuclear wave packets, where the $\Phi_i(\mathbf{R})$ function defines the form of the nuclear wave packet on the corresponding PES. In the coupling regions of the configuration space the incoming nuclear wave packet can split between the interacting PES or few nuclear wave packets can interfere in such regions. This is at the very heart of any NRD process in photochemistry. Various methods have been developed for propagating nuclear wave packets. However, these computations can only be performed in reduced dimensionality, even for smaller molecules, because an enormous number of terms needs to be computed in order to construct a working Hamiltonian of type (3.12).

Up to now nothing has been said about molecular nuclear coordinates, and all previous expressions have been worked out in the laboratory frame of reference. Because, by definition, no external forces exist, the motion of center of mass can easily be extracted and the reference frame centered to it, shifting all dynamics into this new frame. [71] However, the obtained expressions are quite cumbersome, [71, 72] and are omitted here only for simplicity of mathematical expressions. Recently it was also shown by Cederbaum that the BO separation concept cannot exactly separate the motion of full center of mass, but rather the center of nuclear mass from all coordinates. [73] His alternative separation of the molecular Hamiltonian (3.2), similar to the aforementioned approach of Abedi *et al.*, corrects the problem, but on account of introducing a functional dependent term on the full nuclear wave function into the electronic Hamiltonian (3.4) making it more complex to solve. Because the total electronic mass makes in the worst case less than a part in thousand of the total molecular mass, coordinate separation over the nuclear center of mass can be safely applied, and the new frame is shifted to the nuclear center of mass. This means that one of the nuclear coordinates in all expressions depends on the rest of the atomic positions within the molecule.

Separation of the rotation is a slightly more complicated issue, being in principle inseparable from the remaining degrees of freedom. An approximate separation relies on applying the BO concept again, as relative velocities of nuclei are much smaller than for electrons. Under the assumption that relative nuclear velocities are moderate it is possible to neglect the centrifugal and the Coriolis inertial forces on the electrons, and introduce a new rotating reference frame centered also at the nuclear center of mass in which relative nuclear positions will satisfy Eckart's condition [71, 74]

$$\sum_{i=1}^{N_n} M_i \vec{R}_i \times \vec{R}_{0,i} = \vec{0}, \quad (3.13)$$

where $\vec{R}_{0,i}$ are the chosen reference coordinates. Although internal molecular forces cannot induce molecular rotation, small residual torques from computational methods or initial angular momentum can cause molecule to rotate, so each geometry is adjusted to the reference geometry to satisfy the Eckart's condition (3.13). Also, different electronic states have generally different angular momenta (relative to the fixed nuclear frame), and because electromagnetic radiation also possesses angular momentum, in the absorption process the final molecular excited state gains angular momentum. Its electronic angular momentum components can be obtained using operators \hat{L}_x , \hat{L}_y , \hat{L}_z , as well as the spin and total angular momentum operators. But with the use of real electronic wave functions to describe the excited states, their values cannot be obtained, while no such information is coded in the pure real electronic wave function. In the course of NRD process, when the system changes electronic states, the electronic angular momentum changes too, and because the systems total angular momentum is conserved, nuclear angular momentum has to adjust. The details of angular momentum readjustment between particles is going to be omitted here, and any change in molecular angular momentum is going to be transferred on the whole molecule. In other words, the molecule is taken to behave as a rigid rotor, with no partitioning of total angular momentum between particles. So in the NRD process, as the system is allowed to change electronic states, the total nuclear angular momentum changes accordingly with the electronic angular momentum, but is dropped out since only internal motions are considered. Taking into account that no high rotational states are or get populated, the rotational effects on internal degrees of freedom are generally not significant and rotation can be dropped out of description. Adjusting the molecule at any instant to satisfy (3.13), the rotational couplings can be minimized, and in the following text it is implicitly considered that this condition is applied.

Generally, any coordinate type can be used to describe molecular dynamics, but the art of simplifying the molecular Hamiltonian (3.12) is finding the minimum number of specific coordinates which can describe the wave packet propagation in the smallest possible dimension. Methods, e.g. like GARP, [75] have been used to obtain an orthogonal set of coordinates from a minimum reaction path which can then adequately span the important part of the configuration space, but usually rely on some predetermined reaction mechanisms. In short, direct wave packet propagation using TDSE (3.12) is unsuitable for blind search of new NRD pathways. Also, reduction of configuration space means that a certain kind of bias is introduced into the system, which should be avoided when unraveling new mechanisms. Apart from the problem of reaction space, the shape of the kinetic part of Hamiltonian (3.12) complicates solving the set of equations (3.12), while the singularities and unsmoothness of \mathbf{d} matrices can cause numerical instabilities and a significant accumulation of error. Therefore, different method schemes have been

developed, which instead of *a priori* construction of the molecular Hamiltonian (3.12) use combined quantum and classical techniques to simulate full dimensional nuclear wave packet evolution. Prior to turning attention to these alternative approaches for finding unknown NRD pathways, few details about interaction regions that originate from equation (3.12) are given next.

3.2 Conical intersection

The well known photochemical concept of internal conversion has its physical origin in the strong coupling regions of configurations space where the adiabatic PES-s come close together or even become degenerate. These PES-s, as solutions of electronic Hamiltonian (3.5), are strictly ordered by increasing energy, and apart from becoming degenerate they can never cross. However, this rule does not applied to electronic state characters, which becomes evident if the same electronic characters are continuously followed through regions of close encounters between two or more PES-s. The reason for this is the Born-Huang *ansatz* (3.7) which localizes and therefore divides the information of the full electronic wave function into separate terms of PES-s and non-adiabatic coupling vectors. As this simple relation shows

$$\frac{\partial |\psi_i(\mathbf{Q})\rangle}{\partial Q_k} = \hat{I} \frac{\partial |\psi_i(\mathbf{Q})\rangle}{\partial Q_k} = \left[\sum_{j=1}^{\infty} |\psi_j(\mathbf{Q})\rangle \langle \psi_i(\mathbf{Q})| \right] \frac{\partial |\psi_i(\mathbf{Q})\rangle}{\partial Q_k} = \sum_{j=1}^{\infty} |\psi_j(\mathbf{Q})\rangle d_{Q_k,ji},$$

the elements of non-adiabatic coupling vector matrix \mathbf{d} are just changes of the adiabatic electronic wave function characters projected on the same adiabatic basis. \mathbf{Q} is a vector of some generalized coordinates. PES-s and non-adiabatic coupling vector matrices can therefore be *a posteriori* recombined into a single matrix which would recombined the two separate pieces of information. Such conversion is the basis for TDSE transformation from adiabatic into a diabatic representation. Initial adiabatic electronic coefficients are unitary transformed

$$\Phi'_i(\mathbf{Q}, t) = \sum_{j=1} B_{ij}(\mathbf{Q}) \Phi_j(\mathbf{Q}, t), \quad (3.14)$$

until the non-adiabatic coupling vectors are made to vanish from equation (3.12), what consequently also transforms the electronic wave functions into new forms which are independent of nuclear positions

$$\psi'_i(\mathbf{r}) = \sum_{j=1} B_{ij}(\mathbf{Q}) \psi_j(\mathbf{Q}, \mathbf{r}). \quad (3.15)$$

A reverse approach in which one adjusts the electronic functions to satisfied the latter condition gives an equivalent result. [76] Within a complete basis and using the matrix notation, relation (3.14) is written in a form

$$\Phi'(\mathbf{Q}, t) = \mathbf{B}^{-1}(\mathbf{Q})\Phi(\mathbf{Q}, t), \quad (3.16)$$

with the use of an inverse matrix for later convenience. If the inverse of \mathbf{B}^{-1} is assumed to exist a reverse transformation from diabatic to adiabatic representation is possible ($\Phi = \mathbf{B}\Phi'$) and is used to transform the Hamiltonian (3.12) to a new diabatic basis

$$\begin{aligned} {}_i\mathbf{B}(\mathbf{Q})\frac{\partial\Phi'(\mathbf{Q}, t)}{\partial t} &= \mathbf{B}(\mathbf{Q})\hat{T}_n\Phi'(\mathbf{Q}, t) - \frac{1}{2}\sum_{i=1}^{3N_n-6}\left\{2\left(\frac{\partial\mathbf{B}(\mathbf{Q})}{\partial Q_i} + \mathbf{d}_{Q_i}\mathbf{B}(\mathbf{Q})\right)\frac{\partial}{\partial Q_i}\right. \\ &\left.+ \left[\left(\frac{\partial}{\partial Q_i} + \mathbf{d}_{Q_i}\right)\left(\frac{\partial\mathbf{B}(\mathbf{Q})}{\partial Q_i} + \mathbf{d}_{Q_i}\mathbf{B}(\mathbf{Q})\right)\right]\right\}\Phi'(\mathbf{Q}, t) + \mathbf{V}(\mathbf{Q})\mathbf{B}(\mathbf{Q})\Phi'(\mathbf{Q}, t). \end{aligned} \quad (3.17)$$

In the above expression the special $\llbracket \rrbracket$ brackets indicate that the content within has to be evaluated before applying it to vector Φ' . The $3N_n - 6$ generalized coordinates Q_i are sufficient for complete description of internal motions. If now for each coordinate of configuration space the matrix \mathbf{B} satisfies the condition

$$\frac{\partial\mathbf{B}(\mathbf{Q})}{\partial Q_i} + \mathbf{d}_{Q_i}\mathbf{B}(\mathbf{Q}) = 0, \quad (3.18)$$

the above Hamiltonian simplifies to a more compact form

$${}_i\frac{\partial\Phi'(\mathbf{Q}, t)}{\partial t} = \hat{T}_n\Phi'(\mathbf{Q}, t) + \mathbf{B}^\dagger(\mathbf{Q})\mathbf{V}(\mathbf{Q})\mathbf{B}(\mathbf{Q})\Phi'(\mathbf{Q}, t) = \{\hat{T}_n + \mathbf{W}(\mathbf{Q})\}\Phi'(\mathbf{Q}, t). \quad (3.19)$$

The form of relation (3.18) assures that the matrix \mathbf{B} is unitary ($\mathbf{B}\mathbf{B}^\dagger = \mathbf{B}^\dagger\mathbf{B} = \mathbf{I}$), which justifies the assumptions stated at the beginning and simplifies the finding of its inverse (3.16). The coupling terms have now been transferred from the kinetic part into the elements of the new potential matrix \mathbf{W} , whose corresponding elements are

$$W_{ij}(\mathbf{Q}) = \langle\psi'_i|\hat{H}_e(\mathbf{Q})|\psi'_j\rangle_{\mathbf{r}}, \quad (3.20)$$

but due to the relation (3.15) the above diagonal elements are not eigenvalues of the electronic Hamiltonian (3.4). Nonetheless they make the diabatic PES-s, which are smooth continuous functions of nuclear positions that can cross and change alignment in energy ordering. In regions of configuration space where they are well separated, they can be made to take up values of adiabatic PES-s, while in regions of strong interaction between

electronic states, where non-adiabatic coupling vectors for interacting states become large (theoretically infinite) and their electronic characters change abruptly, diabatic PES-s continuously retain their initial electronic character and smoothness. This property makes the diabatic representation numerically superior than the adiabatic representation for wave packet propagation. However, adiabatic to diabatic transformation is far from trivial, and generally it can be achieved only if the adiabatic basis is complete. [77–80] In practice only a *quasi*-diabatic representation with limited number of electronic states can be constructed, where the elements of non-adiabatic coupling vectors do not vanish, but can be made sufficiently small and discarded from consideration. [76, 79] Also, the same transformation by direct use of non-adiabatic couplings is rarely made, [76] and instead \mathbf{B} matrix is constructed by means of smoothing some observable, e.g. energy, dipole and quadrupole moment. [81, 82]

The existence of accidental energy degeneracies depends on the properties of electronic Hamiltonian

$$\mathbf{V} = \mathbf{C}\mathbf{H}_e^{(C)}\mathbf{C}^\dagger = \mathbf{B}\mathbf{W}\mathbf{B}^\dagger, \quad (3.21)$$

where the matrix \mathbf{C} contains adiabatic eigenvectors represented in some basis used by a given method for obtaining eigenvalues of electronic Hamiltonian. Although in practice the first representation is obtained from the second, conditions under which eigenvalues can become degenerate are easily explained in diabatic representation. Expression (3.9) clearly indicates that neighboring adiabatic states can potentially strongly interact, while the non-neighboring states, usually separated with a larger energy gap, do not interact strongly. This is also valid in the other two representations, although their states are not ordered in energy. When states interact weakly or not at all, their off-diagonal elements in matrix \mathbf{W} are close or equal to zeros, which breaks the matrix into block diagonal form

$$\mathbf{W}(\mathbf{Q}) = \begin{bmatrix} W_{1,1} & & & & & & & \\ & \ddots & & & & & & \\ & & \approx 0 & & & & & \\ \approx 0 & & W_{i,i} & W_{i,i+1} & & & & \\ & & W_{i+1,i} & W_{i+1,i+1} & & \approx 0 & & \\ & & & \approx 0 & & & \ddots & \\ & & & & & & & W_{n,n} \end{bmatrix}. \quad (3.22)$$

The case where only two states mutually interact is the most common for reasons explained later. Thus the corresponding two dimensional block of diabatic potential $\mathbf{W}_{2 \times 2}$ can be reexpressed as

$$\mathbf{W}_{2 \times 2}(\mathbf{Q}) = \frac{W_{i,i} + W_{i+1,i+1}}{2} \mathbf{I} + \frac{W_{i,i} - W_{i+1,i+1}}{2} \boldsymbol{\sigma}_z + W_{i,i+1} \boldsymbol{\sigma}_x, \quad (3.23)$$

using Pauli's σ_z and σ_x spin matrices (if the matrix elements $W_{i,i+1}$ are complex numbers, σ_y matrix would also appear in the above expression). The corresponding adiabatic potentials of the above matrix are its eigenvalues

$$V_{\pm}(\mathbf{Q}) = \frac{W_{i,i} + W_{i+1,i+1}}{2} \pm \sqrt{\left(\frac{W_{i,i} - W_{i+1,i+1}}{2}\right)^2 + W_{i,i+1}^2}, \quad (3.24)$$

which become degenerate only when the discriminant vanishes. Because nuclear positions are the only independent parameters in the above equations, degeneracy can be achieved by finding some nuclear configuration \mathbf{Q}_{CI} where the terms

$$W_{i,i}(\mathbf{Q}_{\text{CI}}) - W_{i+1,i+1}(\mathbf{Q}_{\text{CI}}) \text{ and } W_{i,i+1}(\mathbf{Q}_{\text{CI}}) \quad (3.25)$$

are equal to zero. From Wigner and von Neumann's non-crossing rule it follows that any symmetric (Hermitian) matrix possesses double degenerative eigenvalues if the mutual dependence between matrix elements is reduced by two (three) degrees of freedom compared to the non-degenerative eigenvalue matrix. [83] This means that two restraints are necessary to impose on all independent variables to keep two matrix eigenvalues degenerate. Because the matrix elements are functions of only nuclear positions, the non-crossing rule indicates that there exist a part of configuration space where degeneracy between two PES-s is preserved if motion is hindered along two degrees of freedom. This is easily seen from the Taylor expansion of potential matrix (3.23) or relation (3.24) around the \mathbf{Q}_{CI} point in which terms (3.25) vanish

$$\begin{aligned} \mathbf{W}_{2 \times 2}(\mathbf{Q}) = & \frac{(W_{i,i} + W_{i+1,i+1}) \Big|_{\mathbf{Q}_{\text{CI}}}}{2} \mathbf{I} + \sum_{j=1}^{3N_n-6} \left\{ \frac{\partial (W_{i,i} + W_{i+1,i+1}) \Big|_{\mathbf{Q}_{\text{CI}}}}{\partial Q_j} \mathbf{I} \right. \\ & \left. + \frac{\partial (W_{i,i} - W_{i+1,i+1}) \Big|_{\mathbf{Q}_{\text{CI}}}}{\partial Q_j} \sigma_z + 2 \frac{\partial W_{i,i+1} \Big|_{\mathbf{Q}_{\text{CI}}}}{\partial Q_j} \sigma_x \right\} \frac{\delta Q_j}{2} + h.o.d. \end{aligned} \quad (3.26)$$

If the first order derivatives at \mathbf{Q}_{CI} are different from zero, degeneracy is broken if molecular motion has any components along the gradients of terms (3.25), which thus define two degeneracy breaking coordinates, first called tuning coordinate defined along the direction of vector

$$\begin{aligned} \mathbf{g}_0 = & \frac{\mathbf{g}}{|\mathbf{g}|}; \\ \mathbf{g} = & \left[\frac{\partial (W_{i,i} - W_{i+1,i+1}) \Big|_{\mathbf{Q}_{\text{CI}}}}{\partial Q_1} \cdots \frac{\partial (W_{i,i} - W_{i+1,i+1}) \Big|_{\mathbf{Q}_{\text{CI}}}}{\partial Q_j} \cdots \frac{\partial (W_{i,i} - W_{i+1,i+1}) \Big|_{\mathbf{Q}_{\text{CI}}}}{\partial Q_{3N_n-6}} \right]^T \end{aligned} \quad (3.27)$$

and the second called the coupling coordinate along

$$\mathbf{h}_0 = \frac{\mathbf{h}}{|\mathbf{h}|}; \quad \mathbf{h} = \left[\left. \frac{\partial W_{i,i+1}}{\partial Q_1} \right|_{\mathbf{Q}_{\text{CI}}} \cdots \left. \frac{\partial W_{i,i+1}}{\partial Q_j} \right|_{\mathbf{Q}_{\text{CI}}} \cdots \left. \frac{\partial W_{i,i+1}}{\partial Q_{3N_n-6}} \right|_{\mathbf{Q}_{\text{CI}}} \right]^T. \quad (3.28)$$

Apart from symmetry enforced restriction in symmetric molecules, g and h coordinates are not orthogonal, and if not collinear they define the g - h branching plane. Any motion orthogonal to the branching space, at least in a close vicinity of \mathbf{Q}_{CI} point keeps the two PES-s degenerate until the higher order derivative terms (*h.o.d.*) like the second order terms

$$h.o.d. = \sum_{j,k=1}^{3N_n-6} \left[\left. \frac{\partial^2 (W_{i,i} - W_{i+1,i+1})}{\partial Q_j \partial Q_k} \right|_{\mathbf{Q}_{\text{CI}}} \sigma_z + 2 \left. \frac{\partial^2 W_{i,i+1}}{\partial Q_j \partial Q_k} \right|_{\mathbf{Q}_{\text{CI}}} \sigma_x \right] \frac{\delta Q_j \delta Q_k}{2} + \dots \quad (3.29)$$

become significant and begin breaking the degeneracy. This $3N_n - 8$ dimensional topological structure in configuration space for which two PES-s are degenerative defines the CI seam. Thus terms in above expression can be transformed to the new branching and seam space coordinates, which would then shown how strongly the branching and seam coordinates are mutually coupled. The branching plane defined by corresponding vectors is only a localized topological structure in configuration space that can change along the CI seam, and whose linear dependence region is determined by the size of *h.o.d.* Taylor terms (3.29). This linear dependence of matrix elements (3.25) gives the characteristic double cone shape of two adiabatic PES-s in branching space around the conical intersection point (Figure 3.1). The Wigner and von Neumann's non-crossing rule is an existence criterion which does not state anything about how to obtain a CI. The rule does however state indirectly that CI structures between three or more PES-s are rarer than between two states because the dimensionality and consequently the size of corresponding CI seams are increasingly smaller with the number of intersecting states (e.g. a three electronic state CI seam is a topological object of $3N_n - 11$ dimension). As shown in Literature Overview and later in Results sections, various schemes are used to obtain CI or close lying structures and to optimize CI seam elements. Yet, as can be seen from relations (3.21), the accurate topology of the CI and its seam space depends on the electronic structure methods used for obtaining excited electronic states, while different methods construct different types of $\mathbf{H}_e^{(C)}$ matrices. The most troublesome are the single reference electronic structure methods, which obtain the ground and excited states independently, meaning that the $\langle \varphi_i^{(C)} | \hat{H}_e | \varphi_j^{(C)} \rangle$ matrix elements between ground and all excited states are always zero. In single reference methods the $\varphi^{(C)}$ are usually the CIS type electronic wave functions, whose ground electronic state are just singly excited Slater determinants,

and due to Brillouin's theorem these states do not interact. The Brillouin's theorem does not apply to TDDFT, but in linear response ground and excited states also do not possess off-diagonal terms in potential matrix (see subsection 3.4). [84]

Due to this general orthogonality between ground and excited states in single reference methods, from the non-crossing rule follows that one of the restraints necessary to obtain degeneracy between ground and first excited state is lost. [85] This would manifest as one of the branching coordinates being transferred from branching to the seam space, namely the coupling h direction would not be defined, since the off-diagonal diabatic potential element of the W_{0i} used for its construction (3.28) is obtained only from the diagonal terms of the $\mathbf{H}_e^{(C)}$ matrix through unitary transformation connecting the two matrices. The degeneracy breaking now becomes inaccurately described only with the g vector, distorting the diabolic shape of PES-s in branching space to a form similar to the crossing of two diabatic states (consult Figure 3.1). With one direction now transferred to the seam space, whose dimensionality consequently increases to $3N_n - 7$, the size of the CI seam space becomes erroneously larger, giving much wider areas in configuration space where the two states become degenerate, wrong nuclear forces and couplings between ground and excited states. Consequently the (photo)chemistry near such regions of configuration space is inadequately described with the use of single reference electronic structure methods. NRD pathways obtained using these methods should be treated more as an indicative mechanism than accurate description of systems relaxation to the ground electronic state. Fortunately, the CI topology is accurately described between excited electronic states even with single reference methods, so these methods can be safely used in description of NRD processes taking place in excited states. The non-adiabatic conical vectors and their properties can now be derived from expression (3.18) and the relation between adiabatic and diabatic PES-s for a two electronic state CI. The eigenvectors that transform diabatic potential \mathbf{W} to its diagonal form are columns of transformation matrix

$$\mathbf{B}_{2 \times 2}(\mathbf{Q}) = \begin{bmatrix} \cos(\theta(\mathbf{Q})/2) & \sin(\theta(\mathbf{Q})/2) \\ -\sin(\theta(\mathbf{Q})/2) & \cos(\theta(\mathbf{Q})/2) \end{bmatrix}, \quad (3.30)$$

in which the trigonometric variable is

$$\theta(\mathbf{Q}) = \arctan \frac{2W_{i,i+1}(\mathbf{Q})}{W_{i,i}(\mathbf{Q}) - W_{i+1,i+1}(\mathbf{Q})}. \quad (3.31)$$

Inserting matrix (3.30) into (3.18) with taking into account definitions (3.27) and (3.28)

gives expression

$$d_{j,i,i+1}(\mathbf{Q}) = \frac{1}{(W_{i,i} - W_{i+1,i+1})^2 + 4W_{i,i+1}^2} \left[W_{i,i+1} \frac{\partial (W_{i,i} - W_{i+1,i+1})}{\partial g} \Big|_{\mathbf{Q}} \mathbf{g}_{0,j}(\mathbf{Q}) - (W_{i,i} - W_{i+1,i+1}) \frac{\partial W_{i,i+1}}{\partial h} \Big|_{\mathbf{Q}} \mathbf{h}_{0,j}(\mathbf{Q}) \right] ; j = 1, \dots, 3N_n - 6, \quad (3.32)$$

for components of non-adiabatic coupling vectors along generalized coordinates. These are transformed then to Cartesian $3N_n$ space vectors. All terms in previous expression are dependent on positions in configuration space, even the unit vectors of branching space. In close vicinity of CI, first derivatives and the branching vectors can be replaced with corresponding values at the CI point without effecting much the accuracy of expression (3.32). Equation (3.32) clearly shows how the non-adiabatic vectors \vec{d}_{ij} for the most common two state crossings are defined only with the two branching vectors in diabatic representation. As previously seen in relation (3.9), non-adiabatic coupling vectors are undefined at CI points because adiabatic and diabatic potentials become degenerated, while in diabatic representation the off-diagonal element W_{ij} has to vanish additionally. Directions of \mathbf{d}_{ij} vectors are given from linear combination of tuning and coupling vectors, which in a g - h branching plane resemble a circulating vector field (see Figure 3.1). Without the author's previous knowledge similar depiction of the circulation non-adiabatic vector field was recently published by Malhado and collaborators. [86] For single reference electronic structure methods the non-adiabatic coupling vectors between ground and any excited state coincide with the direction of the tuning vector, because the coupling vector is undefined due to the missing linear dependence in the corresponding W_{0i} term which instead of a branching h coordinate gives a direction along which the degeneracy stretches, therefore removes the circulation of non-adiabatic vector field. Generally, the circulation property originates from the monotonic linear dependence of W terms around CI point (left part of Figure 3.1), which consequently makes the adiabatic-to-diabatic transformation matrix B not unique, but doubled value when a full circle around a CI point is made. This also causes wave function phase (sign for real function) to change when a adiabatic-to-diabatic transformation is propagated around a closed circular path that surrounds a single CI point, as can be shown by simply evolving θ function (3.31) along this loop.² The same property can be used as an exact criterion for distinguishing degeneracy point of linearly dependent forms (3.26) from other types of degeneracies like the Renner-Teller intersection points. [88] This statement is also invalid to intersections between ground and excited states obtained with single reference electronic structure

²The acquired phase on single PES is called geometric or Berry's phase, whose mathematical grounds were recently questioned by Min *et al.* [87]

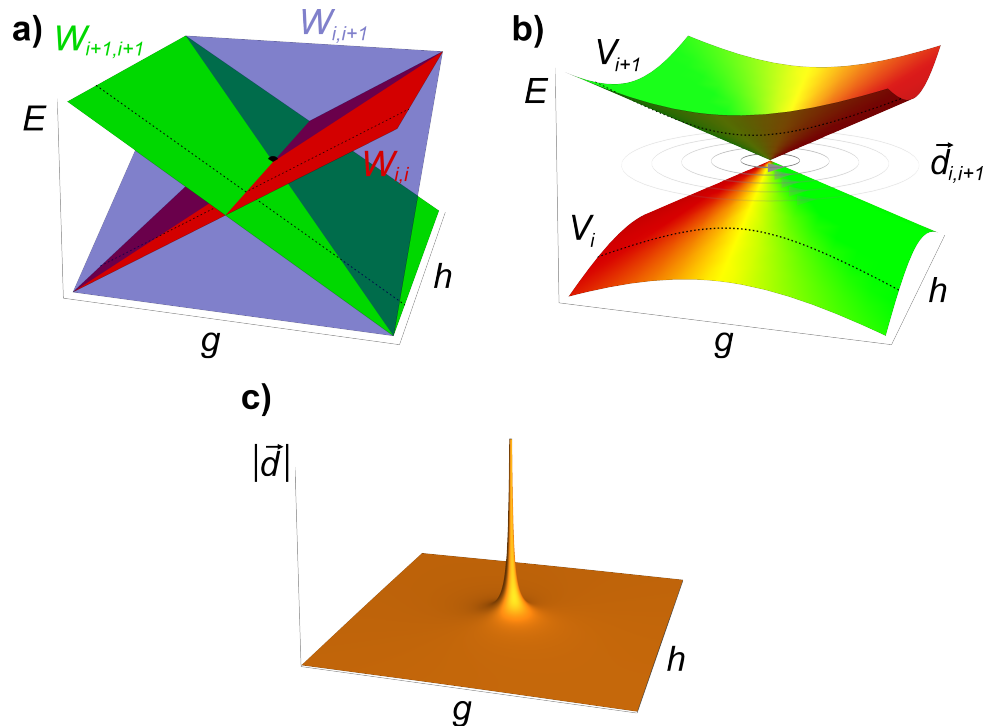


Figure 3.1: Potential energy surfaces in branching space near a two state conical intersection point of the Jan-Teller model shown in a) diabatic and b) adiabatic representations, respectively. A totally symmetric case is shown, which from any general CI differs only in the slopes of each PES. In a configuration point (black dot on figure a) where the two diabatic potential energy terms ($W_{i,i}$ and $W_{i+1,i+1}$) intersect and the coupling term $W_{i,i+1}$ vanishes, a diabolic (meaning double cone) degeneracy in adiabatic representation emerges. Colors (red and green) represent the characters of electronic states that gradually change in adiabatic representation along each PES (V_i and V_{i+1} , respectively), while are fixed for each state in diabatic representations. The circulating vector field on figure b) shows the non-adiabatic coupling vectors ($\vec{d}_{i,i+1}$) that would act on the nuclear wave function on one of the adiabatic PES. In the other state non-adiabatic vectors have reverse orientation. Figure c) shows the absolute magnitude of non-adiabatic vectors. The dotted lines on figures a) and b) show the typical energy profile exhibited along the same path in configuration space in both representations. In case of constructing an intersection between ground ($i = 0$) and first excited electronic state with single reference electronic structure methods the branching space in adiabatic representation resembles the branching space in diabatic representation, because the degeneracy is kept along the h coordinate.

methods. As can be derived from matrix (3.30) the character of adiabatic electronic state changes mostly in the direction of the g coordinate. In Figure 3.1, and later for Figures 3.2 and 3.3, this electronic character change is depicted as a graduate change of green to red color, where the two colors individually represent the diabatic contribution to the total adiabatic state character. It should be noted that the squares of this contributions are depicted on the mentioned figures, while if instead just the contributing values were

displayed (e.g. contribution of one diabatic state to the first adiabatic state is given by $\cos(\theta(\mathbf{Q})/2)$) a physically meaningless change of adiabatic wave function sign would appear after closing the full loop around the CI point. However, using square values a continual change of electronic character is constructed, as could be constructed for any other physical observable. Further details and consequences of adiabatic wave function phase change can be found in reference [76]. More interesting, however, are the relations between CI, non-adiabatic couplings and nuclear population transfer between PES-s in the formulation of non-adiabatic molecular dynamics which is considered next.

3.3 Derivation and concepts of surface hopping non-adiabatic molecular dynamics

A simple derivation of working equations later used to elucidate NRD processes are firstly given by following Tully's derivation [65] which was in detail justified by Curchod *et al.* [89] Afterwards the methodology is going to be connected with the TDDFT electronic structure methods. The interconnection between quantum and classical dynamics is based on Bohm interpretation of quantum dynamics through the use of quantum trajectory method. [90,91] The time evolution of nuclear wave packet in regions of weak interaction with other PES-s is described by BO approximation obtained by neglecting the coupling terms from expression (3.12)

$$i\frac{\partial\Phi_i(\mathbf{R},t)}{\partial t} = \left[-\sum_{j=1}^{N_n} \frac{1}{2M_j} \nabla_j^2 + V_i(\mathbf{R}) \right] \Phi_i(\mathbf{R},t). \quad (3.33)$$

If the nuclear wave function is now expressed in complex exponential form

$$\Phi_i(\mathbf{R},t) = A_i(\mathbf{R},t)e^{iS_i(\mathbf{R},t)}, \quad (3.34)$$

where $A_i(\mathbf{R},t)$ and $S_i(\mathbf{R},t)$ are real functions, and this expansion inserted into equation (3.33), after separating the real and imaginary part two dependent equations emerge,

$$\frac{\partial A_i(\mathbf{R},t)}{\partial t} = -\sum_{j=1}^{N_n} \frac{1}{2M_j} \vec{\nabla}_j \cdot \left[A_i(\mathbf{R},t) \vec{\nabla}_j S_i(\mathbf{R},t) \right] \quad (3.35)$$

and

$$-\frac{\partial S_i(\mathbf{R},t)}{\partial t} = \sum_{j=1}^{N_n} \frac{1}{2M_j} \left[\vec{\nabla}_j S_i(\mathbf{R},t) \cdot \vec{\nabla}_j S_i(\mathbf{R},t) - \frac{\nabla_j^2 A_i(\mathbf{R},t)}{A_i(\mathbf{R},t)} \right] + V_i(\mathbf{R}). \quad (3.36)$$

The last equation is the quantum counterpart of the classical Hamilton-Jacobi equation ($-\partial S/\partial t = H(\mathbf{R}, \partial S/\partial \mathbf{R}, t)$) where the only difference between these two types of equations is in the amplitude dependent terms $\nabla_j^2 A_i/A_i$. Also, from (3.34) it is clear how the amplitude A_i is connected with the probability density of the nuclear wave function ($A_i(\mathbf{R}, t) = |\Phi_i(\mathbf{R}, t)| = \sqrt{\rho_i(\mathbf{R}, t)}$). This allows the rearrangement of equation (3.35) into a continuity conservation expression

$$\frac{\partial \rho_i(\mathbf{R}, t)}{\partial t} + \sum_{j=1}^{N_n} \vec{\nabla}_j \cdot \left[\rho_i(\mathbf{R}, t) \frac{1}{M_j} \vec{\nabla}_j S_i(\mathbf{R}, t) \right] = \frac{\partial \rho_i(\mathbf{R}, t)}{\partial t} + \sum_{j=1}^{N_n} \vec{\nabla}_j \cdot \vec{j}_{i,j}(\mathbf{R}, t) = 0, \quad (3.37)$$

where the second term shows the divergence of the probability density current $\vec{j}_{i,j}$ summed over all nuclei. From the quantum Hamilton-Jacobi (3.36) and the continuity (3.37) equations it can be deduced that the gradient of action function, $S_i(\mathbf{R}, t)$, gives the corresponding vector velocity field (actually it gives the conjugated momentum which is connected to the velocity over a simple relation, $M_j \vec{v}_j = \vec{p}_j$)

$$\vec{R}_j(\mathbf{R}, t) = \vec{v}_j(\mathbf{R}, t) = \frac{1}{M_j} \vec{\nabla}_j S(\mathbf{R}, t), \quad (3.38)$$

where each velocity vector is a normal of the S_i isosurface. Continuity equation (3.37) shows that a change of nuclear wave function in some small volume element (dV) at some fixed point in configuration space is due to inflow and outflow of probability currents over time into this volume element. Taking a gradient of equation (3.36) with respect to some arbitrary nucleus k

$$\frac{\partial \vec{\nabla}_k S_i(\mathbf{R}, t)}{\partial t} = - \sum_{j=1}^{N_n} \frac{1}{M_j} \left[\left(\vec{\nabla}_j S_i(\mathbf{R}, t) \cdot \vec{\nabla}_j \right) \vec{\nabla}_k S_i(\mathbf{R}, t) - \vec{\nabla}_k \frac{\nabla_j^2 A_i(\mathbf{R}, t)}{2A_i(\mathbf{R}, t)} \right] - \vec{\nabla}_k V_i(\mathbf{R}) \quad (3.39)$$

and using the velocity definition (3.38) gives a more familiar expression

$$M_k \left[\frac{\partial \vec{v}_{i,k}(\mathbf{R}, t)}{\partial t} + \sum_{j=1}^{N_n} \vec{v}_{i,j}(\mathbf{R}, t) \cdot \vec{\nabla}_j \vec{v}_{i,k}(\mathbf{R}, t) \right] = - \vec{\nabla}_k Q_i(\mathbf{R}, t) - \vec{\nabla}_k V_i(\mathbf{R}), \quad (3.40)$$

where

$$Q_i(\mathbf{R}, t) = - \sum_{j=1}^{N_n} \frac{1}{2M_j} \frac{\nabla_j^2 A_i(\mathbf{R}, t)}{A_i(\mathbf{R}, t)} \quad (3.41)$$

is the quantum potential. Equation (3.40) gives the evolution of an entire velocity vector field viewed in a fixed, so called Eulerian viewpoint, where the vector field describes a stream of densities (3.37) through space and time. While each velocity vector is a tangent

to some particular stream, a volume (fluid) element, initially fixed in space, can be made to follow a stream and plot out its driving trajectory. If now the density change (3.37) is observed within this volume element, which follows the evolving stream line, an evolution of the system along a trajectory can be obtained. Thus it is then necessary to switch all above expressions into the new Lagrangian viewpoint using the transformation

$$\frac{\partial}{\partial t} + \sum_{j=1}^{N_n} \frac{1}{M_j} \vec{\nabla}_j S_i \cdot \vec{\nabla}_j = \frac{\partial}{\partial t} + \sum_{j=1}^{N_n} \vec{v}_{i,j} \cdot \vec{\nabla}_j = \frac{d}{dt}, \quad (3.42)$$

which gives the set of equations of motion for the trajectory being followed

$$M_k \frac{d\vec{v}_{i,k}^l(\mathbf{R}^l(t))}{dt} = -\vec{\nabla}_k Q_i(\mathbf{R}^l(t)) - \vec{\nabla}_k V_i(\mathbf{R}^l(t)), \quad (3.43)$$

$$\frac{dA_i(\mathbf{R}^l(t))}{dt} = -\frac{A_i(\mathbf{R}^l(t))}{2} \sum_{j=1}^{N_n} \vec{\nabla}_j \cdot \vec{v}_{i,j}^l(\mathbf{R}^l(t)), \quad (3.44)$$

$$\frac{dS_i(\mathbf{R}^l(t))}{dt} = \frac{1}{2} \sum_{j=1}^{N_n} M_j \left| \vec{v}_{i,j}^l(\mathbf{R}^l(t)) \right|^2 - Q_i(\mathbf{R}^l(t)) - V_i(\mathbf{R}^l(t)). \quad (3.45)^3$$

Explicit dependency on time is left out only for simplicity reasons, but it should be kept in mind that time is the only independent variable in the Lagrangian frame. It should be noted that the volume element dynamics is still considered from the starting Eulerian frame of reference. Although equation (3.43) resembles classical Newton's equation of motion, and the same integration techniques can be used to solve it, because the quantum potential (3.41) is not a local term since it depends on the global shape of the amplitude function A_i , trajectories cannot be propagated independently, but rather as a whole ensemble. [89] Therefore, equations (3.43)-(3.45) have to be solved simultaneously for all trajectories. The superscript l indicates a particular trajectory within the ensemble. Equations (3.44) and (3.45) update the value of the wave function along a particular trajectory, while the whole ensemble reconstructs the nuclear wave packet. Initial conditions $\mathbf{R}^l(t_0)$, $\mathbf{v}^l(t_0)$ and $\Phi_i(\mathbf{R}^l(t_0))$ are extracted simultaneously for all trajectories from the initial wave packet $|\Phi_i(t_0)\rangle$ at time t_0 , where velocities are given by equation (3.38). The quantum potential is solely responsible for quantum effects. It drives trajectories over pure classically inaccessible region of configuration space [92, 93] and mutually correlates trajectory motions which manifests as quantum interference. Dropping this term out dismisses all quantum effects and trajectories evolve independently, govern only by classical laws of motion. Also, the volume (fluid) element is not of constant volume but

³The right hand side of equation is the quantum Lagrangian. Its integral along the trajectory is the quantum action which can be obtained from $\int_{t_0}^t \sum_{j=1}^{N_n} M_j \vec{v}_j(t') \cdot d\vec{R}_j(t')$.

changes its shape along the trajectory. The amplitude and density, therefore, vary at a rate according to equation (3.44) along a given trajectory. [91] However, while there are no probability currents associated with Lagrangian volume elements, no outflow or inflow of probability density is possible into the volume element so the probability contribution ($\rho_i(t)\delta V(t)$) of each adiabatic trajectory stays constant. But in regions of configuration space where non-adiabatic coupling terms are significant probability can transfer between electronic states, so in order to describe this transport correctly the coupling terms have to be included. Equations (3.43)-(3.45) therefore acquire additional terms and are of the following forms

$$\begin{aligned}
M_k \frac{d\vec{v}_{i,k}^l(t)}{dt} = & -\vec{\nabla}_k Q_i(\mathbf{R}^l(t)) - \vec{\nabla}_k V_i(\mathbf{R}^l(t)) \\
& - \vec{\nabla}_k \left[\sum_{j=1}^{\infty} \sum_{m=1}^{N_n} \frac{1}{2M_m} D_{m,ij}(\mathbf{R}^l(t)) \frac{A_j(\mathbf{R}^l(t))}{A_i(\mathbf{R}^l(t))} \text{Re}(e^{i\mathfrak{S}_{ji}}) \right. \\
& - \sum_{j \neq i}^{\infty} \sum_{m=1}^{N_n} \frac{1}{M_m} \vec{d}_{m,ij}(\mathbf{R}^l(t)) \cdot \frac{\vec{\nabla}_m A_j(\mathbf{R}^l(t))}{A_i(\mathbf{R}^l(t))} \text{Re}(e^{i\mathfrak{S}_{ji}}) \\
& \left. + \sum_{j \neq i}^{\infty} \sum_{m=1}^{N_n} \frac{1}{M_m} A_j(\mathbf{R}^l(t)) \vec{d}_{m,ij}(\mathbf{R}^l(t)) \cdot \vec{\nabla}_m S_j(\mathbf{R}^l(t)) \text{Im}(e^{i\mathfrak{S}_{ji}}) \right], \quad (3.46)
\end{aligned}$$

$$\begin{aligned}
\frac{dA_i(\mathbf{R}^l(t))}{dt} = & -\frac{A_i(\mathbf{R}^l(t))}{2} \sum_{j=1}^{N_n} \vec{\nabla}_j \cdot \vec{v}_{i,j}^l(\mathbf{R}^l(t)) \\
& + \sum_{j=1}^{\infty} \sum_{k=1}^{N_n} \frac{1}{2M_k} D_{k,ij}(\mathbf{R}^l(t)) A_j(\mathbf{R}^l(t)) \text{Im}(e^{i\mathfrak{S}_{ji}}) \\
& - \sum_{j \neq i}^{\infty} \sum_{k=1}^{N_n} \frac{1}{M_k} \vec{d}_{k,ij}(\mathbf{R}^l(t)) \cdot \vec{\nabla}_k A_j(\mathbf{R}^l(t)) \text{Im}(e^{i\mathfrak{S}_{ji}}) \\
& - \sum_{j \neq i}^{\infty} \sum_{k=1}^{N_n} \frac{1}{M_k} A_j(\mathbf{R}^l(t)) \vec{d}_{k,ij}(\mathbf{R}^l(t)) \cdot \vec{\nabla}_k S_j(\mathbf{R}^l(t)) \text{Re}(e^{i\mathfrak{S}_{ji}}), \quad (3.47)
\end{aligned}$$

and

$$\begin{aligned}
\frac{dS_i(\mathbf{R}^l(t))}{dt} &= \frac{1}{2} \sum_{j=1}^{N_n} M_j \left| \vec{v}_{i,j}^l(t) \right|^2 - Q_i(\mathbf{R}^l(t)) - V_i(\mathbf{R}^l(t)) \\
&\quad - \sum_{j=1}^{\infty} \sum_{k=1}^{N_n} \frac{1}{2M_k} D_{k,ij}(\mathbf{R}^l(t)) \frac{A_j(\mathbf{R}^l(t))}{A_i(\mathbf{R}^l(t))} \text{Re}(e^{i\mathfrak{S}_{ji}}) \\
&\quad + \sum_{j \neq i}^{\infty} \sum_{k=1}^{N_n} \frac{1}{M_k} \vec{d}_{k,ij}(\mathbf{R}^l(t)) \cdot \frac{\vec{\nabla}_k A_j(\mathbf{R}^l(t))}{A_i(\mathbf{R}^l(t))} \text{Re}(e^{i\mathfrak{S}_{ji}}) \\
&\quad - \sum_{j \neq i}^{\infty} \sum_{k=1}^{N_n} \frac{1}{M_k} \frac{A_j(\mathbf{R}^l(t))}{A_i(\mathbf{R}^l(t))} \vec{d}_{k,ij}(\mathbf{R}^l(t)) \cdot \vec{\nabla}_k S_j(\mathbf{R}^l(t)) \text{Im}(e^{i\mathfrak{S}_{ji}}), \quad (3.48)
\end{aligned}$$

with $\mathfrak{S}_{ji} = S_j(\mathbf{R}^l(t)) - S_i(\mathbf{R}^l(t))$. The gradient type terms $\vec{\nabla}_k f(\mathbf{R}^l(t))$ (f stands for A and S) are actually evaluated in Eulerian reference frame for a particular position

$$\vec{\nabla}_k f(\mathbf{R}^l(t)) = \vec{\nabla}_k f(\mathbf{R}) \Big|_{\mathbf{R}^l(t)}. \quad (3.49)$$

A variety of numerical methods developed for computational fluid dynamics can be applied for evaluation of the above terms. [89, 91, 94] The three additional terms in expressions (3.46)-(3.48) described the coupling of the l -th trajectory in the i -th electronic state with the nuclear wave packets in other electronic states. Their negative gradients in equation (3.46) define the non-adiabatic forces that alternate the trajectory motion in regions of significant interaction between electronic states. The above set of equations (3.46)-(3.48) constitute the working equations of the non-adiabatic Bohmian dynamics developed by Tavernelli and co-workers. [89, 95, 96] By dropping out the non-local adiabatic coupling terms, i.e., the quantum force from equations (3.46) and (3.48), the correlation between trajectories in the same electronic state is discarded and, as stated previously, trajectories evolve independently. The rate of fractional change of volume element (divergence of velocities) from expression (3.47) is also dropped out, which removes the description of close bundles of trajectories. While only the change of amplitude and phase are considered in a volume element driven along the trajectory, the kinetic energy term can be removed from equation (3.48) because it only contributes to the global phase factor ($\exp(i/2 \int_{t_0}^t \sum_{i=1}^{N_n} M_i |\vec{v}_i(t')|^2 dt')$) which is completely irrelevant for independent trajectories. This separation is completely analogue to the change of coordinate systems from the Eulerian to the new reference system centered on the volume element which follows the evolving trajectory.⁴ Now equation (3.48) can be recombined with equation (3.47) to

⁴There is no effect of reference change on the geometry which still satisfies the Eckart's conditions. Inertial forces due to reference change are also neglected. [89]

the complex exponential form (3.34) of a nuclear wave function

$$\begin{aligned} \imath \frac{d\Phi_i(\mathbf{R}^l(t))}{dt} = & V_i(\mathbf{R}^l(t))\Phi_i(\mathbf{R}^l(t)) + \sum_{j \neq i}^{\infty} \sum_k^{N_n} \frac{1}{2M_k} D_{k,ij}(\mathbf{R}^l(t))\Phi_j(\mathbf{R}^l(t)) \\ & - \sum_{j \neq i}^{\infty} \sum_k^{N_n} \frac{1}{M_k} \vec{d}_{k,ij}(\mathbf{R}^l(t)) \cdot \vec{\nabla}_k \Phi_j(\mathbf{R}^l(t)) \end{aligned} \quad (3.50)$$

evaluated at position $\mathbf{R}^l(t)$ in configuration space. Also by dropping out the non-local non-adiabatic forces from equation (3.46) one obtains the final Newton's equations for propagating each j atom along the trajectory

$$M_j \frac{d\vec{v}_{i,j}^l(t)}{dt} = -\vec{\nabla}_j V_i(\mathbf{R}^l(t)); \quad j = 1, \dots, N_n. \quad (3.51)$$

From the relation (3.11) between $D_{k,ij}$ terms and non-adiabatic coupling vectors one can conclude that each $D_{k,ij}$ element rises more sharply, but in a narrower part of configuration space than the non-adiabatic coupling vectors, thus they do not shadow the latter terms and can be removed from equation (3.50). Furthermore, one can see that in equation (3.50) all nuclear wave functions are evaluated along the same trajectory driven by forces only from the i -th state. In other words, all values of $\Phi(\mathbf{R}^l(t))$ vector are attached to the same volume element and since trajectories evolve independently this leads inevitably to coherence problems. [89] The gradient terms in (3.50) further complicate obtaining the solution of the same expression, while Eulerian-Lagrangian transformation is necessary. Following [89], a close proximity around any single independent trajectory can be considered as a bundle of similar trajectories, whose distribution is represented by a carrying function of a Gaussian type $g_l(\mathbf{R}, t, \alpha) = (\pi\alpha)^{-1/2} \exp[-(\mathbf{R} - \mathbf{R}^l(t))/\alpha]$ with the center driven along the trajectory. The coefficient α controls the size of the distribution area in configuration space, which should be as narrow as possible. In the limit of $\alpha \rightarrow 0_+$ the carrying function becomes Dirac's delta functions $\delta(\mathbf{R} - \mathbf{R}^l(t))$. Thus the complete nuclear wave function for state i , $\Phi_i(\mathbf{R}, t)$, is approximated as the sum of $A_i(\mathbf{R}^l(t)) \exp[\imath S(\mathbf{R}^l(t))] g_l(\mathbf{R}, t, \alpha)$ terms over all trajectories, whose local continuity is embedded in carrying functions. This only implicates that the gradient terms are dependent only on the carrying function, which in the limit of narrow carrying functions can be replaced with classical trajectories momenta ($\forall k, \vec{\nabla}_k \Phi_j(\mathbf{R}^l(t)) \approx \imath \Phi_j(\mathbf{R}^l(t)) \vec{p}_k^l(t)$). This simplifies the equation (3.50) to a completely solvable form in the Lagrangian frame

$$\imath \frac{d\Phi_i(\mathbf{R}^l(t))}{dt} = V_i(\mathbf{R}^l(t))\Phi_i(\mathbf{R}^l(t)) - \imath \sum_{j \neq i} \Phi_j(\mathbf{R}^l(t)) \left[\sum_k^{N_n} \vec{d}_{k,ij}(\mathbf{R}^l(t)) \cdot \vec{v}_{i,k}^l(t) \right]. \quad (3.52)$$

The right hand side of expression in square brackets can be further simplified by noting that it represents a Lagrangian derivative of adiabatic electronic wave function change along the trajectory

$$\begin{aligned} \sum_k^{N_n} \vec{d}_{k,ij}(\mathbf{R}^l(t)) \cdot \vec{v}_{i,k}^l(t) &= \sum_k^{N_n} \left\langle \psi_i(\mathbf{R}^l(t)) \left| \vec{\nabla}_k \right| \psi_j(\mathbf{R}^l(t)) \right\rangle_{\mathbf{r}} \cdot \frac{d\vec{R}_k^l(t)}{dt} \\ &= \left\langle \psi_i(\mathbf{R}^l(t)) \left| \frac{d}{dt} \right| \psi_j(\mathbf{R}^l(t)) \right\rangle_{\mathbf{r}} = \mathcal{D}_{ij}(\mathbf{R}^l(t)), \end{aligned} \quad (3.53)$$

since adiabatic electronic wave function do not explicitly depend on time. In this form the non-adiabatic couplings between electronic states are implicitly embedded into the change of adiabatic electronic states along the course of trajectory. The implicit form is also more suitable to be obtained numerically than calculating all the necessary non-adiabatic coupling vectors. How electronic wave function derivatives are constructed will be explained later. \mathcal{D} terms are usually called the (non-adiabatic) dynamical couplings. The sum along the electronic states has been truncated while in practice only a limited number of states can be obtained. Also, for non-photoionizing NRD processes the electronic wave function is described sufficiently accurate with only few bound electronic states.

Equation (3.52) can be viewed as an expression for the evolution of total electronic wave function along a trajectory ($\Psi(\mathbf{R}(t), \mathbf{r}, t) = \sum_i \Phi_i(\mathbf{R}(t)) \psi_i(\mathbf{R}(t), \mathbf{r})$) in terms of adiabatic state coefficients Φ_i that construct the full electronic state propagated along a single trajectory. While expression (3.52) is Hermitic, the total electronic wave function is conserved ($\langle \Psi(\mathbf{R}(t), \mathbf{r}, t) | \Psi(\mathbf{R}(t), \mathbf{r}, t) \rangle_{\mathbf{r}} = \sum_i |\Phi_i(\mathbf{R}(t))|^2 = 1$). From quantum wave packet propagation it is known that wave packets branch in strong coupling regions of configuration space, but this effect cannot be simulated with the direct use of equations (3.51) and (3.52). Even though equation (3.52) correctly describes the electronic population change when couplings become significant, the trajectories are fixed to the initial electronic state i and their dynamics governed by the same state even when that state may become totally depopulated. In other words, the nuclear dynamics is not correlated with the evolution of electronic states. For fraction of trajectories that simulate the part of wave packet remaining on the initial state it is not the case, but trajectories which should represent the population transferred to some other electronic state are governed by an inappropriate forces. In diabatic representation the problem is reversed, the nuclei kept on the initial PES are driven by forces from other electronic states after the branching point. In other words, the number of trajectories in state i (N_i) in any small portion of configuration space $\delta\mathbf{R}$ at time t should be

$$\frac{N_i(\delta\mathbf{R}, t)}{N_{\text{traj}}} \approx |\Phi_i(\mathbf{R}, t)|^2 \delta\mathbf{R}, \quad (3.54)$$

where the right hand side of equation is given by solutions of (3.52) for trajectories at t in the same configuration space element

$$|\Phi_i(\mathbf{R}, t)|^2 \delta\mathbf{R} \approx \frac{1}{N_{\text{traj}}} \sum_{\mathbf{R}^j(t) \in \delta\mathbf{R}} |\Phi_i(\mathbf{R}^j(t))|^2. \quad (3.55)$$

The sum of $N_i(\delta\mathbf{R})$ over the entire configuration space and over all states is equal to the total number of trajectories N_{traj} . To equate relations (3.54) and (3.55), at this stage the trajectory surface hopping (TSH) procedure is introduced to restore the correlation between the nuclear and electronic degrees of freedom. The TSH procedure works with some stochastic algorithm that changes the PES along which a single trajectory evolves in a precise way to maintain the fraction of trajectories in a particular electronic state equal to the average population of the same electronic state. Stated in mathematical terms, the TSH algorithm should keep the two sides of relation

$$\frac{N_i(\delta\mathbf{R}, t)}{N_{\text{traj}}} \approx \frac{1}{N_{\text{traj}}} \sum_{\mathbf{R}^j(t) \in \delta\mathbf{R}} |\Phi_i(\mathbf{R}^j(t))|^2 \quad (3.56)$$

as similar as possible. This is the consistency relation between nuclear trajectories and electronic populations, which in practice is hard to realize due to a large number of classical trajectories needed to satisfy the spatial consistency part. Thus the spatial restraint of relation (3.56) is loosened and made to satisfy only the temporal consistency

$$\frac{N_i(t)}{N_{\text{traj}}} \approx \frac{1}{N_{\text{traj}}} \sum_{j=1}^{N_{\text{traj}}} |\Phi_i(\mathbf{R}^j(t))|^2 \quad (3.57)$$

between the number of trajectories in state i and the average electronic population. Unfortunately, individual relations (3.54) and (3.55) do not hold because the same trajectory is used simultaneously for propagation of electronic population along all electronic states, while in reality each wave packet evolves independently after it leaves the coupling region. Population obtained from equation (3.52) may match the exact wave packet solution around coupling regions, but afterwards the populations obtained by propagating equation (3.52) are too coherent. This failure is a direct consequence of using uncorrelated trajectories. If these were correlated they would exchange parts of electronic populations due to the non-local interaction terms. To restore the missing decoherence effect in the independent trajectory approximation, it is necessary to include a further *ad hoc* correction. Thus advanced versions of TSH algorithms which correlate trajectories motion were developed, [97, 98] but such sophisticated approaches are inappropriate for efficient numerical implementation and generally unnecessary at the level of screening for new

NRD mechanisms. Therefore the Tully's fewest switch (TFS) TSH algorithm is used, [99] which does not satisfy the consistency requirement (3.57), [98] but allows an easy way for decoherence correction to be implemented. It goes without saying that a large variety of decoherence corrections were developed for the TFS-TSH procedure. Some of the versatile approaches can be found in references [86, 100–105] and references therein. Here a decoherence correction developed by Zhu *et al.* and adapted by Granucci and Persico [98] is used on grounds of implementational simplicity and easy user adjustments. More details are given in Implementation section. Although some of the consequences of not including decoherence corrections will be discussed later in the Result section on a real example, the decoherence issues in TSH will not be discussed further because they exceed the scope of this thesis and because details are irrelevant for obtaining NRD mechanisms. Focus is returned on TFS procedure.

The key simplicity of TFS-TSH algorithm is that it performs the changes between classically occupied PES-s in a minimum number of ways to satisfied the necessary temporal consistency criterion (3.57). The algorithm does this by allowing stochastic switches or hops between PES-s only when the population of the currently classically occupied PES exhibits a reduction of population $|\Phi_i|^2$. To observe the population change, equation (3.52) is multiplied with a corresponding complex conjugate $\bar{\Phi}_i$ function and rearranged to

$$\frac{d|\Phi_i(\mathbf{R}^l(t))|^2}{dt} = -2 \sum_{j \neq i}^{\infty} \mathcal{D}_{ij}(\mathbf{R}^l(t)) \text{Re} \left[\bar{\Phi}_i(\mathbf{R}^l(t)) \Phi_j(\mathbf{R}^l(t)) \right]. \quad (3.58)$$

where on the left hand side a population change rate can be recognized. The compact dynamical coupling (3.53) is used. Each term in the sum represents the net rate of population transfer between a pair of states, and while the integral of equation (3.58) can only range from -1 to 1 , each term in (3.58) has no limiting value (their integrals have). In a time interval δt a population of state i changes by $-2\mathcal{D}_{ij} \text{Re}[\bar{\Phi}_i(t)\Phi_j(t)]\delta t$ due to the population transfer to state j , which should then be followed by a change of PES occupancy in order to fulfill the consistency relationship (3.57). As was argued by Tully, [99] if the currently occupied state i shows a depopulation of $-2\mathcal{D}_{ij} \text{Re}[\bar{\Phi}_i(t)\Phi_j(t)]\delta t$ and if a negative of this value is divided by the current population value of the state i a probability

$$P_{i \rightarrow j}^l = \max \left\{ 0, \frac{2\mathcal{D}_{ij}^l(t) \text{Re} \left[\bar{\Phi}_i^l(t) \Phi_j^l(t) \right] \delta t}{|\Phi_i^l(t)|^2} \right\} \quad (3.59)$$

by which a change from currently occupied state i to state j can occur is obtained. The maximum value criterion assures that the probability is always positive, and keeps surface hops unidirectional, namely from the state currently undergoing depopulation.

$P_{i \rightarrow j}^l$ is not by strict mathematical definitions a probability function, because its range is not bound to the $[0, 1]$ interval, so various schemes are used to restrain it up to this interval. [106, 107] Nonetheless the term probability was kept. Because the hops are only unidirectional and controlled by the rate of population change, the algorithm assures the number of hops to a minimum. In order to make PES change, the probabilities $P_{i \rightarrow j}$ for the change to the new j state are compared with a random number ξ from a unitary distribution in a cumulative way

$$\sum_{k=0}^{j-1} P_{i \rightarrow k} < \xi \leq \sum_{k=0}^j P_{i \rightarrow k} \quad ; j = 1, \dots, \quad (3.60)$$

where $P_{i \rightarrow 0} = 0$ and the probability to keep propagating trajectory along the currently occupied electronic state i is $P_{i \rightarrow i} = 1 - \sum_{j \neq i} P_{i \rightarrow j}$. When the above condition is met a hop to a new PES takes place. However, to keep the trajectory's total energy conserved, after the hop velocities have to be readjusted. While the quantum force was deliberately discarded, no attempts to move in classical energy forbidden regions of the configuration space will be performed, and the so called frustrated hops are not considered. The non-adiabatic force in expression (3.46) determines how the non-adiabatic coupling influences the nuclear motion around strong interaction regions of configuration space. Unfortunately, this terms are lost in (3.51), and in the TSH approach the velocities are usually readjusted instantaneously when the hop to a different electronic state occurs

$$\vec{v}_{j,k}(t) = \vec{v}_{i,k}(t) + \delta v \vec{n}_k(t) \quad ; k = 1, \dots, N_n \quad (3.61)$$

to keep the total energy balanced

$$V_j(\mathbf{R}(t)) + \frac{1}{2} \sum_{k=1}^{N_n} M_k |\vec{v}_{j,k}(t)|^2 = V_i(\mathbf{R}(t)) + \frac{1}{2} \sum_{k=1}^{N_n} M_k |\vec{v}_{i,k}(t)|^2. \quad (3.62)$$

A number of procedures for selecting the normalized correction vector \mathbf{n} have been invented. Initially, from path integral representation of heavy particles motions the so called Pechukas force had been derived to steer classical trajectories from one well defined initial quantum state to another. [108] This force resembles the non-adiabatic coupling vector \mathbf{d}_{ij} in the limit of instant i -th to j -th quantum state change as encountered in the instant surface switch of TFS-TSH algorithm. Also from study of angular momentum conservation in non-adiabatic scattering problem Tully and Preston had advised that velocities should be scaled along the direction of the non-adiabatic coupling vectors \mathbf{d}_{ij} to conserved the total energy. [109] Further justification of this was made by Herman from refraction of nuclear plane waves in coupling regions, [110] and the former correction has become

the usual procedure for rescaling the nuclear velocities after a non-adiabatic hop. [111] In case when the non-adiabatic coupling vectors are unavailable, scheme to rescale the velocities along the direction of the gradients difference vector between two interacting states was shown not to deviate much from the previous procedure. [112] The question of rescaling direction is still a matter of debate.

Figure 3.2 compares the three different scenarios for trajectory evolution after a surface hop with velocity corrected along the direction of non-adiabatic coupling vector, gradients difference vector, and initial velocity, respectively (see figure captions for more details). In this simplified branching plane defined with branching vectors g and h the first two correction directions are always mutually orthogonal. Nonetheless, the two trajectories deviate only slightly from one another after the surface switch. The scale of the correction effect, that is the magnitude of δv , depends mostly on the PES-s separation when the hop occurs. Because in the close vicinity of CI kinetic energy gain is negligible while the energy separation is also small. In regions where energy separation is larger the correction may become more significant, but again the hopping probability is inversely proportional to state separation, diminishing these kind of surface hops (all non-adiabatic coupling vectors are reciprocally dependent on energy separation, (3.9)). If, however, the same direction of the initial velocity is used for rescaling direction, the obtained trajectory is quite different (blue line in Figure 3.2). As shown on the same figure the use of correction directions along the non-adiabatic vector (\mathbf{n}_d) or gradients difference vector ($\mathbf{n}_{\nabla(V_{i+1}-V_i)}$) gives the trajectory an additional momentum for potential exploration of a much wider configuration space after the non-adiabatic hop than keeping the direction of initial velocity ($\mathbf{n}_v = \mathbf{v}_j/|\mathbf{v}_j|$). Also, there is a significant difference between the corrections arising from energy conservation, i.e., with the use of \mathbf{n}_v direction for velocity rescaling the trajectory exhibiting a hop from a lower to a higher electronic state can virtually lose all of its kinetic energy on account of potential energy difference, while with the use of \mathbf{n}_d or $\mathbf{n}_{\nabla(V_{i+1}-V_i)}$ such events are prohibited by rescaling over a different direction. Therefore, the use of former correction direction enables the hop to take place in a more wider range around interacting regions of PES-s. The adapted procedure of selecting the absolutely smaller value for δv for the latter two correction procedures gives more physically meaningful trajectories while the trajectories are less perturbed and therefore closer to the original as can be seen in Figure 3.2. The orientation of correction vectors \mathbf{n}_d and $\mathbf{n}_{\nabla(V_{i+1}-V_i)}$ plays no effect at all,⁵ as stems from solution of δv . Also, larger velocities and heavier nuclei are less affected by rescaling vectors. Returning shortly to the non-adiabatic potential in expression (3.46) one can see

⁵E.g. the orientation of non-adiabatic coupling vectors is meaningless while the relative sign of adiabatic electronic wave functions is completely arbitrary.

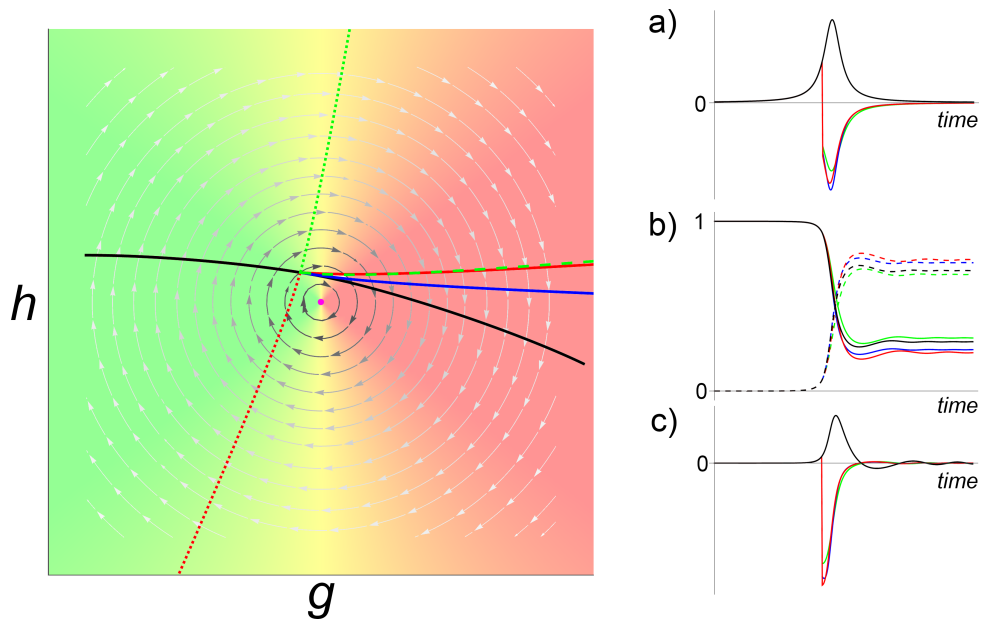


Figure 3.2: Evolution of a classical trajectory in a vicinity of CI shown in branching space. The black line on the left hand side image shows a trajectory propagated exclusively on the upper adiabatic electronic PES of Figure 3.1. The graduate change of green to red background corresponds to the change of electronic state character, while the circulating vector field (gray) displays the corresponding non-adiabatic coupling exhibited by the trajectory on the upper PES. The CI point is shown with a pink dot in the middle of the image. When Tully's fewest switch surface hopping algorithm is used to propagate the trajectory, depending on the choice of used velocity readjusting technique, different scenarios emerge after a surface hop. Three trajectories obtained using velocity rescaling along non-adiabatic coupling vector, gradients difference vector and trajectory's velocity vector after the surface switch are shown with red, dashed green and blue lines, respectively. For curiosity reasons only, the dotted red and green lines show the second root of rescaling algorithm solution using non-adiabatic vector and gradients difference vectors, respectively, which are discarded while clearly give less physical trajectories. The right hand side of figure displays the evolution of dynamical couplings (a), change of electronic populations (b) and the surface hopping probabilities (c) for all four trajectory types displayed on the left image. Same colors have been used for designation. Details of right side figures: a) The dynamical coupling exhibited by the trajectory shows a sudden change of sign when the trajectory is instantly made to propagate on the lower PES. b) The full lines show the population of the upper electronic state, while the dashed lines designate the population of the lower state. No decoherence corrections are applied here. c) Surface hopping probabilities to an unoccupied state obtained with expression (3.59) display a clear cut to negative values once the first surface switch occurs. The cut originates from the sudden change of dynamical coupling sign.

that it depends on the population ratio of both interacting states. However, the major contribution can be traced to its last term which displays how the non-adiabatic potential is proportional to the scalar product of the non-adiabatic coupling vector and nuclear velocity ($\sum_{k=1}^{N_n} \vec{d}_{k,ij} \cdot \vec{v}_{i,k}$). The negative gradient of the last term determines the non-

adiabatic force that alongside with the adiabatic force ($\vec{\nabla}_k V_i$) of the currently occupied PES influences the nuclear motions. The corresponding force field is shown in Figure (3.3), and displays the complexity of forces governing the motion of trajectories around CI regions. Thus, no unique procedure for velocity correction exists, and the choice of procedure is again based on implementation and numerical feasibility. In the Implementation section few additional words about implementation of velocity rescaling along gradient difference vectors will be given.

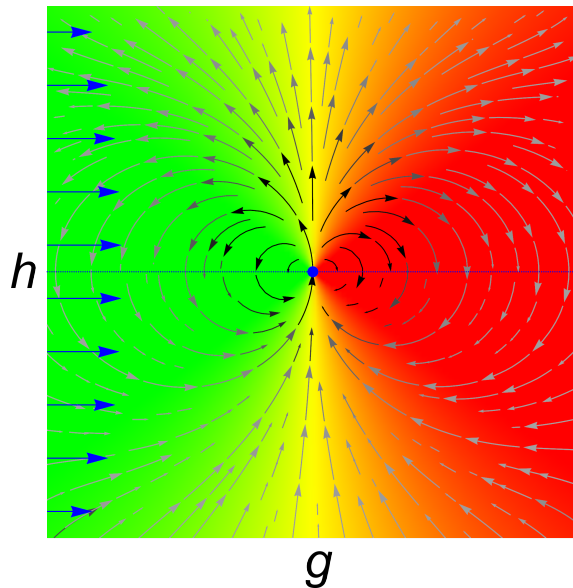


Figure 3.3: Vector field showing an evaluated gradient of $\vec{v}_i \cdot \vec{d}_{ij}$ part of quantum non-adiabatic potential term appearing in expression (3.46) which roughly approximates the major contribution to the quantum non-adiabatic forces acting on trajectories passing near a CI (blue dot). Here a constantly parallel velocity vector field on the upper PES of Figure 3.1 in a direction shown by blue vectors has been chosen to approximate the motion of the incoming trajectories.

The right side of Figure 3.2 further displays the dynamical coupling, electronic populations and surface hopping probabilities along the model trajectories around a CI point represented in the g - h branching plane. Details are given in figure caption.

The implementation of the non-adiabatic dynamics is explain later. As shown above, by dropping out the (Bohmian) quantum forces, the trajectories used in a description of nuclear wave packet propagation become independent. This discards all quantum effects, where particularly the lack of nuclear decoherence cause most problems. Nonetheless, with various correction implementations even the decoherence problem can be reduced to a physically reliable degree, and methods such as TFS-TSH can be used to approximate nuclear wave packet propagation. Of course, depending on the level of needed accuracy, TSH methods score from adequate to complete failure. Numerically, trajectory methods are much simpler, where equations (3.50) and (3.51) for propagating the trajectories are

easily solved on-the-fly. Their computational expense depends however on the size of the system and on the level of accuracy that needs to be reached (with the classical limit included), while they are almost completely limited by calculations of excited electronic state properties (\mathbf{V} , $\nabla\mathbf{V}$ and \mathbf{d}). Ideally wave packet simulation should be conducted with an infinite number of trajectories, but with an adequate sampling of initial conditions this can be achieved using smaller number of trajectories. This is the crucial part of any molecular dynamics simulation, especially when using it for screening unknown reaction mechanism, because truncated initial conditions can leave large parts of phase space totally unexplored. However, this can be later easily corrected by restarting trajectories with some new set of initial conditions. Despite the failures to exactly reproduced wave packet propagation, even a single trajectory has the potential to elucidate a new mechanism. Statistic averring of excited state populations, on the other hand, gives excited state lifetimes and branching ratios of each obtained mechanism. Though, as is going to be later demonstrated on NAPA case, the quality of PES-s determines all potential mechanisms eventually, a fact especially important since the mechanisms are determined by excited state PES-s. TDDFT electronic methods therefore represent a compromise between chemical accuracy and computational efficiency necessary when elucidating new NRD for systems of size as NAPA molecules. While none of the available software for TDDFT excited state calculations output non-adiabatic vectors between excited states, prior to proceeding to the implementation of non-adiabatic molecular dynamics, few important details about the calculation of dynamic couplings in TDDFT formalism are explained next.

3.4 Dynamical couplings in linear response time dependent density functional theory

The dynamical couplings (3.50) can be calculated using the finite difference numerical derivative of adiabatic states change along the trajectory in discrete time steps of δt

$$\begin{aligned} \mathcal{D}_{ij}(t + \delta t/2) &\approx \left\langle \frac{\psi_i(\mathbf{R}(t + \delta t)) + \psi_i(\mathbf{R}(t))}{2} \left| \frac{\psi_j(\mathbf{R}(t + \delta t)) - \psi_j(\mathbf{R}(t))}{\delta t} \right\rangle_{\mathbf{r}} \\ &\approx \frac{1}{2\delta t} \left[\langle \psi_i(\mathbf{R}(t)) | \psi_j(\mathbf{R}(t + \delta t)) \rangle_{\mathbf{r}} - \langle \psi_j(\mathbf{R}(t)) | \psi_i(\mathbf{R}(t + \delta t)) \rangle_{\mathbf{r}} \right], \quad (3.63) \end{aligned}$$

resulting in a difference of adiabatic wave function overlaps between two neighboring points along the trajectory. [106] In the limit of δt approaching zero, the above expression becomes exact with (3.50). In cases when exact non-adiabatic coupling vectors are unavailable at the particular level of theory, the above approximations constitutes the only alternative for obtaining dynamical couplings between electronic states. Plus, it is

computationally less demanding to use (3.63) than to calculate all the components of the non-adiabatic coupling vectors between each pair of electronic states just to obtain the dynamical couplings (as stated, velocity readjustment along the non-adiabatic coupling vector is not crucial, and can be avoided). However, electronic excited state wave functions are necessary if the above formula (3.63) wants to be used. This represents a direct drawback for the use of density functional electronic structure methods, whose essence is to avoid electronic wave function construction in the first place. The solution to the apparently contradictory utilization of density based methods lays in appropriately designing auxiliary many-body wave functions which reproduce all full wave functions observables. First described by Casida in density assignment *ansatz*, [113] auxiliary wave functions (AWF) were used by Hu *et al.* to obtain exact TDDFT non-adiabatic coupling vectors between ground and excited states, [114] and later by Tapavicza *et al.* in expression (3.63) with plane wave basis defined AWF, [115,116] or Mitrić for atomic type basis AWF. [107,117] A rigorous proof of AWF validity for calculation of non-adiabatic coupling vectors (and also other observables) was given by Tavernelli and co-workers, [118–120] who also applied the same formalism to calculation of non-adiabatic couplings between excited electronic states on TDDFT. [121] A short derivation of many-body AWF is reproduced here starting from Casida’s solution of linear response (LR) TDDFT.

Although exact details of electronic transitions are not going to be considered, any vertical transition from ground to some i -th excited state (both states adiabatic) is accompanied by a corresponding electronic density redistribution

$$\delta\rho_{0\rightarrow i}(\vec{r}) = \rho_i(\vec{r}) - \rho_0(\vec{r}), \quad (3.64)$$

where each state density is given by $\rho_i(\vec{r}_1) = \int \bar{\psi}_i(\mathbf{r})\psi_i(\mathbf{r}) d\mathbf{r}_{\vec{r}_1 \notin \mathbf{r}}$. Integration over spin coordinates is assumed. Because the Franck-Condon approximation of fixed molecular geometries in electronic transitions is further assumed, the explicit writing of parametric dependence on nuclear coordinates is left out. The above density difference, however, is only the limiting density change between two well defined states, while in reality the density of state may change in any way with time. Taking the stationary ground electronic state as the initial reference state, the relative change of density is

$$\delta\rho_0(\vec{r}, t) = \rho_0(\vec{r}, t) - \rho_0(\vec{r}, t'), \quad (3.65)$$

due to some external time dependent perturbation $\hat{W}(\mathbf{r}, t)$ acting on the system. At $t' < t$ no external perturbation is present. It remains to examine how does $\delta\rho$ behaves in resonance conditions when it reaches the limit (3.64). To distinguish the adiabatic electronic wave function (ψ) from the time dependent electronic wave functions ($\tilde{\psi}$) which

gives the time dependent density

$$\rho_i(\vec{r}_1, t) = \int \bar{\psi}(\mathbf{r}, t) \tilde{\psi}(\mathbf{r}, t) d\mathbf{r}_{\vec{r}_1 \neq \mathbf{r}}, \quad (3.66)$$

a tilde sign is used. Of course, the time dependent electronic functions $\tilde{\psi}$ can always be expanded into the adiabatic basis which enables the use of time-dependent perturbation theory to examine the change of initial ground state [122]

$$\delta\tilde{\psi}_0(\mathbf{r}, t) = \tilde{\psi}_0(\mathbf{r}, t) - \psi_0(\mathbf{r}) e^{-iV_0 t} \approx -i \sum_{i \neq 0} \psi_i(\mathbf{r}) e^{-iV_i t} \int_{-\infty}^t \langle \psi_i | \hat{W}(t') | \psi_0 \rangle_{\mathbf{r}} e^{i(V_i - V_0)t' - \eta(t-t')} dt'. \quad (3.67)$$

The above expansion is only to the first (or linear) order of the external perturbation. Rigorously the approximate instead of the equal sign should be used between the two sides of the expression, but since only the first order change is going to be considered further, the equal sign will be used. The infinitesimally small real number η appearing in (3.67) is an *ad hoc* introduction of dumping effect, but also work as a safeguard against singularities as is going to be shown later. The lower integration bound is strictly a mathematical simplicity, but can be considered physical in Franck-Condon approximation where the atomic nuclei are fixed. The perturbation term is also taken as simple as possible, an oscillating electric field in some arbitrary direction with a single tuning frequency ω . The interaction with the external perturbation field is strictly through the electronic dipole moment ($\hat{W}(\mathbf{r}, t) = -\sum_{i=1}^{N_n} \vec{E}(t) \cdot \hat{r}_i$), while all higher electric and magnetic multiple moments are ignored. The ground state dipole moment components therefore change accordingly

$$\delta\mu_{0,\beta}(t) = \left\langle \delta\tilde{\psi}_0(t) \left| \hat{\mu}_\beta \right| \tilde{\psi}_0(t) \right\rangle_{\mathbf{r}} + \left\langle \tilde{\psi}_0(t) \left| \hat{\mu}_\beta \right| \delta\tilde{\psi}_0(t) \right\rangle_{\mathbf{r}} \quad ; \quad \beta = x, y, z. \quad (3.68)$$

Inserting expansion (3.67) into the above relation gives the first order (or linear) dependence of molecular dipole moment change to the strength of oscillating field in time. But, more important than the exact description of the time evolution of an observable, is the observable response to the oscillating field frequency, which is given by its Fourier transform where the above expression (3.68) has the following transform⁶

$$\delta\mu_{0,\beta}(\omega) = \sum_{\gamma} \left\{ \lim_{\eta \rightarrow 0} \sum_{i \neq 0} \left[\frac{\langle \psi_0 | \hat{\beta} | \psi_i \rangle_{\mathbf{r}} \langle \psi_i | \hat{\gamma} | \psi_0 \rangle_{\mathbf{r}}}{\omega - V_i + V_0 + i\eta} - \frac{\langle \psi_0 | \hat{\gamma} | \psi_i \rangle_{\mathbf{r}} \langle \psi_i | \hat{\beta} | \psi_0 \rangle_{\mathbf{r}}}{\omega - V_0 + V_i + i\eta} \right] \right\} E_{\gamma}(\omega). \quad (3.69)$$

⁶Used Fourier transform of type $f(\omega) = \int_{-\infty}^{\infty} f(t) e^{i\omega t} dt$. The upper bound of integral (3.68) is replaced with a Heaviside step function, $\theta(t - t')$. [113]

To reduce the variety of designations, $f(\omega)$ stands for a Fourier transform of any function $f(t)$, while β and γ are directions of coordinate axis. The expression in curly brackets can be now recognized as the Fourier transform of the electronic polarizability tensor ($\alpha_{ij} = \partial\mu_i/\partial E_j$)

$$\alpha_{\beta\gamma}(\omega) = \lim_{\eta \rightarrow 0} \sum_{i \neq 0} \left[\frac{\langle \psi_0 | \hat{\beta} | \psi_i \rangle_{\mathbf{r}} \langle \psi_i | \hat{\gamma} | \psi_0 \rangle_{\mathbf{r}}}{\omega - (V_i - V_0) + i\eta} - \frac{\langle \psi_0 | \hat{\gamma} | \psi_i \rangle_{\mathbf{r}} \langle \psi_i | \hat{\beta} | \psi_0 \rangle_{\mathbf{r}}}{\omega + (V_i - V_0) + i\eta} \right]. \quad (3.70)$$

The role of the small number η is now evident when the field frequency matches the frequency difference between the two adiabatic electronic states. Now through finding the poles and residues of the above function one can determine transition energies and transition dipole moments. This is the basis of response theory, where in case of TDDFT the wave function is further replaced with total electronic density.

Written now in the language of density instead of wave function, the dipole moment changes because the total electron density changes

$$\delta\mu_{\beta}(t) = - \int \beta \delta\rho(\vec{r}, t) d\vec{r}, \quad (3.71)$$

which itself changes due to the external perturbation acting on the system, where its change can be expressed analogously to (3.69) as a response or susceptibility of the external field

$$\delta\rho(\vec{r}, t) = \iint \xi(\vec{r}, \vec{r}', t, t') \theta(t - t') w(\vec{r}', t') d\vec{r}' dt', \quad (3.72)$$

with ξ being the response function and w the external perturbation. The Runge-Gross theorem assures the one-to-one mapping between density and potential response and provides the response (susceptibility) function, $\xi(\vec{r}, \vec{r}', t, t')$, with a unique inverse, $\xi^{-1}(\vec{r}, \vec{r}', t, t')$. [123] In above expression the external potential is just reduced with a one-particle form, the oscillating field of type $w(\vec{r}, \omega) = \vec{r} \cdot \vec{E}(\omega)$. The Heaviside step function again assures that in above integration only perturbation effects from past influence the density change. The transition energies can now be obtained by finding the corresponding poles of the density response function. The density response function can be reconstructed from Kohn-Sham (KS) orbitals which describe a set of non-interacting particles (electrons) that tends to reproduce the exact electronic density

$$\rho(\vec{r}, t) = \sum_{i=1}^{N_e} |\tilde{\chi}_i(\vec{r}, t)|^2. \quad (3.73)$$

More about KS concept can be found in references [123] and [124]. $\tilde{\chi}$ -s are the one electron spin KS orbitals whose spatial and temporal part, i.e., the KS molecular orbitals,

are solutions of the corresponding time dependent KS equation

$$i \frac{\partial \tilde{\chi}_i(\vec{r}, t)}{\partial t} = \hat{h}_{\text{KS}}(\vec{r}, t) \tilde{\chi}_i(\vec{r}, t), \quad (3.74)$$

with the one electron KS Hamiltonian

$$\hat{h}_{\text{KS}}(\vec{r}, t) = -\nabla^2 - \underbrace{\sum_{i=1}^{N_n} \frac{Z_i}{|\vec{R}_i - \vec{r}|} + w(\vec{r}, t) + \int \frac{\rho(\vec{r}', t)}{|\vec{r} - \vec{r}'|} d\vec{r}' + v_{\text{xc}}[\rho](\vec{r}, t)}_{v_{\text{KS}}[\rho](\vec{r}, t)}, \quad (3.75)$$

where v_{KS} is the KS effective potential. The terms of one electron KS effective potential (v_{KS}) from left to right are, respectively, the attractive Coulomb potential of the nuclei, the external perturbation field, the repulsive potential of the electrons or the so called Hartree potential term (which includes the interaction of electron with it on self), and lastly and most importantly the time dependent exchange-correlation (xc) potential. The last term, as the Hartree potential, has a functional dependence on the total electronic density (designated with $[\rho]$). These two terms are therefore usually grouped into a single functional Hartree-exchange-correlation (Hxc) potential

$$v_{\text{Hxc}}[\rho](\vec{r}, t) = \int \frac{\rho(\vec{r}', t)}{|\vec{r} - \vec{r}'|} d\vec{r}' + v_{\text{xc}}[\rho](\vec{r}, t). \quad (3.76)$$

When the KS potential is time independent the perturbation term is absent and the exchange-correlation functional becomes time independent simplifying the equation (3.74) to its ground state form

$$\hat{h}_{\text{KS}}(\vec{r}) \chi_{i\sigma}(\vec{r}) = \epsilon_i \chi_{i\sigma}(\vec{r}). \quad (3.77)$$

From (3.77) stationary ground state eigenfunctions $\chi_i(\vec{r})$ with corresponding eigenvalues ϵ_i can be obtained in a self-consistent way. [72, 125] Spin orbital designations are used even though KS equations solve only the spatial part (spatial orthogonality between eigenfunction of different spin states can be forced through the use of restricted-open shell approach for unpaired system). The spatial solution is therefore simply expanded with the appropriate spin state in order to obtain the full spin orbital, where the σ sign designates the particular spin state. All KS spin orbitals are orthonormal, satisfying the $\langle \chi_{i\sigma} | \chi_{j\tau} \rangle = \delta_{ij} \delta_{\sigma\tau}$ relation. The spin orthogonality $\delta_{\sigma\tau}$ relation is going to be implicitly assumed anywhere further where an integral between any pair of spin KS orbitals appears. Since only singlet states are considered here the number of spatial KS molecular orbitals is half the total electron number, while KS functions are complex range functions. From the KS spin orbitals a ground state KS Slater type determinant can be constructed

(see later (3.103)), whose square integrated over all except one electron coordinate and multiplied with the total number of electrons yields the ground state total density (3.73). The KS concept of effective potential can now be applied to obtain the exact density change. Equivalently to (3.72), a KS density response (susceptibility) function ξ_{KS} can be constructed

$$\delta\rho(\vec{r}, t) = \iint \xi_{\text{KS}}(\vec{r}, \vec{r}', t, t') \delta v_{\text{KS}}(\vec{r}', t) d\vec{r}' dt', \quad (3.78)$$

where δv_{KS} is the effective KS potential change that reproduces the exact system density change. The KS response function can be easily formulated in the frequency representation following the procedure similar in deriving the electronic polarizability (3.70). Firstly, the density change (3.73) is expanded as change of KS orbitals when the small external perturbation $w(t)$ is exerted on the system

$$\delta\rho(\vec{r}, t) = \sum_{i=1}^{N_e} \left[\bar{\chi}_i(\vec{r}, t) \tilde{\chi}_i(\vec{r}, t) + \bar{\chi}_i(\vec{r}, t) \delta \tilde{\chi}_i(\vec{r}, t) \right], \quad (3.79)$$

for its occupied states. Using the time dependent perturbation theory in the basis of the ground state KS orbitals the above expansion is expanded into an expression (not shown) analogue to expression (3.67), with the integration just over one coordinate. Inserting the obtained KS orbital difference expansion back into (3.79) and taking its Fourier transform an expression analogue to (3.69) emerges

$$\delta\rho_{\text{KS}}(\vec{r}, \omega) = \int \underbrace{\lim_{\eta \rightarrow 0} \sum_{i=1}^{N_e} \sum_{a > N_e} \left[\frac{\bar{\chi}_i(\vec{r}) \chi_a(\vec{r}) \chi_i(\vec{r}') \bar{\chi}_a(\vec{r}')}{\omega - (\epsilon_a - \epsilon_i) + i\eta} - \frac{\chi_i(\vec{r}) \bar{\chi}_a(\vec{r}) \bar{\chi}_i(\vec{r}') \chi_a(\vec{r}')}{\omega - (\epsilon_i - \epsilon_a) + i\eta} \right]}_{\xi_{\text{KS}}(\vec{r}, \vec{r}', \omega)} w(\vec{r}', \omega) d\vec{r}', \quad (3.80)$$

where ξ_{KS} is the KS response function. Adapting almost generalized convention found in literature, the index a (and later also b) designates virtual KS orbitals only, whose number is theoretically infinite, while in practice is determined by the size of the basis set used to obtain the ground state KS orbitals. Indices i and j are further reserved for occupied KS orbitals, while p and q for adiabatic excited states. The cumbersome expression for KS response function can be rewritten to a more readable form

$$\xi_{\text{KS}}(\vec{r}, \vec{r}', \omega) = \lim_{\eta \rightarrow 0} \sum_{i \neq j} (f_i - f_a) \frac{\bar{\chi}_{ai}(\vec{r}) \chi_{ai}(\vec{r}')}{\omega - (\epsilon_a - \epsilon_i) + i\eta}, \quad (3.81)$$

using

$$f_i = \begin{cases} 1; i \in \text{occ.} \\ 0; i \notin \text{occ.} \end{cases} \quad \text{and} \quad \chi_{ai}(\vec{r}) = \bar{\chi}_a(\vec{r}) \chi_i(\vec{r}), \quad (3.82)$$

where the f discriminate occupied from virtual KS orbitals, while the double index orbitals are composed exclusively from an occupied-virtual pair of KS spin orbitals. Interchanging their indices just gives the complex conjugated orbital. This expansion can be applied to express the KS orbital change in (3.79) using virtual ground state KS orbitals ($\delta\tilde{\chi}_i(\vec{r}, t) = \sum_{a>N_e} C_{ia}(t)\chi_a(\vec{r})$) which then transforms the total system density change (actually its Fourier transform) into

$$\delta\rho(\vec{r}, \omega) = \sum_{i=1}^{N_e} \sum_{a>N_e} [X_{ai}(\omega)\chi_{ai}(\vec{r}) + Y_{ai}(\omega)\bar{\chi}_{ai}(\vec{r})], \quad (3.83)$$

as represented in frequency domain. Coefficients X and Y distinguished between complex conjugated pairs of double index functions, and are frequency dependent. Compared to (3.72) the obtained density change in (3.80) is however not the exact system density change because the effect of density change on the KS Hamiltonian was overlooked, giving just the KS density response instead. But if the external potential is expanded with an additional potential, δv_{SCF} ,

$$\delta v_{\text{KS}}(\vec{r}, \omega) = w(\vec{r}, \omega) + \delta v_{\text{SCF}}(\vec{r}, \omega), \quad (3.84)$$

arising because the Hartree-exchange-correlation potential (3.76) also changes with density. δv_{SCF} can be represented with its functional derivative to the total density

$$\begin{aligned} \delta v_{\text{SCF}}(\vec{r}, \omega) &= \int \frac{\delta v_{\text{Hxc}}[\rho](\vec{r}, \omega)}{\delta\rho(\vec{r}', \omega)} \Big|_{\rho(\vec{r}, \omega)=\rho_0(\vec{r}')} \delta\rho(\vec{r}', \omega) d\vec{r}' \\ &= \int f_{\text{Hxc}}(\vec{r}, \vec{r}', \omega)[\rho_0] \delta\rho(\vec{r}', \omega) d\vec{r}'. \end{aligned} \quad (3.85)$$

Thus a new effective KS potential change (δv_{KS}) can be constructed which together with the KS response function gives the exact density change of the system

$$\delta\rho(\vec{r}, \omega) = \int \xi_{\text{KS}}(\vec{r}, \vec{r}', \omega) \delta v_{\text{KS}}(\vec{r}', \omega) d\vec{r}'. \quad (3.86)$$

The SCF potential change in (3.85) is a consequence of one-to-one mapping between the density and potential and is expressed (analogously to (3.72)) as a potential response function to the electron density change, $f_{\text{Hxc}}(\vec{r}, \vec{r}', \omega)$, which is of the following explicit form

$$f_{\text{Hxc}}(\vec{r}, \vec{r}', \omega) = \frac{1}{|\vec{r} - \vec{r}'|} + f_{\text{xc}}[\rho_0](\vec{r}, \vec{r}', \omega). \quad (3.87)$$

The last functional term on the right is the so-called exchange-correlation kernel, dependent on the ground state density from which the density change is considered. It was

obtained in step (3.85) by taking the functional derivative of xc potential with respect to the total density ($f_{xc} = \delta v_{xc}/\delta\rho$). Combining now contributions (3.81), (3.85) into (3.84), a final relation between systems total density change and external perturbation arises

$$\delta\rho(\vec{r}, \omega) - \iint \xi_{KS}(\vec{r}, \vec{r}', t) f_{Hxc}(\vec{r}', \vec{r}'', \omega) \delta\rho(\vec{r}'', \omega) d\vec{r}'' d\vec{r}' = \int \xi_{KS}(\vec{r}, \vec{r}', \omega) w(\vec{r}', \omega) d\vec{r}'. \quad (3.88)$$

The above expression is entirely composed of, at least in principle, known KS terms. Using implicit integration and coordinate designations the above expression is of the form $[1 - \xi_{KS}f_{Hxc}]\delta\rho = \xi_{KS}w$, which due to the existence of KS response inverse function transforms to $[\xi_{KS}^{-1} - f_{Hxc}]\delta\rho = w$ where the terms in the square brackets group into the inverse of the true systems response function (3.72). By searching for poles of system true response function, exact transition frequencies can be obtained. Because the exact transition frequency cannot match the difference between KS eigenvalues (in practice this can happen due to poor description of exchange-correlation functional), the η term can safely take its limiting value and disappear from calculations of excitation frequencies. [123] Inserting the definitions of terms (3.81) and (3.83) into the previous expression (3.88), the large sum that emerges (not shown) can be decomposed by equating separately the \vec{r} -dependent double index orbitals (χ_{ai}) and their complex conjugated pairs ($\bar{\chi}_{ai}$) on both side of equation into the super-matrix form known as Casida's equation [113, 126]

$$\left\{ \begin{bmatrix} \mathbf{A}(\omega) & \mathbf{B}(\omega) \\ \mathbf{B}^T(\omega) & \mathbf{A}^T(\omega) \end{bmatrix} - \omega \begin{bmatrix} \mathbf{I} & \mathbf{0} \\ \mathbf{0} & -\mathbf{I} \end{bmatrix} \right\} \begin{bmatrix} \mathbf{X} \\ \mathbf{Y} \end{bmatrix} = - \begin{bmatrix} \mathbf{w}(\omega) \\ \bar{\mathbf{w}}(\omega) \end{bmatrix}. \quad (3.89)$$

The super-matrix basis is composed of χ_{ai} and $\bar{\chi}_{ai}$ vectors, thus the super-matrices and super-vectors are of dimension twice the value of the product between number of occupied and virtual KS orbitals. A variant of equation (3.89) with only interchanged signs in second super-identity-matrix also appears in the literature, and leads to same final results. [123] The constituting elements of the two matrices \mathbf{A} and \mathbf{B} are

$$A_{ia,i'a'}(\omega) = \delta_{ii'}\delta_{aa'}(\epsilon_a - \epsilon_i) + K_{ia,i'a'}(\omega) \quad (3.90)$$

and

$$B_{ia,i'a'}(\omega) = K_{ia,a'i'}(\omega), \quad (3.91)$$

respectively, where the K terms are

$$K_{ia,i'a'}(\omega) = \iint \bar{\chi}_{ia}(\vec{r}) f_{Hxc}(\vec{r}, \vec{r}', \omega) \chi_{i'a'}(\vec{r}') d\vec{r} d\vec{r}'. \quad (3.92)$$

The components of the potential vector on the right hand side of equation (3.89) are $w_{ia}(\omega) = \int \bar{\chi}_{ia}(\vec{r}) w(\vec{r}, \omega) d\vec{r}$. The left hand super-matrix is the inverse of the systems true response function in matrix notation whose poles have to be determined now. Providing that the f_{Hxc} functional is real, the submatrices \mathbf{A} and \mathbf{B} are Hermitian, and if further only real KS orbitals are considered, the complex conjugation can be totally dismissed. Nevertheless, obtaining response function poles still remains a challenge since they have to be determined in a self-consistent way. To further simplify obtaining the solutions, the time dependence of the Hartree-exchange-correlation kernel is localized, meaning that all memory effects of density change are dismissed and the kernel depends only on the instant electronic density. This introduces the adiabatic approximation into the exchange-correlation kernel and TDDFT generally. The time dependent form of the kernel is therefore simply

$$f_{\text{Hxc}}(\vec{r}, \vec{r}', t, t') = \delta(t - t') f_{\text{Hxc}}(\vec{r}, \vec{r}'), \quad (3.93)$$

whose Fourier transform is frequency independent. This simplifications enables the use of ground state exchange-correlation functionals in excited state calculations, but with the cost of introducing some errors (see details in [123]). Applying all these approximations the first matrix on the left hand side of equation (3.89) becomes frequency independent and the whole expression can be transformed into a new matrix form (3.72)

$$\mathbf{X} + \mathbf{Y} = \left\{ -2(\mathbf{A} - \mathbf{B})^{1/2} \underbrace{[(\mathbf{A} - \mathbf{B})^{1/2}(\mathbf{A} + \mathbf{B})(\mathbf{A} - \mathbf{B})^{1/2} - \omega^2 \mathbf{I}]^{-1}}_{\mathbf{C}} (\mathbf{A} - \mathbf{B})^{1/2} \right\} \mathbf{v} \quad (3.94)$$

of dimensionality reduced by half (theoretically still infinite, while in practice the dimension just equals the number of occupied orbitals times the number of virtual orbitals). On the left hand side one observes now the coefficients of the total density change (3.83), $\delta\rho_p(\vec{r}) = \sum_{i=1}^{N_e} \sum_{a>N_e} \chi_i(\vec{r}) \chi_a(\vec{r}) (\mathbf{X} + \mathbf{Y})_{p,ia}$, in the completely real basis. When the Hartree-exchange-correlation kernel possesses no exact exchange contribution the above form is particularly useful, while the K terms in matrices \mathbf{A} and \mathbf{B} are identical, leaving only the diagonal KS orbital energy difference when subtracted one from another. The matrix within the curly brackets of (3.94) is the systems total response function whose poles can now easily be obtained by noticing that the whole matrix becomes singular when the external frequency matches the square root value of one of the eigenvalues of matrix \mathbf{C} . This is the transition resonance criterion.⁷ The matrix \mathbf{C} decomposes in its

⁷Due to abandoning the small η number, at resonance the singularity is reached, while by keeping η singularities are avoided but the expressions get complicated. Strubbe *et al.* derived a version of Casida's equation (3.89) incorporating this correction. [127]

eigenvector (\mathbf{F}_p) basis to a diagonal form

$$\mathbf{C} = \mathbf{F} \boldsymbol{\Omega}^2 \mathbf{F}^T = \sum_p \Omega_p^2 \mathbf{F}_p \mathbf{F}_p^T, \quad (3.95)$$

whose square roots of its diagonal elements are the energy difference from the ground state, $\Omega_i = V_i - V_0$. The square of excitation energies appear because the Fourier transform of the response treats the density change in excitation or stimulated emission process on equal footing. For the same reason, \mathbf{X} and \mathbf{Y} coefficients show the contributions of excitation and stimulated emission processes, and are joined into a single density change description once the real KS orbitals are introduced (functions χ_{ai} are considered as particle(i)-hole(a), while $\bar{\chi}_{ai}$ as hole-particle contribution to the transition process). Because of this the poles of the response function come in pair, whose positive values are taken as excitation energies, while their negative counterparts are frequencies of stimulated emission, which are not considered furthermore. The eigenvectors correspond to the characteristic density changes (electronic eigenmodes) in transition processes, and are the first order contribution to the real limiting case (3.64). Because they are described in frequency domain, even an infinitesimally small external perturbation matching some transition frequency can cause an electronic transition. By equating the right side of expression (3.94) (or (3.89)) to zero, [123,128] or finding the functions residues at positive poles, these eigenmodes can be obtained, which after normalization⁸ are of the following form

$$(\mathbf{X} + \mathbf{Y})_p = \frac{1}{\sqrt{V_p - V_0}} (\mathbf{A} - \mathbf{B})^{1/2} \mathbf{F}_p. \quad (3.96)$$

Inserting now the eigensystem expansion (3.95) into the total response function (3.94), then the obtained expression further into (3.71) a matrix formulation of polarizability tensor can be constructed

$$\begin{aligned} \alpha_{\beta\gamma}(\omega) &= 2\boldsymbol{\beta}^T \left[\sum_p (\mathbf{A} - \mathbf{B})^{1/2} \frac{\mathbf{F}_p \mathbf{F}_p^T}{(V_p - V_0)^2 - \omega^2} (\mathbf{A} - \mathbf{B})^{1/2} \right] \boldsymbol{\gamma} \\ &= 2\boldsymbol{\beta}^T \left[\sum_p \frac{(V_p - V_0)(\mathbf{X} + \mathbf{Y})_p (\mathbf{X} + \mathbf{Y})_p^T}{(V_p - V_0)^2 - \omega^2} \right] \boldsymbol{\gamma}, \end{aligned} \quad (3.97)$$

with terms $\beta_{ia} = \int \chi_{ia}(\vec{r}) \beta d\vec{r}$. The above relation can be equate with the polarizability

⁸The eigenvectors of (3.89) satisfy the following orthogonalization criterion $(\mathbf{X} - \mathbf{Y})_p^\dagger (\mathbf{X} + \mathbf{Y})_q = \delta_{pq}$. [128]

(3.70) obtained from full wave function approach (in the limit of η)

$$\sum_p \frac{(V_p - V_0) \langle \psi_0 | \hat{\beta} | \psi_p \rangle_{\mathbf{r}} \langle \psi_p | \hat{\gamma} | \psi_0 \rangle_{\mathbf{r}}}{(V_p - V_0)^2 - \omega^2} = \sum_p \frac{(V_p - V_0) [\beta^{\mathbf{T}}(\mathbf{X} + \mathbf{Y})_p] [(\mathbf{X} + \mathbf{Y})_p^{\mathbf{T}} \gamma]}{(V_p - V_0)^2 - \omega^2}, \quad (3.98)$$

in order to compare the results obtained from the two distinguishable approaches. Up to now, $\hat{\beta}$ has designated position operator, but any Hermitian one-particle operator can be used instead. Keeping just the designation a generalized one-particle operator is further assumed. The equivalent terms between the two numerators can be paired now as

$$\langle \psi_0 | \hat{\beta} | \psi_p \rangle_{\mathbf{r}} = \beta^{\mathbf{T}}(\mathbf{X} + \mathbf{Y})_p, \quad (3.99)$$

which finally connects the many-body observable (defined with some electronic operator $\hat{\beta}$) between ground and excited state with the observable obtained from the corresponding density response. This relation is exact and shows how any many-body observable between the ground and excited state defined with a single-particle operator can be obtained just using the KS-LR-TDDFT formalism.

Of specific interest is the case when the operator on the right hand side is $\partial \hat{H}_e / \partial Q$, from matrix elements consisting of the KS formulation of the total Hamiltonian derivative with respect to nuclear positions, $\int \chi_r(\vec{r}) \partial \hat{H}_e / \partial Q \chi_s(\vec{r}) d\vec{r}$, components of non-adiabatic coupling vectors between ground and excited state can be obtained. Hue *et al.* have accomplished this in plane wave basis. [114] But to avoid the calculation of these matrix elements, AWF can be solely used instead as shown by Tapavicza *et al.* from a more detailed relation between density changes and many-body wave function. [115,116] Using second quantization, [129] the many-body operator on the left side of (3.99) expands to

$$\langle \psi_0 | \hat{\beta} | \psi_p \rangle_{\mathbf{r}} = \sum_{i=1}^{N_e} \sum_{a>N_e} \langle \psi_0 | \hat{a}_i^\dagger \hat{a}_a | \psi_p \rangle_{\mathbf{r}} \int \chi_i(\vec{r}) \beta \chi_a(\vec{r}) d\vec{r} = \sum_{i=1}^{N_e} \sum_{a>N_e} \beta_{ia} \langle \psi_0 | \hat{a}_i^\dagger \hat{a}_a | \psi_p \rangle_{\mathbf{r}}, \quad (3.100)$$

with the use of single molecular orbital creation (\hat{a}^\dagger) and annihilation (\hat{a}) operators, and the KS ground state functions to span the complete basis for the single particle operator $\hat{\beta}$. Terms in (3.100) can now be precisely associated with density obtained values for each excitation

$$\langle \psi_0 | \hat{a}_i^\dagger \hat{a}_a | \psi_p \rangle_{\mathbf{r}} = (\mathbf{X} + \mathbf{Y})_{p,ia}, \quad (3.101)$$

leading again to an exact relation between contributions of wave function differences between excited and ground state with corresponding KS occupied-virtual spin orbital pair. As in expression (3.99) both exact wave functions on the right are completely unknown. Yet, if the ground state wave function is (somehow) known or approximated

then by using the annihilation-creation operators, the excited state wave function can be constructed from the ground state function as

$$|\psi_p\rangle = \sum_{i=1}^{N_e} \sum_{a>N_e} (\mathbf{X} + \mathbf{Y})_{p,ia} \hat{a}_a^\dagger \hat{a}_i |\psi_0\rangle, \quad (3.102)$$

giving the AWF which clearly satisfies the equation (3.101). If this wave function is to be used only to obtain observables of type (3.99), the above expansion is exact again. So a simple Slater type determinant composed of KS spin orbitals (mentioned previously)

$$\langle \mathbf{r} | \psi_0^{\text{AWF}} \rangle_{\mathbf{r}} = \frac{1}{\sqrt{N_e!}} \det(\chi_1(\vec{r}_1) \chi_2(\vec{r}_2) \dots \chi_{N_e}(\vec{r}_{N_e})) \quad (3.103)$$

can be used for a ground state AWF, while from (3.102) the auxiliary excited state wave function is a sum of singly excited Slater determinants, each with a corresponding electron promoted from one occupied χ_i to virtual χ_a orbital

$$\langle \mathbf{r} | \psi_p^{\text{AWF}} \rangle_{\mathbf{r}} = \sum_{i=1}^{N_e} \sum_{a>N_e} (\mathbf{X} + \mathbf{Y})_{p,ia} \langle \mathbf{r} | \hat{a}_a^\dagger \hat{a}_i | \psi_0^{\text{AWF}} \rangle_{\mathbf{r}} = \sum_{i=1}^{N_e} \sum_{a>N_e} (\mathbf{X} + \mathbf{Y})_{p,ia} \langle \mathbf{r} | \psi_i^a \rangle_{\mathbf{r}}. \quad (3.104)$$

The excited state AWF-s are thus expanded in configuration interaction singlets (CIS) basis made of KS orbitals. Since only states of singlet multiplicity are considered, the excited AWF-s need to be spin adapted in order to be also eigenfunctions of total spin operators (\hat{S}_{tot}^2 and $\hat{S}_{\text{tot},z}$). The above expression is rearranged to a form

$$\langle \mathbf{r} | \psi_p^{\text{AWF}} \rangle_{\mathbf{r}} = \frac{1}{\sqrt{2}} \sum_{i=1}^{N_e} \sum_{a>N_e} (\mathbf{X} + \mathbf{Y})_{p,ia} \left(\langle \mathbf{r} | \psi_{i\alpha}^{a\alpha} \rangle_{\mathbf{r}} + \langle \mathbf{r} | \psi_{i\beta}^{a\beta} \rangle_{\mathbf{r}} \right), \quad (3.105)$$

which gives a singlet configuration state function (CSF). With the two types of auxiliary wave functions, ground and excited state, respectively, the dynamical coupling between these two states can now be easily calculated from finite difference approximation (3.63).

The above derivation of observables using LR approach is however limited only to transitions from ground to excited states, while electronic transfer description from one excited to another excited state is beyond LR theory. Following Tretiak *et al.* derivation of non-linear polarizabilities in TDDFT formulation, [130] Tavernelli and co-workers were able to expand the previously applied formalism to equate the equivalent terms obtained

on many-body perturbation theory with terms of second-order density response theory

$$\begin{aligned} \langle \psi_p | \hat{\beta} | \psi_q \rangle_{\mathbf{r}} &= \sum_{i=1}^{N_e} \sum_{a,b>N_e} (\mathbf{X} + \mathbf{Y})_{p,ia} (\mathbf{X} + \mathbf{Y})_{q,ib} \langle \chi_a | \hat{\beta} | \chi_b \rangle_{\bar{r}} \\ &\quad - \sum_{i,j=1}^{N_e} \sum_{a>N_e} (\mathbf{X} + \mathbf{Y})_{p,ia} (\mathbf{X} + \mathbf{Y})_{q,ja} \langle \chi_i | \hat{\beta} | \chi_j \rangle_{\bar{r}}, \end{aligned} \quad (3.106)$$

to prove the validity of TDDFT based observables. [120, 121] Unlike in (3.99), inserting the excited state many-body AWF-s (3.104) into the left hand side of above equation does not reproduced exactly the right hand side of (3.104),

$$\langle \psi_p^{\text{AWF}} | \hat{\beta} | \psi_q^{\text{AWF}} \rangle_{\mathbf{r}} = \langle \psi_p | \hat{\beta} | \psi_q \rangle_{\mathbf{r}} + \left[\sum_{i=1}^{N_e} \langle \chi_i | \hat{\beta} | \chi_i \rangle_{\bar{r}} \right] \sum_{i=1}^{N_e} \sum_{a>N_e} (\mathbf{X} + \mathbf{Y})_{p,ia} (\mathbf{X} + \mathbf{Y})_{q,ia}, \quad (3.107)$$

because a generally non-vanishing term, of type in square brackets above, remains. In order to fulfill the aimed relation (3.106) the second right hand side term has to be subtracted from the left side of equation (3.107). This complicates the direct use of excited state AWF-s in finite difference approach for calculation of dynamical couplings between excited states, while ground state matrix terms of Hamiltonian derivatives need to be subtracted in order to obtained exact couplings. Without explicitly evaluating the general $\langle \chi_i | \partial \hat{H}_e / \partial Q | \chi_j \rangle$ matrix elements it is almost impossible to determine the size relations between various combinations, but it can be approximated that mixed terms (those with indices $i \neq j$) are not in average absolute values much different from terms with the same indices. Thus the contribution of the second left term in (3.107) is mainly controlled by the scalar product of vectors $(\mathbf{X} + \mathbf{Y})$ between the two excited states. Since terms Y_{ia} describe the back-transfer from virtual to occupied KS orbitals, in sense showing the contribution of deexcitation in full density change, for well defined excitations from ground state the \mathbf{Y} -s are usually smaller compared to \mathbf{X} values. So the distinction among $(\mathbf{X} + \mathbf{Y})$ and $(\mathbf{X} - \mathbf{Y})$ is less evident, due to which the orthogonality condition (see footnote 8) becomes approximately valid for $(\mathbf{X} + \mathbf{Y})_p^T (\mathbf{X} + \mathbf{Y})_q \approx \delta_{pg}$. This is the usual case and in numerical terms the scalar product of $(\mathbf{X} + \mathbf{Y})$ vectors between low adiabatic excitation is roughly two orders or magnitudes bellow one or smaller. This allows the second term on the left of (3.107) to be neglected, enabling the AWF approach in calculations of dynamical couplings between excited states using finite difference method (3.63). If Tamm-Dancoff approximation (TDA) is applied in TDDFT calculations, the \mathbf{Y} coefficients are by definition absent and the orthogonality strictly determined with scalar products among \mathbf{X} , which then totally removes the second term from (3.107). But while TDA is a simplification of LR, this does not make the AWF exact for calculation of

excited state couplings. Nonetheless, AWF-s are taken as best possible approximations to many-body wave functions whose overlap factors between pairs of AWF-s in different geometries remain to be determined.

Inserting the definitions for the two types of AWF, ground (3.103) and excited states (3.104), respectively, into (3.63) each of the two factors are calculated from the general relation

$$\left\langle \psi_p^{\text{AWF}} \left| \psi_q^{\text{AWF}} \right. \right\rangle_{\mathbf{r}} = \sum_{i,j}^{N_e} \sum_{a,b>N_e} \bar{C}_{ia} C'_{jb} O_{ia,jb}, \quad (3.108)$$

where the prime denotes the AWF components at time $t + \delta t$, and the very size of the sum as well as the C coefficients depend on the type of AWF involved. If they correspond to the ground state AWF (3.103) only one coefficient with value one appears in the sum, while for excited states coefficients correspond to $(\mathbf{X} + \mathbf{Y})_{ia}$ elements, which are in practice all real numbers. The general overlap between spin adapted determinants at two various positions of KS orbitals appearing on the right hand side of (3.108) in restricted KS scheme takes the following form [107,117]

$$O_{ia,jb} = \begin{vmatrix} \langle \chi_1 | \chi'_1 \rangle & \cdots & \langle \chi_1 | \chi'_b \rangle & \cdots & \langle \chi_1 | \chi'_n \rangle \\ \vdots & \ddots & \vdots & \ddots & \vdots \\ \langle \chi_a | \chi'_1 \rangle & \cdots & \langle \chi_a | \chi'_b \rangle & \cdots & \langle \chi_a | \chi'_n \rangle \\ \vdots & \ddots & \vdots & \ddots & \vdots \\ \langle \chi_n | \chi'_1 \rangle & \cdots & \langle \chi_n | \chi'_b \rangle & \cdots & \langle \chi_n | \chi'_n \rangle \end{vmatrix} \begin{vmatrix} \langle \chi_1 | \chi'_1 \rangle & \cdots & \langle \chi_1 | \chi'_j \rangle & \cdots & \langle \chi_1 | \chi'_n \rangle \\ \vdots & \ddots & \vdots & \ddots & \vdots \\ \langle \chi_i | \chi'_1 \rangle & \cdots & \langle \chi_i | \chi'_j \rangle & \cdots & \langle \chi_i | \chi'_n \rangle \\ \vdots & \ddots & \vdots & \ddots & \vdots \\ \langle \chi_n | \chi'_1 \rangle & \cdots & \langle \chi_n | \chi'_j \rangle & \cdots & \langle \chi_n | \chi'_n \rangle \end{vmatrix} \\ + \begin{vmatrix} \langle \chi_1 | \chi'_1 \rangle & \cdots & \langle \chi_1 | \chi'_j \rangle & \cdots & \langle \chi_1 | \chi'_n \rangle \\ \vdots & \ddots & \vdots & \ddots & \vdots \\ \langle \chi_a | \chi'_1 \rangle & \cdots & \langle \chi_a | \chi'_j \rangle & \cdots & \langle \chi_a | \chi'_n \rangle \\ \vdots & \ddots & \vdots & \ddots & \vdots \\ \langle \chi_n | \chi'_1 \rangle & \cdots & \langle \chi_n | \chi'_j \rangle & \cdots & \langle \chi_n | \chi'_n \rangle \end{vmatrix} \begin{vmatrix} \langle \chi_1 | \chi'_1 \rangle & \cdots & \langle \chi_1 | \chi'_b \rangle & \cdots & \langle \chi_1 | \chi'_n \rangle \\ \vdots & \ddots & \vdots & \ddots & \vdots \\ \langle \chi_i | \chi'_1 \rangle & \cdots & \langle \chi_i | \chi'_b \rangle & \cdots & \langle \chi_i | \chi'_n \rangle \\ \vdots & \ddots & \vdots & \ddots & \vdots \\ \langle \chi_n | \chi'_1 \rangle & \cdots & \langle \chi_n | \chi'_b \rangle & \cdots & \langle \chi_n | \chi'_n \rangle \end{vmatrix}, \quad (3.109)$$

where the generalized overlap elements between two KS orbitals are

$$\langle \chi_i | \chi'_j \rangle = \int \chi_i(\vec{r}, \mathbf{R}(t)) \chi_j(\vec{r}, \mathbf{R}(t + \delta t)) d\vec{r}. \quad (3.110)$$

Note the substitution of i -th row KS orbitals with those corresponding to a , and similarly for columns j and b . The determinant overlap form (3.109) is however dependent on AWF type again. When one of the CSF corresponds to the ground state AWF, the two sum

terms in (3.109) merge, while if both AWF-s are ground electronic state, the overlap is equal to the second determinant of the first term on the right hand side. Now lastly, the overlap between a pair of spatial KS orbitals (3.110) remains to be evaluated, which depends on the basis scheme chosen for construction of KS orbitals. Adapting Mitrić *et al.* Gaussian atomic orbital scheme [107, 117] rather than plane waves approach [115], each KS spatial orbital is a superposition of localized Gaussian atomic orbitals of type

$$\chi_i(\vec{r}, \mathbf{R}(t)) = \sum_j \sum_{k=1}^{N_n} c_{ij}(\mathbf{R}(t)) g_j(\vec{r}, \vec{R}_k(t)), \quad (3.111)$$

centered on each atomic nucleus. Additional centers can be included as well. The molecular KS coefficients $c_{ij}(\mathbf{R})$ are obtained from solving equation (3.77) self-consistently to construct the system DFT ground state solution, while the g functions are usually segmented-contracted Gaussian functions

$$g(\vec{r}, \vec{R}) = \sum_i \beta_i N_i (r_x - R_x)^{l_x} (r_y - R_y)^{l_y} (r_z - R_z)^{l_z} \exp(-\zeta_i |\vec{r} - \vec{R}|^2). \quad (3.112)$$

β and ζ designate the preexponential and exponential factors, respectively, while the powers satisfy $l_x + l_y + l_z = l$, where l is the total angular quantum number of an atomic orbital.⁹ Application of Gaussian function enables an analytic solution of overlap integral (3.111). The use of localized atomic basis over plain wave however introduced an intramolecular basis set superposition error (BSSE) due to the localized nature of atomic orbitals, [131] but this error is discarded in future considerations. Albeit in expression (3.108) a product between two different electronic states vectors ($\mathbf{X} + \mathbf{Y}$) each at a different geometries shows up, which disobeys the orthogonality approximation, it does not violate the use of AWF in calculations of dynamical couplings, while the approximation still holds in each separate geometry. Also, from the above derivation of excited states, the LR- or TDA-TDDFT is strictly a single reference method, with one of the consequence of having wrong PES topology at CI seam between ground and excited state. However, the the CI seam topology among excited states is properly defined as the excited states are constructed by diagonalizing matrix (3.95) (or (3.89)). This completes the description of non-adiabatic dynamics procedure whose implementation into a working code is described next.

⁹The normalization factor is $N_i = \sqrt{(\zeta_i^{l+3/2} 2^{2l+3/2}) / (\pi^{3/2} (2l_x - 1)!! (2l_y - 1)!! (2l_z - 1)!!)}$.

3.5 Implementation of non-adiabatic molecular dynamics procedure

Implementation of the TFS-TSH non-adiabatic molecular dynamics procedure into a Fortran home-made code represents the first objective of this thesis, which is given here rather than in the Results section simply to follow the logical structure of the text. The program propagates a single classical nuclear trajectory along one PES within a manifold of ground and n excited singlet states by solving equations of motion (3.51) in discrete time steps of length Δt . Velocity Verlet algorithm¹⁰ is used to propagate Newton's equations, where at each step the gradient is taken for the currently classically occupied electronic state chosen with TFS algorithm. Eckart's conditions are applied on each newly constructed geometry, where for the reference geometry a structure from the previous step is taken. The nuclear populations are propagated by integrating the coupled set of TDSE (3.52) within one nuclear step using the predictor-corrector ordinary differential equation solver algorithm devised by Shampine and Gordon [132] with a smaller δt time step in $N (\in \mathbb{N})$ iterations satisfying $N = \Delta t / \delta t$. Within each electronic iteration step the surface hopping probability is calculated with the use of (3.59) and compared to a random number (as in (3.60)) to check for a potential surface switch. The random number is recomputed in each iteration, and the classically occupied electronic state from the last iteration is taken as the final selection of occupied electronic state. This modified Tully's procedure, devised by Mitríć *et al.*, through the use of a smaller δt in formula (3.59) assures that the calculated probabilities are always smaller than one. [107] The programs default value for N is set to one thousand, but can be modified. Frustrated hops are not allowed, while procedures for velocity readjustment along the direction of initial velocity or the gradients difference vector have been implemented. Because the gradient of the newly selected electronic state is calculated at the end of the electronic integration, an additional hoping criterion to relation (3.60) for intermediate integration steps does not allow the electronic state energy to exceed the total energy. Once the final state has been chosen, the rescaling along the gradients difference vector can be accomplished (the left hand side of equation (3.61) is replaced by the total energy from the previous step). Albeit Eckart's conditions are applied all the way, velocity Verlet algorithm does not satisfactory conserve total angular momentum,¹¹ so total angular momentum in form of rotational motion is projected from the nuclear velocities and the missing kinetic energy recovered by rescaling the remaining velocities. Rotational motion also affects the dynamical couplings due to different AWF-s overlap so it is encouraged to be removed. The code extracts the total an-

¹⁰ $\mathbf{R}(t + \Delta t) = \mathbf{R}(t) + \mathbf{v}(t)\Delta t - \mathbf{M}^{-1}\nabla V(\mathbf{R}(t))/2$; $\mathbf{v}(t + \Delta t) = \mathbf{v}(t) - \mathbf{M}^{-1}[\nabla V(\mathbf{R}(t + \Delta t)) + \nabla V(\mathbf{R}(t))]/2$.

¹¹Expanding the total angular momentum $\sum_{i=1}^{N_n} M_i \vec{R}_i(t + \Delta t) \times \vec{v}_i(t + \Delta t)$ with the use of terms from the previous step gives non-vanishing torques of type $\sum_{i=1}^{N_n} \vec{\nabla}_i V(t + \Delta t) \times \vec{R}_i(t)$, etc.

gular momentum from the initial conditions as well. In the expression (3.59) for switching probabilities the term in the numerator depends on the phase differences between nuclear coefficients Φ_i and Φ_j , while the denominator is phase independent, so nuclear coefficients can be readjusted with factors like $\exp(-\nu V_i t)$ that remove the strongly oscillating contribution of potential terms. [86] However, the use of predictor-corrector algorithm [132] was shown to be robust enough for problem arising from strongly oscillating functions so no phase alternating factors were included in nuclear population coefficients. In each electronic integration step energies and dynamical couplings are obtained by interpolation/extrapolation between corresponding two predetermined values of a nuclear step. To cope with the coherence problem that causes non-physical surface hops, the *ad hoc* decoherence algorithm from Zhu *et al.*, [100] simplified by Granucci and Persico [98] was implemented at the end of each nuclear time step. The algorithm attenuates the nuclear coefficients of classically unoccupied j states by

$$\Phi_j^{decoh} = \Phi_j \exp(-\Delta t/\tau_{ji}) \quad \text{where} \quad \tau_{ji} = \frac{1}{|V_j - V_i|} \left(1 + \frac{2\alpha}{\sum_{k=1}^{N_n} M_k |\vec{v}_k|^2} \right), \quad (3.113)$$

while the occupied i -th state gains population according to

$$\Phi_i^{decoh} = \frac{\Phi_i}{|\Phi_i|} \sqrt{1 - \sum_{j \neq i} |\Phi_j^{decoh}|^2}. \quad (3.114)$$

Superscripts *decoh* in upper relations stand for decoherented values. For factor α the regular value of 0.1 Hartree as empirically determined by Zhu and collaborators was taken. [100] The program utilizes external TURBOMOLE [133] program package for calculation of ground and excited state energies and their corresponding gradients, and reads in all the parameters (basis set parameters, Kohn-Sham molecular orbital coefficients c_{ij} , X and Y -s vector components for each excited state) necessary for construction of the electronic AWF-s to obtained the dynamical couplings in way shown before (3.63), (3.108)-(3.112). In order to keep the calculated dynamical coupling smooth along the trajectory it is necessary to retain the sign continuity of the Kohn-Sham coefficients as well as CIS expansion factors, which is conducted prior to every excited state calculation by a simple scalar product of current vectors with vectors from previous time step. The overlap matrix (3.110) is evaluated in each nuclear step to construct the elements for (3.109). Employing the Gaussian segmented-contracted basis set, integral (3.110) is solved analytically. Because the total calculation time of overwhelmingly large number of overlap determinants needed for numerical evaluation of dynamical couplings can overshadow even the calculation time of excited states, a threshold parameter for CIS expansion factors reduces the number of determinant calculations, while part of the code performing these

operations was also parallelized using the OpenMP routines to gain additional speed-up. The threshold value has to be adjusted to meet a satisfying smoothness of dynamical couplings without compromising the computational efficiency. For NAPA size molecules, a value of 10^{-3} was empirically determined to give smooth values for \mathcal{D} -s with almost negligible computational load. Apart from non-adiabatic molecular dynamics, the code can perform ground state molecular dynamics for sampling the initial conditions from a ground state trajectory. The simple Berendsen thermostat¹² was implemented to control the energy (temperature) of ground state trajectory. Since there is no difference between LR-TDDFT and LR-HF AWF the code performs for both types of theory, as well as in TDA mode. The program was extensively tested on various molecular systems and validated by reproducing some of the literature value properties obtained using other codes for non-adiabatic molecular dynamics simulations. [107, 117] The code as it is was, aside of elucidating NRD mechanism on NAPA, used by Novak *et al.* to disclose the effects of H-bond motives on the NRD channels in photoexcited formic acid dimers, [134] and by Tuna *et al.* to examine the proposed relaxation mechanisms in kynurenines from a dynamical point of view. [135] The program was also extended by Novak to include the chromophore–solvent interaction through the ONIOM QM/MM scheme with electrostatic embedding necessary to unveil the effect of counterion on the NRD process of retinal chromophore in solution. [136] The source code was also recently updated by Sapunar to include the TURBOMOLE ADC(2) calculations with the corresponding CIS expanded wave function to examine the details of pyrrole excited states NRD mechanisms. [137]

3.6 Methods and program packages

The home-made code for non-adiabatic molecular dynamics was compiled with Intel® Fortran Compiler under the Linux environment.

TURBOMOLE program package was exclusively used for all performed calculations at the TDDFT and CC2 [138] levels. Resolution-of-identity (IR) approximation for speed-up of Coulomb integrals calculations was utilized for all CC2 calculations and only for non-hybrid functionals at the TDDFT level. [139] In TURBOMOLE program package only three hybrid exchange-correlation functionals are available, namely PBE0 [140], B3LYP and BHLYP [141]. From non-hybrid functional only PBE was used. [142, 143] Dunning’s cc-pVDZ [144] and aug-cc-pVDZ [145], and Schäfer *et al.* TZVP [146] basis sets have been used, together with their corresponding auxiliary basis sets for RI calculations [147, 148]. The default multiple integration grid (m3) was used in all (TD)DFT calculations.

¹² $\vec{v}'_i = \vec{v}_i \sqrt{\frac{\Delta t}{\tau} \left(\frac{T_0}{T} - 1 \right) + 1}$; $\forall i$, where $T = \frac{k_B}{3} \sum_{i=1}^{N_n} M_i |\vec{v}_i|^2$, while the T_0 is the final temperature to be reached in expected time τ .

Calculations of ground and excited electronic state Hessians were performed numerically either using the TURBOMOLE Numforce package or performing the finite difference approximation for Hessian matrix elements

$$\left. \frac{\partial^2 V_i}{\partial R_j \partial R_k} \right|_{\mathbf{R}} \approx \frac{1}{2} \left[\frac{\nabla_j V_i(\mathbf{R}; R_k + \Delta R_k) - \nabla_j V_i(\mathbf{R}; R_k - \Delta R_k)}{2\Delta R_k} + \frac{\nabla_k V_i(\mathbf{R}; R_j + \Delta R_j) - \nabla_k V_i(\mathbf{R}; R_j - \Delta R_j)}{2\Delta R_j} \right] \quad (3.115)$$

with an automated script. A value of 0.02 Bohr was used for the nuclear translocation step (ΔR) in all directions. The ground state optimizations and analytic harmonic vibrational analysis at the MP2/6-311+G(2d,p) level for NAPA and NAPMA molecules were performed with Gaussian 09 program package. [149]

CI points between two electronic PES-s were obtained from geometries in which two PES-s intersect. These geometries were either obtained from geometrical optimizations, either full or constrained, or linear interpolation path (LIP) procedures. The LIP is constructed by linearly interpolating the internal coordinates between the two end molecular geometries, and transforming them to Cartesian coordinates. While both used methods, TDDFT and RI-CC2, for calculation of excited state are based on LR approximation, both exhibit instabilities at CI between ground and excited state, so an energy gap of 0.2 eV or less was taken as the criterion for CI. For CI between excited states, generally obtained from LIP-s, apart from the energy criterion an observed swap of electronic characters along the LIP additionally confirmed the presence of CI point. For CI between excited states the threshold value for CI is decreased to 0.02 eV or less. Due to the non-hermitian nature of CC2 electronic Hamiltonian, [150] CC2 method cannot even reproduce exact excited state PES-s degeneracies, thus the lower CI gap was restricted also to a value of 10^{-5} eV. Linear interpolation of internal coordinates and transformation between internal and Cartesian coordinates, and *vice versa*, was performed using the Wolfram Mathematica® program package. [151] The minimum energy conical intersection (MECI) and minimum distance conical intersection (MDCI) points were obtained using the sequential penalty optimization procedure devised by Levine *et al.* and implemented in their CIOpt program package [152] which was coupled to TURBOMOLE.

Basis set superposition errors (BSSE) were completely discarded from considerations because with the use of aforementioned methods and approximations the errors introduced from finite basis sets are expected to be insignificant.

Concerning the double excitation nature of excited states and the validity of CC2 method for their description, TURBOMOLE's intrinsic diagnostic values (\mathcal{T}_1 and \mathcal{T}_2) were used as indicators of double excitation contributions to excited states. In all considered

cases, including the CI with energy gaps approaching the lower limit, double contributions were always below the recommended 15%, which confirms the validity of CC2 method for their description. [133, 150] On the other hand, the \mathcal{D}_1 recommended value, [153, 154] which quantifies the multireference characters of ground state, was exceeded for every considered geometry at CC2, but also at the MP2 level of theory. However, taking into account the recent reconsiderations of \mathcal{D}_1 threshold values, [155] the CC2 method turns completely valid for present ground state calculations. [150]

Mathematica program package and Adobe® Photoshop were used for every image construction. The isodensity surfaces and molecular orbitals were visualized using the GaussView program. [156]

4 Results and Discussion

4.1 Nature and energetics of NAPA conformers excited states

Excitation spectra were recomputed for the three NAPA conformers at the CC2 and TDDFT levels using a number of basis sets. While electronic transitions are highly sensitive on molecular geometries, special caution was applied when constructing the absorption spectrum. For vertical excitations, ground state geometries were taken either as the reference MP2/6-311+G(2d,p) structures or the geometries were reoptimized at the same level of theory used for excited state calculations. To compute the adiabatic transitions geometrical optimization in the excited state of interest was conducted. Adiabatic transitions are further corrected with harmonic ZPE in order to include the nuclear contribution to the relative stability of electronic states. Since the photochemistry of the first excited state is of main interest, only three additional excited states (S_2 - S_4) were computed. The obtained S_1 excitations are compared to the reference CASSCF(8,8)/MS-CASPT2/cc-pVDZ and experimental values (see Table 2.3). The character of each state was determined from the major contributions of canonical HF orbitals of the CIS expansion of the LR-CC2 description of electronic change or from the coefficients ($X_{p,ia}^2 - Y_{p,ia}^2$) of the occupied-virtual KS ia orbital pair in LR-TDDFT. In Tamm-Dancoff approximation $X_{p,ia}^2$ coefficients determine the KS orbital contribution. When the character is ambiguous from molecular orbital representation a more physical description of electronic excitation is used instead by reconstructing the electronic density change between the excited and ground electronic states. This approach enables a direct visualization of excitation localization. Two ways of depiction are used to represent the electronic density change (see Figure 4.1 caption).

4.1.1 NAPA excited states

It is observed that CC2 method seriously overestimates the conformers ground state relative stability. Analogue to the electronic energy MP2 and CASSCF/CASPT2 calculations [38] the CC2 method predicts the conformer B as the most stable structure (~ 1.3 kcal mol $^{-1}$ below conformers A and C). However, the ZPE corrections at the RI-CC2/cc-pVDZ level are insufficient to rectify the energy ordering as in the case at the MP2 level of theory. With ZPE corrections included at the RI-CC2/cc-pVDZ level of theory the NAPA conformer B is still 0.8 and 1.1 kcal mol $^{-1}$ more stable than conformers A and C, respectively. Also, one of the reported inadequacies of using the CC2 method for description of ground state properties is the problem of overestimated bond lengths. [157] In NAPA conformers this is mainly manifested as the over-expanded phenyl ring in S_0 state. For comparison, the optimized NAPA phenyl ring at CC2 level is almost identical

to the optimized benzene molecule at the same level of theory, where the latter has significantly longer bond lengths compared to the reference structure (at RI-CC2/cc-pVDZ level $\Delta d(\text{C-C}) = 0.011 \text{ \AA}$, $\Delta d(\text{C-H}) = 0.009 \text{ \AA}$ compared to reference benzene structure in [39]). When comparing NAPA ground state geometries obtained at CC2 and MP2 level, the bond lengths at the former level of theory are in average 0.008 \AA longer, where the phenyl C-C bonds solely differ by 0.01 \AA . These geometrical difference will manifest as differences between electronic transitions calculated for the two structures.

Table 4.1 lists four lowest transitions obtained using the RI-CC2 method with cc-pVDZ and TZVP basis sets. From columns two and three one can observe the differences between excitations obtained at the RI-CC2/cc-pVDZ level of theory using the CC2/cc-pVDZ and MP2/6-311+G(2d,p) ground state geometries. All vertical $S_0 \rightarrow S_1$ transitions obtained with the MP2 S_0 geometries are 0.09 eV blue shifted to the corresponding values obtained using the CC2 level structures. This is expected since the MP2 minima do not overlap with the CC2 S_0 minimum structures. Higher vertical excitations, however, do not deviate significantly in average between the two geometries. On the other hand, the adiabatic $S_0 \rightarrow S_1$ transitions are 0.15 eV blue shifted for CC2 geometries, as also for the ZPE corrected adiabatic transitions. This 0.15 eV discrepancy originates from the stabilization energy at the CC2 ground state level due to the erroneous expansion of bond lengths at this level of theory. Nevertheless, the obtained transitions even at these geometries reproduce the experimentally observed ordering of $S_0 \rightarrow S_1$ transitions which the theoretical reference method is unable to reproduce. The reason for this latter failure is probably due to the use of CASSCF geometry for CASPT2 energy calculations. The character of the S_1 excited state is the phenyl first $\pi\pi^*$ excited state completely localized on the benzene ring (Figure 4.1). It corresponds to the symmetry perturbed B_{2u} state of benzene or B_2 state of toluene. Energetically, $\pi\pi^*$ vertical transitions for all NAPA conformers are $\sim 0.1 \text{ eV}$ lower than the calculated benzene $A_{1g} \rightarrow B_{2u}$ excitation at the same level of theory. [158] The difference is even more pronounced for adiabatic transitions. Compared to toluene S_1 excitation, the differences are reduced to $\sim 0.02 \text{ eV}$ in favour of NAPA conformers, indicating the favorable interactions between the phenyl moiety and the backbone that lower the S_1 - S_0 gap. This gap is the largest in NAPA conformer B and is correctly reproduced in all CC2 obtained transitions. However, this gap is not well enough described at the CASSCF level, since conformer C appears to possess the largest transition value, while also at the CASSCF level conformer B is the most stable structure on the S_0 PES. It seems that the CC2 methods describes the electronic correlations better in the excited states as it correctly predicts the conformer B $\pi\pi^*$ state to be the less stable than in the other two conformers. However, as evident from comparison of vertical and adiabatic S_1 transitions of columns two, three and four with the corresponding reference

theoretical values in column five, the S_1 PES at CC2 level is more sloped around its local excited state minima. Vertical structures undergo ~ 0.2 eV energy stabilization when transformed to local S_1 minima structures, which is even larger when the MP2 based geometry is transformed to corresponding CC2 excited state minimum. Again, this is due to the over-expansion of bond lengths at the CC2 level, especially for the excited phenyl ring C–C and C–H bonds ($\Delta d(\text{C–C})$ and $\Delta d(\text{C–H}) \sim 0.01$ Å compared to S_1 reference values [39]). Nonetheless, with the inclusion of ZPE corrections the CC2 S_1 transitions, especially the ones calculated from MP2 ground state geometries, are in good agreement with the experimental values, being blue shifted in average by only 0.05 eV. The values obtained on a smaller basis set are almost equal to those obtained with the larger TZVP basis set, which is particularly useful regarding the computational expense of the latter basis set. The inclusion of diffuse augmented functions into the cc-pVDZ basis set does not improve the quality of electronic transitions (results not shown), because Rydberg type transitions severely contaminate all electronic states. Because of non-physical characters of the lowest excited states as well as the fact that Rydberg type transitions in peptide systems are expected to appear higher in energy, [54–56] the RI-CC2 method with the augmented basis set severely underestimate Rydberg transitions, indicating how the aug-type basis sets are not adequate for the systems at hand.

Table 4.1: Four lowest vertical transition energies along with the (*adiabatic*) and [**ZPE corrected adiabatic**] S_1 transition energies of the three NAPA conformers calculated at the RI-CC2/cc-pVDZ and RI-CC2/TZVP level of theories. (I) indicates the use of RI-CC2/cc-pVDZ level of theory for the construction of the corresponding ground state minimum geometries and ground state ZPE corrections while (II) indicates the use of MP2/6-311+G(2d,p) level of theory for analogue set of calculations. All excited state ZPE-s were calculated at the RI-CC2/cc-pVDZ level of theory. All values are in eV.

	RI-CC2			Reference values	
	cc-pVDZ (I)	cc-pVDZ (II)	TZVP (II)	Theor. [38]	Exp. [20]
A	5.168 (<i>4.964</i>) [4.750] 5.849 5.977 6.427	5.252 (<i>4.801</i>) [4.587] 5.868 5.962 6.475	5.163 (<i>4.785</i>) [4.571] 5.799 5.841 6.395	4.827 (<i>4.707</i>) 5.946	4.650
B	5.183 (<i>4.982</i>) [4.766] 5.668 5.851 6.471	5.273 (<i>4.830</i>) [4.613] 5.723 5.874 6.537	5.179 (<i>4.822</i>) [4.605] 5.578 5.817 6.450	4.882 (<i>4.769</i>) 6.012	4.663
C	5.170 (<i>4.968</i>) [4.758] 5.713 5.909 6.499	5.261 (<i>4.810</i>) [4.600] 5.784 5.949 6.571	5.167 (<i>4.807</i>) [4.597] 5.652 5.883 6.474	4.913 (<i>4.778</i>) 6.040	4.654

Unfortunately, while no higher excited state of the three NAPA conformers was probed,

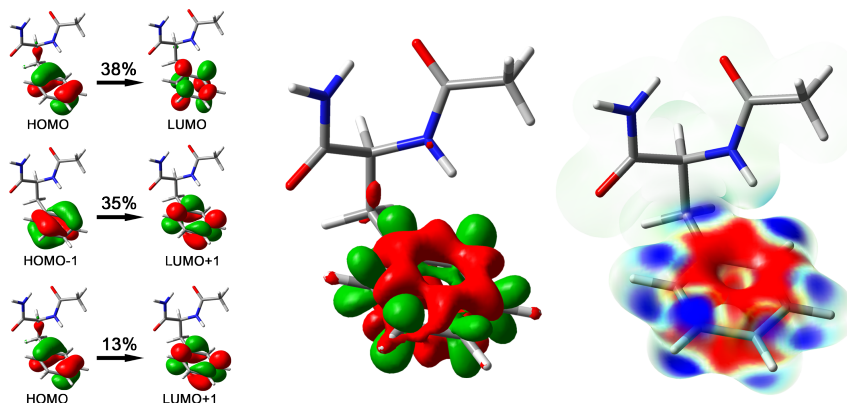


Figure 4.1: Three complementary depictions of the electronic structure change in the S_1 vertical excitation of NAPA conformer B using isosurfaces. Left: Contributions of the occupied-virtual canonical HF molecular orbital pairs with the corresponding fraction (percentage on the black arrow) to the total wave function change, where the orbital pairs are designated using the relative HOMO-LUMO nomenclature. Middle: Change of electronic density displayed with isosurfaces of 0.001 \AA^{-3} absolute values along regions of space with positive (green) and negative (red) difference between excited and ground state electronic densities. Right: The 0.02 \AA^{-3} ground state total density isosurface mapped with the electronic density difference between S_1 and S_0 state showing regions of electron density increase (decrease) with blue (red) color relative to the ground state density.

theory and experimental results of analogue chromophoric systems remain the only reference values against which to compare the higher lying transition energies. The second vertical transition determined by Došlić *et al.* in NAPA conformers corresponds to the benzene $A_{1g} \rightarrow B_{1u}$ transition with very similar energies (vertical S_2 energy in benzene is estimated to 6.09 eV [39]). The vertical transition to the S_4 state in NAPA conformers determined at the CC2 level is by character the closest transition to the former reference transition. In energy the CC2 transitions deviate by approximately 0.4 eV from the reference values. Although the canonical HF orbitals indicate a clearly localized excitation on the phenyl ring (Figure 4.2) the density representations also show the 14% contribution of CT character from the lower portion of the backbone to the phenyl ring. This fraction of CT character originates from the mixing of the S_4 state with the neighbouring S_5 state which is only 0.2 eV above the former and is of pure CT character from the backbone to the phenyl ring (Figure 4.3). Population analysis [159] confirms the depletion of charge from oxygen and nitrogen atoms on the backbone and increase of negative charge on the entire benzyl group. In the literature, CT states of the former type in similar systems were only discussed in the context of the proposed mechanism for Trp fluorescence quenching in aqueous solutions to explain the experimentally observed substitution of H atom with D on the indole ring. [160, 161] On the reaction pathway for the proposed mechanism of H atom transfer from the protonated Trp amino group ($-\text{NH}_3^+$) to indole ring Blancafort

and co-authors observed an indole L_a with a significant CT charge transfer contribution between the two groups. [162] Although this state appears in an early stage of reaction pathway constructed at the CASSCF/6-31G(d) level, the authors do not address it in the Franck-Condon region. Nonetheless, the appearance of such state at the CASSCF level of theory is consistent with the observations on the CC2 level as will be shown later. This indicates that NAPA S_5 CT state is not an artefact of the CC2 method, but apart of the former reference no other source that addresses this particular type of CT states in peptide systems is known to the author. A particularly interesting feature of this CT state is the pronounced electronic density build up in the region indicated by dashed ellipse on Figure 4.3. Consequences of this electron density increase will be addressed later.

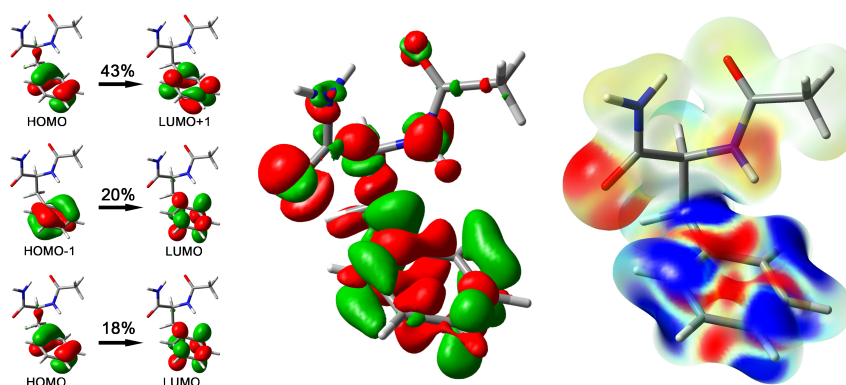


Figure 4.2: Character of the S_4 vertical excitation in NAPA conformer B. For picture details see Figure 4.1 caption.

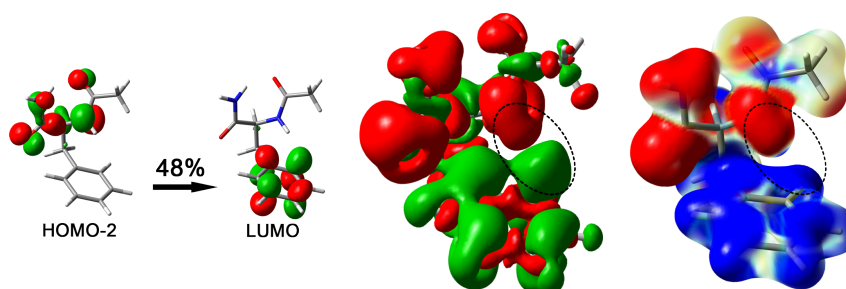


Figure 4.3: Character of the S_5 vertical excitation in NAPA conformer B. For picture details see Figure 4.1 caption.

The two remaining transitions (S_2 and S_3) intercalated between the two phenyl type transitions in the Franck-Condon region are of $n\pi^*$ character, as is evident from Figures 4.4 and 4.5. Each state is localized on only one amide group. For convenience they are further designated as $n\pi^*_{(I)}$ and $n\pi^*_{(II)}$, where the former is localized on the first amide group, while the latter on the second. As clearly shown from the density difference maps, less from major contributing molecular orbitals, the electrons from the oxygen n orbital are transferred to the π^* orbital of the same C=O bond, while the electron density also

increases on the nitrogen atom of the same amide group. Non-bonding O and N orbitals could not be included into the active space calculations of Došlić *et al.* Thus reference transition energies are missing. Because the size of active space would increase drastically with the inclusion of missing orbitals (at least four additional non-bonding orbitals with eight electrons would be needed to include into the former NAPA active space) such CASSCF/CASPT2 calculations were not repeated. However, S_2 and S_3 transitions fall in the reference energy window determined by Serrano-Andrés *et al.* for the $n\pi^*$ type transitions. [54, 55] In conformers B and C the $n\pi^*_{(II)}$ excited state is lower in energy than the $n\pi^*_{(I)}$ excitation. In conformer A this order is reversed. Both observations are consistent with the $n\pi^*$ energy trend displayed in two geometries of Gly dimer which resemble the γ_L and β_L secondary structures. [56] However, contrary to the reported results of Serrano-Andrés and collaborators, population analysis reveals no electron depletion on the nitrogen atom of the amide group involved in the excitation. Instead, a small increase on negative charge was found on the N atom, which is in accordance with the observed density increase seen in density difference plots (Figures 4.4 and 4.5). Geometrical optimization of the $n\pi^*_{(II)}$ excited state in NAPA conformers, started from the vertical geometry, resulted in a CI with the lower $\pi\pi^*$ state just within few optimization steps. This trend is completely imitated by the other $n\pi^*_{(I)}$ state, with the only difference that the lower state in the CI is the lower $n\pi^*_{(II)}$ state. Such behavior of the $n\pi^*$ states in the Franck-Condon region is also consistent with the properties of the state $n\pi^*$ in formamide molecule. [57, 58] Already these findings suggest the presence of few CI points and few potential mechanisms from which the first phenyl $\pi\pi^*$ excitation can be transferred to amide groups as shown by Shemesh and co-workers. [30–32, 62] Therefore, the next logical step is to utilize the non-adiabatic molecular dynamics for screening of NRD mechanisms. But prior to that, the vibronic properties of NAPA conformers are addressed first, followed by the necessary evaluation of the best exchange-correlation functional used later in non-adiabatic molecular dynamics. NAPMA absorption spectrum is also examined.

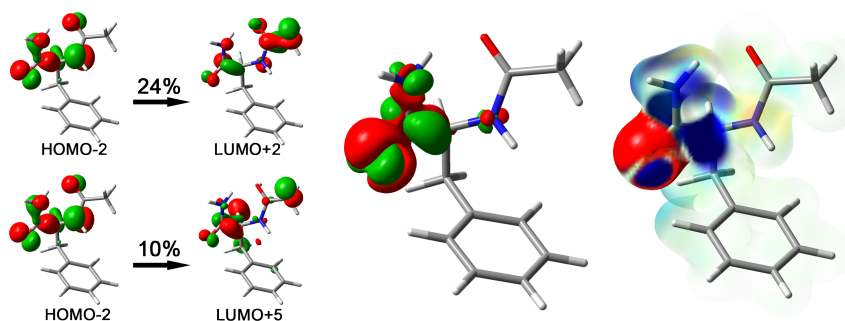


Figure 4.4: Character of the S_2 vertical excitation in NAPA conformer B. For picture details see Figure 4.1 caption.

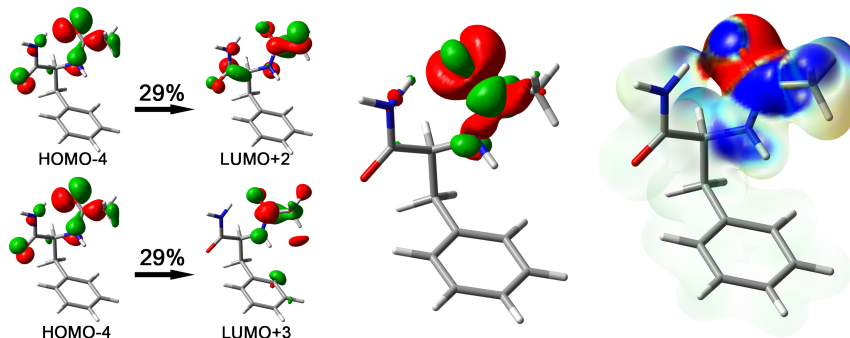


Figure 4.5: Character of the S_3 vertical excitation in NAPA conformer B. For picture details see Figure 4.1 caption.

4.1.2 NAPA vibronic states

Because NAPA conformer S_1 minima geometries and their vibrational properties will play a key role in explaining NRD mechanisms later, it is worth while to examine them in more details. In the S_1 $\pi\pi^*$ minimum structure the phenyl ring is notably expanded. With the S_1 and S_0 minima computed at the RI-CC2/cc-pVDZ and MP2/6-311+G(2d,p) levels, respectively, the obtained average difference between S_1 and S_0 phenyl C–C bond lengths (0.047 Å) slightly overestimates the reference difference value for benzene (0.040 Å) [39]. In absolute terms, the average phenyl S_1 C–C bond lengths at the RI-CC2/cc-pVDZ level differ from the reference benzene bond lengths by 0.01 Å, [39] exactly much as they deviate in the ground state. The interaction with the backbone contributes negligibly to the phenyl bond lengths as they are almost identical to corresponding benzene S_1 values obtained at the RI-CC2/cc-pVDZ level. In all three NAPA conformers S_1 minimum structures all bonds are slightly more longer then in the ground state. From the global geometrical changes, conformer A exhibits a small shift of its phenyl ring toward the second amid group through rotation around the C_α – C_β bond. This causes a decrease of distance between N_{II} and phenyl ring center by 0.11 Å. Conformers B and C also exhibit a slight rotation of phenyl ring around the C_β – C_{ipso} bond away and towards, respectively, from the backbone. While conformer A shows no change in the geometry of the backbone, NH_2 groups of the second amide group of conformers B and C undergo a small additional deplanarization, slightly larger in the latter conformer. In conformer B (C) the γ_L -ring H-bond shortens by 0.025 Å (0.014 Å). Because all bond lengths expand in the $\pi\pi^*$ state, vibrational frequencies should consequently decrease. This trend is observed between the S_1 and S_0 calculated harmonic frequencies.

Figure 4.6 displays the change of frequencies and types of normal modes between the two states in conformer B. It shows how almost all S_1 modes are red-shifted compared to their corresponding ground state modes, where most of the modes with frequencies above 1000 cm^{-1} preserve their type, while lower frequency modes undergo significant recom-

binations. The other two conformers display a similar pattern in vibrational properties. Due to the general red-shift of the S_1 normal modes the S_1 ZPE is ~ 0.2 eV smaller than the ground state ZPE value in all conformers. Exactly this ZPE change between the two states upon deuterium isotope substitution causes the blue-shifts of absorption transitions which are experimentally observed in certain NAPA conformers isotopologues (see Figure 2.2). For this reason, vibrational frequencies were computed for all NAPA deuterated isotopologues given in Table 2.1. Because exact experimental transition blue-shifts have not been tabulated, the calculated values are not listed. However, from Figure 2.2 one can observe that experimental blue-shifts fall in range from 0 to approximately 5 cm^{-1} . The calculated blue-shifts are in range $3\text{-}30 \text{ cm}^{-1}$. It is naive to expect the calculated values to exactly match the experimental values, but nonetheless the used harmonic approximation is enough sensitivity to show the difference between substitutions of protium involved in an H-bond from the distal protium of NH_2 group, where the former displays a larger transition shift due to deuterium substitution.

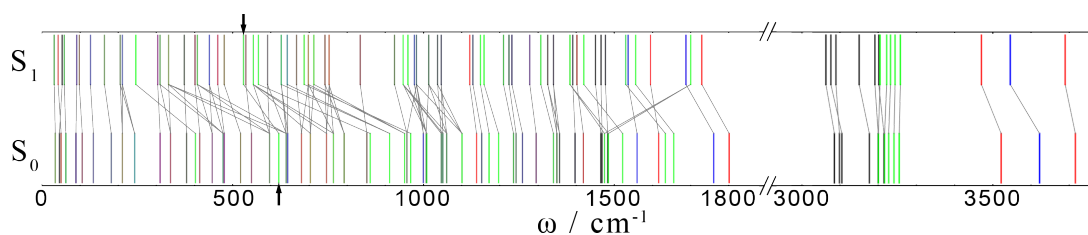


Figure 4.6: Comparison of the NAPA conformer B harmonic frequencies between the $\pi\pi^*$ and ground electronic state. The S_1 and S_0 frequencies were computed at the RI-CC2/cc-pVDZ and MP2/6-311+G(2d,p) level of theory, respectively. Colors indicate contributions of certain atoms to the motions of the entire normal mode. Green, blue, red and black colors designate atoms of the phenyl, first amide, second amide group and others, respectively. The grey lines connect each S_1 normal mode with the most similar normal mode of the S_0 state. The two black arrows show the frequency change of the normal mode potentially involved in the $6b_0^1$ vibronic transition.

Furthermore, the computational vibrational analysis of a particular electronic state can be used to evaluate the quality of the level of theory used for the construction of the PES. Unfortunately, apart from the $6b_0^1$ vibronic transition in conformers A and B, and the progression lines of conformer A, no other experimental insight into the excited state vibrational structure of NAPA molecule is available. The 17 cm^{-1} separated progression lines in NAPA conformer A have no counterpart in the $A_1 \rightarrow B_2$ vibronic transition spectrum of toluene, [41] but fall in the order of toluene methyl group internal rotational states. [163] The equidistantly separated progression lines could indicate that internal rotation of acetyl methyl group is hindered and only allowed to oscillate around the equilibrium geometry. Coincidentally, the harmonic frequency of CH_3 internal rotation in NAPA conformer A at the RI-CC2/cc-pVDZ level of theory has a value of 10 cm^{-1} .

However, owing to the imprecision of numerical Hessian and the general inability to treat internal or any other low energy motion harmonically such vibronic assignment is questionable and requires further examinations. Therefore, the CH₃ group rotation around the C_{Ac}-C bond was examined in NAPA and NAPMA conformers for later purposes, but also to evaluate the validity of harmonic approximations for such low frequency modes. For the internal rotation of a completely symmetric acetyl CH₃ group a barrier of 46 cm⁻¹ was found both in S₁ and S₀ states. By neglecting the vibrational couplings with the methyl group internal rotational motion the methyl group can be considered as a rigid rotor with a *B* rotational constant of 5.2 cm⁻¹. With such a low barrier and *B* constant the exact solution¹³ displays that the methyl group can easily rotate by tunneling between the three symmetrically equivalent minima. However, an order larger and non-equidistant energy levels for internal methyl group rotation do not fit the experimental progression. Even by restraining the CH₃ motion to simple harmonic oscillation, the energy levels are still four times larger compared to the experimental values. Although vibrational couplings and nuclear statistic do alter the methyl group internal rotational pattern, the observed effect of increasing the progression lines separation to 22 cm⁻¹ in NAPMA conformer A upon methylation of the second amide group is not consistent with the assignment of progression lines to internal acetyl group rotation. Thus, the progression pattern in NAPA and NAPMA conformer A is due to some other internal motion which is strongly affected by methylation, but remains unknown. The analysis reveals how underestimated is the internal rotational mode in harmonic approximation for NAPA conformer A, whereas for NAPA conformer B the internal rotation harmonic frequency (50 cm⁻¹) obtained from Hessian coincides pretty well with the value obtained from the rotational barrier (52 cm⁻¹). In all NAPA and NAPMA conformers the acetyl methyl rotation is accomplished by tunneling (rotation time between symmetric minima estimated to 2 ns from the two lowest energy levels).

Contrary to the former unknown vibronic state, the 530 cm⁻¹ vibrational state of the S₁ electronic state can be computationally assigned. The RI-CC2/cc-pVDZ level of theory predicts that the in plane ring distortion normal mode (Figure 4.7) analogue to the B₂ normal mode in toluene should best match this observed vibrational state in NAPA conformers. [164] The calculated mode frequencies of 523, 528 and 523 cm⁻¹ for conformers A, B and C, respectively, are in good agreement with the theoretical reference value of 538 cm⁻¹ for toluene computed at the TD-B3LYP/aug-cc-pVTZ level of theory. [163] The experimental reference value in S₁ state of toluene appears at 532 cm⁻¹. This B₂ mode in NAPA conformers is also preserved in the ground electronic state, but blue-shifted to frequency of 625 (620) cm⁻¹ in all conformers as computed at the MP2/6-311+G(2d,p)

¹³Obtained using Fourier series.

(RI-CC2/cc-pVDZ) level of theory. The calculated ground state mode frequencies match the theoretical 638 cm^{-1} and experimental 623 cm^{-1} reference values of toluene. [163] The blue-shift is caused by the increase of phenyl ring stiffness in the ground state.

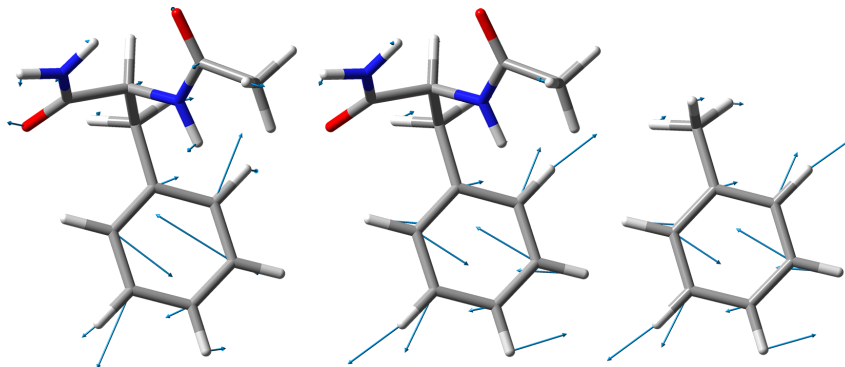


Figure 4.7: Cartesian displacement vectors representing the normal mode of the populated vibrational state in the vibronic $6b_0^1$ transition of NAPA conformer B calculated at the RI-CC2/cc-pVDZ level of theory (left image). The same corresponding normal mode in the ground state of NAPA (middle) and toluene (right) molecule at the MP2/6-311+G(2d,p) level of theory.

The same type of analysis was conducted on NAPA ground state PES obtained at the MP2/6-311+G(2d,p) and RI-CC2/cc-pVDZ levels of theory, where now the experimental stretch frequencies of the N–H and C=O bonds are available for comparison. Since ground state properties are not the main issue these results are not shown. However, in short, the MP2 level shows a better agreement with the reference experimental and theoretical values of Došlić *et al.* [38] than the CC2 ones. This was expected since already significant errors were introduced in the ground state structure with the use of CC2 level. Nevertheless, CC2 still performs adequately for the excited states.

In overall, it can be concluded that the RI-CC2/cc-pVDZ level of theory reproduces the reference excited state properties of relatively high accuracy with an acceptable computational cost. As no selection of active space is needed in CC2, the same method enables a much easier construction of PES-s. Thus all further calculations are conducted at the RI-CC2/cc-pVDZ level of theory.

4.1.3 NAPA excited states at the LR-TDDFT level of theory

Table 4.2 lists four lowest vertical excitation energies computed using PBE, B3LYP, PBE0 and BHLYP functionals to systematically examine the contribution of the exact Hartree-Fock exchange on the accuracy of excited states. cc-pVDZ basis set was used for all calculations. As can be clearly seen in Table 4.2 excitation transition obtained at the TDDFT level of theory severely deviate in energy as well as in character from the reference and CC2

obtained values (Table 2.3). The non-hybrid PBE functional underestimates experimental S_1 transition energies by 0.5-0.7 eV, while hybrid functionals overestimate transitions even by 0.9 eV. Higher excited states in Franck-Condon region are closely packed, and the four lowest excited state fit in an energy window of 0.5 eV. Vertical transition energies computed with a particular functional on the reference ground state MP2/6-311+G(2d,p) level geometries deviate from the energies computed on the geometries optimized with the same concerned functional by 0.2 eV or less. Deviations between these two values are almost negligible when using PBE and B3LYP functionals, are the largest for BHLYP, while for PBE0 fall between the two extremes. The observed differences are a cumulative sum of errors originating from the description of ground state geometries and the shapes of PES-s in these geometries. In terms of geometrical differences PBE0 ground states have almost identical bond lengths as the reference geometries in all conformers. PBE obtained geometries differ the most in bond lengths while all BHLYP geometries have in average slightly contracted bond lengths compared to reference values. Regarding the whole geometry, just as in case at the CC2 level, conformer A deviates the most from the reference MP2/6-311+G(2d,p) level structure due to the shift of phenyl ring position relative to the backbone. Difference between conformer B structures obtained at CC2 and DFT levels are in the relative position of the second amide group to the rest of the molecule. DFT predicts a more planar NH_2 moiety with the $\text{C}=\text{O}$ group of the second amide group more closer to the phenyl $\text{C}-\text{H}$ and a slightly shorter H-bond of the γ_{L} ring. Conformer C structures vary very little from the reference structure. All these geometrical properties are reflected in making the conformer B the most stable structure as calculated with all four used exchange-correlation functional.

More important are the properties of excited state PES-s, which vary more significantly among the four functionals. Regarding the used functional, at least one among four lowest excited states is contaminated with a low lying CT state. This case is the worst for PBE functional where all states are of CT character. A strong mixing of CT is seen with the use of B3LYP where only the two lowest states still have some localized excitation, while the rest is CT from the backbone to the phenyl ring. PBE0 and BHLYP performed better than the former two functionals giving quite well defined states. Compared to RI-CC2/cc-pVDZ values, PBE0 is slightly better in the description of the S_1 vertical excitation energy. Nonetheless, both functionals suffer from overstabilization of the second phenyl state which falls below one of the $n\pi^*$ states, where in case of PBE0 the second phenyl state has more CT character. This problem becomes particularly severe if a geometrical optimization of S_1 states is performed. For conformers B and C no $\pi\pi^*$ PES state minima could be constructed using PBE, PBE0 and B3LYP functionals. Instead, a proton from the neighboring $\text{N}_{\text{Phe}}-\text{H}$ group is transferred to the closest *ortho* C atom of the phenyl

ring, which causes the ground state energy immediately to rise, ending up in the CI with S_1 state. This computational observation is consistent with the build-up of electronic density in this particular region seen in the S_5 state obtained at the CC2 level of theory, but the three functionals at the TDDFT level inadequately described the energetic of this state which results in its mixing with the lower states. This is due to the missing interaction term ($1/R$) between the particle-hole pair which in adiabatic f_{Hxc} functional is largely given with the exact Hartree-Fock exchange. [123,165] Since only a fraction or none of the exact exchange is present in the three troublesome functionals, the systematic problem of lowering of the CT state cannot be avoided. A very shallow minimum was, however, found on the conformer B S_1 PES constructed using B3LYP functional with a small optimization step. No frequency analysis was carried out to determine the real nature of this critical point, while such a low barrier, if there is any at all, play no significant role. Only conformer A exhibits the S_1 PES minimum with all four functionals.

Table 4.2: Four lowest vertical transition energies computed at the LR-TDDFT/cc-pVDZ level of theory using the designated adiabatic exchange-correlation functional. The corresponding excited state character (determined from largest coefficients of occupied-virtual KS orbital pairs) is given in the subscript. Values not in brackets were obtained on the reference MP2/6-311+G(2d,p) geometries, while values in curly brackets were obtained on geometries optimized at the DFT/cc-pVDZ level using the involved functional. Italicized values in parenthesis designate the S_1 adiabatic transitions, where the $(-)$ sign shows that no S_1 minimum could be obtained. \dagger designates an unstable minimum structure. All values are in eV.

	PBE	B3LYP	PBE0	BHLYP
A	3.906 _{CT} {3.896} (<i>2.937</i>) 3.983 _{CT} {4.000} 4.363 _{CT} {4.383} 4.455 _{CT} {4.465}	5.271 _{$\pi\pi^*$+CT} {5.286} (<i>4.634</i>) 5.384 _{$n\pi^*$(II)+CT} {5.418} 5.544 _{CT} {5.597} 5.591 _{CT} {5.666}	5.368 _{$\pi\pi^*$+CT} {5.405} (<i>5.205</i>) 5.571 _{$n\pi^*$(I)}} {5.623} 5.697 _{CT} {5.796} 5.834 _{$n\pi^*$(I)+CT} {5.885}	5.595 _{$\pi\pi^*$} {5.674} (<i>5.543</i>) 5.986 _{$n\pi^*$(I)}} {6.129} 6.027 _{$\pi\pi^*$} {6.140} 6.097 _{$n\pi^*$(II)}} {6.294}
B	4.136 _{CT} {4.115} (-) 4.165 _{CT} {4.126} 4.552 _{CT} {4.667} 4.592 _{CT} {4.680}	5.276 _{$\pi\pi^*$+CT} {5.303} (<i>4.686</i>) \dagger 5.396 _{$n\pi^*$(II)+CT} {5.418} 5.448 _{CT} {5.488} 5.569 _{CT} {5.602}	5.393 _{$\pi\pi^*$} {5.430} (-) 5.487 _{$n\pi^*$(II)}} {5.568} 5.674 _{CT} {5.703} 5.694 _{$n\pi^*$(I)}} {5.775}	5.616 _{$\pi\pi^*$} {5.690} (<i>5.554</i>) 5.832 _{$n\pi^*$(II)}} {5.978} 6.046 _{$\pi\pi^*$+$n\pi^*$(I)}} {6.184} 6.114 _{$n\pi^*$(I)}} {6.194}
C	3.924 _{CT} {3.895} (-) 4.064 _{CT} {4.011} 4.493 _{CT} {4.513} 4.611 _{CT} {4.604}	5.298 _{$\pi\pi^*$+CT} {5.292} (-) 5.367 _{CT} {5.383} 5.463 _{$n\pi^*$(I)+$n\pi^*$(II)}} {5.451} 5.501 _{CT} {5.523}	5.406 _{$\pi\pi^*$+CT} {5.423} (-) 5.530 _{$n\pi^*$(II)}} {5.585} 5.629 _{CT} {5.638} 5.760 _{CT} {5.781}	5.602 _{$\pi\pi^*$} {5.676} (<i>5.542</i>) 5.838 _{$n\pi^*$(II)}} {5.965} 6.095 _{$\pi\pi^*$} {6.182} 6.113 _{$n\pi^*$(I)}} {6.231}

No improvement of PES energies or characters is observed using larger TZVP or aug-cc-pVDZ basis sets in TDDFT calculations. The same observations also hold for TDDFT excited state calculations performed using the Tamm-Dancoff approximation. Considering TDHF method as an extreme of BHLYP with no correlation part but with only exact exchange, one can test whether exchange part dominates over the electronic correlation. But as the TDHF results show, without the electronic correlation the two phenyl $\pi\pi^*$

states become the lowest states followed by the two amide $n\pi^*$ states, where all states end up in an even smaller energy window. In all, it can be concluded that the BHLYP functional balances between enough electronic correlation and exchange necessary to obtain a set of well defined excited states, but which still hugely deviate from the reference values. Although it seems that BHLYP outperforms PBE0 functional, it is important to point out that the comparison between the two functionals was made in a very narrow part of configuration space (around Franck-Condon to be precise). Because NRD pathways span a much wider part of configuration space it is still necessary to examine the two functionals in parts of configuration space further away from absorption region. This will be done in the following subsection. It is now definitely clear that the TDDFT methods (in LR or TDA setup) cannot match the reference CC2 method, but must be viewed instead as a necessary compromise for construction of the PES in screening of new NRD mechanisms. With the intrinsic failures of small energy gaps between excited states and a significant CT contamination, a kind of bias is introduced into the system as will be more evident later. However, through detail reexamination of the potential NRD mechanism using higher CC2 level calculations all incorporated errors can be corrected.

4.1.4 NAPMA ground and excited states

The three NAPMA conformers are structurally completely analogue to the three conformers of NAPA (Figure 4.8).

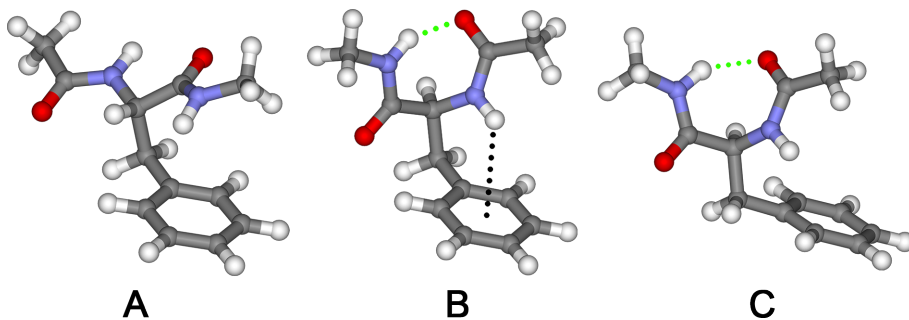


Figure 4.8: NAPMA conformers A ($\beta_L(a)$), B ($\gamma_L(g+)$) and C ($\gamma_L(g-)$). The green dotted lines represent the N-H \cdots O H-bonds within the seven member γ_L rings of NAPMA conformers B and C, while the black dotted line indicates the N_{Ph}-H \cdots π interaction in NAPMA conformer B.

The perturbative effect of the additional methyl group on the electronic structure of NAPMA molecule is most strongly exhibited in conformer A. Population analysis reveals that the attached methyl group on the second amide group decreases the amount of negative charge on the nitrogen atom, which is consistent with the results of Serrano-Andrés *et al.* [54] Interestingly, the charge of the H atom attached to the same N atom does not change, but instead the nearest phenyl *ortho* C atom becomes more negatively

charged. This distribution of charge causes an attractive interaction between the amide and the phenyl group, due to which the separation between the two groups decreases. The distance between N_{II} atom and the center of the phenyl ring reduces by 0.12 Å compared to NAPA conformer A. When compared to conformer B, the separation is still large enough not to classify the new interaction as an N–H ···π interaction. However the interaction is strong enough to make the conformer A more stable than conformer B as shown by the corresponding conformer electronic energies computed at the MP2/6-311+(2d,p) level of theory. On the other hand, the perturbative effect in conformers B and C is barely observable. Apart from a 4° increase of the ω₁ angle of the second amide group (ω = dih(C_{α,i+1}(H_{i+1})–N_{i+1}–C_i–C_{α,i})) in NAPMA conformer B towards a more planar amide group compared to NAPA conformer B, there is no other significant geometrical difference between NAPMA and NAPA paired conformers B and C. Regarding the relative positions of C–H bonds of the newly methyl group to the nearby N–H and C=O bonds in ground state minima, the methyl group is rotated to maximally increase the distance of its two H atoms from the C=O group while the third C–H bond slightly eclipses the neighbouring N–H bond.

Perturbation effects are further enhanced in the first phenyl ππ* state, where NAPMA conformers display significant geometrical changes compared to corresponding NAPA pairs. Again, the effect is the strongest in conformer A, in which the distance between the second amide group and phenyl ring has decreased for an additional 0.16 Å. Population analysis of conformer A S₁ minimum indicates a new weak electrostatic interaction between the H atom of the new methyl group and the closest *meta* C atom that might be responsible for enhanced interaction between amide and phenyl groups. These interactions cause additional stabilization of NAPMA conformer A ππ* which is stronger than in ground state and manifests as the red-shift of conformer A absorption band in the spectrum origin (see Figure 2.3). Table 4.3 lists transition energies calculated at the RI-CC2/cc-pVDZ level. One can clearly see how the experimental 0.022 and 0.013 eV energy difference between the conformer A and conformers B and C absorption bands, respectively, are computationally reproduced within an error of only 0.02 eV. The absolute deviations between experimental and calculated values are in 0.02–0.04 eV range, which is smaller than in NAPA case (deviations of 0.05–0.06 eV). These errors are completely negligible compared to the used method absolute uncertainty. The NAPMA conformer B ππ* minimum geometry exhibits the same set of geometrical changes relative to its S₀ structure as NAPA conformer B. The major difference, however, between the two structures is the complete planarization (ω₁ = 180°) of the NAPMA conformer B second amide group in S₁ minimum geometry. Also contrary to its S₀ structure the methyl group in S₁ minimum is rotated around the C–N bond in a way to increase the distance

of its two C–H bond maximally from the neighbouring N–H group, while the third C–H bond now becomes parallel with the C=O bond of the same amide group. This methyl rotation is common to all NAPMA conformer S_1 minimum structures. The rotational barrier around the C–N bond is 150 cm^{-1} for both the excited and ground electronic states. However, compared to acetyl methyl group, this high energy barrier completely hinders the CH_3 group rotation. The estimated internal rotational frequency of 85 cm^{-1} for the CH_3 group oscillation around the equilibrium from the rotational barrier matches almost exactly the value obtained with Hessian (89 cm^{-1}) and confirms the quality of obtained Hessian. Apart from this second methyl group rotation, NAPMA conformer C $\pi\pi^*$ minimum exhibits no additional geometrical change to its corresponding NAPA pair. The perturbative effect on higher excited states in NAPMA conformer is relatively low, shifting energies up or down only by 0.05 eV. The order of the four lowest NAPMA excited state characters exactly matches the order of corresponding NAPA excited states in all conformers.

Table 4.3: Four lowest vertical transition energies in NAPMA conformers with the corresponding (*adiabatic*) and [**ZPE corrected adiabatic**] S_1 transition computed at the RI-CC2/cc-pVDZ level of theory. The second and third column correspond to energies computed using the ground state geometries and ZPE-s obtained at the RI-CC2/cc-pVDZ and MP2/6-311+G(2d,p) levels of theory, respectively. All values are in eV.

	RI-CC2/cc-pVDZ		Exp. [33]
	RI-CC2/cc-pVDZ	MP2/6-311+G(2d,p)	
A	5.145 (<i>4.944</i>) [4.727] 5.837 5.937 6.350	5.235 (<i>4.878</i>) [4.659] 5.857 5.920 6.419	4.640
B	5.182 (<i>4.993</i>) [4.774] 5.768 5.869 6.456	5.272 (<i>4.922</i>) [4.702] 5.730 5.873 6.505	4.662
C	5.168 (<i>4.978</i>) [4.765] 5.790 5.904 6.485	5.260 (<i>4.906</i>) [4.693] 5.778 5.945 6.557	4.653

The origins of geometric changes in NAPMA conformers B and C excited state structures can also be traced to the changes of second amide group electronic structure. The addition of methyl group decreases the amount of negative charge on the neighboring N atom, compared to NAPA counterparts. However, at the same time, the positive charge on the C_{Phe} atom slightly decreases, while the negative charge on O_{Phe} increases, indicating

a redistribution of charge in the $C_{\text{Phe}}=\text{O}$ group. Thus in NAPMA the polarization of atoms in the second amide group is less than in NAPA conformers, showing a more prominent conjugation between amid group atoms in the methylated system. This is in complete contrast to conclusions of Serrano-Andrés *et al.* [54], while the addition of methyl group strengthens the $C_{\text{Phe}}-\text{N}$ bond. Conjugation is also exhibited by a small increase of $C_{\text{Phe}}=\text{O}$ bond length (see later tabulated values), completely consistent with the charge redistribution. The amount of negative charge on the second amide group methyl group is only half the value of the methyl on the first amide group, with less pronounced polarization of its $\text{C}-\text{H}$ bonds. In contrast to [54] the methyl group attached to N atom acts as an electron donating group and stabilizes the amide group. Detailed population analysis further reveals how this effect is slightly more pronounced in the excited state as more negative charge is redistributed between atoms, which causes a more stronger $C_{\text{Phe}}-\text{N}$ conjugation responsible for the observed total planarization of the second amide group. $\text{C}-\text{H}$ bonds are also less polarized in the S_1 state compared to S_0 values, indicating a possible interaction of $\text{C}-\text{H}$ bonds with the delocalized electrons of $C_{\text{Phe}}-\text{N}$ bond. This stabilizing effect is completely absence in NAPA conformers, whose consequences will become evident.

Except from the three 22 cm^{-1} separated progression bands of NAPMA conformer A, no other vibronic transition was experimentally determined, thus the relation between experimental and calculated vibrational frequencies in the excited state remains unknown. However, due to the similarities between NAPA and NAPMA molecules it is reasonable to assume that the used RI-CC2/cc-pVDZ level is adequate for the description of NAPMA vibrational properties.

The substitution of NAPA distal H atom with methyl group causes only minor changes in the electronic structure, at least in the absorption region of configuration space, where the effect is mostly exhibited for conformer A. However, the thirtyfold increase of $\pi\pi^*$ excited state lifetime in NAPMA conformer B compared to NAPA conformer B lifetime indicates a significant influence of the additional methyl group on NRD mechanisms. It remains now to elucidate the NRD pathways active in NAPA and NAPMA conformers and explain the methyl substitution effect on them.

4.2 Non-adiabatic molecular dynamics of NAPA conformer B

NAPA conformer B represented the logical choice for NRD mechanisms elucidation due to its experimentally measured short excited state lifetime, as well as for structurally exhibiting both the γ_{L} -ring H-bond and the $\text{N}-\text{H}\cdots\pi$ interaction. The simulation of 1.5 ns excited state lifetime is, however, beyond the reach of non-adiabatic molecular dynamics capabilities. From this aspect, the non-adiabatic dynamics is only used for elucidation of

new, potentiality active, NRD mechanism. Also no statistical analysis was made, which helped reduce the total number of trajectories. By avoiding the approximation of exact wave packet propagation with non-adiabatic dynamics simulations, the necessary condition that the set of initial conditions for trajectory propagation reproduces the initial nuclear wave packet as best as possible can be loosened. Also, the failure of LR-TDDFT method to exactly reproduced the excited state PES-s discards the need to exactly simulate the nuclear wave packet evolution. For this reason nuclear initial conditions (positions and velocities) were not obtained from the S_1 vibrationless quantum state, but rather from a classical ground state trajectory equilibrated to room (298 K) temperature. The benefits from the latter choice will be explained later. The ground state NAPA conformer B trajectory was propagated at the DFT RI-PBE/cc-pVDZ level of theory with a 0.5 fs nuclear time step for a total time length of 50 ps. The Berendsen thermostat with $\tau = 400$ fs characteristic time was used to reach the desired room temperature. The first 10 ps long trajectory equilibration period was dropped out, and 44 initial conditions were sampled randomly from the remaining part of the trajectory. Translational and rotational contribution to the total velocity were projected out from the initial conditions. The internal kinetic energies of initial conditions are normally distributed in range 0.8–1.3 eV (220–360 K)¹⁴, with a mean temperature of 294 K. The non-adiabatic trajectories were propagated in a manifold of ground and four excited electronic states obtained on-the-fly at the TDDFT level. All trajectories were started from the first excited electronic state. The nuclear time step was 0.25 fs long, while a thousand times smaller time step was used for propagation of electronic populations (3.52). Each trajectory was allow to propagate up to 5000 nuclear integration steps. The applied Eckart conditions assured that effects from any residual forces and torques are removed along the trajectory.

PBE0 and BHLYP functionals with the cc-pVDZ basis set were both used for the construction of PES-s. Although the latter functional outperforms the former, test simulations revealed that the use of BHLYP functional gives longer trajectories, with some of them remaining in the same initial (first) electronic state displaying no state change along the entire allowed propagation time. On the other hand, simulations started from the same initial conditions only using the PBE0 functional all yielded some NRD mechanism within a significantly shorter propagation time. Because the main goal is obtaining new possible NRD pathways, PBE0 functional was also utilized. Test simulations also shown that the small energy gap between excited state PES-s persist in configuration space regions further away from the initial structures, and that states frequently changes their characters. Not even all initial electronic S_1 states correspond to the phenyl $\pi\pi^*$ character. Test simulations have clearly demonstrated how ill-defined are the excited

¹⁴The equipartition relation, $\sum_{i=1}^{N_n} M_i |\vec{v}_i|^2 = (3N_n - 6)k_B T$, is used for conversion.

state PES-s obtained in the rest of configuration space at the TDDFT level of theory, with respect to the employed functional. But at the same time, test simulations revealed few potential NRD mechanisms of photochemical interest. This was however only possible on account of propagating trajectories with higher kinetic energy, than would the wave packet approximating the vibrationless initial state have (only ZPE to be precise). For this reason trajectories are able to span larger portions of configuration space and due to larger dynamical couplings because of higher velocities (3.53), trajectories can change PES-s more frequently. Exactly this had enabled them to overshoot critical regions of configuration space such as the pathologically CT contaminated S_1 absorption region at the PBE0 level, or to easily escape from the S_1 minimum at the BHLYP level. The use of higher kinetic energies accelerates the screening procedure for new potential NRD pathways, and justifies the choice of obtaining initial condition at a room temperature. Also, a sample of trajectories were propagated without the use of electronic state coherence rectification. This causes severe frequent hops between non-neighboring excited states resulting with physically unrealistic trajectories. However, it also represents a way for bypassing ill-defined regions and screening of wider portions of configuration space for new NRD mechanisms. Similar non-physical surface hops are observed when velocity readjustment is used along the initial velocity vector instead of rescaling along the direction of gradients difference vector, whether decoherence corrections are switched on or off. An example of trajectory without decoherence correction and with velocity scaling along its velocity vector will be demonstrated later.

4.2.1 Mechanism II

Figure 4.9 displays the time evolution of ground and four lowest excited state PES-s in a representing trajectory of the most common pattern of NRD mechanisms observed among 25 of 44 trajectories at the PBE0/cc-pVDZ level of theory. The representing trajectory starts from a well defined phenyl $\pi\pi^*$ state which after 150 fs evolves into the $n\pi^*_{(II)}$ excited state. This finding represents the first ever observed excitation transfer mechanism from the phenyl $\pi\pi^*$ state to the primary amide group $n\pi^*$ state. Thus it is appropriately designated as mechanism II. The average evolution time for the entire ensemble of 25 trajectories is less than 100 fs, but such short lifetime is due to a lot of state character mixing present in a number of initial conditions. Once the trajectories have reached the $n\pi^*_{(II)}$ some of them remained in it for the rest of trajectory propagation time while others resulted in the intersection between the excited and ground electronic state. 17 out of 25 trajectories had reached the intersection with the ground electronic states within the 1.25 ps total trajectory time.

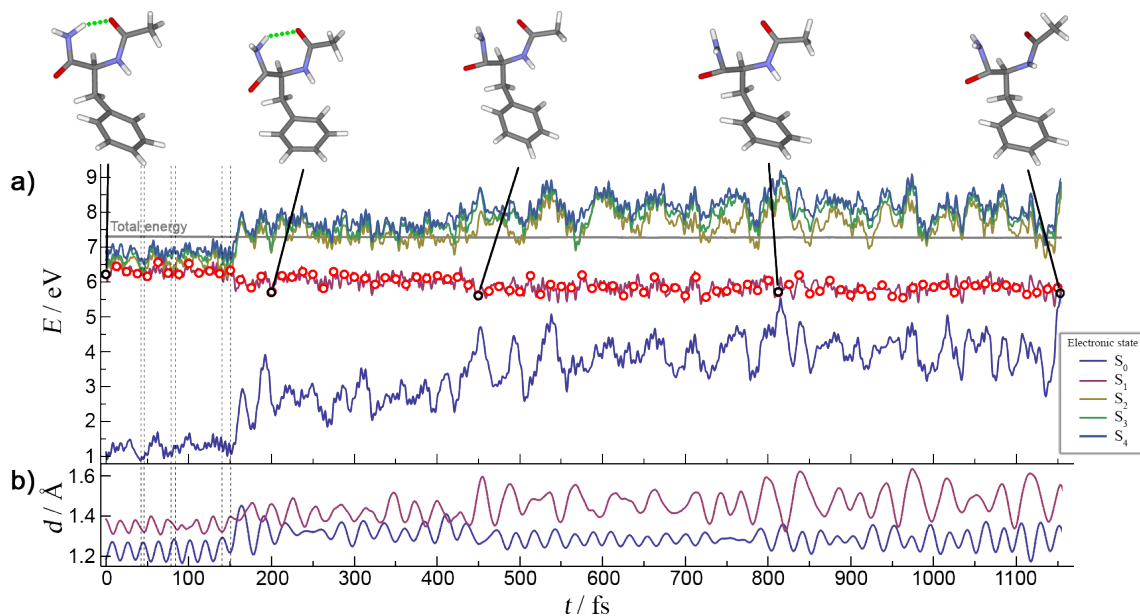


Figure 4.9: a) Time evolution of ground and four lowest excited adiabatic electronic states along the trajectory exhibiting mechanism II. The red circles designate the trajectory's currently occupied state. Inset graphics represent few selected geometries along the trajectory (black circle). Vertical dashed lines indicate the occurrence of trajectory surface hops. The energies are relative to the NAPA conformer B minimum energy. b) The change of $C_{\text{Phe}}=\text{O}$ (blue) and $C_{\text{Phe}}-\text{N}$ (bordeaux) bond lengths along the trajectory.

Figure 4.10 shows the details of the first 200 fs of above trajectory. In this time span, surface hopping between the neighboring S_1 and S_2 states had occurred six times, which can be paired in three separate events of $S_1 \rightarrow S_2 \rightarrow S_1$ type. In the first two the change of states is so rapid that basically the electronic populations just swap between the two adiabatic states. This is also indicated from an instant increase of dynamical coupling between the states. The electronic population and characters of states therefore behave diabatically around these two regions, and after the second interaction region ($t \geq 85$ fs) the system still remains in the initial $\pi\pi^*$ state. The third encounter of strong interaction region, however, exhibits a steadily monotonic increase of dynamical coupling as a consequence of a smooth change of electronic state characters. As electronic density difference graphs shows, the initial $\pi\pi^*$ character acquires a $n\pi^*_{(\text{II})}$ excitation due to the mixing between the two states. This gradual mixing of electronic characters is due to trajectory passing by the S_1/S_2 CI point but through the region in configuration space where the non-adiabatic coupling are smaller than in the previous four cases of close encounters of the PES-s (see the path designated with black line in model 3.1). For comparison, the minimum energy gap between the two states in this considered interaction region is 0.09 eV larger than in the CI encountered at the 42 fs time mark in which the states are separated by a merely 6 meV gap. This is exactly the case represented on the

adiabatic CI model 3.2 which shows how non-adiabatic coupling vectors have the largest influence on electronic populations is close vicinity around CI points. Due to the gradual change of dynamical couplings in this region, the S_1 electronic population display a similar monotonic decrease and the whole transition between states is adiabatic. The characters of S_1 and S_2 states in 145 fs are almost indistinguishable due to equal mixing of adiabatic electronic states. This equal contribution between states is immediately broken in the following few steps, and again the last $S_2 \rightarrow S_1$ surface hop is more diabatic in type, as the more narrower dynamical coupling shows. But this diabaticity of surface hop is necessary to preserve the character of the new state. After the 150 fs mark, the trajectory S_1 state has completely evolved into the $n\pi^*_{(II)}$ character, while all other higher excited states rising abruptly in energy (see Figure 4.9a). The energies of S_2 and higher excited states soon surpass the systems total energy and thus do not influence the dynamics in any way. The effects of the new forces come immediately at their display as the benzene ring C–C bonds are contracted by 0.02 Å, while the $C_{\text{Phe}}=\text{O}$ and $C_{\text{Phe}}-\text{N}$ bonds increase their lengths by 0.18 and 0.12 Å, respectively (Figure 4.9b). At this point the H-bond is still preserved. The system modest gain in kinetic energy of 0.25 eV after the last surface hope is completely channeled into the $C_{\text{Phe}}=\text{O}$ and $C_{\text{Phe}}-\text{N}$ stretching modes, which shortly redistribute their energy into distortion modes. The initial planarity of the second amide group is completely lost due to the breaking of conjugation between C_{Phe} and N atoms. Local groups of both C_{Phe} and N atoms become strongly deplanarized from their initial planes and the O atom moves away from the phenyl ring side. Although these geometrical changes are not strongly manifested on the energetic of S_1 PES the accompanied ground state exhibits a sudden rise in energy by almost 2 eV. At around the 300 fs mark the twisting and waging motions of the NH_2 become so excited that they eventually break the γ_{L} -ring H-bond. The NH_2 group can now almost freely rotate around the $C_{\text{Phe}}-\text{N}$ bond. After the next 100 fs part of the $C_{\text{Phe}}=\text{O}$ vibrational energy is transferred to the $C_{\text{Phe}}-\text{N}$ stretch vibration as can be seen from the alternation of corresponding bond lengths. The global structure of the γ_{L} ring remains even though the two Ramachandran angles strongly fluctuate around their equilibrium values. The combination of backbone strain and heavy distortion of the second amide group contribute to the ground state instability due to which the S_0 PES shows large oscillations and in few occasion the S_1 - S_0 energy gap decreases to less than 0.5 eV. Such is the last point of the trajectory in which excited state calculation is aborted due to numerical instabilities of solutions of Cassida's equation ((3.89) or (3.94)) near the true intersection point. [116] Because TDDFT method cannot describe the S_1/S_0 CI topology properly, the last point of the trajectory is merely taken as indication that a real S_1/S_0 CI point is located nearby. Interestingly, if the non-adiabatic trajectory is recomputed using the same initial conditions of the above

representative trajectory but with BHLYP functional, the system remains in the initial $\pi\pi^*$ state during the whole trajectory propagation time.

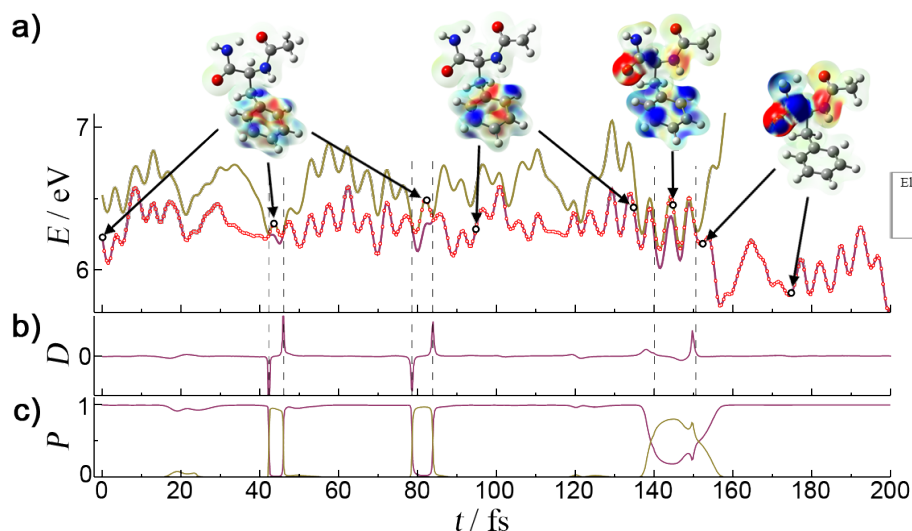


Figure 4.10: Details of the first 200 fs of trajectory displayed in Figure 4.9. a) Close up of S_1 and S_2 adiabatic states. The red circles designate the currently classically occupied state, while the electronic density difference insets designate the state character for a selected trajectory point. Vertical dashed lines indicate the occurrence of trajectory surface hops. The energies are relative to the NAPA conformer B minimum energy. b) Dynamical coupling between S_1 and S_2 adiabatic states scaled to its absolute maximum value. c) Evolution of S_1 and S_2 electronic populations.

Although not performed for this particular case, DFT ground state dynamics simulations were continued from the S_1/S_0 intersection points. They showed (results not displayed) that the most frequent pattern of excess kinetic energy distribution is trough braking of any preserved γ_L -ring structure and the separation of the two amide groups. In some trajectories the amide groups repositioned themselves into the local β_L conformation, and even a full transformation of backbone to β_L secondary structure was observed. Questions of potential light driven conformer isomerization mechanisms wont be addressed further. In the ground state the whole molecule is vibrationally excited. Interestingly, no potential rapture of any covalent bond was observed, meaning that no bond predissociative states were found. While no experiment has up to now examined the NAPA, or similar peptide system, internal vibrational energy redistribution, fragmentation etc. in ground state after an NRD process, no deeper theoretical insight into the ground state processes is attempted further. Also, no experimental insight into the nature of NAPA $n\pi^*$ states has been conducted up to date. Thus without the experimental reference the main focus will remain on the properties of NAPA phenyl $\pi\pi^*$ state.

4.2.2 Mechanism III

11 out of 44 trajectories computed using the PBE0 functional ended in the problematic CT state. As Figure 4.11 clearly shows, after the initial 30 fs the higher S_2 state begins mixing with the S_1 in over a series of CI-s in which the $\pi\pi^*$ state becomes contaminated with a CT from the second C=O group. This character evolves in the next 50 fs to a complete CT state from the backbone to the phenyl ring which then triggers the H atom subtraction from the N_{Phe} atom to the neighboring phenyl *ipso* or *ortho* C atom. The addition of the H atom to the phenyl system completely disrupts the ground state ring conjugation due to which consequently the ground state energy rises abruptly and ends soon in an intersection (abortion) point with the first excited state. Dynamics started from the last point in the ground state showed H atom back transfer to the N_{Phe} atom. The excess kinetic energy initially stored in the excited $N_{\text{Phe}}\text{-H}$ stretch vibration redistributes first to the amide group modes, then to the rest of internal degrees of the molecule. For reasons more apparent later, this mechanism is designated as mechanism III. If the initial conditions of the trajectory in Figure 4.11 are repropagated using the BHLYP functional, a trajectory displaying mechanism II is obtained. Parallely to the publication of these results, Tomasello *et al.* have reported their results on the non-adiabatic molecular dynamics of Tyr in gas and aqueous phase at the PBE0/SVP level of theory. [166] Their simulations of neutral Tyr NRD pathways in gas phase revealed only a single NRD mechanism exhibiting H atom transfer from the NH_2 group to phenol ring, which is simultaneously accompanied with H atom transfer from the COOH to N atom. From their electron density difference plots it can be concluded that this mechanism is completely analogue to mechanism III. The authors, however, made no refinement of their proposed NRD mechanism beyond the used level of theory, but referred to the earlier published CC2

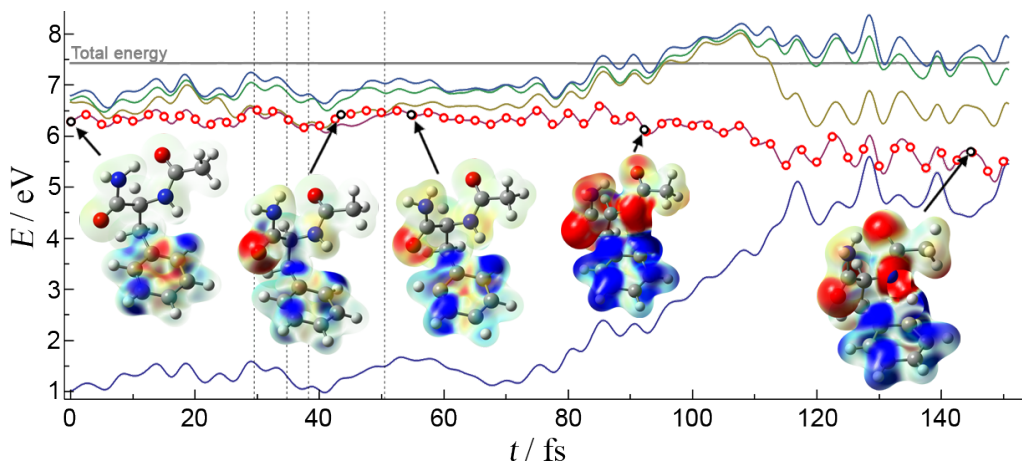


Figure 4.11: Time evolution of ground and four lowest excited adiabatic electronic states along a trajectory exhibiting mechanism III. For details see captions of Figures 4.9 and 4.10.

results on analogue internal H-transfer NRD mechanism in *N*-protonated Tyr. [167]

4.2.3 Mechanism I

Lastly, Figure 4.12 displays a trajectory propagated without utilizing the decoherence correction algorithm and using the current velocity for velocity readjustment direction after a surface hop. The initial S_1 $\pi\pi^*$ state also shows contamination with the CT state involving the second amide C=O group. As in the previous case of mechanism III trajectory the initially contaminated state with CT character evolves within 60 fs into a full CT state displaying electron density transfer from the backbone amide groups to the phenyl ring. Because of different initial nuclear conditions (geometry and velocities) the onset of mechanism III is postponed to a later time (see Figure 4.12), but at a 120 fs mark, a surface hop to S_2 state is exhibited even though the dynamical coupling in this point (and few earlier) is practically zero. This non-physical change of states is caused by the population residue of higher excited states (S_3 and S_4) which has not been attenuated from the first coupling region (50 fs mark), which induce fluctuations of the S_1 through the \mathcal{D}_{13} and \mathcal{D}_{14} dynamical coupling terms. The fluctuation is significant enough for TFS algorithm to interpret it as S_1 depopulation change to completely randomly chosen S_2 state. Because the velocity rescaling is completed along the current velocity direction, no additional prohibition to the surface switch is imposed. The trajectory hops to the S_2 state with an 0.7 eV kinetic energy reduction. This significantly slows the nuclear motion

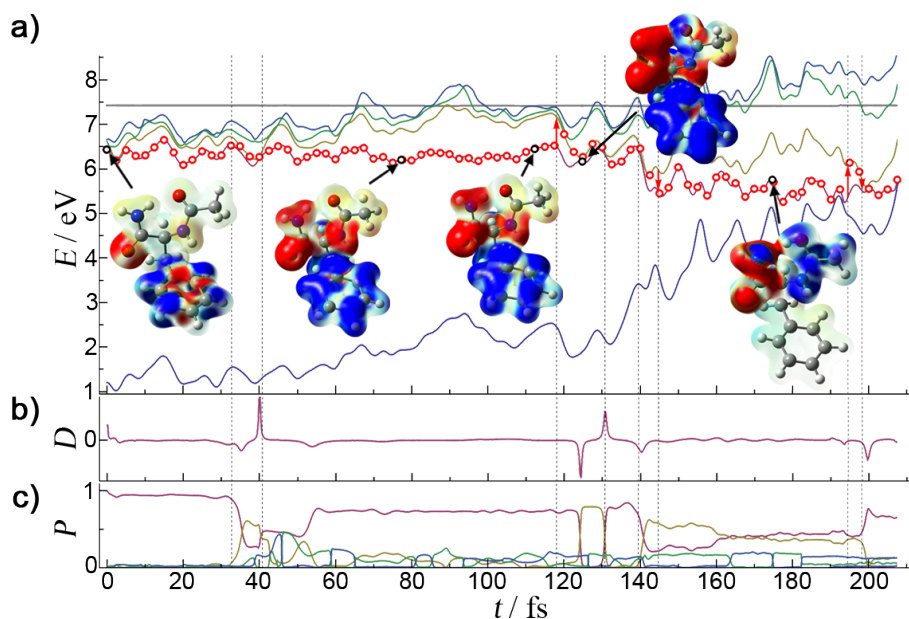


Figure 4.12: Time evolution of ground and four lowest excited adiabatic electronic states along a trajectory exhibiting mechanism I. The red vertical arrows also indicate surface hops. For details see captions of Figures 4.9 and 4.10.

which additionally increases the effects of the new forces on the dynamics. Immediately, the excited state has acquired a new CT to the first amide group contribution to its total character. In the next 50 fs, this state completely evolves into the CT character from the second to the first amide group. The H atom of NH₂ group follows the charge redistribution to the O_{Ac} atom. Needless to say that this nuclear rearrangement destabilizes the ground state and leads to the intersection of the two. The first amide group geometry near the intersection point matches that of NATMA obtained by Shemesh *et al.* [32] This potential NRD mechanism is designated as mechanism I.

Although it can be argued that the use of non-physical trajectories does not guarantee the validity of the obtained mechanisms, nonetheless essential critical CI points were obtained. Also, the non-physical hop at $t = 120$ fs can be viewed as an accelerator of the non-adiabatic dynamics simulations, speeding-up the reach of the system's critical parts of configuration space.

Apart from the three described NRD pathways, no other NRD relaxation pattern appeared among non-adiabatic trajectories. The use of moderate room temperature (298 K) in generating initial conditions assured that NRD pathways with high activation barrier are left out of the simulations. For example the phenyl ring puckering NRD mechanism, which alone requires at least 3000 cm⁻¹ excess energy localized on the phenyl ring, is not observed in any trajectory. The absence of such mechanisms also validates the used level of theory in simulations. Although it may appear that a number of 44 initial conditions is

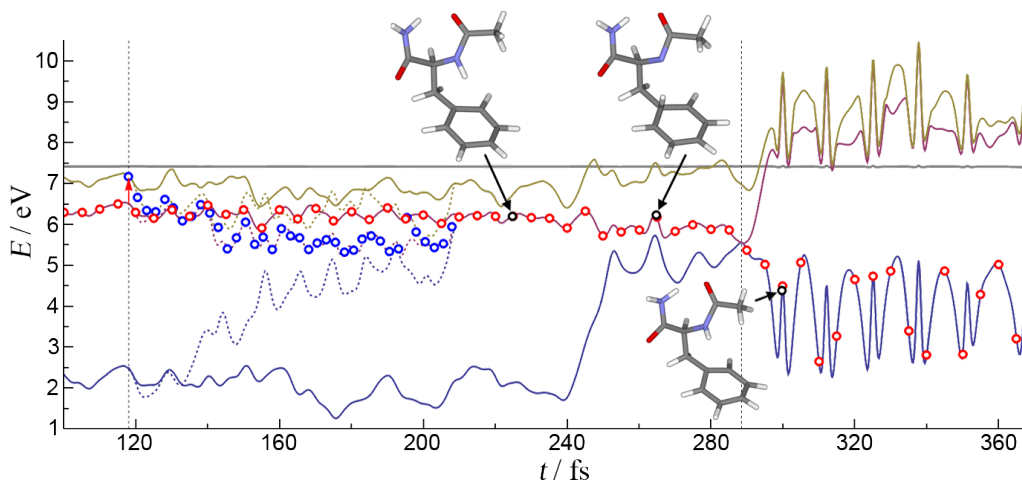


Figure 4.13: The course of trajectory in Figure 4.12 if the non-physical surface hop at 120 fs (red arrow) was prevented. The trajectory deactivates to the ground state over mechanism III displaying H atom transfer to *ipso* C phenyl atom position as shown by inset structures. After the S₁/S₀ intersection the trajectory was propagated in ground state. The S₁/S₀ intersection was reconstructed *a posteriori* using interpolation while excited state calculations do not converge in this region. The dashed lines with blue circles superimposed the time evolution of PES-s from figure 4.12. For details see captions of Figures 4.9 and 4.10.

small, the stochastic nature of the TFS algorithm guarantees that a variety of mechanisms can originate from a single initial condition (see Figure 4.13). However, the major contributions to the problem are the small energy gaps between excited state PES-s and the problematic CT states present in calculations of both used functionals. For this very reason, no attempt was made to simulate real NRD processes in NAPA conformer B, but instead a set of potential NRD mechanisms was obtained, which is now refined at a much higher level of theory.

4.3 Refinement of NRD mechanisms

The non-adiabatic molecular dynamics had revealed three types of $\pi\pi^*$ state NRD deactivation pathways. Designated as NRD pathway I, II and III they exhibit excitation transfer from the phenyl $\pi\pi^*$ state to the $n\pi_1^*$, $n\pi_{II}^*$ and CT excited states, respectively, through corresponding CI-s. The latter excited states then evolve and end-up in the CI-s with the ground state, transforming all absorbed light energy into nuclear vibrations. For each NRD pathway the non-adiabatic trajectories have indicated whole series of CI structures, motions, excited state plateaus where excited state populations reside etc. These are all refined through constructions of corresponding reaction paths and CI-s at the RI-CC2/cc-pVDZ level for all three conformers of NAPA and NAPMA. All refinement procedures will be explicitly demonstrated on NAPA conformer B.

4.3.1 Refinement of mechanism III

For start mechanism III is examined first because of a series of implications originating from it. Because CT states are seriously underestimated at the TDDFT level of theory, mechanism III which stems from population transfer to CT state may be a complete artifact of the used method. Therefore it is necessary to reexamine this potential NRD mechanism at a more accurate CC2 level.

Trajectories undergoing mechanism III suggest that the access to CT state can be triggered by stretching of the $N_{\text{Phe}}\text{-H}$ bond in the direction of the phenyl ring. Thus constrained optimizations of the first excited state for a series of fixed $N_{\text{Phe}}\text{H}$ distances were performed starting from the minimum of the initial $\pi\pi^*$ state, designated from now as $M_{\pi\pi^*}$. Figure 4.14 shows PES-s of ground and five lowest excited states plotted against the increasing $N_{\text{Phe}}\text{H}$ distance. Up to ~ 1.17 Å the force between N_{Phe} and H atoms is attractive in S_1 and S_0 states, but already the destabilization of S_5 state, which is of CT character, can be observed. Extending the $N_{\text{Phe}}\text{H}$ distance beyond 1.2 Å the force between N_{Phe} and H becomes repulsive, while it becomes attractive between H and *ortho* C atom. At this point the constrained geometry is heavily perturbed. The

deplanarization of the *ortho* position and the near vicinity of intruding H atom disrupt the ground state phenyl ring π conjugation and cause a large increase of ground state energy. The S_1 state character has completely changed to CT character at this point, while the S_2 state is now of $\pi\pi^*$ character. Any further constrained optimization started from this point through increasing the $N_{\text{Phe}}\text{H}$ distances lowers the S_1 and increases the S_0 state energies. To save the effort, a full S_1 excited state optimization was started from the last constrained point, and immediately led the S_1 state into a crossing with the ground state. Because CC2 is a single reference method, the intersection point is not the exact CI point, but is taken as its best guess. The constrained scan however failed to reproduce a unique interchange between the attractive and repulsive part of S_1 PES, and gives a discontinuous change of states instead. To resolve this issue a LIP was constructed between two close isoenergetic geometries of $\pi\pi^*$ and CT characters on the S_1 PES. A double avoided curve shape exhibiting a gradual change of electronic character was obtained, which is a typical cat through configuration space near the CI point (see model in Figure 3.1b) indicating the presence of a nearby true CI point. The LIP obtained barrier maximum is 0.48 eV above the $M_{\pi\pi^*}$. A transition state (TS) was constructed starting from the LIP maximum as its best guess structure and also with a complete Hessian matrix calculated at the same level of theory at the same starting geometry. The obtained TS is 0.39 eV above the S_1 minimum and features a $N_{\text{Phe}}\text{H}$ bond length of 1.187 Å. The TS structure appears to be more of a $\pi\pi^*$ than CT character, while the energy gap from S_2 state is 0.63 eV. Using the energy difference constrained optimization procedure of Levine *et al.* [152] and the TS or LIP maximum structures as the starting guess geometry, a MECI was constructed for this CI seam. Unlike the avoided crossing, the LIP from $M_{\pi\pi^*}$ through MECI exhibits a clear exchange of electronic state characters (Figure 4.14). Although the MECI structure lays 0.76 eV above the $M_{\pi\pi^*}$ minimum, the 0.39 eV S_1 TS represents the best barrier estimate for the proposed NRD mechanism. Only LIP based barriers of 0.55 and 0.64 eV were estimated for mechanism III in NAPA conformers A and C, respectively (see Figure 4.15), while expensive Hessian calculations were avoided. These values, including the NAPA conformer B TS, are greater than the experimental reference 3000 cm^{-1} (0.37 eV) barrier for the ring puckering mechanism in benzene. However, the participation of the light H atom with such a large amplitude motion in the proposed NRD mechanism can indicate a potential tunneling through the barrier. Also the excited state lifetime in NAPA conformer B appears consistent with the 2 ± 1 ns lifetime of excited vibrationless phenol S_1 state, [168] which was shown to undergo NRD mechanism including tunneling under a CI with a barrier of similar height as in NAPA conformers. [61] Thus strong indication towards the possible activity of mechanism III in NAPA conformer B existed. It was these conclusion

based on preliminary results of non-adiabatic dynamics simulations that stimulated the experimental measurements of NAPA isotopologue excited state lifetimes. Showing no significant deuterium isotope effect on the prolongation of excited state lifetime in any NAPA conformer (Table 2.1), it was finally concluded that mechanism III is not active in the vibrationless $\pi\pi^*$ state of NAPA molecules. The experimental results also eliminate the need for a more accurate computational re-examination of mechanism III potential tunneling effect. The experiment confirms that the RI-CC2/cc-pVDZ level is in energetic sense accurate enough to predict the infeasibility of mechanism III, albeit the potential mechanism could not be totally discarded just on electronic facts without including the vibrational states. All observations confirm that mechanism III is an artifact of TDDFT methods and therefore wont be considered further.

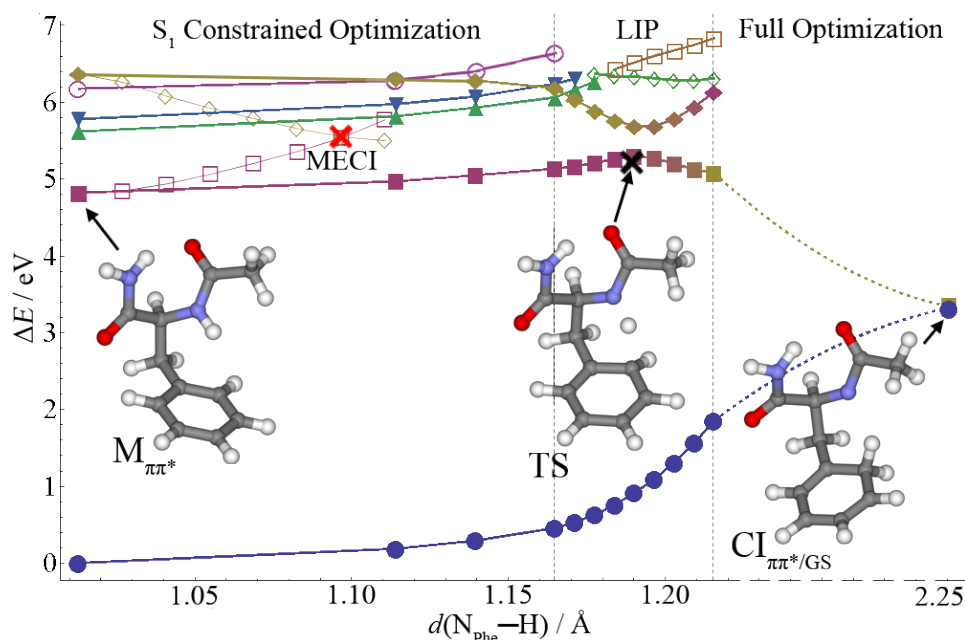


Figure 4.14: Relative RI-CC2/cc-pVDZ energies of the ground and the four lowest excited states (ΔE) against the $N_{\text{Phe}}\text{-H}$ distance ($d(N_{\text{Phe}}\text{-H})$) for the H transfer from the $N_{\text{Phe}}\text{H}$ group to the *ortho* C atom of the phenyl ring in the NAPA conformer B. Vertical delineators indicate different computational strategies: regions of optimizations at fixed $N_{\text{Phe}}\text{-H}$ distances (left), single point calculations on the linearly interpolated path (LIP, middle) and full optimizations (right). The ground state (blue circles), the initial $\pi\pi^*$ state (bordeaux squares), and the CT state (gold diamonds) are shown together with higher-lying electronic states. The insets show the three critical structures: $M_{\pi\pi^*}$ minimum (left), S_1 barrier maximum (middle) and S_1/S_0 intersection point (right). The black cross marks the optimized TS structure. The red cross marks the position of the MECI point between the $\pi\pi^*$ and CT states in terms of $N_{\text{Phe}}\text{-H}$ bond length, where the LIP connecting it with $M_{\pi\pi^*}$ structure (open squares and diamonds) show the clear change of PES characters.

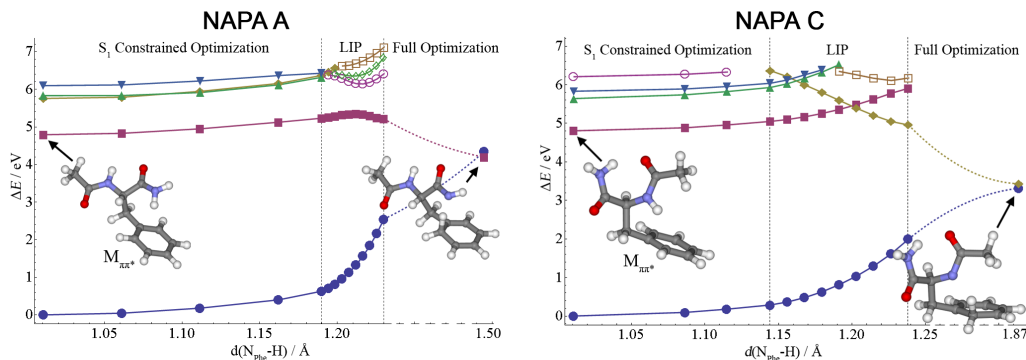


Figure 4.15: Mechanism III reproduced for NAPA conformers A (left) and C (right). For details see caption of Figure 4.14. NAPA conformer A displays no character change in the LIP range of reaction path, while conformer C encounters a CI between the $\pi\pi^*$ and CT states.

4.3.2 Refinement of mechanism I

All non-adiabatic dynamics trajectories undergoing NRD relaxation through mechanism I exhibit a distortion of the first amide group after which H-transfer from NH_2 to O_{Ac} drives the system into the ground electronic state. These results represent the first-ever full atom non-adiabatic simulation of the earlier proposed NRD mechanism by Shemesh and collaborators. [30–32, 62] In order to apply their relaxation mechanism on NAPA and NAPMA molecules, the first amide groups in conformers B and C were distorted in a way to match the distorted amide group geometry of NATMA conformer C in the LE state. [32] Geometrical optimizations performed in S_1 state delivered the corresponding $n\pi^*_{(1)}$ state minima in NAPA and NAPMA conformers B and C which are structurally completely analog to NATMA C LE geometry. From now these local $n\pi^*_{(1)}$ PES minima are designated as M_{Ia} . Because the additional methyl group in NAPMA second amide group does not significantly perturb the electronic structure of the first amide group the upcoming conclusions were all constructed on NAPA conformers (particularly conformer B) and can be easily generalized on NAPMA conformers.

The energies of M_{Ia} structures lay well below the $M_{\pi\pi^*}$ corresponding minimum energy (Table 4.4). CI of $n\pi^*_{(1)}$ with the $\pi\pi^*$ state were estimated from LIP-s constructed between $M_{\pi\pi^*}$ and M_{Ia} minima. The CI energies which act as barriers for excitation transfer between the two states are also listed in Table 4.4. Due to the absence of γ_{L} -ring H-bond no corresponding M_{Ia} structure exists in conformer A. From Table 4.4 it is evident that no significant differences between NAPA and NAPMA CI-s exist.

Using the $\text{N}_{(11)}-\text{H}$ bond length as the driving coordinate a minimum energy path was constructed on $n\pi^*_{(1)}$ PES from the M_{Ia} structure towards the intersection with the ground electronic state (Figure 4.16). Contrary to NATMA conformer C case, no additional CI of $n\pi^*_{(1)}$ with the CT state between amide groups was found on the minimum energy

Table 4.4: Relative energies of local NAPA and NAPMA conformers M_I type minima on the $n\pi^*_{(I)}$ state PES relative to their corresponding $M_{\pi\pi^*}$ minima structures. The $\pi\pi^*/n\pi^*_{(I)}$ CI points were constructed from LIP-s between $M_{\pi\pi^*}$ and corresponding M_I minimum. All values are in eV.

NAPA										
	Ia		Ib		Ic		Id		Ie	
	CI	M_{Ia}	CI	M_{Ib}	CI	M_{Ic}	CI	M_{Id}	CI	M_{Ie}
A	–	–	0.25	–0.65	–	–	–	–	–	–
B	0.36	–0.78	0.26	–0.69	0.23	–0.72	0.77	–0.58	0.32	–0.68
C	0.51	–0.73	0.32	–0.69	0.30	–0.66	0.43	–0.66	0.39	–0.64
NAPMA										
	Ia		Ib		Ic		Id		Ie	
	CI	M_{Ia}	CI	M_{Ib}	CI	M_{Ic}	CI	M_{Id}	CI	M_{Ie}
A	–	–	0.28	–0.63	–	–	–	–	–	–
B	0.37	–0.79	0.26	–0.71	0.24	–0.71	0.74	–0.58	0.32	–0.69
C	0.47	–0.74	0.32	–0.69	0.32	–0.67	0.43	–0.66	0.39	–0.65

path. Instead, a critical region where forces between $N_{(II)}$ and H atoms changes from attractive to repulsive is bypassed with a LIP from which a barrier for H atom transfer reaction could be estimated. For NAPA conformers B and C these barriers are 0.15 and 0.25 eV, respectively, above the M_{Ia} . The at least 0.7 eV energy gain obtained by reaching the M_{Ia} structure appears sufficient to overcome the small barriers for the H-transfer process. For this reason H-transfer was not considered in NAPMA conformers. However, the question of internal energy redistribution among vibrational states is left unanswered while a dynamical insight is necessary. Thus it is difficult using the above approach to conclude exactly how H-transfer is triggered once and if the system reaches the $n\pi^*_{(I)}$ state. Unfortunately, the $n\pi^*_{(I)}$ state is severely contaminated with CT at the PBE0/cc-pVDZ level of theory, thus no M_{Ia} minimum could be obtained at the same level. Instead, optimizations end-up with H-transfer to O_{Ac} , which explains why all non-adiabatic trajectories exhibiting mechanism I show the same pattern of deactivation. This is another example of PBE0 failure for the system at hand due to CT description problem. On the other hand, BHLYP functional reproduces the exact M_{Ia} minimum, but at the same time its does not give any non-adiabatic trajectory exhibiting mechanism I. Thus the use of both functional, due to their own reasons, disallows the use of non-adiabatic simulations for examination of vibrational energy redistribution in mechanism I.

Interestingly, Shemesh *et al.* did not considered the 0.1 Å prolongation of $C_{Ac}=O$ bond length nor the results of formamide $n\pi^*$ state deactivation from which it is known that C=O and C–N bonds extension should also drive the system towards the S_1/S_0 CI. [57,58]

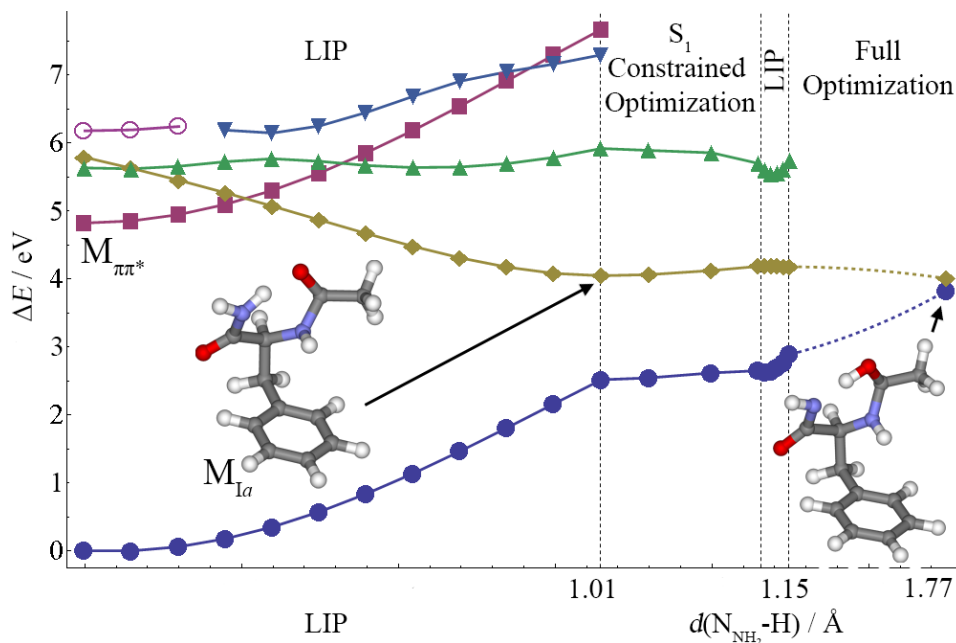


Figure 4.16: Energy profile for the mechanism I over the M_{Ia} minimum region of configuration space. See Figure 4.14 caption for more details. The leftmost part of the plot represents a LIP between $M_{\pi\pi^*}$ and M_{Ia} minima for which the corresponding horizontal axis only represents a fraction of the two structures.

Therefore, minimum reaction paths with $C_{Ac}=O$ bond lengths as the driving coordinates were constructed from M_{Ia} geometry, which shown even an earlier CI with the ground state. Also, in the course of $C_{Ac}=O$ bond extension the H atom gets subtracted from NH_2 group by the neighbouring O atom. This also sound as a more probable mechanism for triggering H-transfer process, while the excess energy is initially stored in the first amide group after the $\pi\pi^*/n\pi^*_{(1)}$ CI. Although no other types of $n\pi^*_{(1)}$ minimum structures than M_{Ia} were observed from non-adiabatic trajectories, it was reasoned that similar geometries but with differently deplanarized C and N regions of the first amide group should exist on the $n\pi^*_{(1)}$ PES. A variety of structures were located, where in one the γ_L -turn is totally disrupted due to large distortions of the first amid group. Designated as M_{Ie} , it is shown in Figure 4.17 together with the three other new local S_1 minima, which include two new structures, M_{Ib} and M_{Ic} , and an analogue of M_{Ia} , designated as M_{Id} , which is different from the former in the direction of C_{Ac} atom pyramidalization. Table 4.5 compares the most relevant bond lengths among the $n\pi^*_{(1)}$ local minima in NAPA conformer B. Apart from ways in which the first amide group is distorted, the newly obtained local M_{Ib} , M_{Ic} and M_{Ie} minima differ from the M_{Ia} and M_{Id} in $C_{Ac}=O$ and $C_{Ac}-N$ bond lengths, where the former set has a significantly extended $C_{Ac}=O$ bond, while the latter the $C_{Ac}-N$ bond. This is due to slightly different character of $n\pi^*_{(1)}$ state in the latter two structures. Density difference analysis reveals that in M_{Ia} structure the N_{Phe} n orbital electrons contribute

mostly to the population of $\pi_{C=O}^*$ orbital, where the role of γ_L -ring H-bond is probably to stabilize this structure, since the M_{Ia} minimum is more stable than the other structures (Table 4.4). The M_{Id} is of identical character, but less stable because the acetyl methyl group has been repositioned above the phenyl ring. The characters of M_{Ib} , M_{Ic} and M_{Ie} structures are analogue to the character of $n\pi_{(I)}^*$ state in vertical geometry (see Figure 4.5), where most of the electron density is drained from the O_{Ac} n orbital into the $\pi_{C=O}^*$. From LIP constructed between M_{Ia} and M_{Ib} (M_{Ic}) minima a smooth barrier of 0.77 (0.22) eV is obtained on a single S_1 PES which exhibits a gradual change of contributing orbitals to the total $n\pi_{(I)}^*$ excitation.

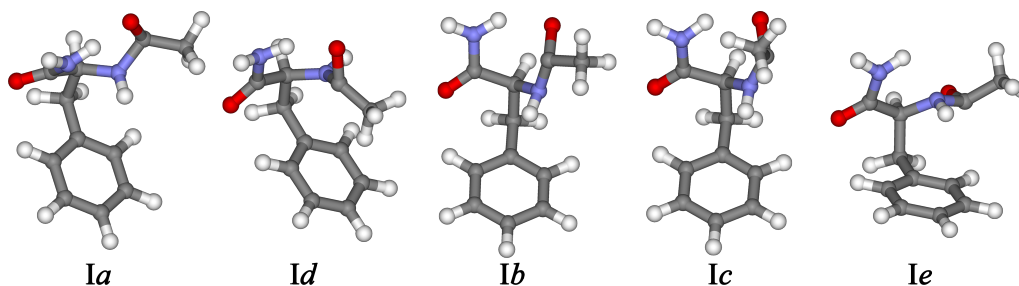


Figure 4.17: Five local M_I type minima on the $n\pi_{(I)}^*$ PES of NAPA conformer B.

Table 4.5: Lengths of the most representative bonds in the first amide group for the five M_I NAPA conformer B type minima displayed in Figure 4.17. NAPA conformer B $M_{\pi\pi^*}$ corresponding values are given for comparison. All values are in Å.

	$C_{Ac}=O$	$C_{Ac}-N$	$N_{(II)}-O_{Ac}$	$H_{(II)}-O_{Ac}$
$M_{\pi\pi^*}$	1.247	1.365	2.859	1.946
M_{Ia}	1.344	1.465	2.783	1.828
M_{Ib}	1.505	1.392	2.810	1.923
M_{Ic}	1.510	1.379	2.846	1.940
M_{Id}	1.362	1.428	2.739	1.785
M_{Ie}	1.469	1.400	—	—

Based on electronic contributions of the S_1 excited state, it is evident that motions which further disrupt the electronic structure of the ground state will lead the system into the S_1/S_0 CI-s. These motions are the $C_{Ac}=O$ and $C_{Ac}-N$ bond extensions or any combined motion that leads to the prolongation of two former bonds, e.g., like bending the $N_{Phe}-C_{Ac}-O$ angle under 90° . However, $C_{Ac}=O$ bond extension represents the most convenient way to reach the CI with the ground state (example in Figure 4.18), which lays ~ 0.1 eV above the corresponding M_I minimum. Again the details of intersection between S_1 and S_0 are obscured with single reference CC2 method. However, the kinetic energy gained by the system from descending down the slope of S_1 PES towards some M_I minimum

seems sufficient enough to eject the singlet O atom by homolytic C=O bond dissociation, especially since the slope is mostly defined by the negative gradient for C=O bond extension. This force excites the C=O bond stretch motion to large amplitude oscillations immediately after the $\pi\pi^*/n\pi^*_{(I)}$ CI, due to which the C=O bond has increased probability of reaching the critical CI seam with the ground state. The presence of γ_L -ring seems irrelevant for the activity of mechanism I, and classifies the proposed NRD mechanism of Shemesh and collaborators merely as one possible pathway for reaching the ground electronic state. Nonetheless, it shows how the H-transfer process could effectively hinder the reactive O atom ejection.

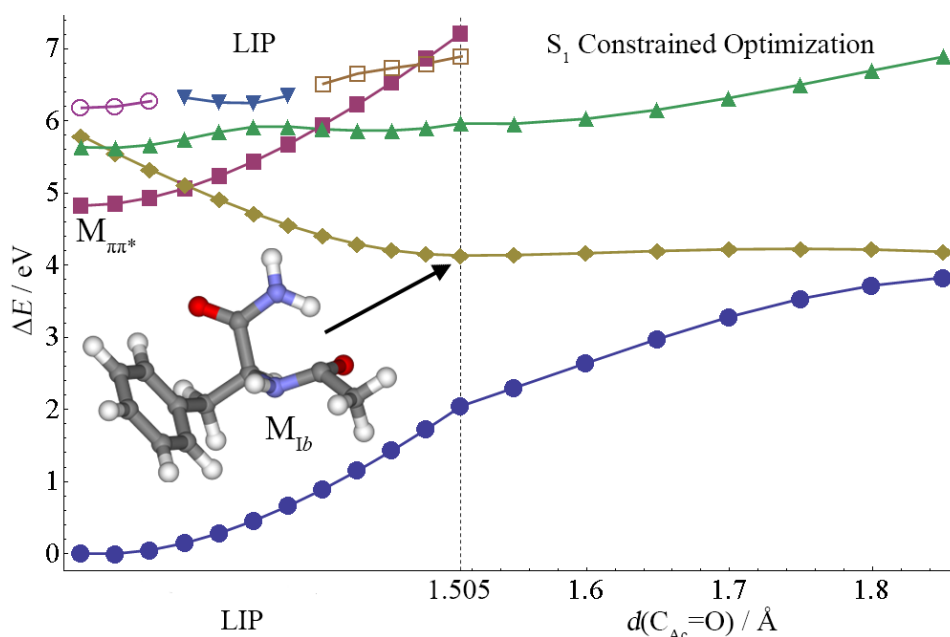


Figure 4.18: Energy profile for the mechanism I over the M_{Ib} minimum region of configuration space. See Figure 4.16 caption for more details.

However, the answer to the very process of excitation transfer from $\pi\pi^*$ to $n\pi^*_{(I)}$ state remains unanswered. Table 4.4 points that the smallest barriers are among pathways which access the configuration space regions towards M_{Ib} and M_{Ic} minima structures. This is in accordance with smaller geometrical rearrangements the $M_{\pi\pi^*}$ minimum first amide group has to undergo to access the $\pi\pi^*/n\pi^*_{(I)}$ CI seam. All CI points listed in Table 4.4 are part of the same CI seam. It should be noted that their structures and energies are approximated from LIP, which generally can only overestimate the barrier. Also, based on the shapes of PES represented in Figure 4.14 one can ask whether the system really needs to cross through the CI or pass near it over an avoided crossing of maybe lower energy. From geometrical comparison of equivalent atom positions and other structural parameters no significant difference can be found between NAPA and NAPMA conformers CI-s of mechanism I, while energies between corresponding pairs are virtually

the same. Also, no significant differences in frequencies or normal modes related to the first amide group or phenyl ring can be observed between NAPA and NAPMA conformers $M_{\pi\pi^*}$ structures. The absence of any significant difference between NAPA and NAPMA first amide group imposes a logical conclusion that mechanism I cannot be responsible for the observed lifetime difference between NAPA and NAPMA conformer B. Therefore, the focus is now only on the CI seam of mechanism II.

4.4 Refinement of mechanism II

Mechanism II is analogous to mechanism I. It involves excitation transfer from $\pi\pi^*$ phenyl state to $n\pi^*_{(\text{II})}$ state localized on the second amide group, after which the $n\pi^*_{(\text{II})}$ state de-populates to the ground electronic state. The excited second amide group can be modeled as $n\pi^*$ excited acetamide for which Eckert-Maksić and co-workers have recently found a variety of potential deactivation mechanism to the ground state. [169] However the energy gain in NAPA (NAPMA) systems from reaching the $n\pi^*_{(\text{II})}$ state from starting $M_{\pi\pi^*}$ structure (see later) is only half the energy gain of acetamide relaxation from vertical excitation geometry due to which only deactivation channels with low activation barrier are expected to be involved in NAPA (NAPMA) $n\pi^*_{(\text{II})}$ state NRD processes. For acetamide these are the C–N dissociation and the O=C–N angle bend NRD pathways whose corresponding CI-s structures with the ground state were observed among the deactivating non-adiabatic trajectories. The TDDFT method favors the latter pathways, while the refined pathways at the RI-CC2 level, as in case of mechanism I, show that the $C_{\text{Phe}}=\text{O}$ stretching has the most easily accessible CI with the S_0 state. Trajectories and CC2 pathways after the intersection with the ground state were not continued because of a failure of both methods to accurately describe the S_1/S_0 CI and because the restricted densities/wave function are inadequate for the description of homolytic bond cleavage. Depending on the amount of vibrational energy concentrated in each bond and the IVR processes dissipating it, the dissociation pathways may or may not be active in second amide group after the population passes through the CI with the ground electronic state.

The focus here is exclusively on the first part of mechanism II, i.e., the population transfer from $\pi\pi^*$ to $n\pi^*_{(\text{II})}$ state through the corresponding CI seam and especially the differences between NAPA and NAPMA conformers B $\pi\pi^*/n\pi^*_{(\text{II})}$ CI seams, because only by addressing the latter can the experimental huge discrepancy between NAPA and NAPMA conformer B $\pi\pi^*$ excited state lifetimes be fully explained. Therefore, it is absolutely necessary to get an insight into the $\pi\pi^*/n\pi^*_{(\text{II})}$ CI seam. For start, local minima on the $n\pi^*_{(\text{II})}$ PES-s of NAPA and NAPMA conformer B are screened in order to construct the initial CI points of the $\pi\pi^*/n\pi^*_{(\text{II})}$ CI seams using the outlined LIP procedure for mechanism I. It should be noted that from now on only NAPA and NAPMA conformers B are considered,

while the mechanisms in other conformers will be reconstructed later from findings in the previous two.

4.4.1 Local minimum structures of $n\pi^*_{(\text{II})}$ state

Because $n\pi^*_{(\text{II})}$ state is completely analogous to $n\pi^*_{(\text{I})}$ state, it also possesses local minima on the $n\pi^*_{(\text{II})}$ PES. The latter are designated as M_{II} structures. Already non-adiabatic dynamics trajectories exhibiting mechanism II had shown that after the population transfer to $n\pi^*_{(\text{II})}$ state trajectories reside on the $n\pi^*_{(\text{II})}$ PES until reaching the intersection with the ground state. Some of them reside in the new S_1 state for the entire dynamics run time. This is due to the presence of stable minimum structures on the $n\pi^*_{(\text{II})}$ PES as confirmed with S_1 state optimizations at the TDDFT level started from few selected points along the trajectory. Unlike mechanism I and mechanism III, the $n\pi^*_{(\text{II})}$ state suffers less contamination with CT character when PBE0 functional is in use. Although these S_1 minima plateaus can be used to extract the initial geometries for RI-CC2/cc-pVDZ optimizations, it is far simpler to systematically scan the torsional angles defining the second amide group in search of $n\pi^*_{(\text{II})}$ minimum structures. Figure 4.19 shows the definition of the three torsional angles, ϑ_C , ϑ_N and ω_2 , which are also used for classification of obtained minimum structures.

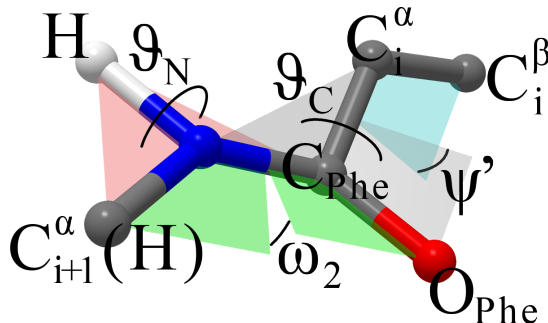


Figure 4.19: Pyramidalization of the second amide group and definition of the torsional angles ϑ_C , ϑ_N , ω_2 and ψ' .

Six minima with a preserved γ_L secondary structure motive were obtained, and were immediately categorized in two set of structures based on the pyramidalization direction of C_{Phe} group which is defined with the ϑ_C angle. The ϑ_C angle basically determines the direction in which the $C_{\text{Phe}}=O$ bond moves outside the initial plane of $M_{\pi\pi^*}$ structure, where negative values indicate that the O_{Phe} atom moves away from the phenyl ring side, while positive towards the phenyl ring. For convenience, structures with negative and positive ϑ_C angle values are designated as M_a and M_b , respectively, while numerical notations 1, 2, and 3 are used for structures within the set. Table 4.6 lists relative energies and the five most important geometrical parameters defining the significant changes within

the second amide group of $M_{(II)}$ structures in NAPA and NAPMA conformer B, respectively. Within each set, geometries distinguished themselves mostly in the direction the amine group is distorted and whether H-bond is preserved within the γ_L -ring or not. The NH_2 and $NHCH_3$ groups, respectively, were shown to pyramidalize in directions parallel or opposite to C_{Phe} distortion, while the N–H (N– CH_3) bonds can assume directions in which they eclipse or not the neighboring $C_{Phe}=O$ and $C_{Phe}-C_\alpha$ bonds. The span of ω_2 angle which defines the positions of N–H (N– CH_3) bond is however limited in minimum structures due to the non-bonding interaction with the neighboring $C_{Phe}=O$ and $C_{Phe}-C_\alpha$ bonds and due to the H-bond which can fix the proximal H atom position. For this reason only three minimum structures exist in M_a and M_b sets, respectively.

Table 4.6: Relative energies (ΔE) of M_{II} minimum structures to corresponding $M_{\pi\pi^*}$ structures for NAPA and NAPMA B conformers and five most distinctive geometrical parameters (three torsional angles ϑ_C , ϑ_N and ω_2 ; and $C_{Phe}=O$ and $C_{Phe}-N$ bond lengths) characterizing the significant deviations of the second amide group. Corresponding $M_{\pi\pi^*}$ minima parameters are given for comparison. Energies are in eV, angles in degrees, while bond lengths in Å.

	NAPA B M_{II}						NAPMA B M_{II}					
	ΔE	ϑ_C	ϑ_N	ω_2	$d_{C=O}$	d_{C-N}	ΔE	ϑ_C	ϑ_N	ω_2	$d_{C=O}$	d_{N-C}
$M_{\pi\pi^*}$	0.00	-178.7	-159.4	-6.9	1.239	1.363	0.00	-178.3	-178.5	1.6	1.243	1.362
$a1$	-0.71	-127.6	-122.3	33.2	1.378	1.437	-0.72	-121.8	-147.8	61.7	1.329	1.476
$a2$	-0.69	-131.5	-124.9	-1.6	1.450	1.400	-0.63	-130.7	-139.5	-7.1	1.479	1.387
$a3$	-0.64	-128.2	130.7	56.9	1.464	1.392	-0.62	-128.4	140.2	50.0	1.476	1.387
$b1$	-0.73	125.4	120.7	-36.8	1.368	1.448	-0.74	121.4	143.4	-61.7	1.328	1.482
$b2$	-0.72	129.9	125.7	3.5	1.451	1.400	-0.68	128.2	140.9	9.2	1.477	1.390
$b3$	-0.69	125.6	-127.4	-44.9	1.464	1.400	-0.67	125.7	-139.2	-41.5	1.475	1.392

Correlations between relative M_{II} minimum energies and their structures can be traced to the relative position of the bonds in the amino and the neighbouring carbonyl groups within the second amide group. When all bonds eclipse each other between the two groups (structure 3) the corresponding energy is higher than in geometries 1 and 2 where bonds are less mutually eclipsed. Also, one can observed that structures $a1$ and $b1$, which are the least eclipsed geometries, have a slightly different trend with respect to the $C_{Phe}=O$ and $C_{Phe}-N$ bond lengths. Instead of a systematic $M_{\pi\pi^*}$ $C_{Phe}=O$ bond length increase by 0.21 and 0.23 Å in NAPA and NAPMA M_{II} 2 and 3 minimum structures, respectively, structures 1 compensate the lesser increase of $C_{Phe}=O$ bond lengths with larger increase of $C_{Phe}-N$ bonds. For structures $a1$ and $b1$ the $M_{\pi\pi^*}$ minimum $C_{Phe}-N$ bonds extend by additional 0.08 and 0.12 Å in NAPA and NAPMA, respectively, compared to 0.04 Å increase in other structures. The origin of this discrepancy was found from population analysis which shows that in addition to O_{Phe} atom negative charge reduction, N atom also undergoes electron density depletion in M_{a1} and M_{b3} structures. Locally, the second

amide group minimum structures resemble the $n\pi^*$ minima of acetamide. [169] The most stable $a1$ and $b1$ geometries are completely analogue to the most stable acetamide S_1 minimum obtained at the CASSCF(10,8)/6-31G(d) and MR-CISD/6-31G(d) levels. $a3$ and $b3$ structures are analogue to the next higher acetamide minimum. $a2$ and $b2$ geometries do not have the acetamide counterpart, as the third acetamide minimum has no analog structure in NAPA and NAPMA. Although bond length values differ between single and multireference methods, the trend between $C_{\text{Phe}}=\text{O}$ and $C_{\text{Phe}}-\text{N}$ bond lengths in 1, 2 and 3 minimum types is also exhibited in acetamide minima at the MR-CISD level. This similarity between different molecules further validates the RI-CC2 method.

$C_{\text{Phe}}=\text{O}$ and $C_{\text{Phe}}-\text{N}$ bonds of the pyramidalized C_{Phe} atom position themselves to the best staggered position relative to neighboring $C_{\alpha}-C_{\beta}$, $C_{\alpha}-\text{N}_{\text{Phe}}$ and $C_{\alpha}-\text{H}$ bonds in order to minimize the mutual repulsions. Generally, from the torsional angles the local second amide M_a and M_b structures appear as mirror images of each other. In M_b structures the $C_{\text{Phe}}=\text{O}$ bonds positioned their O atoms above the phenyl ring. This causes a small rotation of the phenyl ring around the $C_{\beta}-C_{\text{ipso}}$ bond necessary to accommodate the O atom. Also, the populated $\pi_{\text{C}=\text{O}}^*$ orbital increases the electronic density on the O atom just in the direction of line connecting O atom with the H atom of the neighboring $\text{N}_{\text{Phe}}-\text{H}$ bond. Due to this enhanced electrostatic interaction, which geometrically appears very similar to the interaction within the five-membered ring of $\beta_{\text{L}}(a)$ backbone, the first amide group exhibits a small change of its Ψ angle.

Table 4.6 clearly shows the differences between NAPA and NAPMA M_{II} structures. Apart from the second amide group where almost all discrepancies lay, the rest of geometrical difference between NAPA and NAPMA structures are insignificant. If the NH_2 and NHCH_3 groups, or just the distal H and CH_3 groups on N atom, are omitted from NAPA and NAPMA corresponding pairs, the remaining geometries are practically identical copies of each other (root-mean square deviations between geometries are in order of 0.01–0.08 Å, slightly larger for M_b type minima).

Regarding the second amide groups of NAPA and NAPMA M_{II} structures various variation of geometrical parameters can be observed. The pyramidalization angle ϑ_{C} has the smallest variation between NAPA and NAPMA pairs, reflecting the fact that the additional methyl group has no significant influence on the deplanarization of the C_{Phe} atom. However, the methyl group strongly influences the other four remaining geometrical parameters, whose variations are particularly exhibited within the $a1$ and $b1$ pair structures between NAPA and NAPMA. These structures show a reverse of observable trend that in NAPMA M_{II} structures $C_{\text{Phe}}=\text{O}$ and $C_{\text{Phe}}-\text{N}$ bond lengths are slightly longer than the corresponding NAPA bonds. This is due to the depletion of electronic charge only from the N atom of methylated amino group in NAPMA as population analysis reveals,

where as in NAPA the O_{Phe} atom also undergoes substantial reduction of electron charge density. The extensive prolongation of the $C_{\text{Phe}}\text{-N}$ bond is also accompanied by a larger torsion of the ω_2 angle in *a1* and *b1* NAPMA structures. In the other four remaining minimum structures only O_{Phe} atoms undergo charge depletion on account of C_{Phe} atom density increase. The slightly longer $C_{\text{Phe}}\text{=O}$ bond lengths in the latter NAPMA M_{II} minima is due to increase repulsion between $C_{\text{Phe}}\text{=O}$ and the methyl groups. The distal H atom cannot induce such significant repulsion in NAPA system.

Lastly, geometrical differences between M_{II} minima and the starting $M_{\pi\pi^*}$ structures are, as expected, large and exhibited through the entire structure. The repositioning of the $C_{\text{Phe}}\text{=O}$ bond in M_{II} minima opens space in which the phenyl ring shifts around the $C_{\alpha}\text{-C}_{\beta}$ bond due to its non-bonding interactions with the backbone. Depending on how the NH_2 (NHCH_3) group is rotated, the γ_{L} -ring H-bond can be preserved or not. Except for structure *b1* in all other structures the H-bond length has increased, while structures *a1* and *b3* do not display the characteristic geometrical pattern of H-bonded structures, i.e. the collinearity of $\text{N-H}\cdots\text{O}$ atoms. Because the excitation is transferred from the phenyl system, the ring C-C bonds shrink their length to the ground state values in excitation transfer process. Unfortunately, since the PES is calculated at the CC2 level, they are overestimated from the exact ground state values. Also, but only related to NAPMA conformers is the preservation of the orientation of the methyl group relative to the proximal N-H bond, which is in staggered position relative to the methyl C-H bonds. The torsional angles between C-H and N-H bonds in M_{II} type minima exactly match the values of $M_{\pi\pi^*}$ minimum. This is due to the further increase of barrier for methyl group internal rotation around the N-CH₃ bond to value of 500 cm^{-1} , which completely hinders any possibility of methyl group rotation and fixes the methyl group relative orientation to the proximal N-H bond. Thus any change of N-H bond position relative to the second amide group in NAPMA conformers will also be accompanied with the methyl group orientation relative to it.

All these changes will now appear to a certain degree in the LIP obtained CI points.

4.4.2 $\pi\pi^*/n\pi_{(\text{II})}^*$ CI points

Six CI points between $\pi\pi^*$ and $n\pi_{(\text{II})}^*$ state PES-s (procedure explained in caption of Figure 4.20) were obtained from the LIP connecting the $M_{\pi\pi^*}$ with the corresponding M_{II} minimum structures. Table 4.7 lists the CI points relative energies and their structural parameters. By comparing the obtained structural parameters with M_{II} structures in Table 4.6 one can clearly see how geometrical differences among M_{II} minimum structures are embedded in CI-s as well. All LIP obtained CI points belong to the same CI seam between $\pi\pi^*$ and $n\pi_{(\text{II})}^*$ states, but as two types of minima can be distinguished on the

$n\pi^*_{(\text{II})}$ PES, so is the case for CI seam. This is confirmed by optimizing every CI point with the restrain of keeping the S_2-S_1 gap as small as possible using the Levine's et al. code. [152] Two distinguished MECI points were located on $\pi\pi^*/n\pi^*_{(\text{II})}$ CI seam characterized also by the direction of C_{Phe} atom pyramidalization. The two structures act as global minima (attractors) for local M_a and M_b structures and are therefore designated as MECIa and MECIb. Also a minimum distance CI (MDCI) point was located on the seam. When these structures are compared to LIP structures, the geometrical as well as energetic differences are significant. This is because along LIP-s all geometrical changes are linear, e.g., all LIP obtained CI points display a 30% increase of $C_{\text{Phe}}=O$ bond lengths and simultaneously C–C bond lengths in phenyl ring reduce by 30%, which is not the case for MECI structures. The simultaneous linear change of $3N_n - 6$ internal coordinates is non-physical, even though other internal coordinates change non-linearly. Therefore the variation between the choice of internal coordinates used for LIP construction plays no significant difference, although precaution must be taken into account. The internal coordinates were selected based on a criterion that the nearest atoms connected with covalent bonds are used for description of internal coordinates. This keeps the changes in internal coordinates at minimum. Also, for the case of NAPMA conformer B LIP-s, the torsional angle used for description of C-terminal CH_3 group was chosen in a way to keep the C–H bonds relative position fixed to the proximal N–H bond, because the rotational barrier hinders the methyl group rotation. One choice of internal coordinates was then applied to all LIP-s.

Table 4.7: Relative energies (ΔE) and five most distinctive geometrical parameters (torsional angles ϑ_C , ϑ_N and ω_2 ; $C_{\text{Phe}}=O$ and $C_{\text{Phe}}-N$ bond lengths) of CI points belonging to the $\pi\pi^*/n\pi^*_{(\text{II})}$ CI seam of NAPA and NAPMA conformers B, respectively. Energies (in eV) are relative to corresponding NAPA and NAPMA conformer B $M_{\pi\pi^*}$ structures, respectively. Angles are given in degrees while bond lengths are in Å.

	NAPA B CI _{II}						NAPMA B CI _{II}					
	ΔE	ϑ_C	ϑ_N	ω_2	$d_{C=O}$	d_{C-N}	ΔE	ϑ_C	ϑ_N	ω_2	$d_{C=O}$	d_{N-C}
$M_{\pi\pi^*}$	0.00	-178.7	-159.4	-6.9	1.239	1.363	0.00	-178.3	-178.5	1.6	1.243	1.362
MECIa	0.13	-174.9	-131.9	-15.1	1.286	1.386	0.17	-176.4	-141.4	-11.5	1.293	1.383
a1	0.22	-164.3	-147.9	6.2	1.278	1.384	0.32	-161.0	-168.8	23.0	1.270	1.397
a2	0.19	-166.2	-149.4	-4.6	1.295	1.372	0.24	-164.7	-166.7	0.0	1.311	1.369
a3	0.25	-164.0	179.8	12.8	1.304	1.371	0.25	-163.6	168.8	17.1	1.312	1.369
MECIb	0.16	-176.9	134.4	23.6	1.289	1.385	0.17	-179.3	142.7	19.5	1.296	1.382
b1	0.42	164.1	175.2	-18.6	1.279	1.389	0.45	162.6	169.1	-21.8	1.270	1.400
b2	0.35	166.2	177.8	-5.1	1.301	1.373	0.33	166.4	169.1	2.6	1.310	1.370
b3	0.29	166.8	-150.2	-18.1	1.298	1.372	0.32	165.9	-166.8	-11.8	1.309	1.371
MDCI	0.22	-178.3	-156.1	-8.7	1.314	1.361	0.28	-177.9	-178.2	1.9	1.328	1.359

A significant difference in relative energies between *a* and *b* type CI-s can be generally observed. This is mostly caused by the increase strain between the $C_{\text{Phe}}=O$ group O atom

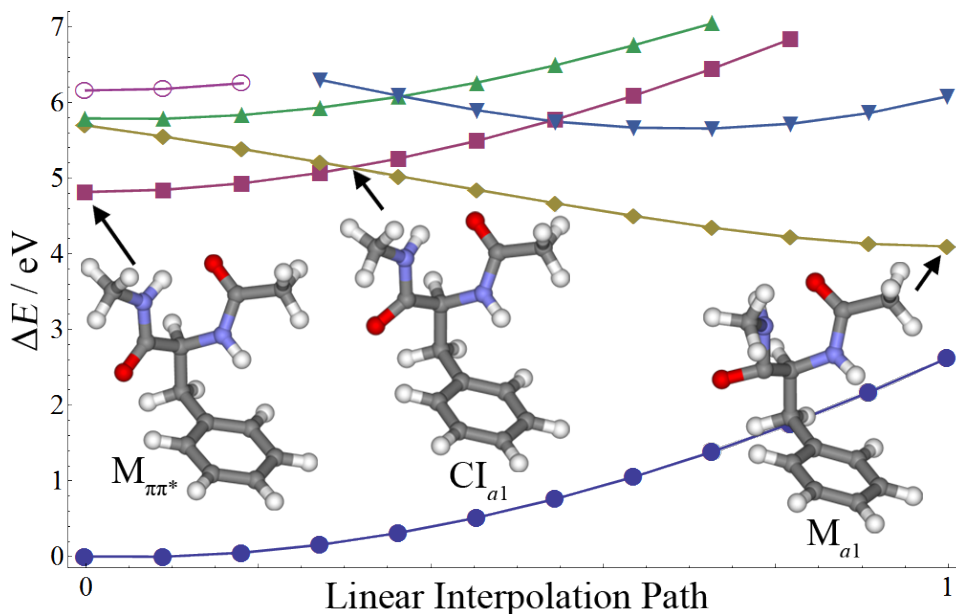


Figure 4.20: Energy profile of ground (blue dots) and four lowest excited states obtained from a linear interpolation path between the NAPMA conformer B $M_{\pi\pi^*}$ and M_{a1} minimum geometries (left and right insets) at the RI-CC2/cc-pVDZ level. The horizontal axis shows the fraction of the latter structure. Marks indicate single point calculations. Although all states are adiabatic they are coloured according to their character. From the intersection of $\pi\pi^*$ (bordeaux squares) and $n\pi\pi^*$ (gold diamonds) states the corresponding CI geometry is obtained (middle inset) whose energy is reevaluated by single point calculation.

which comes in close proximity to the phenyl ring H atom in *b* type CI-s. Because the LIP fails to describe the adequate repositioning of the phenyl ring, which is exhibited in MECI*b* structure, the energies of *b* type CI-s are larger than the *a* type CI points. Nevertheless, LIP obtained CI-s give an estimate of CI seam span in terms of geometrical differences. Other differences between CI energies can be contributed to relative orientations of NH_2 (NHCH_3) and $\text{C}_{\text{Phe}}=\text{O}$ groups and other geometrical differences already encountered in M_{II} minimum structures.

It should be noticed how the MECI*b* structures have a negative ϑ_C angle, but are still classified as *b* type CI-s simply because they are local attractors for the remaining *b* type CI structures and because are completely distinctive from MECI*a* structures.

The MDCI structure displays the minimum set of geometrical changes necessary to reach the CI point. Compared to corresponding $M_{\pi\pi^*}$ geometries, the conformer B MDCI structures exhibit only a large extension of $\text{C}_{\text{Phe}}=\text{O}$ bonds, the rest of geometrical parameters change almost insignificantly. The phenyl ring C–C bonds also undergo the smallest reduction of length compared to other CI-s. The NAPMA MDCI geometry exhibits a 0.01 Å, longer $\text{C}_{\text{Phe}}=\text{O}$ bond than NAPA MDCI structure.

All differences between NAPA and NAPMA conformer B originate from the methyl group on the second amide group. Table 4.4.2 lists the root-mean square differences between equivalent geometrical parameters in NAPA and NAPMA conformer B CI_{II} seam structures in which the distal H atom and CH₃ group were omitted from the second amide group of NAPA and NAPMA molecules, respectively. It clearly shows how the differences between the two types of CI structures are small, and if the second amide group is entirely omitted from comparison (cleaved at the C_α-C_{Phe} bond) the differences are a whole order smaller. But this geometrical similarity between NAPA and NAPMA geometries only reflects the more important and underlying electronic structure similarity between the two molecules. The energy differences between NAPA and NAPMA conformer B CI pairs are also small, except for *a1* type CI. Based on such significant geometrical similarity and relative energies of CI points it will be further assumed that electronic properties between NAPA and NAPMA conformer pairs, especially conformers B, do not deviate significantly in CI seam region. This is particularly important for the non-adiabatic couplings, which unfortunately are currently unavailable at the present level of theory (although non-adiabatic coupling vectors could be estimated using the numerical difference approximation (3.63), such insight at the CC2 level was not undertaken while it exceeds the scope of the present thesis). Under the present assumption how coupling between states

Table 4.8: Root-mean square deviations (RMSD) between equivalent geometrical parameters of NAPA and NAPMA conformer B selected CI_{II} points and M_{ππ*} for comparison. I: Minimum residual RMSD between equivalent Cartesian atom positions; II: RMSD of bond lengths; III: RMSD of bond angles; IV: RMSD of torsional angles. The latter three internal coordinates are based on the same Z-matrix used for LIP construction. The right hand side image shows the equivalent atom pairs in NAPA (pink) and NAPMA (gray).

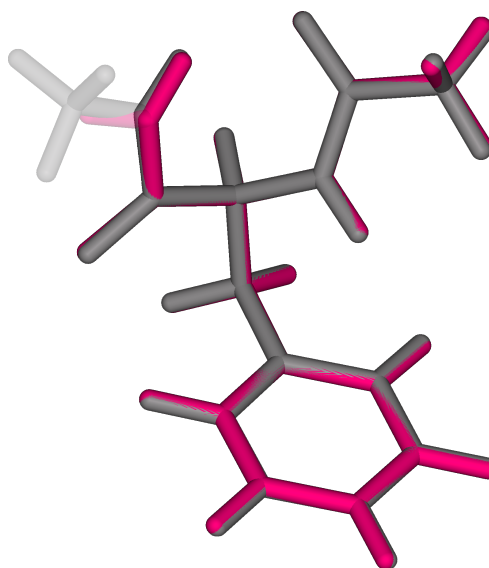
CI	I ^a	II ^b	III ^c	IV ^d
M _{ππ*}	5.9	1.5	3.9	2.6
MECIa	5.2	1.7	2.6	2.3
<i>a1</i>	4.7	3.1	3.1	2.0
<i>a2</i>	4.6	3.1	3.8	2.2
<i>a3</i>	3.8	1.6	3.5	2.2
MECIb	7.0	1.7	3.3	3.3
<i>b1</i>	5.2	2.8	3.0	2.5
<i>b2</i>	6.9	1.9	3.3	3.3
<i>b3</i>	4.2	2.2	3.7	2.3
MDCI	5.8	3.4	4.3	2.7

^a 10² RMSD/Å,

^b 10³ RMSD/Å,

^c 10 RMSD/°,

^d RMSD/°.



in NAPA and NAPMA are similar the differences between their excited state lifetime has to originate from the size and accessibility of their CI seams.

4.5 Accessibility of the $\pi\pi^*/n\pi_{(\text{II})}^*$ CI seam

The nanosecond range of excited $\pi\pi^*$ state lifetimes reflects the fact that the excited state population resides in a minimum of excited $\pi\pi^*$ PES and depopulates to the energetically close excited states through the corresponding CI seams. Scheme 4.21 depicts the simplified model of $\pi\pi^*$ PES in interaction with the $n\pi_{(\text{II})}^*$ PES where both PES-s are represented as diabatic states of corresponding character in the two dimensional configuration space. The intersection of two diabatic $3N_n - 6$ dimensional PES-s is shown as a simplified crossing (black) line. In order for this intersection to be conical as well, the diabatic coupling term ($W_{\pi\pi^*/n\pi_{(\text{II})}^*}$) between the two states must varies linearly and has to vanish at the very intersection of two PES-s (see model in Figure 3.1). This conditions give the characteristic local diabolic shapes of two interacting adiabatic states defined by the two branching directions (\mathbf{g}_0 and \mathbf{h}_0). The PES degeneracy is broken in any direction containing the two branching vectors while preserved along the remaining $3N_n - 8$ other directions which define the CI seam. The configuration space in Figure 4.21 is deliberately depicted with excess curvature to emphasize the complexity of the seam space. As will be explain more later, simply on account of large geometrical diversity between obtained CI points (Table 4.7) the CI seam is defined by a number of internal coordinates

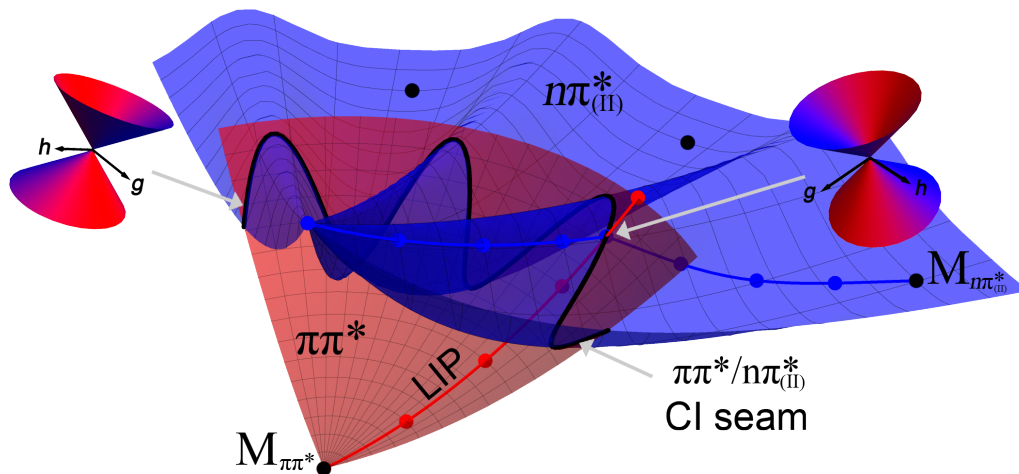


Figure 4.21: Two-dimensional model of $\pi\pi^*/n\pi_{(\text{II})}^*$ CI seam for NAPA/NAMPA mechanism II. The $\pi\pi^*$ and $n\pi_{(\text{II})}^*$ states are displayed in diabatic representation and mutually intersect in a CI seam depicted with black line, while the local PES minima points are depicted with black dots. A LIP connecting $M_{\pi\pi^*}$ with one $n\pi_{(\text{II})}^*$ minimum is also displayed. At every CI seam point the adiabatic PES-s branch and are here only figuratively shown as diabolic surfaces defined with the two branching vectors, \mathbf{g} and \mathbf{h} . Note how the branching vectors can change their directions on the seam.

which may not be easily to separate and used to described the seam space adequately in reduced dimension. Figure 4.21 also illustrates the coordinate dependence of branching space vectors, (3.27) and (3.28), which further complicate the unique description of the seam space.

The CI seam is characterized with its topographical features such as the points of minimum energy (MECI), points of minimum distance from the reference point (MDCI), maxima (barriers) between characteristic seam points, etc. In terms of population transfer the CI seam represents a region of configuration space for the most efficient population transfer between adiabatic states. This is due to the large non-adiabatic off-diagonal coupling terms which couple the neighbouring electronic states (3.12) and completely transfer the population from one state to another. Basically, the infinite non-adiabatic coupling vectors in CI act as a direct switch between PES-s forcing the population to reside on the PES of the same initial character as if no intersection was present at all. In terms of adiabatic state character, at regions with extremely localized non-adiabatic couplings the adiabatic PES-s display a clear cut between electronic characters (see Figure 4.22). The electronic populations just follows the state character, or simply, it behaves diabatically. Examples of such behavior were previously encountered in non-adiabatic simulations when the trajectory encounters peaked dynamical couplings. The dynamical coupling depends also on the velocity (3.63), which also manifests in adiabatic nuclear wave packet propagation where the coupling elements depend on the derivative of nuclear wave function ($\vec{\nabla}_k$ in (3.8)). However, even when the nuclear wave packet does not change rapidly, as is the usual case for stationary low energy bounded states, non-adiabatic coupling can be particularly strong due to scalar $D_{k,ij}$ terms. The latter terms couple the wave functions over multiplication (3.8) and are particularly significant when the non-adiabatic coupling vectors exhibit a rapid change (because of $D_{k,ij} \approx \vec{\nabla}_k \cdot \vec{d}_{ij}$ dependence, (3.11)) which always accompanies swift adiabatic character changes. Cederbaum *et al.* had shown that CI point similar to the one depicted on Figure 4.21 can act as an effective trap of nuclear population even if the other state is completely non-bonding due to resonance behavior between the two states. [170] A stationary quasi-bonding state (or a resonance state as the authors address it) emerges from the exact solution of two coupled states, which slowly depopulates through the CI branching region. If the diabatic off-diagonal terms are small, the nuclear population may reside in the initial state for long time. This is called the “diabatic trapping” [171] and number of works have addressed this problem analytically using the non-equilibrium Fermi golden rule approach. [171–173] However, for the problem at hand even the use of time-independent Fermi golden rule is out of reach mainly because the diabatic coupling terms are unavailable between $\pi\pi^*$ and $n\pi_{(II)}^*$ vibrational states and other reasons explain latter.

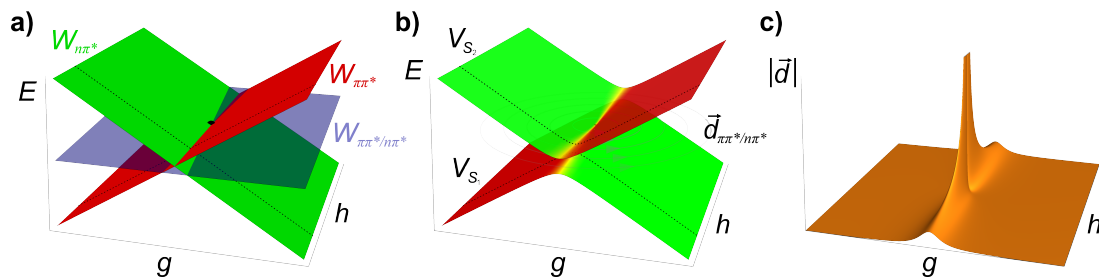


Figure 4.22: Analogue of CI model depicted in Figure 3.1 but with a ten times smaller off-diagonal W term shown in a) diabatic and b) adiabatic representation. c) Absolute magnitude of non-adiabatic coupling vectors. Notice the extended region of non-adiabatic coupling in adiabatic representation when compared to the one of Figure 3.1. For details see Figure 3.1 caption.

NAPA and NAPMA systems can be definitely represented with the above model system on the following facts: (i) the calculated CI points, including MECI-s, are all energetically higher than the initial $M_{\pi\pi^*}$ structure; (ii) the character at every obtained CI point (Table 4.7) changes immediately and no avoided crossings like the one encountered in NAPA B mechanism III were observed; (iii) finally the order of the experimental $\pi\pi^*$ lifetime is not in range of ultra-fast phenomena (fs and ps depopulation time range) which indicates a significant trapping of initial $\pi\pi^*$ population. Unfortunately, with the currently used CC2 level non-adiabatic coupling vectors or \mathbf{g} and \mathbf{h} vectors are unavailable, while the size of system active space prohibits the use of multireference methods for calculations of the missing terms. Therefore the insight into the CI seam and its neighbouring region is examined in terms of PES properties.

For start, Figure 4.21 clearly shows how LIP obtained CI-s are completely arbitrary in view of entire CI seam. If a different set of internal coordinates is used for LIP construction, a slightly different CI point is obtained. Nonetheless, the new CI points display the same characteristically clear cut between characters of adiabatic PES-s. All obtained CI points are just approximations to the true real CI points. They were all defined as CI due to having energy gaps lower than the 0.02 eV ($\approx 160 \text{ cm}^{-1}$) threshold, which is completely arbitrary. Even at this energy separation the characters of adiabatic states are well defined and without the mutual mixing. The exception is the NAPA conformer B *a3* CI point where the LIP obtained geometry has a gap smaller than 0.01 eV. At it the adiabatic character of S_1 and S_2 states are completely equal ($\sim 50\% \pi\pi^*$, $\sim 50\% n\pi^*_{(\text{II})}$) and the corresponding gradients are also equal. This point would lay in the region colored yellow in Figure 4.22. An effort was made to reoptimize the MECI-s points below 1 meV energy separation and although the goal was achieved, the CIOpt code convergence algorithms were insufficient to parallelly obtained a minimum on the CI seam. Nonetheless, the use validates that adiabatic states have equal character contributions when the

gap becomes small (>0.01 eV). CC2 method also proved stable when approaching true excited state CI points.

To examine the depopulation of $\pi\pi^*$ state the diabatic representation is a better choice. In it the population of $\pi\pi^*$ state can be express using the diabatic TDSE (3.19) with definitions and derivations of section 3.3

$$\begin{aligned} \frac{\partial \rho_{\pi\pi^*}(\mathbf{R}, t)}{\partial t} = & - \sum_{k=1}^{N_n} \frac{1}{M_k} \vec{\nabla}_k \cdot \left[\rho_{\pi\pi^*}(\mathbf{R}, t) \vec{\nabla}_k S'_{\pi\pi^*}(\mathbf{R}, t) \right] \\ & + 2 \operatorname{Im} \left(\sum_{j \neq \pi\pi^*} W_{\pi\pi^*,j}(\mathbf{R}) \bar{\Phi}'_{\pi\pi^*}(\mathbf{R}, t) \Phi'_j(\mathbf{R}, t) \right), \end{aligned} \quad (4.1)$$

with $\rho_{\pi\pi^*}(\mathbf{R}, t) = \bar{\Phi}'_{\pi\pi^*}(\mathbf{R}, t) \Phi'_{\pi\pi^*}(\mathbf{R}, t)$ and $\Phi'_{\pi\pi^*}(\mathbf{R}, t) = A'_{\pi\pi^*}(\mathbf{R}, t) e^{iS'_{\pi\pi^*}(\mathbf{R}, t)}$. The first right-hand side term is the divergence of the probability current of the same $\pi\pi^*$ state, whose integral over the entire configuration space should be small on account that the current mostly preserves the population within the same state. Also, with the assumption that the nuclear state is the zero-point energy bounded state of $M_{\pi\pi^*}$ minimum the $\Phi'_{\pi\pi^*}$ wave function changes less rapidly so the current term can be neglected. The second term is the probability density flux between states given by the imaginary part of the wave function product with the diabatic coupling. It clearly shows how the $\pi\pi^*$ PES density couples with other state only in regions where the $W_{\pi\pi^*,j}(\mathbf{R})$ terms differ from zero, which corresponds to the near vicinity of CI point (see Figure 4.22a). Because the adiabatic terms are reciprocal to diabatic, (3.32), the adiabatic wave function would reside on the same state in configuration space regions where the non-adiabatic coupling vectors are the smallest (Figure 4.22c). Integrating the above expression over the entire configuration space gives on the left-hand side the total rate of $\pi\pi^*$ population change

$$\frac{\partial \rho_{\pi\pi^*}(t)}{\partial t} \approx 2 \sum_{\substack{j \neq \pi\pi^* \\ \text{CI space}}} \int_{\substack{\pi\pi^*/j \\ \text{CI space}}} W_{\pi\pi^*,j}(\mathbf{R}) \operatorname{Im} \left(\bar{\Phi}'_{\pi\pi^*}(\mathbf{R}, t) \Phi'_j(\mathbf{R}, t) \right) d\mathbf{R}, \quad (4.2)$$

while the integration on the right-hand side is reduced only to region around the corresponding CI seam region where the diabatic $\pi\pi^*$ and j state PES-s cross and the couplings differ from zero. To avoid the construction of missing Φ'_j wave function it is simply assumed that they are proportional to $\Phi'_{\pi\pi^*}$ from the TDSE (3.32) due to which the right-hand side of (4.2) can be approximated as

$$\frac{\partial \rho_{\pi\pi^*}(t)}{\partial t} \approx \sum_{\substack{j \neq \pi\pi^* \\ \text{CI space}}} \int_{\substack{\pi\pi^*/j \\ \text{CI space}}} \kappa_{\pi\pi^* \rightarrow j}(\mathbf{R}, t) \rho_{\pi\pi^*}(\mathbf{R}, t) d\mathbf{R}. \quad (4.3)$$

The coupling terms and proportionality factors are all included in the $\kappa_{\pi\pi^* \rightarrow j}$ terms which can be interpreted as the probability of crossing the diabatic CI seam, or in adiabatic representation, the probability of residing on the same surface at the seam. Based on the assumption that the populations of the j states do not evolve in time back to $\pi\pi^*$ state, only the population transfer from $\pi\pi^*$ to j -th states is considered. Thus the rate of $\pi\pi^*$ population change reduces to the product of probability of nuclear wave function residing in the CI seam region ($\rho_{\pi\pi^*}$) with the probability of crossing the CI coupling region ($\kappa_{\pi\pi^* \rightarrow j}$). Finally, by separating the temporal from spatial dependence, $\rho_{\pi\pi^*}(\mathbf{R}, t) = P_{\pi\pi^*}(t)\rho_{\pi\pi^*}(\mathbf{R})$, and neglecting the time dependence of the coupling terms simplifies the above expression into (4.3) to

$$\frac{\partial P_{\pi\pi^*}(t)}{\partial t} \approx -k_{\pi\pi^*}P_{\pi\pi^*}(t), \quad (4.4)$$

with

$$k_{\pi\pi^*} = - \int_{\substack{\pi\pi^*/j \\ \text{CI space}}} \kappa_{\pi\pi^* \rightarrow j}(\mathbf{R})\rho_{\pi\pi^*}(\mathbf{R}) d\mathbf{R}. \quad (4.5)$$

The proportionality of the rate on the nuclear probability $P_{\pi\pi^*}(t)$ in (4.4) leads to the monoexponential decay of the initial nuclear population with the rate constant $k_{\pi\pi^*}$ given by (4.5). By removing the time dependence from nuclear density any insight into the wavepacket evolution description is abandoned and the density simply corresponds to the *quasi*-bonded nuclear state which should be under the present experimental circumstances the zero-point (vibrationless) state. Although the sum in above expression goes over all NRD channels, the differences between NAPA and NAPMA conformers B should lay in the terms connected with the $\pi\pi^*/n\pi^*_{(\text{II})}$ CI seam of mechanism II. It was already argued that based on the electronic structure similarities between NAPA and NAPMA conformers B their couplings should be similar for equivalent CI geometries and therefore their corresponding probabilities for crossing the CI seam region should also be similar. The differences between the two molecules would then completely lay in the properties of their nuclear wave function in the CI seam region.

Expression (4.5) requires at least the knowledge of nuclear wave function. It goes without saying that exact solution for systems of this size are impossible and approximations have to be used. If the $\pi\pi^*$ state PES is approximated with the Taylor expansion around the $M_{\pi\pi^*}$ minimum up to the second order, the harmonic potential

$$W_{\pi\pi^*}(\mathbf{R}) - W_{\pi\pi^*}(\mathbf{R}_{M_{\pi\pi^*}}) = \frac{1}{2}(\mathbf{R} - \mathbf{R}_{M_{\pi\pi^*}})^T \mathbf{L}^T \boldsymbol{\omega}^2 \mathbf{L} (\mathbf{R} - \mathbf{R}_{M_{\pi\pi^*}}) = \frac{1}{2} \sum_{i=1}^{3N_n-6} \omega_i^2 Q_i^2 \quad (4.6)$$

and the corresponding solutions of the harmonic Hamiltonian

$$\Phi'_{\pi\pi^*}(\mathbf{Q}) = \prod_{i=1}^{3N_n-6} \left(\frac{\omega_i}{\pi}\right)^{1/4} \exp\left(-\frac{\omega_i Q_i^2}{2}\right) \quad (4.7)$$

can be used to approximate the exact system nuclear properties. Normal mode coordinates Q_i are related with Cartesian coordinated over the linear transformation $Q_i = (\mathbf{L})_i(\mathbf{R} - \mathbf{R}_{M_{\pi\pi^*}})$ where square roots of atomic masses are embedded in L_{ij} elements, while the ω_i are the normal mode corresponding harmonic frequencies stacked into the diagonal matrix $\boldsymbol{\omega}$. The $\mathbf{L}^T \boldsymbol{\omega}^2 \mathbf{L}$ term is the PES Hessian ($\mathbf{H}_{\pi\pi^*}$). The quality of harmonic approximation depends on the anharmonicity of the system PES-s, and can be examined from third or higher order PES derivative terms or by comparing the analytic with the exact values. The former terms were not calculated due to the computational expense, while the latter procedure was used only to examine two modes, a low frequency mode corresponding to torsion of the entire molecule around the C_α - C_{Phe} bond and a $C_{\text{Phe}}=\text{O}$ stretch mode (Figure 4.23). The analysis is shown for NAPA conformer B, but the same conclusions also hold for NAPMA conformer. As expected, the torsional motion is less well described with harmonic approximation, especially after exceeding the torsional angle by more than $\pm 6^\circ$ from its equilibrium value when the quartic terms becomes significant. This term localizes the motion and the corresponding wave function, whose exact ZPE is 32 cm^{-1} compared to 20 cm^{-1} harmonic value.¹⁵

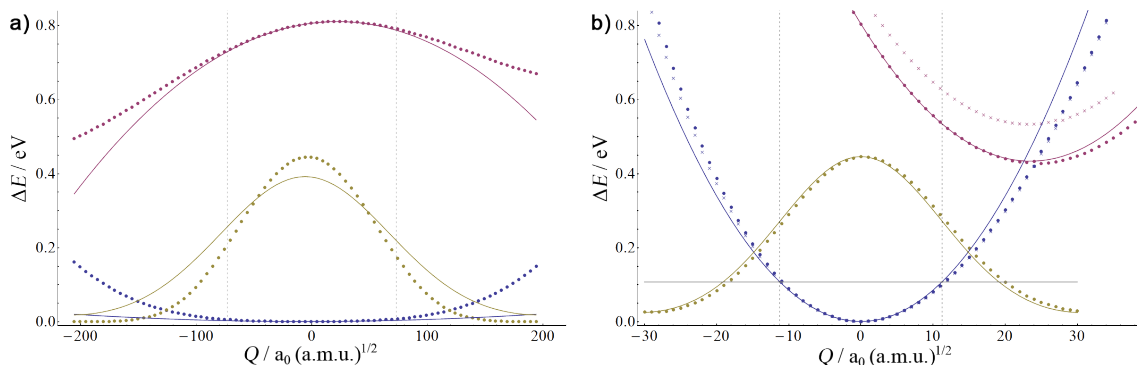


Figure 4.23: Comparison of harmonic (shown with lines) and exact calculated (dots) $\pi\pi^*$ (blue color) and $n\pi^*_{(\text{II})}$ (bordeaux) state PES-s along the coordinates for a) 41 and b) 1732 cm^{-1} modes of NAPA conformer B $M_{\pi\pi^*}$ minimum. The $\pi\pi^*$ state corresponding harmonic mode wave function is shown with a golden color line, while the exact calculated using golden dots. The vertical dotted black lines represent the harmonic oscillator classical turning point, while the horizontal black line on figure b the mode ZPE. On b part of figure exact NAPMA conformer B energies for the analogue mode are shown with crosses.

¹⁵The exact value was obtained using the equidistant Fourier grid Hamiltonian method. [72, 174]

On the other hand, the anharmonic cubic term perturbs the potential energy less for the $C_{\text{Phe}}=\text{O}$ bond stretch, making the wave function and its corresponding energy almost identical to corresponding harmonic values. Simultaneously, the analysis was also used to examine the Taylor second order expansion of the $n\pi^*_{(\text{II})}$ PES ($W_{n\pi^*}(\mathbf{R}) = W_{n\pi^*}(\mathbf{R}_{M_{\pi\pi^*}}) - W_{n\pi^*}(\mathbf{R}_{M_{\pi\pi^*}}) + \mathbf{G}_{n\pi^*}^T(\mathbf{R} - \mathbf{R}_{M_{\pi\pi^*}}) + 1/2(\mathbf{R} - \mathbf{R}_{M_{\pi\pi^*}})^T \mathbf{H}_{n\pi^*}(\mathbf{R} - \mathbf{R}_{M_{\pi\pi^*}})$), where \mathbf{G} is the gradient vector evaluated in $\mathbf{R}_{M_{\pi\pi^*}}$, and the same conclusions can be made as for the S_1 state.

Apart from the mixed characters in the point nearest to the true CI (<0.01 eV gap) PES-s in Figure 4.23b have well defined electronic characters and demonstrate how well localized is the $\pi\pi^*/n\pi^*_{(\text{II})}$ CI seam. Figure 4.23b is consistent with the previous observation that the $C_{\text{Phe}}=\text{O}$ stretch mode leads the system to the CI, but alone contributes very little because the CI point is extremely high in energy (in NAPMA case even higher). Thus only combined motion along modes affecting the geometry of second amide, phenyl and the backbone can effectively drive the system into the seam.

Unfortunately, the use of S_1 and S_2 harmonic diabatic PES-s for construction of the CI seam through finding points where the two surfaces intersect ($W_{\pi\pi^*}(\mathbf{R}) = W_{n\pi^*}(\mathbf{R})$ criterion) drastically fails due to large anharmonicities of motions corresponding to low frequency modes. The same problem is encountered in the seam construction using the harmonic $n\pi^*_{(\text{II})}$ potential evaluated at the M_{II} minima. Although this conclusion was generalized only from considerations of $a1$ minimum Hessian, the number of $n\pi^*_{(\text{II})}$ minimum structures further complicates this construction, but it also justifies the seam anharmonicity. Both problems together with the absence of PES-s coupling terms prohibit the use of Fermi golden rule for calculation of decay rates. [171]

The expression (4.5) was also examined from the CI seam point of view. If relations defining the CI seam can be derived, then the right-side integral can be evaluated. From the analytic considerations of a Hessian matrix obtained in the near vicinity of model CI systems, e.g. Figures 3.1 and 4.22, interesting properties emerge. Firstly, two Hessian eigenvectors are linear combinations of \mathbf{g}_0 and \mathbf{h}_0 vectors, while all other eigenvectors correspond to motions along the seam which preserves the PES-s degeneracy. Therefore, the eigenvectors between Hessian of lower and higher excited state should coincide in directions. Secondly, one of the two eigenvectors are characterized by a large negative and large positive eigenvalues for the lower and higher excited states, respectively, since they coincide with the steepest slope direction of the corresponding PES. The second eigenvector exhibits the same properties but generally has a smaller eigenvalue. However, as explained later, for more realistic CI-s these properties may substantially differ from the properties obtained on idealized peaked CI model types depicted in Figures 3.1 and 4.22. Nonetheless, general characteristic should be preserved among Hessian matrices

obtained in the near vicinity of real CI points. To distinguish the two branching eigenvectors from the remaining Hessian eigenvectors, it is wise to construct the Hessian matrix in the MECI structure, while all other S_1 PES eigenvectors have positive corresponding eigenvalues. Thus, numerical Hessians for both the S_1 and S_2 states were constructed in the MECIa NAPA and NAPMA conformer B geometries to examine the neighborhood of corresponding CI seams. Because the NAPMA case turned out to be completely similar to NAPA, only observations for the latter system are described. The Hessians matrices obtained using the finite difference method (3.115) suffer from numerical inaccuracies when evaluated near the CI point. A well converged CI with small energy gap is therefore necessary to obtain the desired Hessian properties. Consistently with the analytic model, the S_1 PES Hessian has two negative eigenvalues, where one is $\sim 1.5 \cdot 10^5$ times larger than the other. Two S_2 state Hessian eigenvectors coincide in directions with the two former S_1 eigenvectors, respectively, but have positive eigenvalues. However, one of the S_2 Hessian eigenvectors, which is collinear with the S_1 eigenvector that has the largest positive eigenvalue, has a negative eigenvalue instead. Thus S_1 and S_2 Hessian matrices instead of two, give three eigenvectors along which the PES-s are split in harmonic approximation of (3.26). When all three eigenvectors are projected from the Hessian matrices the remaining $3N_n - 9$ eigenvectors preserved the PES-s degeneracy. At first, this is completely contrary to the $3N_n - 8$ dimensionality of the CI seam. By detailed examination of the three obtained branching modes, two eigenvectors with the largest absolute eigenvalues, turned out to have the largest contributions of the two branching directions. Figure 4.24a shows the S_1 and S_2 PES-s spanned in subspace by these two Hessian eigenvectors, which clearly demonstrates the branching of PES characters along the direction depicted with the black arrow. The orthogonal direction (depicted with the black line) preserves the state characters, while along the same apparent intersection line between the two PES-s (black line) degeneracy also breaks linearly, but with ~ 20 times smaller factor than for the former direction. Additionally the energy also rises quadratically along the latter direction. All these PES topological properties deformed the usual diabolic cone, which is only preserved in the nearest vicinity of the MECI point, but heavily extended along the direction of black line. Thus, the obtained PES-s at the CI resembles the model depicted in Figure 4.22 and because they exhibits the very sudden change of adiabatic state characters at the apparent intersection of two PES-s, it is an indirect sign that the coupling between diabatic $\pi\pi^*$ and $n\pi^*_{(\text{II})}$ states is small and confined to a narrow region of space around the degeneracy point. These finding, at least at the present CC2 level of theory, confirm the assumed low coupling between the two states at the $\pi\pi^*/n\pi^*_{(\text{II})}$ CI seam. The corresponding Cartesian displacement vectors are shown in Figure 4.24b for the branching vector depicted with the black arrow, while the orthogonal motion is associated mostly

with the deformation of the second amide group and expansion of the phenyl ring (not shown). Since the motion along the former vector changes characters of adiabatic state, its corresponding vector can be associated with the \mathbf{g}_0 branching space direction. And as Figure 4.24b shows, this vector describes the simultaneous change of $C_{\text{Phe}}=\text{O}$ and phenyl C–C bonds associated with the excitation transfer between $\pi\pi^*$ and $n\pi^*_{(\text{II})}$ states.

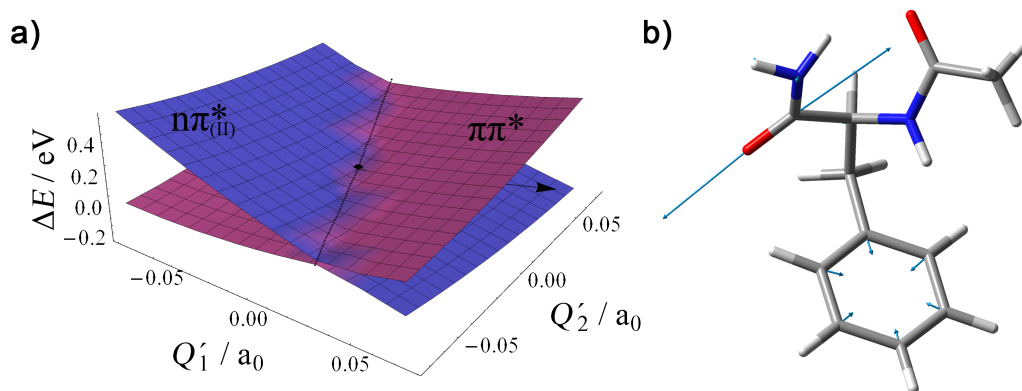


Figure 4.24: a) NAPA conformer B S_1 and S_2 adiabatic PES-s span with the two eigenvectors around the MECIa point (black dot). The two eigenvectors have the largest absolute eigenvalues of S_1 and S_2 Hessian matrices, which were numerically obtained at the MECIa point. The blue and bordeaux colors represent the $\pi\pi^*$ and $n\pi^*_{(\text{II})}$ state characters, respectively, which were used for branching vectors (black arrow and black line) construction. b) The Cartesian displacement vectors in MECIa geometry for the branching vector along the black arrow in a) part of figure. For NAPMA conformer B completely analogous PES-s and branching vector are obtained.

Because states preserved their characters along the orthogonal direction (black line) the same direction can be taken as the best guess of the \mathbf{h}_0 coupling direction. However, contrary to the \mathbf{g}_0 direction which can be associated with the difference in slopes of adiabatic surfaces in the weak coupling regime (3.27), it is more difficult to uniquely determine the coupling vector since coupling terms are missing (3.28). Therefore, a complete analysis of motions along all remaining S_1 Hessian eigenvectors was made in effort to elucidate the missing contributions of the branching vectors by constructing one-dimensional cuts through PES-s along every eigenvector. Analysis of PES-s dependence along each eigenvector direction showed that linear degeneracy braking terms are at most an order smaller than the term associated with the guess \mathbf{h}_0 vector. Even the eigenvector corresponding to the second negative eigenvalue of S_1 Hessian which brakes the degeneracy in harmonic approximation, preserves the PES-s degeneracy in the close vicinity of the MECIa point, but then its quadratic terms brake the degeneracy at larger distances from the CI. Thus this eigenvector acts as the *h.o.d.* term which breaks the degeneracy further away from the CI point, and can be used to evaluate where the CI seam along this direction breaks apart. The same observation could be then reproduced for all remaining eigenvectors,

but without the exact insight into the coupling terms the limits where the two PES-s split is somehow arbitrary, while the CI seam curvature further complicates the uniqueness of limits (see below). Therefore, such procedure was not considered but the latter eigenvector was also examined as potential coupling vector. Its corresponding Cartesian displacement vectors are shown in Figure 4.25, which simultaneously describe the pyramidalization of the C_{Phe} atom, the twisting of the NH_2 group and the repositioning of the phenyl ring. If a subspace is spanned with this eigenvector and with the obtained \mathbf{g}_0 vector no characteristic diabolic branching could be obtained, but a parabolic seam originating from intersections of two parabolic PES-s with well defined characters is obtained instead (Figure 4.25c). The bonding and repulsive nature of $\pi\pi^*$ and $n\pi^*_{(\text{II})}$ PES-s, respectively, along the motion represented with the negative eigenvector are consistent with previously observed electronic properties for these two states. It also explains the negative and positive eigenvalues of S_1 and S_2 Hessian eigenvalues, respectively. But more importantly this eigenvector clearly shows how highly curved is the CI seam in the configuration space (Figure 4.25c), which complicates the simple determination of branching space directions. Nonetheless, in the close vicinity of $\text{MECI}a$ point the two S_1 or S_2 Hessian eigenvectors depicted in Figure 4.24a are an adequate representation of the corresponding branching space. The problem however arises when the same vectors are applied for the description of some other CI point belonging to the seam in Figure 4.25c simply because Cartesian vectors determined at one particular point in configuration space are inadequate for the description of branching PES-s at some other geometry. But regardless of that Figure 4.25c clearly shows how the motion along the \mathbf{g}_0 direction breaks degeneracy.

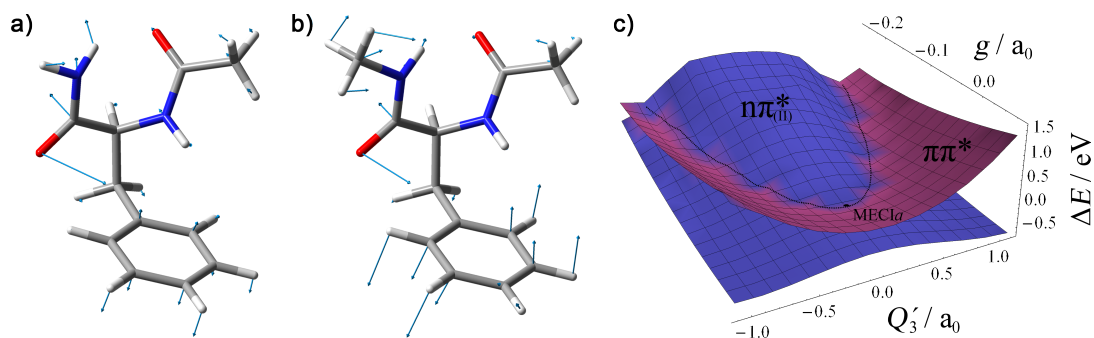


Figure 4.25: The Cartesian displacement vectors corresponding to a) NAPA and b) NAPMA conformer B second eigenvector with negative eigenvalue of the corresponding $\text{MECI}a$ S_1 Hessian matrices. c) NAPA conformer B S_1 and S_2 PES-s span in subspace defined with vector a) and \mathbf{g}_0 vector of Figure 4.24 around the $\text{MECI}a$ point (black dot). The black parabola indicates the closest approach of the two adiabatic PES-s. Motion along positive values of Q'_3 coordinate deplanarizes the C_{Phe} atom towards the a type CI points, while along negative towards the b type CI-s. PES-s are completely analogous for NAPMA conformer B.

Figure 4.25c shows how the eigenvector associated with the second negative S_1 Hessian eigenvalue significantly contributes to the degeneracy breaking of all CI points and how the branching space defined with the Hessian eigenvectors shown in Figure 4.24 acquires more significant contribution from the Hessian eigenvector depicted in Figure 4.25a, especially for seam points further away from the MECIa structure. Therefore, unlike the \mathbf{g}_0 vector (Figure 4.24) a general \mathbf{h}_0 direction cannot be uniquely defined for NAPA (NAPMA) system. A potential solution to the problem at hand might be the use of internal instead of Cartesian vectors, which however is avoided on account of complicating later expressions. Nevertheless, for the problem of assessing nuclear wave function probability in the $\pi\pi^*/n\pi^*_{(II)}$ CI space (4.5) the true branching space can be taken as the space between the two limiting branching spaces depicted in Figures 4.24 and 4.25. Both limiting branching spaces are defined with the same \mathbf{g}_0 vector, but differ in the choice of the \mathbf{h}_0 direction. Also, both branching spaces exhibit a sudden change of electronic state characters at the intersections, which indicates how in both spaces the coupling between the PES-s is small. Detailed analysis for both branching spaces shows how after the S_1 and S_2 PES Hessian matrices are adjusted for rotation of the \mathbf{g}_0 containing eigenvectors and the approximate \mathbf{g}_0 and \mathbf{h}_0 vectors are projected out, the $3N_n - 8$ remaining Hessian eigenvectors adequately define the seam space. Separation of branching space depicted in Figure 4.25 from the seam space gives better result because it was this particular \mathbf{h}_0 eigenvector that mostly break the degeneracy in harmonic approximation. But even with the use of this branching space, one of the seam vectors with low eigenvalue still contains residual branching space directions and distorts the degeneracy. This is due to the inability to exactly separate the remaining small contributions of branching space vectors from all Hessian eigenvectors, as was shown from full analysis of all Hessian eigenvectors, but also partly due to inaccuracies of numerical Hessians and the convergence of MECIa point, which specially contributes to the differences between the numerical S_1 and S_2 Hessian matrices as encountered later. But because the S_1 and S_2 eigenvalues of the troublesome seam eigenvector are similar and do not significantly break the degeneracy and simultaneously lifts the PES-s, for the present level of consideration the seam space is adequate enough. The difficulty with rotation and obtaining the \mathbf{h}_0 branching vector might also be due to its small contribution of the off-diagonal $W_{\pi\pi^*/n\pi^*_{(II)}}$ coupling terms (3.28). If these terms are small, then its corresponding coupling vector direction might also vary significantly. The extended intersections depicted in Figures 4.24 and 4.25 as well as the clear cuts between PES characters support this assumption, but unfortunately while no exact computational non-adiabatic coupling terms are available, this hypothesis remains unproven. Nonetheless, approximate branching space vectors were constructed from the information of the shape of PES-s around the CI point, which are sufficient enough for the

construction of the $3N_n - 8$ CI seam around the MECI $_a$ point and a rough approximation of nuclear probability in CI space.

In the vicinity of the CI point the two PES-s are described with expression (3.26). By projecting out the branching space from (3.26), the remaining $3N_n - 8$ coordinate dependent terms keep the PES-s degenerate within some region around the initial CI point. Therefore, the seam space around the CI point can be approximated with the Taylor series up to the second order

$$W_{S_1/S_2}(\mathbf{Q}') = W(\mathbf{R}_{\text{MECI}_a}) + \mathbf{G}_{\text{MECI}_a}^T \mathbf{Q}' + \frac{1}{2} \mathbf{Q}'^T \mathbf{H}_{\text{MECI}_a} \mathbf{Q}', \quad (4.8)$$

where the same expression describes both PES-s due to degeneracy. The gradient and Hessian terms in above expression are derived from corresponding $W_{i,i} + W_{i+1,i+1}$ and *h.o.d.* (3.29) elements in (3.26), where the latter terms break the degeneracy at some point. The \mathbf{Q}' represents some generalized $3N_n - 8$ seam coordinates related to Cartesian over a simple linear relation

$$\mathbf{Q}' = \mathbf{L}'(\mathbf{R} - \mathbf{R}_{\text{MECI}_a}), \quad (4.9)$$

where \mathbf{L}' is an arbitrary orthogonal matrix. The Hessian eigenvectors can be used to construct the \mathbf{L}' matrix, where for later convince the two branching vectors are also included, but their corresponding g and h coordinates are restrained to zero. In the CI seam the diabatic and adiabatic PES-s are equivalent (3.24), which enables their direct construction. Additionally, in the true MECI point the seam gradient components also vanish, but in the approximate MECI point residual components remain and are kept in expansion (4.8) to compensate for errors of numerically obtained Hessian matrices. Since coupling or *h.o.d.* terms are unavailable, it is impossible to determine where the seam harmonic expansion (4.8) breaks apart, due to which the CI seam becomes non-physically infinite. This generally disproves the validity of (4.8) for the description of seam, but because the $\pi\pi^*$ harmonic wave function (4.7) attenuates very rapidly from the close lying CI points (see later), the harmonic expansion is taken as the best analytic construction of the $\pi\pi^*/n\pi_{(\text{II})}^*$ seam. In practice degeneracy breaking does happen, because the numerical S_1 and S_2 Hessian matrices are not equal. Thus for the construction of seam around MECI $_a$ point the S_1 terms are used in (4.8). The harmonic CI seam approximation (4.8) overestimate the true LIP CI-s and the MDCl energies by 0.05–0.37 eV (0.05–0.9 eV) in NAPA (NAPMA) a seam region, while more than 1 eV the b part of CI seam. The latter discrepancy originate from inadequacies of expression (4.8) to correctly describe the CI seam curvature.

Nevertheless, by adapting the CI seam harmonic approximation (4.8), estimates of nuclear wave function probabilities in the $\pi\pi^*/n\pi_{(\text{II})}^*$ CI seam were calculated for NAPA

and NAPMA conformers B, respectively. Since the transition probabilities between states are unknown, only the contribution of the ρ part in (4.5) is addressed further. The system's probability for residing in the CI seam region is given by the square of the nuclear wave function (4.7) integrated in the CI space region

$$P_{\pi\pi^*/n\pi^*_{(\text{II})}} = \left[\prod_{i=1}^{3N_n-6} \left(\frac{\omega_i}{\pi} \right)^{1/2} \right] \int_{\pi\pi^*/n\pi^*_{(\text{II})}} \exp(-\mathbf{Q}^T \boldsymbol{\omega} \mathbf{Q}) d\mathbf{Q}, \quad (4.10)$$

which is written in matrix compact notation. The integration is carried out over all $3N_n - 6$ coordinates, which include the seam and branching spaces at this stage. By expressing the normal modes in terms of the generalized coordinates (4.9)

$$\mathbf{Q} = \mathbf{L}(\mathbf{L}'^T \mathbf{Q}' + \mathbf{R}_{\text{MECI}a} - \mathbf{R}_{\text{M}_{\pi\pi^*}}), \quad (4.11)$$

the exponent of the integrand function is rearranged into

$$\mathbf{Q}^T \boldsymbol{\omega} \mathbf{Q} = \mathbf{Q}'^T \mathbf{A} \mathbf{Q}' + 2\mathbf{B}^T \mathbf{Q}' + C, \quad (4.12)$$

with the factors

$$\mathbf{A} = \mathbf{L}' \mathbf{L}'^T \boldsymbol{\omega} \mathbf{L} \mathbf{L}'^T, \quad (4.13)$$

$$\mathbf{B} = (\mathbf{R}_{\text{MECI}a} - \mathbf{R}_{\text{M}_{\pi\pi^*}})^T \mathbf{L}'^T \boldsymbol{\omega} \mathbf{L} \mathbf{L}'^T, \quad (4.14)$$

$$C = (\mathbf{R}_{\text{MECI}a} - \mathbf{R}_{\text{M}_{\pi\pi^*}})^T \mathbf{L}'^T \boldsymbol{\omega} \mathbf{L} (\mathbf{R}_{\text{MECI}a} - \mathbf{R}_{\text{M}_{\pi\pi^*}}). \quad (4.15)$$

\mathbf{A} is a $3N_n - 6$ dimensional square matrix, \mathbf{B} is a vector of the same dimension and C is a scalar. The right-hand side integral of equation (4.10) is now transformed into

$$e^{-C} \det(\mathbf{J}) \int_{\text{seam space}} \int_{\text{branching space}} \delta(g) \delta(h) \exp(-\mathbf{Q}'^T \mathbf{A} \mathbf{Q}' - 2\mathbf{B}^T \mathbf{Q}') d\mathbf{Q}'_{\text{seam}} dg dh, \quad (4.16)$$

where $\mathbf{J} = \partial \mathbf{Q} / \partial \mathbf{Q}'$ is the Jacobian matrix originating from the coordinate transformation (4.11). The Jacobian is not an orthogonal matrix since normal modes are mass weighted. The whole integration over the CI space is now divided into the seam and branching space, and because the coupling terms $W_{\pi\pi^*/n\pi^*_{(\text{II})}}$ are unknown, the integration is only conducted in the seam space, as g and h coordinates are restrained to zero by introducing the two Dirac delta functions into the integral. This has the effect of removing the two branching space vectors from matrix \mathbf{L}' and the integration is performed solely in the $3N_n - 8$ seam space. Rigorously, the probability (4.10) is transformed into the probability density in

seam space evaluated at the seam space origin, but because its dependence on the seam coordinates is not examined it is simply designated as probability. The remaining integral is solved by diagonalizing the quadratic form where the newly obtained Gaussian type integrals are solved analytically and give the final expression for the nuclear wave function probability in the seam space

$$P_{\text{CI seam}}^{\pi\pi^*/n\pi_{(\text{II})}^*} = \frac{\det(\mathbf{J})}{\pi} \left(\prod_{i=1}^{3N_n-6} \omega_i^{1/2} \right) \left(\prod_{i=1}^{3N_n-8} \alpha_i^{-1/2} \right) \exp \left(\sum_{i=1}^{3N_n-8} \frac{\beta_i^2}{\alpha_i} - C \right). \quad (4.17)$$

The used integration limits were infinite, while the information of true limits are unavailable because couplings and *h.o.d.* terms are missing. The α -s are the matrix \mathbf{A} eigenvalues, which is now of $3N_n - 8$ dimension, while β -s are the \mathbf{B} vector components in eigenvector basis of matrix \mathbf{A} . Therefore, a number of terms determine the nuclear wave function probability in the seam space, e.g. the C factor is similar to ZPE energy accessibility discussed later (see (4.18)). The colinearity between normal modes and seam eigenvectors determines the values of α and β terms, but since seam eigenvectors are just arbitrary direction for integration, any unitary transformation of seam space vectors will give the same result while the probability is determined by the nuclear wave function. Without going into further details, probabilities for nuclear wave functions residing in $\pi\pi^*/n\pi_{(\text{II})}^*$ CI seam were calculated for NAPA and NAPMA. Taking the branching space of Figure 4.24 a 18 times larger probability is obtained for NAPA conformer B compared to NAPMA counterpart, while the ratio increases to 25 if the branching space on Figure 4.25 is used. Actually, any branching space defined with the linear combination of corresponding \mathbf{h}_0 vectors of Figures 4.24 and 4.25 will always give a ratio of probability larger for NAPA than for NAPMA conformer because the terms invariant to branching space rotation are in favor of NAPA conformer. With the restrain that the same rotation of branching spaces is used for NAPA and NAPMA conformers the obtained ratio used to estimate the ratio of NRD mechanisms rate (4.5), with taking into account other potential NRD channels and the transition probability, but only descriptively, is however underestimated. Nonetheless, the obtained ratio gives a clear indication that the $\pi\pi^*/n\pi_{(\text{II})}^*$ CI seam is more accessible for the *quasi*-bounded $\pi\pi^*$ state in NAPA conformer B than in NAPMA conformer B.

The seam probability ratio is mostly underestimated due to the infinite sizes of the two comparing CI seams, because parts of configuration space which do not have degenerate PES-s were taken into the total probability sum (4.10). This can only be corrected with the use of coupling terms, which are unfortunately unknown here. Furthermore, since numerical MECIa S_1 and S_2 Hessian matrices are not equal, they have slightly different contributions of residual branching vectors, which was particularly strongly exhibited in

the estimates of the \mathbf{h}_0 branching vector. In case of NAPMA conformer B this coupling vector should also include the internal rotational motion of the second methyl group, while it was observed that this motion breaks degeneracy. Using the eigenvectors of S_2 state Hessian instead of the lower S_1 state eigenvectors, the probability ratio increases to 113. The allowed rotation of \mathbf{h}_0 vector introduces some flexibility into the branching space, while in reality branching space is not necessary fixed but also configuration space dependent. One can now systematically build a better branching space, but this does not change the fact that the seam size is still overestimated and that the Taylor expansion to the second order (4.8) can only adequately describe the CI seam around the initial MECIa point. Although the above considerations clearly indicate how the difference between NAPA and NAPMA conformer B $\pi\pi^*$ state lifetimes should be controlled by the seam accessibility, this assumption needs to be further strengthened.

The anharmonicity of $\pi\pi^*$ state normal modes further adds to the probability error. Table 4.9 validates the quality of combined mode description and the $\pi\pi^*$ PES harmonic approximation by comparing the harmonic energies for corresponding CI-s of Table 4.7 calculated using expression (4.6) with the exact values. One can immediately observed how the CI seam around the MECIb attractor is inadequately described within the harmonic approximation. The exception is the *b2* CI geometry. The errors are less for structures around the MECIa and MDCI part of CI seam, apart from the NAPMA conformer B MECIa structure whose harmonic potential energy is overestimated. Thus it is further necessary to validate the above estimate of the nuclear wave function residing in the $\pi\pi^*/n\pi_{(II)}^*$ CI seam. The alternative would be the construction of the reaction Hamiltonian, and although general procedures are developed, [75] the dimensionality of the model would still exceed the computational feasibility due to the number of motion necessary to take into account (see later). Therefore, the harmonic approximation of $\pi\pi^*$ state is kept and only a qualitative description between the difference of NAPA and NAPMA conformer B population decays is given.

Instead of calculating the expression (4.5) for the $\pi\pi^*/n\pi_{(II)}^*$ CI seam one can only examine the normal mode wave functions contribution at the CI points. As the normal modes are independent in harmonic approximation, each contribution can be examined individually. Also, to simplify the Gaussian probability density dependence of the normal mode wave function the exact probability density is examined in terms of a reference density of a classical oscillator part of the configuration space, for which the probability density is simply taken to be uniformly equal.¹⁶ Beyond the classical oscillator turning points the oscillator tunnels through the classically inaccessible region to reach a certain

¹⁶For classical harmonic oscillator the probability density is actually $\rho(Q) = (1/\pi)\sqrt{\omega/(2E - \omega^2Q^2)}$, where E is the total oscillator energy.

Table 4.9: LIP obtained CI relative energies (LIP) of Table 4.7 compared to the calculated $\pi\pi^*$ state potential energies in CI geometries using the harmonic approximation (HAR) (4.6) for NAPA and NAPMA conformer B. Energies are relative to corresponding $M_{\pi\pi^*}$ minimum values. The root-mean square distance (RMSD) are between the CI and corresponding $M_{\pi\pi^*}$ minimum structures. Structures designated with bold font are classically accessible. Energies are in eV, RMSD in Å.

	NAPA B CI _{II}			NAPMA B CI _{II}		
	LIP	HAR	RMSD	LIP	HAR	RMSD
MECIa	0.13	0.13	0.09	0.17	0.34	0.20
a1	0.21	0.20	0.09	0.32	0.38	0.17
a2	0.19	0.17	0.06	0.24	0.25	0.12
a3	0.25	0.26	0.07	0.25	0.26	0.09
MECIb	0.16	0.95	0.19	0.17	0.66	0.25
b1	0.42	0.78	0.17	0.45	0.88	0.18
b2	0.35	0.34	0.15	0.33	0.33	0.24
b3	0.29	0.24	0.15	0.32	0.43	0.21
MDCI	0.22	0.25	0.01	0.28	0.31	0.01

configuration point. Thus the nuclear wave function is split in classically accessible and classically inaccessible portion of configuration space, where in the latter the probability density attenuates. The population decay probability, and with it the $\pi\pi^*$ depopulation rate (4.5), are simply determined now by the fraction of $\pi\pi^*/n\pi^*_{(II)}$ CI seam divided between the two portion of configuration space. Unfortunately, the inability to exactly reconstruct the CI seam hinders again the possibility to calculate and compare the contributions of both configuration space parts.

While the nuclear part of the system is in the zero point (vibrationless) state, each normal mode contribution can now be examined in respect to its corresponding ZPE. In the independent mode approximation the corresponding ratio

$$\frac{W_i(Q_{i,CI})}{ZPE_i} = \frac{\frac{1}{2}\omega_i^2 Q_{i,CI}^2}{\frac{1}{2}\omega_i} \begin{cases} \leq 1; \text{classically accessible} \\ > 1; \text{classically inaccessible} \end{cases} \quad (4.18)$$

determines whether the normal mode coordinate Q_i for a particular CI point is in a classically accessible or inaccessible part of configuration space. $\omega_i/2$ is the i -th mode ZPE (in atomic units) and W_i is the normal mode potential energy function whose sum over all modes give the total harmonic potential (4.6). Note that the factors contributing to the C term in (4.15) are the right-hand side terms of the above relation (4.18). Figure 4.26 displays the above fractions for the NAPA and NAPMA conformer B MECIa structures. Firstly, Figure 4.26 clearly shows how the largest contribution to the geometrical changes

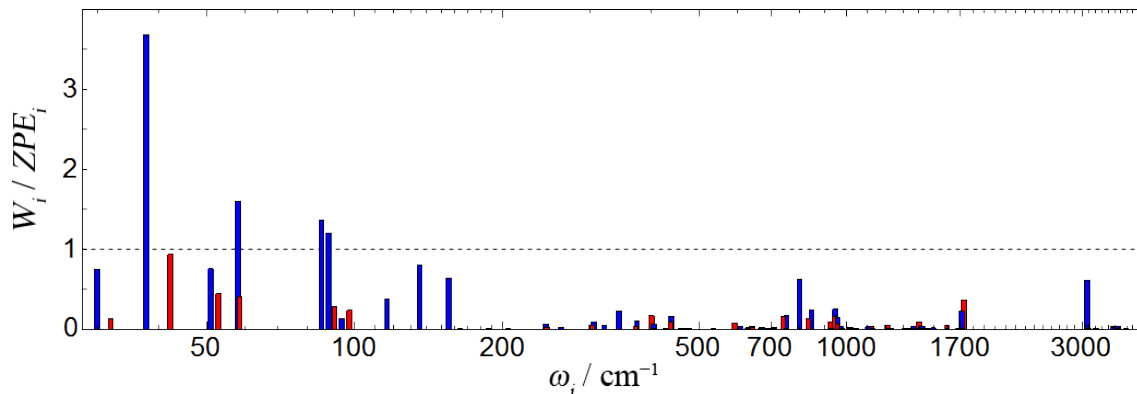


Figure 4.26: Ratio of corresponding mode’s potential energy and its ZPE (4.18) at the NAPA (red) and NAPMA (blue) MECIa structure. The mode’s potential energy is the normal mode harmonic energy ($W_i = \omega_i Q_i^2/2$) for the normal coordinate Q_i in specified geometry. For coordinates whose W_i/ZPE_i ratio exceed one are taken as classically inaccessible.

are among the normal modes with the lowest frequencies ($<200 \text{ cm}^{-1}$). These modes correspond to relative oscillations of whole groups within the NAPA (NAPMA) structure and are also the most anharmonic. Usually in vibrational analysis these modes are discarded from considerations, but here they are kept while their motions have physical meaning, only their exact energies are probably inaccurate. Secondly, the difference between normal mode accessibility is clear for NAPA and NAPMA, where for the former molecule all modes are classically accessible. The critical 38 cm^{-1} NAPMA mode is completely analogue to the NAPA 41 cm^{-1} oscillation of the second amide group around the $C_\alpha-C_{\text{Phe}}$ bond which was shown to be highly anharmonic (see Figure 4.23a). Nonetheless, even if the exact wave function is taken for this mode, its rapid decay beyond the classical turning point (see 4.23a) for large extension of this mode is consistent with the mode’s inaccessibility in harmonic approximation. The large extension of this mode in NAPMA MECIa geometry compared to NAPA is associated with a larger geometrical change of the second amide group, because the same mode also describes the slight pyramidalization of the NHCH_3 (NH_2) group which is more significant in NAPMA molecule (see Table 4.7). The three remaining classically inaccessible modes in NAPMA with frequencies 58, 86 and 89 cm^{-1} also correspond to relative motions of backbone groups and the phenyl ring relative repositioning to the backbone, respectively, and all possess a fraction of second amide group distortional motion. When the remaining CI structures in Table 4.7 are analyzed in terms of normal mode accessibility, all NAPA conformer B structures belonging to the MECIa local attractor of the CI seam are classically accessible, while in NAPMA only geometries *a2* and *a3* are. Classically accessible structures are designated with bold font in Table 4.9. None of the structures belonging to the *b* part of CI seam as well as the MDCI structures are classically accessible in NAPA and NAPMA.

Although their harmonic potential energies are highly anharmonic, even the harmonic $b2$ CI structures are inaccessible due to the modes involving significant repositioning motions of the second amide and phenyl groups. Figure 4.27a shows the difference between NAPA and NAPMA normal mode accessibility in the $a1$ CI geometries. Additionally to the differences between the low frequency modes in NAPMA $a1$ CI, a 800 cm^{-1} mode corresponding to concerted $\text{C}_{\text{Phe}}=\text{O}$ and $\text{N}-\text{CH}_3$ out-of-plane bending stands above the classical limit. For comparison, the distortional motions in NAPA necessary to reach the corresponding $a1$ CI structure are split among two consecutive normal modes, the 755 and 835 cm^{-1} which correspond to NH_2 twist and distortion and C_{Phe} out-of-plane distortion, respectively. In NAPMA due to the similar masses of the $\text{C}_{\text{Phe}}=\text{O}$ and $\text{N}-\text{CH}_3$ fragments their undergoing distortional motions are collected into a single motion, while the lower 754 cm^{-1} normal mode corresponds solely to the proximal $\text{N}-\text{H}$ bond out-of-plane bending motion. Thus additionally to the electronic differences between the NAPA and NAPMA second amide groups are also different vibrational contributions.

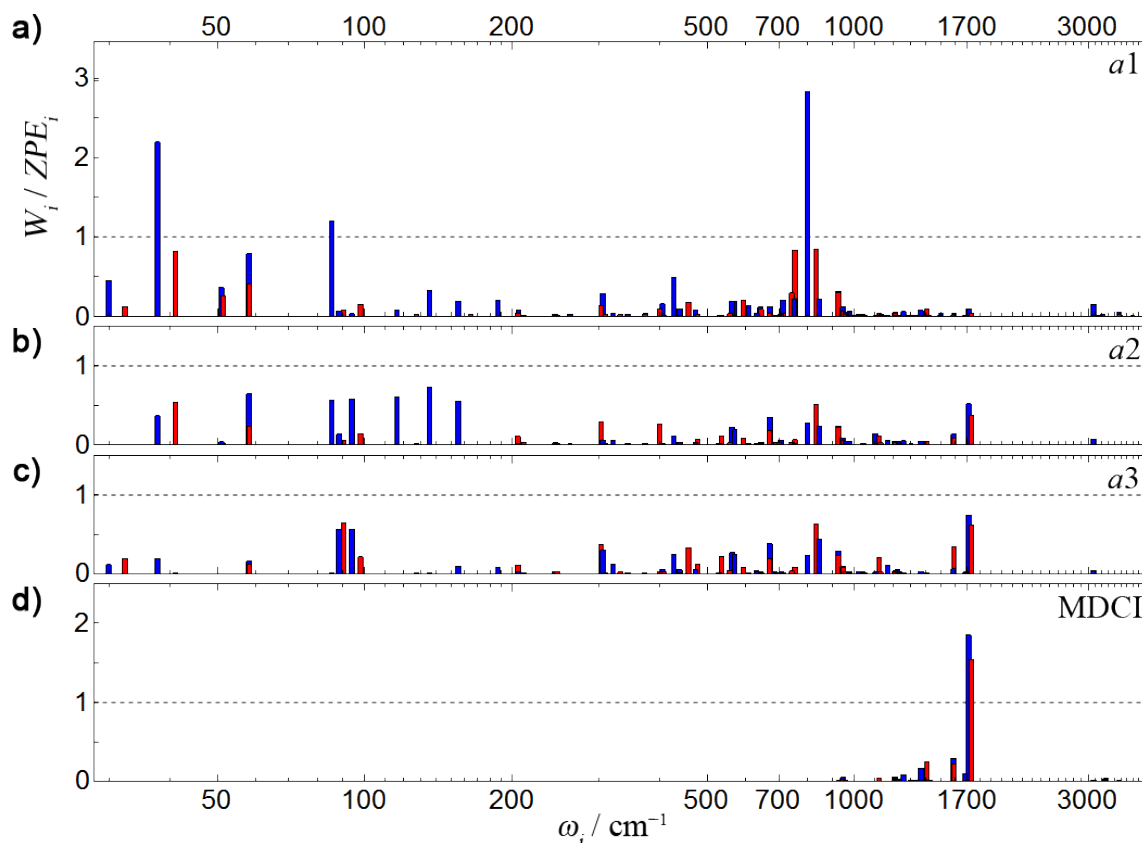


Figure 4.27: Ratio of mode's corresponding potential energy and its ZPE for NAPA (red) and NAPMA (blue): a) $a1$; b) $a2$; c) $a3$ and d) MDCI structures.

Figure 4.27 further compares the vibrational contribution between MDCI and the rest of a type CI points. While the MDCI-s are basically associated only with the extension of $\text{C}_{\text{Phe}}=\text{O}$ and contraction of phenyl $\text{C}-\text{C}$ bonds, analogue normal mode motions largely

contribute in reaching the MDCI points. The $C_{\text{Phe}}=\text{O}$ stretching mode needs to exceed the classical limit for its corresponding wave function to show a significant increase of probability density in the CI region, or in semiclassical viewpoint it needs to tunnel through the barrier in order to reach the corresponding CI point. Because this mode is strongly harmonic (see Figure 4.23) one can conclude how excitation of this mode into its first and second vibrational state would increase the probability density in the MDCI region, but these state are roughly 1730 and 3460 cm^{-1} above the ZPE energy. The $C_{\text{Phe}}=\text{O}$ mode has the largest contribution to the motion along the \mathbf{g}_0 vector. However, as vibrational analysis reveals, in all *a* type CI points the $C_{\text{Phe}}=\text{O}$ mode contribution does not exceed the classical limit. This is because the deformations of the second amide group stabilizes the MDCI type geometries and make the CI seam more accessible, but only through concerted motions of these additional deformation modes. The latter is because, as the MECIa Hessian analysis revealed, the \mathbf{h}_0 branching vector has significant contributions divided among the $\pi\pi^*$ second amide group deformation modes, while the same modes have very small contributions of the \mathbf{g}_0 vector which is associated with the $C_{\text{Phe}}=\text{O}$ stretch mode. Also, the NAPA $n\pi^*_{(\text{II})}$ state Hessian determined in $M_{\pi\pi^*}$ minimum had revealed four normal modes which involve C_{Phe} and N atom out-of-plane distortions as well as the NH_2 twisting and bending which all destabilize the S_2 state and lead to low energies intersections with S_1 state. This confirms the versatility of ways the second amide group can be deformed in order to reach the $\pi\pi^*/n\pi^*_{(\text{II})}$ CI seam (the five geometrical parameters in Table 4.7), but also indicates the necessary large size of reaction space needed to described the CI seam. Thus at least four additional coordinates, which would described the C_{Phe} and N out-of-plane deformation, the twisting of each N–H (N– CH_3) bonds (which could be incorporated into a single twisting motion in NAPA) and the extension of the $C_{\text{Phe}}\text{--N}$ bond, would be needed to include with the \mathbf{g}_0 vector in order to properly described the NAPA CI seam. All other modes would, to some certain extent, conserved the PES-s degeneracy. However, this already leads to a five/six dimensional reaction space necessary to construct and solve. In NAPMA it was also observed that the rotation of the N– CH_3 group breaks the degeneracy, so this motion could also be included in the reaction Hamiltonian. Due to anharmonicity of remaining modes which would also eventually break the degeneracy, unfortunately at at unknown energies, they would also be required to include in reaction Hamiltonian. For these reasons no attempts of exact reaction Hamiltonian constructions were made.

Nevertheless, a part of exact CI seam can be constructed using previously obtained CI-s. Because concerted motion is necessary when dealing with second amid group deformation to indirectly remove the troublesome \mathbf{h}_0 branching vector in order to keep the degeneracy, the LIP procedure between existing CI can be applied. Using the same defi-

nition of internal coordinates as in previous LIP-s, new geometries were constructed from linear interpolation and extrapolations of doublets and triplets of existing CI structures. Because the seam is analyzed in terms of classical accessibility, vibrational analysis was immediately employed in the construction of new geometries, where only the ZPE accessible were kept. The procedure is iterative, meaning that the newly constructed classically accessible geometry can be used as a starting geometry for obtaining new. Also, one can play with different variations of internal coordinates definitions. However, since the validation of PES-s degeneracy is required in every constructed structure using electronic structure calculations, the procedure becomes computationally demanding. The other problem is the very presentation of the multidimensional seam. In order to reduce the immense computational effort needed to reconstruct the $\pi\pi^*/n\pi^*_{(\text{II})}$ CI seam, construction procedure was utilized only on the *a* part of the CI seam where the starting CI-s are already classically accessible. MDCI structure was also included to examine its contribution to the seam. The procedure was run for only two iteration steps, while the second step displayed an almost converged region of ZPE accessible seam when compared to the results from the first step (not explicitly shown in results). Since the *a* type CI-s are characterized with the same ϑ_C distortion angle, two remaining angles, ϑ_N and ω_2 , together with the $C_{\text{Phe}}=\text{O}$ bond length are selected for the presentation of the CI seam, while the same coordinates change the most. Results for NAPA and NAPMA conformer B *a* part of ZPE accessible CI seam are shown in Figure 4.28.

Figure 4.28 displays the projections of the obtained CI seam surfaces (see Figure 4.28 caption). The choice of ϑ_N and ω_2 is the most obvious for subspace of projection while all discrepancies between parts of CI seam are within these two angles. The insets show further the subspace defined by $d(C_{\text{Phe}}=\text{O})$, which is the other major distinction coordinate of CI seam. Figure 4.28 clearly shows the differences between areas of classically accessible portions of $\pi\pi^*/n\pi^*_{(\text{II})}$ CI seams in NAPA and NAPMA conformer B. In some parts of the accessible area the energy gap is a bit larger (approaching 0.04 eV states separation), simply because the branching space could not be adequately separated or *h.o.d.* contribution of seam modes become more significant. The vibrational characteristics of LIP CI points are sharply exhibit and consistent with Figure 4.27, where in NAPA case the MECI*a* and *a1* are on the edge of classically accessible, while *a2* and *a3* CI are deep in the ZPE accessible region. For NAPMA, MECI*a* and *a1* are far from the classical portion. The MDCI in NAPA B does not belong to the classical part of CI seam as the inset graphic demonstrates. The relative position differences of CI points in terms of ϑ_N and ω_2 angles indicate how very similar are the CI seams of NAPA and NAPMA by size. This is an important observation because it enables the direct qualitative comparison of NAPA and NAPMA CI seams. The significant planarity of the NHCH_3 group in NAPMA is the main

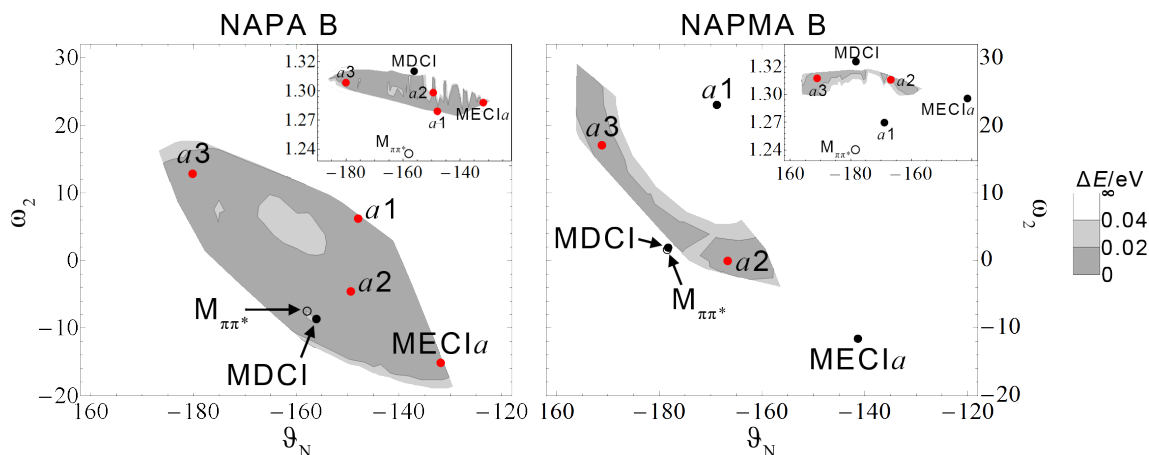


Figure 4.28: Two-dimensional projection of the classically accessible parts of $\pi\pi^*/n\pi^*_{(II)}$ a portion of NAPA (left) and NAPMA (right) CI seams in subspace spanned with ϑ_N and ω_2 angles (in degrees) obtained from 153 NAPA and 63 NAPMA structures by inter- and extrapolation procedure between doublets and triplets of existing CI structures and the first set of constructed CI geometries. The reference classically accessible LIP/MECI structures are shown with red dots, while the inaccessible by black dots. The open circle indicates the corresponding $M_{\pi\pi^*}$ structure. Shades of gray indicate the size of calculated gap between the two adiabatic states. The insets contains the same portion of the CI seam only projected to $d(C_{\text{Phe}}=\text{O})$ (vertical axis, in Å) and ϑ_N (horizontal axis, in degrees) subspace.

distinction between the two molecules second amide groups, especially prominent in the NAPMA $M_{\pi\pi^*}$ structure. The NAPA second amide NH_2 group is initially bend in $M_{\pi\pi^*}$ minimum, thus requires less change to reach the CI seam compared to NAPMA. Also NAPMA $a1$ and MECIa related parts of CI seam require significant distortion of peptide bond and $C_{\text{Phe}}=\text{O}$ bond prolongation than NAPA, which makes it vibrationally harder to access. In conclusion, the second amide group in NAPMA conformer B is more rigid than in NAPA counterpart, which for the consequence makes the NAPMA classically accessible region smaller and the classically inaccessible region larger. Any LIP constructed from the $M_{\pi\pi^*}$ minimum to CI structure is of 4.21 type, the difference being in the energy of CI and the probability density of the nuclear wave function.

To estimate the attenuation of the density probability due to the wave function passing through the barrier, the semiclassical approach of Makri and Miller for unimolecular reactions on adiabatic potential is used. [175] But with the present harmonic model only the first part of lower adiabatic $\pi\pi^*$ state PES can be described up to the CI point because the model potential for the remaining part of the barrier, which is of $n\pi^*_{(II)}$ character, is unavailable. Thus the attenuation is considered only from the classical turning point to the CI. As the authors have shown, the probability for a classical system to tunnel through the barrier and reach the CI point in one attempt once it is at the classical turning point

$(Q_{i,0})$ is

$$P_{i,\text{CI}} = |\Phi'_i(Q_{i,\text{CI}})|^2 = e^{-2\text{Im}(S_{i,\text{CI}})}, \quad (4.19)$$

where S_i is the classical action (definition in footnote 3) of the i -th normal mode in the barrier region

$$S_{i,\text{CI}} = \int_{Q_{i,0}}^{Q_{i,\text{CI}}} \dot{Q}_i dQ_i = \int_{Q_{i,0}}^{Q_{i,\text{CI}}} i\sqrt{\omega_i^2 Q_i^2/2 - \omega_i/2} dQ_i.$$

The above integral is purely imaginary while the potential energy exceeds the total. Substituting the $Q_i/Q_{i,0}$ ratio with $\alpha_i = \sqrt{W_i/ZPE_i}$ and inserting the solved integral into (4.19) finally gives the probability in the CI point

$$P_i(\alpha_i) = e^{-\alpha_i \sqrt{\alpha_i^2 - 1}} \left(\alpha + \sqrt{\alpha_i^2 - 1} \right). \quad (4.20)$$

A similar attenuation probability can be derived from the ratio of squared normal mode wave function evaluated at the CI and classical turning point giving $P_i(\alpha_i) = \exp(1 - \alpha_i^2)$ which takes into account the mode's oscillatory motion in the barrier. Regardless of the used probability formulation the final probability for the system to reach a certain CI point is the product of each mode individual probabilities

$$P(\mathbf{Q}_{\text{CI}}) = \prod_{i=1}^n P_i(\alpha_{i,\text{CI}}), \quad (4.21)$$

where only the n classically inaccessible modes are taken in the product (or the probability of classically accessible is one). Now the calculated probabilities for reaching the MECIa and a1 CI point in NAPMA conformer B are 0.10 and 0.15, respectively, compared to corresponding NAPA conformer B CI-s which are both classically accessible, and which make the former CI-s 10 and 6.7, respectively, times less accessible than the latter. Since the reduction of probability in CI seam reduces the decay constant through (4.5), the previous values roughly estimate the ratio of NAPMA conformer B and NAPA conformer B $\pi\pi^*$ excited state lifetimes to the same order as the experimental ratio ($\tau_{\text{NAPMA,B}}/\tau_{\text{NAPA,B}} = 32 \pm 6$). The wave function still needs to tunnel from the CI to the exiting classical turning point on the other side of the barrier which further reduces the probability of surface crossing. Although the probabilities need to be integrated over the entire CI seam to obtain the correct decay parameters, (4.5), the analysis shows that in the close vicinity of classically accessible part of CI seam, only few normal modes are generally inaccessible and contribute to probability reduction on the same order as NAPMA conformer B MECIa and a1 CI.

The conclusions drawn from the semiclassical consideration of the CI seam accessi-

bility are completely consistent with the approximate estimates of nuclear wave function probability in seam space. Critics might go to the use of harmonic $\pi\pi^*$ state wave function in both approaches, but as the vibrational analysis of anharmonic low frequency modes indicates only reduction of exact probability densities compared to harmonic values, the anharmonic regions of CI seam are expected not to show any significant increase of nuclear probability density. Therefore, anharmonic regions of CI seam are less accessible, and the harmonic regions of the CI seams is responsible for the difference between the systems. For the NAPA and NAPMA conformers B it is the *a* region of the CI seam that makes the distinction between molecules lifetimes. The two approaches of calculating the total probability in seam space and seam semiclassical accessibility complement each other. The former approach gives directly the probability residing in the seam, but overestimates it due to the infinite size of the seam and is built on approximate and fixed branching space. On the other hand, using accessibility considerations a real part of the CI seam was constructed, but it is only a cut through the seam space. Since classically accessible region is associated with a larger probability density, a larger ZPE cut through the seam space means a larger probability in the seam. While the ZPE accessible part of NAPA and NAPMA conformers B were constructed on the same way, but for the former conformer is larger, it validates the obtained larger total probability in NAPA conformer B seam space. Also because the branching spaces between the two systems are almost identical, they indicate how the cuts through the two seams should be equally orientated. Therefore, the two approaches clearly complement each other, and lead to the joint conclusion how the $\pi\pi^*/n\pi_{(\text{II})}^*$ CI seam in NAPA conformer B is more accessible to the $\pi\pi^*$ population than in NAPMA conformer B. Taking into account the transition probability to change diabatic states or remain in the initial adiabatic state, the nuclear population of $\pi\pi^*$ state can tunnel more efficiently through the $\pi\pi^*/n\pi_{(\text{II})}^*$ CI seam in NAPA conformer B than in NAPMA conformer B simply because the former system has a larger classically accessible part of the CI seam.

4.5.1 Mechanism II in NAPA and NAPMA conformers A and C

NAPA and NAPMA conformer C mechanisms II are completely analogue to conformer B, as similar minimum and CI structures, with similar geometrical parameters to the latter conformers, were found on their corresponding $n\pi_{(\text{II})}^*$ PES-s. Nonetheless, few significant differences exist between conformer C and conformer B structural pairs in NAPA and NAPMA, respectively. Regarding the $n\pi_{(\text{II})}^*$ PES minima, no *a2* type minimum could be obtained for NAPA conformer C and its related CI structure is also missing. But, as Table 4.10 clearly shows, only one MECI structure was found for NAPA conformer C, the MECI_b type structure which is completely analogue to the corresponding conformer B

structure. No other MECI structure could be obtained in conformers C. This is because in conformers C the phenyl ring is not in the vicinity of the O_{Phe} atom of the second amide group, which in case of NAPA conformer B divides the CI seam into two parts. Although the C_{Phe} atom pyramidalizes in both directions of ϑ_C angle, the neighbouring NH_2 group deplanarizes in only one direction when reaching the CI seam which is due to the H-bond within the γ_{L} -ring that keeps the proximal H atom always in the initial position. Apart from the structural changes in the second amide group, NAPA conformer C CI structures exhibits also a slight readjustment of their first amide group towards the second. These kind of readjustments are more pronounced in *b* type structures, where some structure also show slight phenyl ring rotation around the $C_{\beta}-C_{\text{ipso}}$ bond. Unfortunately, due to the absence of *a2* structure in NAPA conformer C, the CI seam part defined with negative ϑ_{N} angle values was left unexplored. Although results in Table 4.10 suggest how significantly narrower is the $\pi\pi^*/n\pi^*_{(\text{II})}$ CI seam size in terms of internal coordinates, since no CIs with negative ϑ_{N} angle were obtained, nothing regarding the electronic structure of NAPA conformer C supports this fact. The span of ϑ_C and ω_2 values is comparable to those of NAPA conformer B. Thus, *a priori* it cannot be concluded that the CI seam is smaller in NAPA conformer C, however, vibrational analyses indicate that the seam might be smaller on account of the classically accessible region compared to NAPA conformer B. Already, *a1* CI, which potentially leads to a minimum with negative ϑ_{N} angle, is classically inaccessible on account of NH_2 twisting modes. Values in Table 4.10 indicate how the classically accessible portion of the CI seam is restricted to a narrower variation of ϑ_C , ϑ_{N} and ω_2 values, which mostly define the size of the CI seam.

Results for NAPMA conformer C are similar to previous NAPA results. NAPMA conformer C also exhibits the restriction of N atom deplanarization to positive ϑ_{N} and up to most planar values, but it posses the *a2* type CI structures. NAPMA conformer C also has only one MECI structure, here designated as MECI*b* even though its ϑ_C value is negative. However, in strict harmonic approximation none of the obtained CI geometries are classically accessible. Anharmonicity is very significant and reflects the rigidity of the second amide group $C_{\text{Phe}}-\text{N}$ bond. Although no analogue classically accessible portions of CI seams nor the approximate branching spaces were constructed for NAPA and NAPMA conformer C as in conformer B case, the obtained results are in agreement with the experimental $\pi\pi^*$ lifetimes. The indicative classically accessible CI seam in NAPA conformer C is thus by size similar to the classically accessible part of seam in NAPMA conformer B, while the NAPMA conformer C has the smallest (not explicitly determined) classically accessible $\pi\pi^*/n\pi^*_{(\text{II})}$ CI seam among the considered γ_{L} -ring structures.

In NAPA and NAPMA conformers A the closeness of the second amide group relative to the phenyl ring fixes the former group position, which consequently narrows the size of

Table 4.10: NAPA and NAPMA conformer C $\pi\pi^*/n\pi_{(\text{II})}^*$ CI seam structures obtain from LIP-s and optimizations on the CI seam. Exact (LIP) and harmonic potential (HAR) energies are given for comparison together with the five most distinctive geometrical parameters (ϑ_C , ϑ_N , ω_2 , $d(\text{C}_{\text{Phe}}=\text{O})$ and $d(\text{C}_{\text{Phe}}-\text{N})$). The geometrical parameters for corresponding $M_{\pi\pi^*}$ structures are included as well. Classically accessible structures (4.18) are designated with bold font. Energies are in eV, torsional angles in degrees, bond lengths in Å.

	NAPA C CI _{II}							NAPMA C CI _{II}						
	LIP	HAR	ϑ_C	ϑ_N	ω_2	$d_{\text{C}=\text{O}}$	$d_{\text{C}-\text{N}}$	LIP	HAR	ϑ_C	ϑ_N	ω_2	$d_{\text{C}=\text{O}}$	$d_{\text{N}-\text{C}}$
$M_{\pi\pi^*}$	0.00	0.00	-178.9	147.4	14.1	1.237	1.369	0.00	0.00	-179.5	162.1	8.1	1.241	1.366
<i>a1</i>	0.38	0.51	-160.4	177.7	23.1	1.280	1.393	0.42	0.68	-158.8	179.7	29.6	1.269	1.407
<i>a2</i>	-	-	-	-	-	-	-	0.24	0.33	-164.0	-179.0	4.6	1.314	1.371
<i>a3</i>	0.21	0.23	-165.5	140.0	23.8	1.300	1.376	0.25	0.28	-164.9	153.3	18.7	1.311	1.372
MECI <i>b</i>	0.15	0.14	179.4	128.4	20.2	1.289	1.390	0.18	0.16	-179.7	139.3	16.6	1.298	1.385
<i>b1</i>	0.25	0.58	165.2	139.5	-4.9	1.271	1.392	0.36	0.47	162.4	156.8	-18.2	1.266	1.402
<i>b2</i>	0.23	0.24	167.5	141.2	12.7	1.298	1.374	0.28	0.31	165.9	155.5	8.4	1.311	1.371
<i>b3</i>	0.36	0.64	164.5	173.6	-5.7	1.307	1.376	0.35	0.56	163.8	-179.1	-8.3	1.315	1.372
MDCI	0.22	0.25	-179.2	145.7	15.6	1.312	1.364	0.28	0.31	-179.8	161.4	8.2	1.326	1.361

$n\pi_{(\text{II})}^*$ configuration space directly accessible from the $M_{\pi\pi^*}$ structure. Only two near local minima were obtained, distinguished by the differences in the distortions of the second amide group. The energetically more stable minimum is characterized by the $\text{C}_{\text{Phe}}=\text{O}$ group deplanarization in direction towards the phenyl ring, the other in opposite. CI-s constructed from corresponding LIP-s connecting two two minima are high in energy and both classically inaccessible. The additional methyl group in NAPMA increases the former CI energy. Corresponding MECI structures constructed from the starting LIP CI-s are lower in energy but still classically inaccessible. Thus the $\pi\pi^*/n\pi_{(\text{II})}^*$ CI seam, apart from being more narrower than the seams in conformers B and C, appears completely inaccessible in harmonic approximation, as the case of NAPMA conformer C.

Experimentally it was also observed how deuterium substitution of NH groups in the system slightly prolongs the $\pi\pi^*$ state lifetimes (Table 2.1). This is due to the ZPE effects of on the systems where particularly the constriction of the normal mode wave functions involving deuterium atom motions should be significantly exhibited. Although this effect would be captured using the full description of the CI seam accessibility which would accurately described the tunneling, with the use of rough approximations and the semiclassical approach the deuterium effect is completely unnoticeable.

4.6 Phenyl ring-puckering mechanism

Lastly, the ring-puckering mechanism of benzene [44] is reconstructed for NAPA conformer B to examine any potential effect of the backbone on the barrier of this NRD mechanism. The phenyl moiety was separately optimized at the RI-CC2/cc-pVDZ level

as benzene ring to the lowest prefulvene symmetrical MECI between the first excited and the ground electronic state using the CIOpt code and the starting structural parameters from reference [44]. The obtained S_1/S_0 CI intersection is more as an indication of the true CI. Since six distinctive positions and two puckering direction are possible in the bounded phenyl ring of NAPA, only three sites, *ortho*, *meta* and *para* closest and in direction to the $N_{\text{Phe}}\text{-H}$ bond were selected. The puckered benzene ring was then appropriately attached to the backbone and the system reoptimized to obtain the new S_1/S_0 MECI structure. The puckered phenyl ring in NAPA conformer B does not deviate much geometrically from the starting benzene CI structure. The change of the phenyl ring relative position to the backbone depends on the puckering C atom, but its effects on the local backbone structure are small, without any effect on the $N_{\text{Phe}}\text{-H}$ group, regardless of the puckering position. Constructed LIP-s between CI-s and the $M_{\pi\pi^*}$ minimum revealed approximately 0.65, 0.63 and 0.74 eV barriers for phenyl ring-puckering at *ortho*, *meta* and *para* positions, respectively. The estimated barriers are larger than the reported literature values for benzene, [43, 44] so the S_1 transition states (TS) are needed for better evaluation.

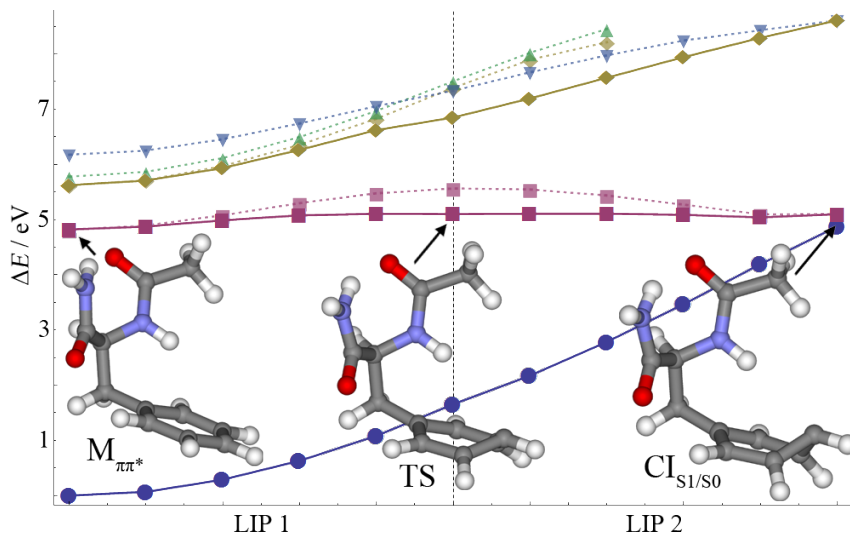


Figure 4.29: Energy profiles of two lowest excited and ground electronic states for phenyl ring-puckering NRD mechanism at the *para* C atom position in NAPA conformer B. The insets show the $M_{\pi\pi^*}$ minimum, the S_1 TS and the S_1/S_0 CI structure, respectively. The TS structure was obtained by reoptimizing the starting maximum energy geometry taken from the initial LIP between $M_{\pi\pi^*}$ and CI geometry (bordeaux dashed line). Two separate LIP-s between $M_{\pi\pi^*}$ minimum and the TS (LIP1) and between TS and CI (LIP2) are fused to obtain the full reaction profile.

The LIP maximum energy geometry was used as the best TS guess structure, while the eigenvector with negative eigenvalue for TS search was devised from the Hessian matrix of the separate benzene moiety adapting the phenyl ring structure of the TS guess structure. Figure 4.29 displays the obtained TS structure together with the MECI geometry along

the ring-puckering pathway at the *para* C position. Full vibrational analysis confirmed one imaginary frequency in the TS structure. TS-s 0.28 eV above the $M_{\pi\pi^*}$ minimum were obtained for all three ring-puckering mechanisms, which at the present level of theory are ~ 0.1 – 0.2 eV lower than the reference MC-SCF values. [43, 44]. But apart from this discrepancy in barrier height, no significant effects of the backbone on the ring-puckering mechanisms were observed. From the vibrational point of view, the ring-puckering mechanisms are inaccessible from the vibrationless states of NAPA and NAPMA conformers, as in agreement with previous theoretical studies of benzene. [28, 43–47]

4.7 Interplay of NRD mechanisms

The four obtain NRD mechanisms are among the energetically lowest deactivation pathways along which the vibrationless $\pi\pi^*$ state population can potentially deactivate to the ground state. The population competes and branches among the available NRD pathways, where the most accessible NRD channel is the dominating. As expression (4.5) indicates, under the low nuclear energy regime the accessibility of each NRD channel is determined by the probability of nuclear population reaching and passing through the corresponding CI seam. Thus the model shown in Figure 4.21 should be expanded with two additional PES of $n\pi^*_{(1)}$ and *CT* characters to take the mechanisms I and III into account and with the ring-puckering portion of the $\pi\pi^*$ PES as well. While the coupling terms are missing, details of transition probabilities could only be assess qualitatively through considerations of PES topography and vibrational accessibility of selected parts of full configuration space. But even this level proved sufficient enough to disclose the main differences between NAPA and NAPMA conformers B. However, few additional details need to be mentioned. Vibrational accessibility analysis was conducted on the remaining NRD mechanisms. As expected due to high barriers mechanism III and ring-puckering mechanism are classically inaccessible from the vibrationless state, while at the same time their tunneling contribution to the total NRD processes are completely negligible. This is because mechanism III, apart from having the highest barrier among the obtained mechanisms, is also characterized with a very wide barrier for H atom transfer to the phenyl ring. Mechanism III was also excluded experimentally since no primary kinetic isotope effect was observed, while ring-puckering mechanism is known from experimental studies on benzene not to be active in the origin of the spectrum. [42] Mechanism I, however, displays a small part of CI seam which is classically accessible. In all NAPA and NAPMA conformers this part is centered around the *Ib* type CI point which geometrically deviates the least from the $M_{\pi\pi^*}$ minimum structure and the configuration space around it is highly harmonic. But since the additional methyl group in NAPMA exhibits no significant electronic nor vibrational perturbation on the first amide group, mechanism II would

contribute to the NRD processes in NAPA and NAPAM conformers equally. Therefore, as experiment also indicates, mechanism II does not contribute to the NAPA conformer B lifetime anomaly. Lastly, the contribution of the inter system crossing (ISC) is considered on the qualitative level. ISC is the main deactivation channel of vibrationless $\pi\pi^*$ states of benzene and toluene, where the latter chromophore lifetime of 86.4 ns [29, 41] is very similar to NAPA and NAPMA lifetimes, with the exception of NAPA conformer B. It was also generalized by El-Sayed how the ISC rate in case for singlet $\pi\pi^*$ to triplet $n\pi^*$ state transfer between phenyl and N atom containing groups might be on the order of few tens of ns. [176] However, all of his observations were based in non-peptide systems. To include the triplet states in description of NRD mechanisms of NAPA and NAPMA conformers, spin coupling terms between states of different multiplicity would be required, which are unfortunately unavailable at the presently used levels of theory. Nonetheless, in Figure 4.30 representing the LIP between the $M_{\pi\pi^*}$ and $1a$ minimum all triplet triplet states within the energy window span by the singlet states were included. Figure 4.30 confirms the general trend of triplet state stability over the corresponding singlet state, which consequently makes triplet states more denser than singlet states, indicating a large possibility of mutual interaction. But the main focus is on the triplet ${}^3n\pi_{(II)}^*$ state which intersects with the phenyl singlet ${}^1\pi\pi^*$ prior to the singlet ${}^1n\pi_{(II)}^*$ PES. The ${}^1\pi\pi^*/{}^3n\pi_{(II)}^*$ intersection in Figure 4.30 is barely 0.01 eV above the $M_{\pi\pi^*}$ minimum and is classically accessible, indicating the large potential contribution of this and analogue ISC pathways. However, this observation should be generalized with grate caution. Firstly, the spin-orbit coupling terms are unknown, but behave differently from non-adiabatic coupling elements (3.9). [177,178] Secondly, due to the more pronounced stability of triplet states most of the ${}^1\pi\pi^*/{}^3n\pi_{(II)}^*$ seams are classically accessible in all NAPA and NAPMA conformers, which in a scenario where spin-orbit coupling terms are equal as non-adiabatic terms would potentially contradict the proposed mechanism in explaining the observed experimental discrepancy. Therefore, a more plausible scenario of the proposed mechanism II is that ISC between ${}^1\pi\pi^*$ and ${}^3n\pi_{(II)}^*$ states is less dominating than the singlet-singlet interaction term, or that when expression (4.5) when properly evaluated for singlet-triplet interaction behaves completely analogue to proposed mechanism II singlet-singlet decay contribution. An experimental insight into the optically dark state would help revealed the puzzling questions.

However, regardless whether mechanism II is of only single multiplicity or acquires a fraction of single-triplet state mixing, the more favorable accessibility of the second amide group $n\pi^*$ state over other low laying states determines its larger contribution in the NRD processes of NAPA conformers. As was clearly shown, methylation of the NAPA primary NH_2 group causes a significant increase of second amide group rigidity towards

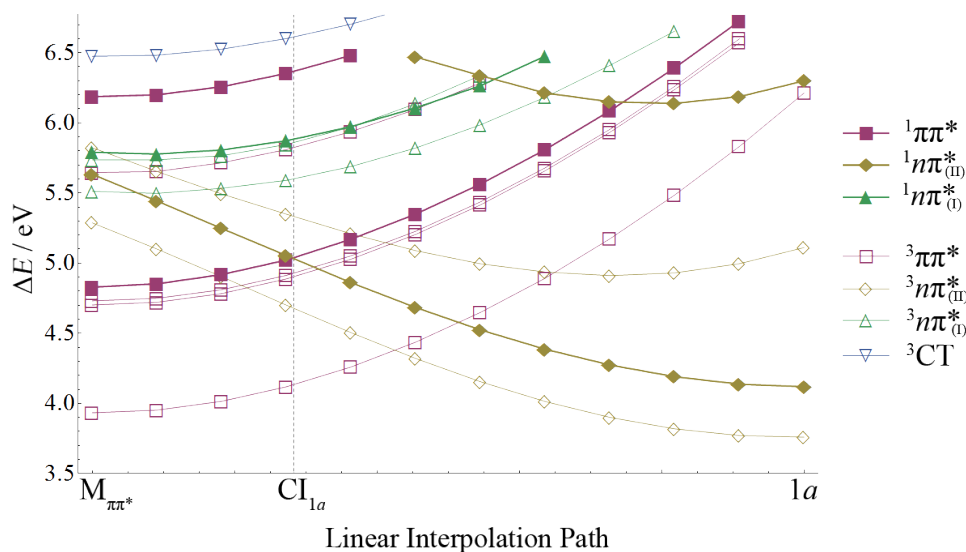


Figure 4.30: LIP between $M_{\pi\pi^*}$ and M_{a1} minima geometries with included triplet excited states. The vertical deliniator indicates the position of the ${}^1\pi\pi^*/{}^1n\pi_{(II)}^*$ CI. The adiabatic states are designated according to their characters (legend on the right side of image), which are here distinguished only by excitation location within the molecule.

out-of-plane distortional motions which are solely responsible for the accessibility of lower energy parts of $\pi\pi^*/n\pi_{(II)}^*$ CI seam. The increase of the second amide group rigidity is caused by the change of second amide group local electronic structure, but also to the increase of mass attached to it. The methyl group acts as electron donating group and stabilizes the entire amide group by strengthening the $C_{\text{Phe}}\text{-N}$ conjugation as well as the N-CH_3 bond, but also the $C_{\text{Phe}}=\text{O}$ and beyond through non-bonding interactions. The increase of mass on the position of the distal H atom changes the normal mode composition of the second amide group, which also influences other modes in the molecule and the total ZPE. The increase of mass basically increases the inertia of second amide group towards its distortion, which in quantum description is simply the narrowing of the corresponding mode wave function. Both effects contribute to the decrease of accessibility of the $\pi\pi^*/n\pi_{(II)}^*$ CI seam, which in semi-classical approximation is regarded as the reduction of classically available part of the same CI seam. In the full description, the effect is simply determined by tunneling efficiency through the entire CI seam, (4.5). This difference is highly pronounced between NAPA and NAPMA conformers B, while the trend is also exhibited between NAPA and NAPMA conformers C but on a reduce scale. The difference between NRD mechanism II efficiency in conformers B and C is caused by the phenyl ring position, where in the latter case the absence of phenyl ring interactions with the second amide group, mostly through the non-bonding interaction with the $C_{\text{Phe}}=\text{O}$ group, increases the stiffness of the same amide group, which consequently reduces the ZPE accessible part of CI seam. The size and highly unfavorable accessibility

of analogue CI seams in NAPA and NAPMA conformers A hinders the mechanism II up to a level where it competes equally or is even surpassed by the singlet-triplet phenyl state ISC NRD mechanism as the similarities between conformer A excited state lifetimes and toluene lifetime indicate. On equal grounds one can consider the contribution of ISC mechanism in NAPMA conformer C.

5 Conclusion

NAPA and NAPMA conformers display a large variety of NRD mechanisms due to a number of low lying dark electronic states. However, under the investigated vibrationless conditions only the lowest most accessible NRD mechanisms are relevant. Among them all theoretical and available experimental evidence point out that mechanism II should be the dominating one. In all other conformers mechanism II appears less dominating and competes with other available NRD pathways, where the ISC seems to be the best alternative choice when mechanism II is hindered. The contribution of each NRD channel is controlled by the nuclear wave function accessibility of each CI seam. Thus any excess of vibrational energy in a particular mode, which promotes the nuclear population towards a particular CI seam, is expected to increase the activity of certain NRD mechanisms. Such observations were made recently by Loquias *et al.* on a particular Ac-Gly-Phe-NH₂ conformer whose lowest progression states above the S₁ origin exhibit a decrease of excited state lifetime compared to the origin lifetime. [179] This conformer is of 2₇ secondary structure whose local -CO-Phe-NH₂ part resembles exactly the NAPA conformer C structure. Because its methylated counterpart (Ac-Gly-Phe-NHMe) shows no effect of excited state lifetime dependence on the excess of vibrational energy of its lowest progression modes one can conclude how mechanism II is at play in Ac-Gly-Phe-NH₂ conformer. Although the details are missing, the mechanism clearly displays the dependence of its activity on the excess of vibrational energy. In line with previous conclusions, these observations confirm how methylation of the second amide group inactivates mechanism II. Additionally, the complete structural analogy between NAPMA conformer B and NATMA conformer C [32] indicates how mechanism II can significantly contribute to the explanation of observed phenomena [27] in the latter conformer.

The strategy of refining potential NRD mechanisms obtained from non-adiabatic molecular dynamics simulations was also proven fruitful. Because no direct attempts were made to reproduce the exact wave packet propagation and with it the experimental lifetime, initial conditions for non-adiabatic trajectories were deliberately chosen with excess kinetic energy for efficient screening of potential NRD mechanisms. Even as the LR-TDDFT method generally proved inadequate for the problem at hand, nonetheless, with meticulous refinement of all observed mechanism at the CC2 level three potential NRD processes in NAPA were obtained. Thus, additionally to mechanism II, mechanism I and mechanism III were obtained and characterized, and although not active under the present conditions, mechanisms represent potential NRD processes in Phe containing peptide systems. Mechanism I is completely analogue to mechanism II. Viewing the first amide group as second but only with reversed orientation in respect to the C_α atom, the rigidness of the first amide group is immediately evident. Additionally to the phenyl ππ*

state depopulation mechanisms, NRD pathways to the ground electronic state were also considered for excited amide groups within the model peptide and confirmed the analogy with the NRD pathways of formamide [58] and acetamide [169]. Even though deactivation mechanism involving CT state and accompanied with H atom transfer [30–32,62] was observed among non-adiabatic trajectories, its relevance, however, to the NRD processes bringing the system to the ground state appear no more important than the deactivation mechanisms involving simple C=O bond predissociation.

One can now generalized all conclusions to any Phe containing peptide system. The presence of amide group of peptide bonds endow the system with a number of low laying dark excited states which enable the excitation transfer mechanism from phenyl $\pi\pi^*$ to amide group $n\pi^*$ states, from which the excited state population can further deactivate to the ground state in a number of favorable NRD process. Therefore, the rigidity of the amide group towards its own out-of-plane distortions determines its contribution to the total activity of the population transfer mechanisms, where the stiff portions of peptide chain are expected to contribute less than the more flexible ones. Thus glutamine (Gln) and asparagine (Asn) side chains, which posses a primary amide group, can act as potential quenchers of phenyl, or any other conjugated ring, $\pi\pi^*$ excitation. Also, as theory and experiment predict, any excess of vibrational energy due to vibronic excitation or simply temperature, which is expected under real life circumstances, further enhances the activity of proposed NRD mechanisms.

6 References

- [1] R. F. Steiner, I. Weinryb, *Excited States of Proteins and Nucleic Acids*, Plenum Press, New York and London, 1971.
- [2] J. R. Lakowicz, *Principles of Fluorescence Spectroscopy*, 3rd Edition, Springer, Singapore, 2006.
- [3] L. J. Mittal, J. P. Mittal, E. Hayon, *J. Am. Chem. Soc.* **95** (1973) 6203–6210.
- [4] G. Laustriat, C. Hasselmann, *Photochem. Photobiol.* **22** (1975) 295–298.
- [5] D. V. Bent, E. Hayon, *J. Am. Chem. Soc.* **97** (1975) 2612–2619.
- [6] D. V. Bent, E. Hayon, *J. Am. Chem. Soc.* **97** (1975) 2599–2606.
- [7] D. V. Bent, E. Hayon, *J. Am. Chem. Soc.* **97** (1975) 2606–2612.
- [8] O. P. Ernst, D. T. Lodowski, M. Elstner, P. Hegemann, L. S. Brown, H. Kandori, *Chem. Rev.* **114** (2014) 126–163.
- [9] T. Barros, W. Kühlbrandt, *Biochim. Biophys. Acta* **1787** (2009) 753–772.
- [10] Y.-C. Cheng, G. R. Fleming, *Annu. Rev. Phys. Chem.* **60** (2009) 241–262.
- [11] R. Y. Tsien, *Annu. Rev. Biochem.* **67** (1998) 509–544.
- [12] N. C. Shaner, G. H. Patterson, M. W. Davidson, *J. Cell Sci.* **120** (2007) 4247–4260.
- [13] T. D. Craggs, *Chem. Soc. Rev.* **38** (2009) 2865–2875.
- [14] C. Sagan, *J. Theor. Biol.* **39** (1973) 195–200.
- [15] A. L. Sobolewski, W. Domcke, *ChemPhysChem* **7** (2006) 561–564.
- [16] A. L. Sobolewski, W. Domcke, *Phys. Chem. Chem. Phys.* **12** (2010) 4897–4898.
- [17] W. Domcke, A. L. Sobolewski, *Nat. Chem.* **5** (2013) 257–258.
- [18] F. Tekaia, E. Yeramian, B. Dujon, *Gene* **297** (2002) 51–60.
- [19] T. Hashimoto, Y. Takasu, Y. Yamada, E. Takayuki, *Chem. Phys. Lett.* **421** (2006) 227–231.
- [20] W. Chin, M. Mons, J.-P. Dognon, R. Mirasol, G. Chass, I. Dimicoli, F. Piuzzi, P. Butz, B. Tardivel, I. Compagnon, G. von Helden, G. Meijer, *J. Phys. Chem. A* **109** (2005) 5281–5288.

- [21] H. Valdés, V. Spiwok, J. Rezac, D. Řeha, A. Abo-Riziq, M. deVries, P. Hobza, *Chem. Eur. J.* **14** (2008) 4886–4898.
- [22] C. Toniolo, *CRC Crit. Rev. Bio.* **9** (1980) 1–44.
- [23] M. Mališ, Y. Loquais, E. Gloaguen, H. S. Biswal, F. Piuzzi, B. Tardivel, V. Brenner, M. Broquier, C. Jouvét, M. Mons, N. Došlić, I. Ljubić, *J. Am. Chem. Soc.* **134** (2012) 20340–20351.
- [24] H. Valdés, D. Řeha, P. Hobza, *J. Phys. Chem. B* **110** (2006) 6385–6396.
- [25] A. Šarić, T. Hrenar, M. Mališ, N. Došlić, *Phys. Chem. Chem. Phys.* **12** (2010) 4678–4685.
- [26] B. C. Dian, A. Longarte, S. Mercier, D. A. Evans, D. J. Wales, T. S. Zwier, *J. Chem. Phys.* **117** (2002) 10688–10702.
- [27] B. C. Dian, A. Longarte, T. S. Zwier, *J. Chem. Phys.* **118** (2003) 2696–2706.
- [28] B. R. Smith, M. J. Bearpark, M. A. Robb, F. Bernardi, M. Olivucci, *Chem. Phys. Lett.* **242** (1995) 27–32.
- [29] T. G. Dietz, M. A. Duncan, R. E. Smalley, *J. Phys. Chem.* **76** (1982) 1227–1232.
- [30] D. Shemesh, C. Hattig, W. Domcke, *Chem. Phys. Lett.* **482** (2009) 38–43.
- [31] D. Shemesh, A. L. Sobolewski, W. Domcke, *J. Am. Chem. Soc.* **131** (2009) 1374–1375.
- [32] D. Shemesh, A. L. Sobolewski, W. Domcke, *Phys. Chem. Chem. Phys.* **12** (2010) 4899–4905.
- [33] M. Mališ, Y. Loquais, E. Gloaguen, C. Jouvét, V. Brenner, M. Mons, I. Ljubić, N. Došlić, *Phys. Chem. Chem. Phys.* **16** (2014) 2285–2288.
- [34] Y. Loquais, Chaines peptidiques modèles en détente supersonique: Refroidissement conformationnel, structures et dynamique des états excités étudiés par modélisation monte-carlo, spectroscopies laser et chimie quantique, Ph.D. thesis, Université Paris-Sud, Orsay, France (2013).
- [35] M. Gerhards, C. Unterberg, A. Gerlach, A. Jansen, *Phys. Chem. Chem. Phys.* **6** (2004) 2682–2690.

- [36] G. A. Chass, R. S. Mirasol, D. H. Setiadi, T.-H. Tang, W. Chin, M. Mons, I. Dimicoli, J.-P. Dognon, B. Viskolcz, S. Lovas, B. Penke, I. G. Csizmadia, *J. Phys. Chem. A* **109** (2005) 5289–5302.
- [37] A. Šarić, Vibracijska analiza najstabilnijih konformera zaštićenih dipeptida, Master's thesis, Faculty of Science, University of Zagreb (2008).
- [38] N. Došlić, G. Kovačević, I. Ljubić, *J. Phys. Chem. A* **111** (2007) 8650–8658.
- [39] A. Bernhardsson, N. Forsberg, P.-A. Malmqvist, B. O. Roos, L. Serrano-Andrés, *J. Chem. Phys.* **112** (2000) 2798–2809.
- [40] J. Li, C.-K. Lin, X. Y. Li, C. Y. Zhu, S. H. Lin, *Phys. Chem. Chem. Phys.* **12** (2010) 14967–14976.
- [41] C. G. Hickman, J. R. Gascooke, W. D. Lawrance, *J. Chem. Phys.* **104** (1996) 4887–4901.
- [42] B. K. Selinger, W. R. Ware, *J. Chem. Phys.* **53** (1970) 3160–3168.
- [43] A. L. Sobolewski, C. Woywod, W. Domcke, *J. Chem. Phys.* **98** (1993) 5627–5641.
- [44] I. J. Palmer, I. N. Ragazos, F. Bernardi, M. Olivucci, M. A. Robb, *J. Am. Chem. Soc.* **115** (1993) 673–682.
- [45] A. Toniolo, A. L. Thompson, T. J. Martínez, *Chem. Phys.* **304** (2004) 133–145.
- [46] B. Lasorne, M. J. Bearpark, M. A. Robb, G. A. Worth, *J. Phys. Chem. A* **112** (2008) 13017–13027.
- [47] Q. Li, D. Mendive-Tapia, M. J. Paterson, A. Migani, M. J. Bearpark, M. A. Robb, L. Blancafort, *Chem. Phys.* **377** (2010) 60–65.
- [48] B. K. Selinger, W. R. Ware, *J. Chem. Phys.* **52** (1970) 5482–5483.
- [49] J. H. Callomon, J. E. Parkin, R. Lopez-Delgado, *Chem. Phys. Lett.* **13** (1972) 125–131.
- [50] E. Riedle, H. J. Neusser, E. W. Schlag, *J. Phys. Chem.* **86** (1982) 4847–4850.
- [51] C. E. Otis, J. L. Knee, P. M. Johnson, *J. Phys. Chem.* **87** (1983) 2232–2239.
- [52] M. Sumitani, D. V. O'Connor, Y. Takagi, N. Nakashima, K. Kamogawa, Y. Udagawa, K. Yoshihara, *Chem. Phys.* **93** (1985) 359–371.

- [53] D. Parker, R. Minns, T. Penfold, G. Worth, H. Fielding, *Chem. Phys. Lett.* **469** (2009) 43–47.
- [54] L. Serrano-Andrés, M. P. Fülcher, *J. Am. Chem. Soc.* **118** (1996) 12190–12199.
- [55] L. Serrano-Andrés, M. P. Fülcher, *J. Am. Chem. Soc.* **118** (1996) 12200–12206.
- [56] L. Serrano-Andrés, M. P. Fülcher, *J. Am. Chem. Soc.* **120** (1998) 10912–10920.
- [57] D. Liu, W.-H. Fang, X.-Y. Fu, *Chem. Phys. Lett.* **318** (2000) 291–297.
- [58] I. Antol, M. Eckert-Maksić, M. Barbatti, H. Lischka, *J. Chem. Phys.* **127** (2007) 234303.
- [59] J. Lundell, M. Krajewska, M. Räsänen, *J. Phys. Chem. A* **102** (1998) 6643–6650.
- [60] A. L. Sobolewski, W. Domcke, C. Hättig, *Proc. Natl. Acad. Sci. U.S.A.* **102** (2005) 17903–17906.
- [61] R. N. Dixon, T. A. A. Oliver, M. N. R. Ashfold, *J. Chem. Phys.* **134** (2011) 194303.
- [62] D. Shemesh, W. Domcke, *ChemPhysChem* **12** (2011) 1833–1840.
- [63] E. Gloaguen, F. Pagliarulo, V. Brenner, W. Chin, F. Piuuzzi, B. Tardivel, M. Mons, *Phys. Chem. Chem. Phys.* **9** (2007) 4491–4497.
- [64] S. R. Mercier, O. V. Boyarkin, A. Kamariotis, M. Guglielmi, I. Tavernelli, M. Cascella, U. Rothlisberger, T. R. Rizzo, *J. Am. Chem. Soc.* **128** (2006) 16938–16943.
- [65] J. C. Tully, *Farad. Discuss.* **110** (1998) 407–419.
- [66] J.-Y. Fang, S. Hammes-Schiffer, *J. Chem. Phys.* **110** (1999) 11166–11175.
- [67] M. D. Hack, D. G. Truhlar, *J. Phys. Chem. A* **104** (2000) 7917–7926.
- [68] A. Abedi, N. T. Maitra, E. K. U. Gross, *Phys. Rev. Lett.* **105** (2010) 123002.
- [69] F. F. de Carvalho, M. E. F. Bouduban, B. F. E. Curchod, I. Tavernelli, *Entropy* **16** (2013) 62–85.
- [70] R. P. Feynman, *Phys. Rev.* **56** (1939) 340–343.
- [71] P. R. Bunker, P. Jensen, *Molecular Symmetry and Spectroscopy*, 2nd Edition, NRC Research Press, Ottawa, Canada, 1998.
- [72] M. Mališ, Tuneliranje uzrokovano cijepanje osnovnog vibracijskog stanja u dimerima mravlje kiseline, Master's thesis, Faculty of Science, University of Zagreb (2009).

- [73] L. S. Cederbaum, *J. Chem. Phys.* **138** (2013) 224110.
- [74] C. Eckart, *Phys. Rev.* **47** (1935) 552–558.
- [75] I. Matanović, N. Došlić, B. R. Johnson, *J. Chem. Phys.* **128** (2008) 084103.
- [76] M. Baer, *Beyond Born-Oppenheimer: Electronic Nonadiabatic Coupling Terms and Conical Intersections*, John Wiley and Sons, Inc., Hoboken, New Jersey, 2006.
- [77] C. A. Mead, D. G. Truhlar, *J. Chem. Phys.* **77** (1982) 6090–6098.
- [78] M. Baer, R. Englman, *Mol. Phys.* **75** (1992) 293–303.
- [79] W. Domcke, D. R. Yarkony, H. Köppel, *Conical Intersections: Electronic Structure, Dynamics and Spectroscopy*, Advanced Series in Physical Chemistry, World Scientific, Singapore, 2004.
- [80] T. V. Voorhis, T. Kowalczyk, B. Kaduk, L.-P. Wang, C.-L. Cheng, Q. Wu, *Annu. Rev. Phys. Chem.* **61** (2010) 149–170.
- [81] H. J. Werner, W. Meyer, *J. Chem. Phys.* **74** (1981) 5802–5807.
- [82] C. E. Hoyer, X. Xu, D. Ma, L. Gagliardi, D. G. Truhlar, *J. Chem. Phys.* **141** (2014) 114104.
- [83] D. R. Yarkony, *J. Phys. Chem. A* **105** (2001) 6277–6293.
- [84] S. Yang, T. J. Martínez, Ab initio multiple spawning: First principles dynamics around conical intersections, in: W. Domcke, D. R. Yarkony, H. Köppel (Eds.), *Conical Intersections: Theory, Computation and Experiment*, Advanced Series in Physical Chemistry, World Scientific, 2011.
- [85] B. G. Levine, C. Ko, J. Quenneville, T. J. Martínez, *Mol. Phys.* **104** (2006) 1039–1051.
- [86] J. P. Malhado, M. J. Bearpark, J. T. Hynes, *Frontiers in Chemistry* **2** (2014) 1–21.
- [87] S. K. Min, A. Abedi, S. Kim, E. Gross, *arXiv:1402.0227v1* .
- [88] D. Yarkony, *Rev. Mod. Phys.* **68** (1996) 985–1013.
- [89] B. F. E. Curchod, I. Tavernelli, *J. Chem. Phys.* **138** (2013) 184112.
- [90] C. L. Lopreore, R. E. Wyatt, *Phys. Rev. Lett.* **82** (1999) 5190–5193.

- [91] R. E. Wyatt, *Quantum Dynamics with Trajectories: Introduction to Quantum Hydrodynamics*, Springer, Dordrecht, 2006.
- [92] J. Suñé, X. Oriols, *Phys. Rev. Lett.* **85** (2000) 894–894.
- [93] C. L. Lopreore, R. E. Wyatt, *Phys. Rev. Lett.* **85** (2000) 895–895.
- [94] B. K. Kendrick, *J. Chem. Phys.* **119** (2003) 5805–5817.
- [95] B. F. E. Curchod, I. Tavernelli, U. Rothlisberger, *Phys. Chem. Chem. Phys.* **13** (2011) 3231–3236.
- [96] I. Tavernelli, *Phys. Rev. A* **87** (2013) 042501.
- [97] I. Horenko, C. Salzmann, B. Schmidt, C. Schtte, *J. Chem. Phys.* **117** (2002) 11075–11088.
- [98] G. Granucci, M. Persico, *J. Chem. Phys.* **126** (2007) 134114.
- [99] J. C. Tully, *J. Chem. Phys.* **93** (1990) 1061–1071.
- [100] C. Zhu, S. Nangia, A. W. Jasper, D. G. Truhlar, *J. Chem. Phys.* **121** (2004) 7658–7670.
- [101] C. Zhu, A. W. Jasper, D. G. Truhlar, *J. Chem. Phys.* **120** (2004) 5543–5557.
- [102] C. Zhu, A. W. Jasper, D. G. Truhlar, *J. Chem. Theory Comput.* **1** (2005) 527–540.
- [103] G. Granucci, M. Persico, A. Zocante, *J. Chem. Phys.* **133** (2010) 134111.
- [104] N. Shenvi, J. E. Subotnik, W. Yang, *J. Chem. Phys.* **135** (2011) 024101.
- [105] N. Shenvi, W. Yang, *J. Chem. Phys.* **137** (2012) 22A528.
- [106] S. Hammes-Schiffer, J. C. Tully, *J. Chem. Phys.* **101** (1994) 4657–4667.
- [107] R. Mitrić, U. Werner, V. Bonačić-Koutecký, *J. Chem. Phys.* **129** (2008) 164118.
- [108] J. C. Tully, *Int. J. Quant. Chem.* **40** (1991) 299–309.
- [109] J. C. Tully, R. K. Preston, *J. Chem. Phys.* **55** (1971) 562–572.
- [110] M. F. Herman, *J. Chem. Phys.* **81** (1984) 754–763.
- [111] M. Barbatti, *Wiley Interdiscip Rev. Comput. Mol. Sci.* **1** (2011) 620–633.

- [112] M. S. Topaler, T. C. Allison, D. W. Schwenke, D. G. Truhlar, *J. Phys. Chem. A* **102** (1998) 1666–1673.
- [113] M. E. Casida, Recent advances in density functional methods, Vol. Volume 1 of *Recent Advances in Computational Chemistry*, World Scientific, Singapore, 1995, Ch. Time-dependent density-functional response theory for molecules, p. 155.
- [114] C. Hu, H. Hirai, O. Sugino, *J. Chem. Phys.* **127** (2007) 064103.
- [115] E. Tapavicza, I. Tavernelli, U. Rothlisberger, *Phys. Rev. Lett.* **98** (2007) 023001.
- [116] E. Tapavicza, I. Tavernelli, U. Rothlisberger, C. Filippi, M. E. Casida, *J. Chem. Phys.* **129** (2008) 124108.
- [117] U. Werner, R. Mitrić, T. Suzuki, V. Bonačić-Koutecký, *Chem. Phys.* **349** (2008) 319–324.
- [118] I. Tavernelli, B. F. E. Curchod, U. Rothlisberger, *J. Chem. Phys.* **131** (2009) 196101.
- [119] I. Tavernelli, E. Tapavicza, U. Rothlisberger, *J. Chem. Phys.* **130** (2009) 124107.
- [120] B. F. E. Curchod, U. Rothlisberger, I. Tavernelli, *ChemPhysChem* **14** (2013) 1314–1340.
- [121] I. Tavernelli, B. F. E. Curchod, A. Laktionov, U. Rothlisberger, *J. Chem. Phys.* **133** (2010) 194104.
- [122] C. Cohen-Tannoudji, B. Diu, F. Laloë, *Quantum Mechanics (2 vol. set)*, Wiley-Interscience, 1992.
- [123] C. A. Ullrich, *Time-Dependent Density-Functional Theory: Concepts and Applications*, Oxford University Press Inc., New York, 2012.
- [124] M. A. L. Marques, N. T. Maitra, F. M. S. Nogueira, E. K. U. Gross, A. Rubio (Eds.), *Fundamentals of Time-Dependent Density Functional Theory*, Vol. 837 of *Lecture Notes in Physics*, Springer Berlin Heidelberg, 2012.
- [125] E. J. Baerends, O. V. Gritsenko, *J. Phys. Chem. A* **101** (1997) 5383–5403.
- [126] M. E. Casida, *Comp. Theor. Chem.* **914** (2009) 3–18.
- [127] D. A. Strubbe, L. Lehtovaara, A. Rubio, M. A. L. Marques, S. G. Louie, Response functions in tddft: Concepts and implementation, in: M. A. Marques, N. T. Maitra,

- F. M. Nogueira, E. Gross, A. Rubio (Eds.), Fundamentals of Time-Dependent Density Functional Theory, Vol. 837 of *Lecture Notes in Physics*, Springer Berlin Heidelberg, 2012, pp. 139–166.
- [128] F. Furche, *J. Chem. Phys.* **114** (2001) 5982–5992.
- [129] A. Szabo, N. S. Ostlund, *Modern quantum chemistry: introduction to advanced electronic structure theory*, Dover publications, Inc., New York, 1996.
- [130] S. Tretiak, V. Chernyak, *J. Chem. Phys.* **119** (2003) 8809–8823.
- [131] D. Marx, J. Hutter, *Ab Initio Molecular Dynamics: Basic Theory and Advanced Methods*, Cambridge University Press, Cambridge, 2009.
- [132] L. Shampine, M. Gordon, *Computer Solution of Ordinary Differential Equations: The Initial Value Problem*, Freeman, 1975.
- [133] TURBOMOLE V6.6 2014, a development of University of Karlsruhe and Forschungszentrum Karlsruhe GmbH, 1989-2007, TURBOMOLE GmbH, since 2007; available from <http://www.turbomole.com>.
- [134] J. Novak, M. Mališ, A. Prlj, I. Ljubić, O. Kühn, N. Došlić, *J. Phys. Chem. A* **116** (2012) 11467–11475.
- [135] D. Tuna, N. Došlić, M. Mališ, A. L. Sobolewski, W. Domcke, *J. Phys. Chem. B* **119** (2015) 2112–2124.
- [136] J. Novak, M. Mališ, G. Zgrablić, F. Parmigiani, D. Nađa, Ultrafast non-reactive deactivation induced by excited state hole transfer from retinal chromophore to counterion, manuscript submitted for publication (2015).
- [137] M. Sapunar, S. Chaiwongwattana, M. Momir, A. Prlj, A. Ponzi, P. Decleva, D. Nađa, Timescales of N-H bond dissociation in pyrrole: a nonadiabatic dynamics study, manuscript submitted for publication (2015).
- [138] C. Hättig, F. Weigend, *J. Chem. Phys.* **113** (2000) 5154–5161.
- [139] C. Hättig, A. Hellweg, A. Köhn, *Phys. Chem. Chem. Phys.* **8** (2006) 1159–1169.
- [140] C. Adamo, V. Barone, *J. Chem. Phys.* **110** (1999) 6158–6170.
- [141] A. D. Becke, *J. Chem. Phys.* **98** (1993) 1372–1377.
- [142] J. P. Perdew, K. Burke, M. Ernzerhof, *Phys. Rev. Lett.* **77** (1996) 3865–3868.

- [143] J. P. Perdew, K. Burke, M. Ernzerhof, *Phys. Rev. Lett.* **78** (1997) 1396–1396.
- [144] T. H. Dunning, *J. Chem. Phys.* **90** (1989) 1007–1023.
- [145] R. A. Kendall, T. H. Dunning, R. J. Harrison, *J. Chem. Phys.* **96** (1992) 6796–6806.
- [146] A. Schäfer, C. Huber, R. Ahlrichs, *J. Chem. Phys.* **100** (1994) 5829–5835.
- [147] F. Weigend, A. Köhn, C. Hättig, *J. Chem. Phys.* **116** (2002) 3175–3183.
- [148] F. Weigend, M. Häser, H. Patzelt, R. Ahlrichs, *Chem. Phys. Lett.* **294** (1998) 143–152.
- [149] M. J. Frisch, G. W. Trucks, H. B. Schlegel, G. E. Scuseria, M. A. Robb, J. R. Cheeseman, G. Scalmani, V. Barone, B. Mennucci, G. A. Petersson, H. Nakatsuji, M. Caricato, X. Li, H. P. Hratchian, A. F. Izmaylov, J. Bloino, G. Zheng, J. L. Sonnenberg, M. Hada, M. Ehara, K. Toyota, R. Fukuda, J. Hasegawa, M. Ishida, T. Nakajima, Y. Honda, O. Kitao, H. Nakai, T. Vreven, J. A. Montgomery, Jr., J. E. Peralta, F. Ogliaro, M. Bearpark, J. J. Heyd, E. Brothers, K. N. Kudin, V. N. Staroverov, R. Kobayashi, J. Normand, K. Raghavachari, A. Rendell, J. C. Burant, S. S. Iyengar, J. Tomasi, M. Cossi, N. Rega, J. M. Millam, M. Klene, J. E. Knox, J. B. Cross, V. Bakken, C. Adamo, J. Jaramillo, R. Gomperts, R. E. Stratmann, O. Yazyev, A. J. Austin, R. Cammi, C. Pomelli, J. W. Ochterski, R. L. Martin, K. Morokuma, V. G. Zakrzewski, G. A. Voth, P. Salvador, J. J. Dannenberg, S. Dapprich, A. D. Daniels, . Farkas, J. B. Foresman, J. V. Ortiz, J. Cioslowski, D. J. Fox, Gaussian 09 Revision D.01, Gaussian Inc. Wallingford CT 2009.
- [150] F. Plasser, R. Crespo-Otero, M. Pederzoli, J. Pittner, H. Lischka, M. Barbatti, *J. Chem. Theory Comput.* **10** (2014) 1395–1405.
- [151] Mathematica Version 10.0, Wolfram Research Inc., Champaign, Illinois, 2014.
- [152] B. G. Levine, J. D. Coe, T. J. Martínez, *J. Phys. Chem. B* **112** (2008) 405–413.
- [153] C. L. Janssen, I. M. Nielsen, *Chem. Phys. Lett.* **290** (1998) 423–430.
- [154] I. M. Nielsen, C. L. Janssen, *Chem. Phys. Lett.* **310** (1999) 568 – 576.
- [155] A. Köhn, C. Hättig, *J. Chem. Phys.* **119** (2003) 5021–5036.
- [156] R. Dennington, T. Keith, J. Millam, GaussView Version 5, Semichem Inc. Shawnee Mission KS 2009.
- [157] Z. Wang, F. Wang, *Theor. Chem. Acc.* **133** (2014) 1579.

- [158] C. Ove, K. Henrik, J. Poul, H. Trygve, *Chem. Phys. Lett.* **263** (1996) 530–539.
- [159] A. E. Reed, R. B. Weinstock, F. Weinhold, *J. Chem. Phys.* **83** (1985) 735–746.
- [160] I. Saito, H. Sugiyama, A. Yamamoto, S. Muramatsu, T. Matsuura, *J. Am. Chem. Soc.* **106** (1984) 4286–4287.
- [161] H. Shizuka, M. Serizawa, T. Shimo, I. Saito, T. Matsuura, *J. Am. Chem. Soc.* **110** (1988) 1930–1934.
- [162] L. Blancafort, D. González, M. Olivucci, M. A. Robb, *J. Am. Chem. Soc.* **124** (22) (2002) 6398–6406.
- [163] A. M. Gardner, A. M. Green, V. M. Tamé-Reyes, V. H. K. Wilton, T. G. Wright, *J. Chem. Phys.* **138** (2013) 134303.
- [164] H. F. Hameka, J. O. Jensen, *Comp. Theor. Chem.* **331** (1995) 203–214.
- [165] W. Hieringer, A. Görling, *Chem. Phys. Lett.* **419** (2006) 557–562.
- [166] G. Tomasello, M. Wohlgemuth, J. Petersen, R. Mitrić, *J. Phys. Chem. B* **116** (2012) 8762–8770.
- [167] G. Grégoire, C. Jouvét, C. Dedonder, A. L. Sobolewski, *J. Am. Chem. Soc.* **129** (2007) 6223–6231.
- [168] R. J. Lipert, G. Bermudez, S. D. Colson, *J. Phys. Chem.* **92** (1988) 3801–3805.
- [169] M. Eckert-Maksić, I. Antol, M. Vazdar, *Comp. Theor. Chem.* **1040-1041** (2014) 136–143.
- [170] L. S. Cederbaum, R. S. Friedman, V. M. Ryaboy, N. Moiseyev, *Phys. Rev. Lett.* **90** (2003) 013001.
- [171] A. F. Izmaylov, D. Mendive-Tapia, M. J. Bearpark, M. A. Robb, J. C. Tully, M. J. Frisch, *J. Chem. Phys.* **135** (2011) 23410.
- [172] R. D. Coalson, D. G. Evans, A. Nitzan, *J. Chem. Phys.* **101** (1994) 436–448.
- [173] J. S. Endicott, L. Joubert-Doriol, A. F. Izmaylov, *J. Chem. Phys.* **141** (2014) 034104.
- [174] C. C. Marston, G. G. Balint-Kurti, *J. Chem. Phys.* **91** (1989) 3571–3576.
- [175] N. Makri, W. H. Miller, *J. Chem. Phys.* **91** (1989) 4026–4036.

- [176] M. A. El-Sayed, *Accounts of Chemical Research* **1** (1968) 8–16.
- [177] J. Tatchen, N. Gilka, C. M. Marian, *Phys. Chem. Chem. Phys.* **9** (2007) 5209–5221.
- [178] F. Franco de Carvalho, B. F. E. Curchod, T. J. Penfold, I. Tavernelli, *J. Chem. Phys.* **140** (2014) 144103.
- [179] Y. Loquais, E. Gloaguen, M. Alauddin, V. Brenner, B. Tardivel, M. Mons, *Phys. Chem. Chem. Phys.* **16** (2014) 22192–22200.
- [180] A. L. Sobolewski, W. Domcke, C. Dedonder-Lardeux, C. Jouvet, *Phys. Chem. Chem. Phys.* **4** (2002) 1093–1100.
- [181] O. Christiansen, H. Koch, P. Jorgensen, *Chem. Phys. Lett.* **243** (1995) 409–418.
- [182] M. Schreiber, M. R. Silva-Junior, S. P. A. Sauer, W. Thiel, *J. Chem. Phys.* **128** (2008) 134110.
- [183] C. A. Guido, S. Knecht, J. Kongsted, B. Mennucci, *J. Chem. Theory Comput.* **9** (2013) 2209–2220.

Curriculum vitae

Personal data:

Date and place of birth: March 31, 1986, Ogulin, Croatia

Education:

- 07/2004-07/2009 Study of Chemistry at the Faculty of Science, University of Zagreb, diploma thesis: *Calculating the vibrational ground state tunneling splittings of formic acid dimer isotopologues* (in Croatian), supervisor Dr. Nađa Došlić
- 01/2010- Postgraduate study of Physical chemistry at the Faculty of Science, University of Zagreb

Employment:

- 07/2009-12/2009 Research Assistant at Ruđer Bošković Institute on the ReCompSoLS project
- 01/2010- Assistant at the Ruđer Bošković Institute, supervisor Dr. Nađa Došlić
- 10/2011-02/2013 Teaching Assistant in *Quantum chemistry* course at the Faculty of Science, University of Zagreb

Scholarships:

- 2005-2009 State scholarship, 'A' category
- 2007-2008 Rotary club Zagreb
- 2010 Ph.D. financial support from the Croatian Ministry of science, education and sports

Attended conferences and summer schools:

- 07/2014 *Gordon Research Conference: Atomic and Molecular Interactions*, Easton, Massachusetts (USA), poster presentation
- 06/2014 *CVTCT "FemEx-Oslo"*, Oslo (Norway), oral and poster presentation
- 03/2014 *International Workshop on the Micro/Nano-Technology and Materials for Environment and Power Energy Applications*, Osaka (Japan), oral presentation
- 08/2013 *Summer school 2013 Alexander von Humboldt Linkage: Program on Computational Life Sciences on Open Shell Species*, Primošten (Croatia), summer school, oral presentation
- 04/2013 *Faraday Discussion 163 Photo-initiated Quantum Molecular Dynamics*, Nottingham (UK), poster presentation

- 04/2012 *Multidisciplinary Endeavor in Nanobiology, Nanoscience and Environment*, Split (Croatia), summer school
- 10/2011 *Japanese-Croatian Workshop on Material Science*, Zagreb (Croatia), oral presentation
- 09/2011 *Workshop on Dynamics and Control of Atomic and Molecular Processes Induced by Intense Ultrashort Pulses - CM0702 WG2, WG3 meeting*, Debrecen (Hungary), oral presentation
- 05/2011 *European School on the Dynamics of Molecular Excited States Induced by Ultrashort Pulses, ZCAM 2011*, Zaragoza (Spain), summer school
- 09/2010 *1st Adriatic School on Nanoscience*, Dubrovnik (Croatia), summer school
- 08/2010 *Sustainable Sources of Energy*, Brijuni (Croatia), poster presentation
- 03/2010 *COST Training School on Molecular and Material Science Grid Applications*, Trieste (Italy), summer school
- 09/2009 *3rd Adriatic Meeting on Computational Solutions in the Life Science*, Primošten (Croatia), poster presentation
- 04/2009 *XXI Croatian Meeting of Chemists and Chemical Engineers*, Trogir (Croatia), poster presentation
- 08/2008 *Hydrogen: A Universal Saga*, Brijuni (Croatia), poster presentation

Short visits to foreign institutions:

- 03/2014 Osaka University in Osaka, Japan, group of Prof. Hideaki Kasai, part of the Croatian-Japan bilateral project
- 02/2014 Abdus Salam International Centre for Theoretical Physics, Trieste, Italy, invited visit
- 11/2012-12/2012 CEA Saclay, Gif-sur-Yvette, France, group of Prof. Michel Mons, part of the Croatia-French bilateral project and RBI-French embassy one month long scholarship
- 08/2012-09/2012 University of Rostock, Rostock, Germany, group of Prof. Oliver Kühn, part of the Croatia-German bilateral project
- 02/2011-03/2011 Osaka University in Osaka, Japan, group of Prof. Hideaki Kasai, part of the Croatian-Japan bilateral project
- 09/2010-10/2009 Friedrich-Alexander-University Erlangen-Nürnberg, Erlangen, Germany, group of Prof. Ana-Sunčana Smith, collaboration

Publications:

1. Marin Sapunar, Sermsiri Chaiwongwattana, Momir Mališ, Antonio Prlj, Aurora Ponzi, Piero Decleva, Nađa Došlić *Timescales of N-H bond dissociation in pyrrole: a nonadiabatic dynamics study* Submitted
2. Jurica Novak, Momir Mališ, Goran Zgrablić, Fulvio Parmigiani, Nađa Došlić *Ultrafast non-reactive deactivation induced by excited state hole transfer from retinal chromophore to counterion* Submitted

3. Deniz Tuna, Nađa Došlić, Momir Mališ, Andrzej L. Sobolewski, Wolfgang Domcke *Mechanisms of Photostability in Kynurenines: A Joint Electronic-Structure and Dynamics Study* Journal of Physical Chemistry B **119** (2015) 2112
4. Zlatko Brkljača, Momir Mališ, David M Smith, Ana-Sunčana Smith *Calculating CD Spectra of Flexible Peptides: An Assessment of TD-DFT Functionals* Journal of Chemical Theory and Computation **10** (2014) 3270
5. Momir Mališ, Yohan Loquais, Eric Gloaguen, Christophe Juvet, Valérie Brenner, Michel Mons, Ivan Ljubić, Nađa Došlić *Non-radiative relaxation of UV photoexcited phenylalanine residues: probing the role of conical intersections by chemical substitution* Physical Chemistry Chemical Physics **16** (2014) 2285
6. Momir Mališ, Yohan Loquais, Eric Gloaguen, Himansu S. Biswal, François Piuze, Benjamin Tardivel, Valérie Brenner, Michel Broquier, Christophe Juvet, Michel Mons, Nađa Došlić, Ivan Ljubić *Unraveling the Mechanisms of Non-Radiative Deactivation in Model Peptides Following Photoexcitation of a Phenylalanine Residue* Journal of the American Chemical Society **134** (2012) 20340
7. Jurica Novak, Momir Mališ, Antonio Prlj, Ivan Ljubić, Oliver Kühn, Nađa Došlić *Photoinduced Dynamics of Formic Acid Monomers and Dimers: The Role of the Double Hydrogen Bond* Journal of Physical Chemistry A **116** (2012) 11467
8. Nikola Basarić, Nađa Došlić, Jakov Ivković, Yu-Hsuan Wang, Momir Mališ, Peter Wan *Very efficient generation of quinone methides via excited state intramolecular proton transfer (ESIPT) to carbon atom* Chemistry - A European journal **18** (2012) 10617
9. Mirta Rubčić, Krunoslav Užarević, Ivan Halasz, Nikola Bregović, Momir Mališ, Ivica Đilović, Zoran Kokan, Robin S. Stein, Robert E. Dinnebier, Vladislav Tomišić *Desmotropy, polymorphism, and solid-state proton transfer: four solid forms of an aromatic o-hydroxy Schiff base* Chemistry - A European journal **18** (2012) 5620
10. Nađa Došlić, Vjerran Gomzi, Momir Mališ, Ivana Matanović, Juergen Eckert *Fluxionality of hydrogen ligands in $Fe(H)_2(H_2)(PEtPh_2)_3$* Inorganic chemistry **50** (2011) 10740
11. Anđela Šarić, Tomica Hrenar, Momir Mališ, Nađa Došlić *Quantum mechanical study of secondary structure formation in protected dipeptides* Physical chemistry chemical physics **12** (2010) 4678
12. Momir Mališ, Ivana Matanović, Nađa Došlić *A computational study of electronic and spectroscopic properties of formic acid dimer isotopologues* Journal of Physical Chemistry A **113** (2009) 6034